AD-A263 216

PL-TR-93-2027(II)

PROCEEDINGS OF THE SPACECRAFT CHARGING TECHNOLOGY CONFERENCE, 1989
VOLUME II

Editor:

R. C. Olsen

Naval Postgraduate School
Physics Department
MC 61-05
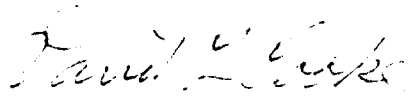Monterey, CA 93943

November 1989

DTIC
ELECTE
S APR 0 1 1993
E D

PHILLIPS LABORATORY
AIR FORCE MATERIEL COMMAND
HANSCOM AIR FORCE BASE, MA 01731-3010

93-06650

93 3 31 089

" This technical report has been reviewed and is approved for publication "

[signature]

DAVID L. COOKE
Contract Manager

[signature]

CHARLES P. PIKE
Branch Chief

REPORT DOCUMENTATION PAGE

Public reporting burden for this collection of information is estimated to average 1 hour per response, including the time for reviewing instructions, searching existing data sources, gathering and maintaining the data needed, and completing and reviewing the collection of information. Send comments regarding this burden estimate or any other aspect of this collection of information, including suggestions for reducing this burden. to Washington Headquarters Services, Directorate for Information Operations and Reports. 1215 Jefferson Davis Highway, Suite 1204, Arlington, VA 22202-4302 and to the Office of Management and Budget, Paperwork Reduction Project (0704-0188) Washington DC 20503

1. AGENCY USE ONLY (Leave blank)	2. REPORT DATE	3. REPORT TYPE AND DATES COVERED
	Nov 1989	Scientific Final 1 Oct 88-3 Nov 89

4. TITLE AND SUBTITLE

Proceedings of the Spacecraft Charging Technology Conference 1989, Vol 2

6. AUTHOR(S)

Editor: R.C. Olsen

5. FUNDING NUMBERS

PE 62101F
PR 7601
TA 760130
WU 760130CK
MIPR #FY71219000005

7. PERFORMING ORGANIZATION NAME(S) AND ADDRESS(ES)

Naval Postgraduate School
Physics Dept, MC 61-05
Monterey, CA 93943

8. PERFORMING ORGANIZATION REPORT NUMBER

9. SPONSORING/MONITORING AGENCY NAME(S) AND ADDRESS(ES)

Phillips Laboratory
29 Randolph Road
Hanscom AFB, MA 01731-3010

Contract Monitor: David L. Cooke/PL/WSSI

10. SPONSORING/MONITORING AGENCY REPORT NUMBER

PL-TR-93-2027 (II)

11. SUPPLEMENTARY NOTES

12a. DISTRIBUTION/AVAILABILITY STATEMENT

Approved for public release; distribution unlimited

12b. DISTRIBUTION CODE

13. ABSTRACT (Maximum 200 words)

The Spacecraft Charging Technology Conference was held at the Naval Postgraduate School, Monterey, California, from 31 October to 3 November 1989. This was the fifth in a series of meetings jointly sponsored by the Air Force and NASA to deal with spacecraft environment interactions. The meeting was attended by 108 people with 60 talks presented. The majority of the speakers have chosen to present their work in these two volumes. Volume 1 contains pages 1 through 333, Volume 2 contains pages 334 through 624.

14. SUBJECT TERMS

spacecraft, spacecraft charging, space environment, space plasma, interactions

15. NUMBER OF PAGES

300

16. PRICE CODE

17. SECURITY CLASSIFICATION OF REPORT	18. SECURITY CLASSIFICATION OF THIS PAGE	19. SECURITY CLASSIFICATION OF ABSTRACT	20. LIMITATION OF ABSTRACT
Unclassified	Unclassified	Unclassified	SAR

Table of Contents

PREFACE

The Spacecraft Charging Technology conference was held at the Naval Postgraduate School, Monterey, California, from 31 October to 3 November, 1989. This was the fifth in a series of meetings jointly sponsored by NASA and the Air Force to deal with spacecraft environment interactions. The meeting was attended by 108 people, with 60 talks presented. The majority of the speakers have chosen to present their work in this volume.

We wish to thank NASA and the Air Force for providing financial support for the meeting. This allowed funding for travel by 6 students, and the convenor's time. The Naval Postgraduate School provided the facilities, and the local chapter of IEEE provided invaluable administrative aid. My special thanks to Dr. S. Gnanalingam, Dr. Jeff Burl, and Lt. M. E. Young for their help prior to and during the meeting.

Richard Christopher Olsen
Naval Postgraduate School
14 January 1991

SPACE STATION FREEDOM SOLAR ARRAY PANELS PLASMA INTERACTION TEST FACILITY

Donald F. Martin and Kenneth D. Mellott

National Aeronautics and Space Administration
Lewis Research Center
21000 Brookpark Road
Cleveland, Ohio 44135

ABSTRACT

The Space Station Freedom and its Polar Orbiting Platform (POP) will operate in Low Earth Orbit (LEO). The electrical environment present at LEO (equatorial) consists of ionized species ranging in density from 10^3 ions/cm^3 to 10^6 ions/cm^3 dependent upon whether the environment is in the sunlight or sunshade period. The electrical environment present at LEO (polar) has a much lower ion density but contains a high energy electron flux which could cause surface charging.

The Space Station Freedom Power System will make extensive use of Photovoltaic (PV) Power Generation. The phase I power system consists of two PV Power Modules each capable of delivering 37.5 KW of conditioned power to the user. Each PV Module consists of two solar arrays. Each solar array is made up of two solar blankets. Each solar blanket contains eighty-two PV Panels. The PV Power Modules provide a 160 V nominal operating voltage. As such, the Space Station Freedom PV Modules will be the highest voltage photovoltaic power system ever used on an American spacecraft.

Previous research has shown that there are electrical interactions between a plasma

environment and a photovoltaic power source. These interactions appear to be related to both the plasma density and the source operating voltage. The interactions take two forms:

1. parasitic current loss - occurs when the current produced by the PV Panel leaves at a high potential point and travels through the plasma to a lower potential point, effectively shorting that portion of the PV Panel.

2. arcing - occurs when the PV Panel electrically discharges into the plasma.

The PV Solar Array Panel Plasma Interaction Test was conceived to evaluate the effects of these interactions on the Space Station Freedom type PV Panels as well as to conduct further research into these interactions.

The test article consists of two active solar array panels in series. Each panel consists of two hundred 8 cm X 8 cm silicon solar cells. The two panels are held together by a hinge pin and are electrically connected in series. The two panels in series provide the aforementioned 160 volts.

The test requirements issued by the Photovoltaic Power Module Division (which is responsible for the design, development and construction of the PV Module) dictated specifications in the following areas:

Plasma Environment/Plasma Sheath
Outgassing
Thermal Requirements
Solar Simulation
Data Collection Requirements

These requirements were incorporated into the design of the PV Plasma Interaction Test Facility. The facility consists of a vacuum tank, cage, solar simulator, cold wall, plasma sources, and a data acquisition/control system.

INTRODUCTION

The Space Station Freedom's nominal operating voltage for photovoltaic power sources has been selected as 160 volts. In order to qualify this operating point, it was necessary to test two full size Space Station Freedom type Photovoltaic Panels (PV Panels) each 420 cm X 40 cm (165" X 15") in a simulated low earth orbit (LEO) environment with respect to pressure, temperature, and plasma. Solar flux was also simulated but at 0.30 solar constant. The primary area of concern was the plasma environment which can cause two undesirable effects:

1.   **PARASITIC CURRENT LOSS**--This results when current from a photovoltaic array leaves the array at a high potential point and travels through the plasma to a low potential point, effectively bypassing the output of the array.

2.   **ARCING**--This results when a array electrically discharges into the plasma.

Both of these phenomena tend to be functions of the array operating voltage and the plasma density of the environment.

The test (which ran from March to October, 1989) was located in the Electric Power Laboratory (EPL--Building 301) at Lewis Research Center (LeRC). Vacuum Tank 5 was used to provide the LEO pressure simulation, a gaseous nitrogen (GN2) cold wall provided the temperature simulation, a light-bank provided the solar flux simulation and various types of plasma sources provided the plasma environment simulation. The data for the test was collected by a PC-based data acquisition system designed specifically for the test. The test is modeled on tests previously performed by the Power Technology Division at LeRC. This test was unique in that it utilized state-of-the-art, large-size solar cells (8 cm X 8 cm) that are planned for use on the Space Station Freedom's photovoltaic arrays. It is critical to ensure this technology can be safely incorporated onto the Space Station Freedom. This report will present detailed descriptions of the major components that constituted the facility for the PV Panel Plasma Interaction Test.

TEST DESCRIPTION

The test assembly was built on a large cage structure (see Fig. 1) which could roll in and out of the vacuum tank to decrease tank "down time." Most electrical connections used quick-disconnect type connectors for the same

reason. The two PV Panels were placed in this cage on a vertical plane along the vacuum tank's centerline. On one side, the PV Panels were illuminated by a solar simulator and on the reverse side they were cooled by a GN2 cold wall. The solar simulator was also cooled on its reverse side by radiation to a GN2 cold wall known as the solar simulator cooler. The PV Panels were electrically loaded using a variable resistance load bank with provisions for short circuit and open circuit conditions. Array temperatures were monitored and recorded by means of thermocouples mounted on the PV Panels positioned to provide optimal statistical data. A bias supply that could be connected to either the positive or negative terminal of the PV Panels, with either positive or negative polarity applied, was provided to drive the PV Panels positive or negative with respect to the voltage potential of the plasma (see Fig. 2). This bias supply was connected in series with the PV Panels. A digital storage oscilloscope was used to capture and record arc waveforms. Electrical parameters were recorded and displayed by a computer controlled data acquisition system. To improve test speed, accuracy, and repeatability, the computer also controlled variation of the test parameters. Automatic calibration features assured data validity.

Essentially, the test involved biasing the PV Panels to positive voltages with respect to plasma voltage potential and measuring/recording the current flow from the bias power supply to the array. This current represents the parasitic plasma current. The PV Panels were then driven negative (while recording plasma currents) until arcing occurred. These tests were done for plasma densities of 10^2 to 10^6 particles/cm^3 (10^3 to 10^7 particles/in^3). Finally, tests were done to investigate and characterize arcing. In order to provide baseline performance data of the PV Panels, they were flash tested at atmospheric pressure at the beginning of the test. This required illuminating the PV Panels with a high intensity (1 solar constant), short duration light source and placing a variable load across the PV Panels' output. This provided a complete current vs. voltage (I-V) curve for the array. The PV Panels were flash tested periodically throughout the test to verify their operational integrity.

CAGE

The photovoltaic test panels and all vacuum exposed support hardware for the PV Plasma Interaction Test were mounted on a self-supported aluminum structure referred to as the "cage" (see Fig. 1). Primarily, the cage was designed to fulfill two functions:

1. To support the vacuum exposed test components as a single transportable package

2. To provide appropriate positioning between the test article and the support hardware

By supporting the vacuum package on one structure which was easily inserted or extracted from the vacuum tank, the facility could accommodate other users by reducing tank "down time." Constructed of ASA 6061-T6 aluminum alloy channel, the cage structure rolled in or out of the tank on removable 304 stainless steel rails. The shape of the cage is approximately an octagonal cylinder and its dimensions are 4.3m H X 3.7m W X 5.2m L (14.0' H X 12.0'W X17.0' L).

To obtain a large volume to accurately simulate the plasma environment of LEO, all test support hardware was required to remain clear of a 168 cm (66") region around the PV Panels called the "plasma sheath." The cage allowed the array to be mounted within the plasma sheath and also provided clearance from the diffusion pump protrusions near the bottom of the vacuum tank.

SOLAR SIMULATOR

The solar simulator (see Fig. 3) was designed to provide a 0.20 solar constant --275 W/m^2 +/- 10% (25 W/ft^2)--within 168cm (66") of the solar array test article while minimizing the amount of heat flux transmitted to the cold wall. The solar simulator was required to evenly illuminate an area of 420 cm X 80 cm (165" X 30") which was the area of the test article.

Two hundred and fifty-two (252) type 'DED' Multi-Mirror Phillips lamps were chosen for use on the solar simulator. These bulbs reject 60% of their infrared (IR) output to the rear. The lamps were chosen for use on the solar simulator based on the following criteria:

1. more optically efficient than line voltage lamp
2. low wattage
3. operation at full voltage possible which would result in good spectral characteristics
4. will not overheat at full voltage
5. ability to be mounted through a solid panel so that no shielding of electrical connections from the plasma environment would be needed.
6. narrow beam approaches a collimated light source.

Sample bulbs were vacuum tested to ensure longevity under test conditions. The bulbs lasted the life of the test.

The solar simulator was controlled by adjusting the output voltage of eight (8) Sorensen DCR 150-70A and two (2) Sorensen DCR 40-250A DC power supplies used to provide power (20 KWe). The supplies were individually monitored and controlled. Bulb burnout was detected by monitoring and comparing the current flow through parallel strings of lamps. It was necessary to calibrate the power supply settings for each operating point. This was done by monitoring the current output of a calibrated solar cell that was swept across the area of the PV Panel at atmospheric conditions and adjusting each supply until the flux met specifications. Power supply settings were then recorded.

After initial operation in vacuum, it was discovered that bulb base temperatures were exceeding manufacturers recommendations. This problem was rectified by adding cooling to the face plate of the solar simulator. This was done by bolting square tubing to the face plate and passing compressed air through it.

COLD WALL

To ensure that the PV Panels maintained an operating range of +20°C to +45°C (+68°F to +113°F), a cold wall (see Figs. 4,5,6) that provided 28 m^2 (306 ft^2) of radiative heat-absorbing surface at -73°C (-100°F) was used to remove heat from the PV Panels. One source of heat was the solar simulator which subjected the PV Panels to a significant heat input (5.0 kWt nominal). In addition to the cold wall, a solar simulator cooler was provided to absorb heat directly from the rear of the solar simulator to reduce the incidence of stray heating.

The cold wall used a regenerative blower to circulate gaseous nitrogen through fin-tube aluminum extrusions to provide the heat-absorbing surface (see Fig. 5). The gas temperature was controlled by injecting liquid nitrogen (LN2) as needed, and by venting GN2 to maintain the 10 PSIG operating pressure. LN2 use was 640 l/hr (170 gal/hr) to maintain operating temperature.

The cold wall system was controlled by means of two independent single-input closed-loop process controllers. They controlled the position of the LN2 inlet valve and GN2 vent valve respectively. The blower output pressure was sensed by means of a high output pressure transducer. The cold wall exit temperature was sensed by means of a type 'T' thermocouple. These two parameters were the control variables. Each of these signals went to a separate Process Controller. The units accepted a variety of inputs and provided an output of 4-20ma based on a PID control algorithm. The current outputs of the

controllers went to Electro - Pneumatic (EP) transducers which converted the electrical signal into a pneumatic pressure of 3-15 psi. The pneumatic signals were used to drive the liquid nitrogen valve and the vent valve. The system was designed for fail-safe operation and included such safety features as:

1. Each valve failed to a safe condition under loss of electrical power or air pressure.

2. Loss of electrical power to gaseous nitrogen blower resulted in system shutdown.

3. A thermocouple was used to detect LN2 accumulating in the cold wall. If detector was tripped, system shutdown resulted.

4. If the above LN2 detector tripped and the LN2 valve failed to close, an alarm sounded and the operator was instructed to manually close the LN2 valve.

5. If the LN2 detector failed to detect liquid nitrogen, there was a second separate detector that activated which instructed the operator to shut the cold wall system down.

6. If the facility lost power, a battery powered alarm notified the operator to close the LN2 valve.

7. If the pressure level of the vacuum tank exceeded a setpoint, the cold wall system shut down.

8. The system was protected by means of electrical relays and burst disks from being started incorrectly or operated in an unsafe manner.

PLASMA SOURCES

The PV Plasma Interaction Test utilized two types of plasma sources to provide the range of densities and types of plasma desired for this test.

CHAMBER DISCHARGE TYPE

Six (6) Pennington-style, hot filament, chamber discharge type plasma sources (see Fig. 7) were used (see Fig. 6) to provide the low density plasma--10^2 to 10^4 particles/cm₃(10^3 to 10^5 particles/in³). The mechanism of plasma production with this source is as follows. Argon gas is introduced into the discharge chamber at a very low flow rate--10^{-9} standard cm³/sec(10^{-10}) standard in³/sec)--and is passed over a hot filament. High energy electrons from the filament strike the argon atoms and remove an electron leaving a positively charged argon ion. A coil around the chamber produces a magnetic field which causes all electrons to travel in a spiral path from the filament to the anode. This longer path length produces a more efficient plasma, as a higher percentage of the atoms are impacted by electrons. Electrons freed from atoms have sufficient energy level to ionize other atoms that they collide with. This cascading effect causes a sharp rise in the anode current as the freed electrons join the electrons from the filament. This rise in anode current (300%+) indicates the production of plasma. There is no accelerating voltage for the plasma. Discharge is accomplished by the higher pressure inside the chamber due to the introduction of the argon. This type of plasma source is controlled by adjusting the DC power supplies that provide electrical power to them. The sources were positioned asymmetrically along the cage.

DIVERGENT FIELD TYPE

A 30 cm diameter J-Series divergent field ion thruster (without the high voltage extraction optics) was utilized for this test to provide the high density plasma--10^5 to 10^6 particles/cm³(10^6 to 10^7 particles/in³). This source creates plasma by passing argon down a tube (hollow cathode) and initiating a catalytic reaction to produce plasma (see "Plasma Contactors for Electrodynamic Tether," NASA Tech Memo 88850 for further description). This acts as a keeper or sustainer anode. Gas is then injected around the perimeter of the source which has a positive potential relative to cathode common. This acts as a discharge chamber which provides the high density plasma. The source was placed at one end of the vacuum tank along the centerline of the cage.

DATA ACQUISITION AND INSTRUMENTATION

The PC-based data system--IBM-AT equivalent--(see figs.10,11) used for this test made extensive use of the IEEE-488 General Purpose Interface Bus (GPIB). This enabled instruments of different manufacture to be utilized simultaneously to make a highly specialized test and measurement system with a common interface to a computer. The instruments used for this test and their functions are as follows:

1. KEITHLEY 177 (DIGITAL MULTIMETER)--Array Bias Current measurement

2. KEITHLEY 617 (ELECTROMETER)--Plasma Characterization

3. TEKTRONIX 2430A (DIGITAL STORAGE OSCILLOSCOPE)--Arc Detection and Characterization

4. SORENSEN DAP 488 (DIGITAL TO ANALOG PROGRAMMER)--Bias Power Supply Control

The data system also made use of other computer interfaces. Computer interface cards made by Metrabyte Corporation allowed the computer to read thermocouples and control relays. An Analog-to-Digital (A/D) card was used to read/record such miscellaneous data points as bias voltage, load current, load voltage, electron acceleration voltage, and array end potentials (by reading scaled output of Trek non-contacting voltage probes). All of the data parameters were saved to disk in ASCII format so as to be accessible to such programs as Lotus 1-2-3. In order to characterize the plasma (density, electron temperature,ion temperature, voltage potential), eleven (11) Langmuir probes were used. They were monitored individually using the Keithley 617 mentioned above and a relay card controlled by the computer (see above). The PV Plasma Data System was controlled by software written specifically for this test. This software provided a menu driven program which allowed real time display of performance parameters and other data points as well as provisions for alarm setpoints and graphic displays.
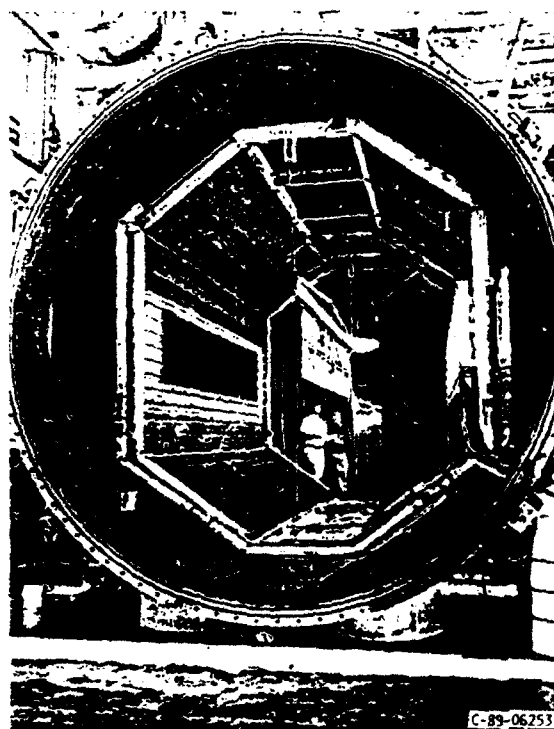
FIGURE 1. - PV PLASMA INTERACTION TEST RIG.
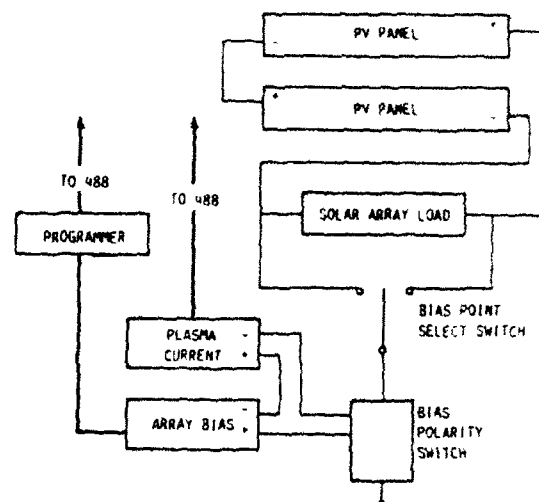
FIGURE 2. - BIAS SUPPLY CONNECTIONS.
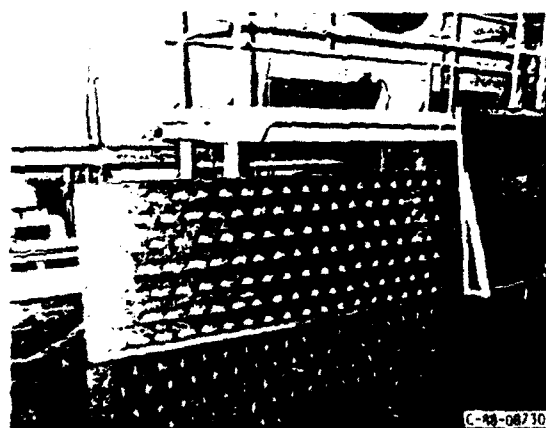
FIGURE 3. - SOLAR SIMULATOR.
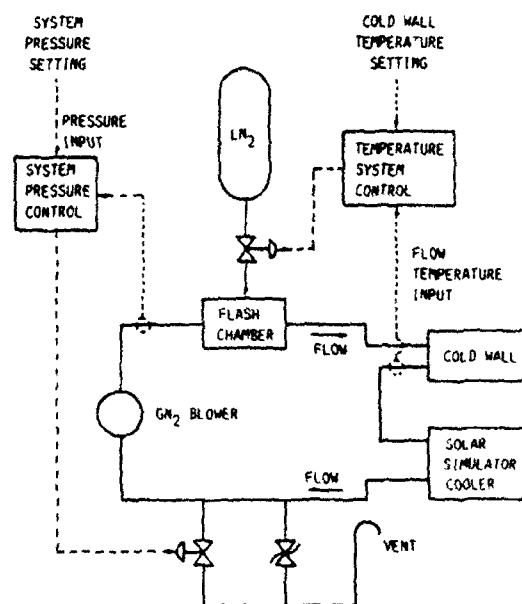
FIGURE 4. - COLD WALL SYSTEM SCHEMATIC.

243
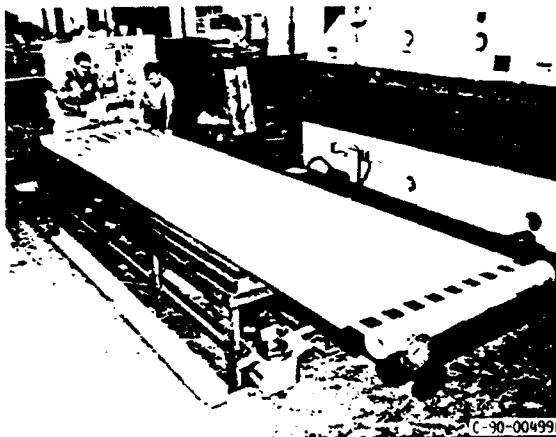
FIGURE 5. - COLD WALL PANEL.
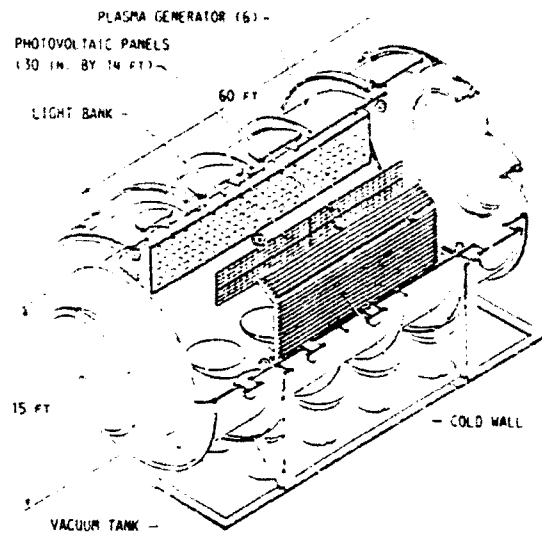
FIGURE 6. - COLD WALL ILLUSTRATION.
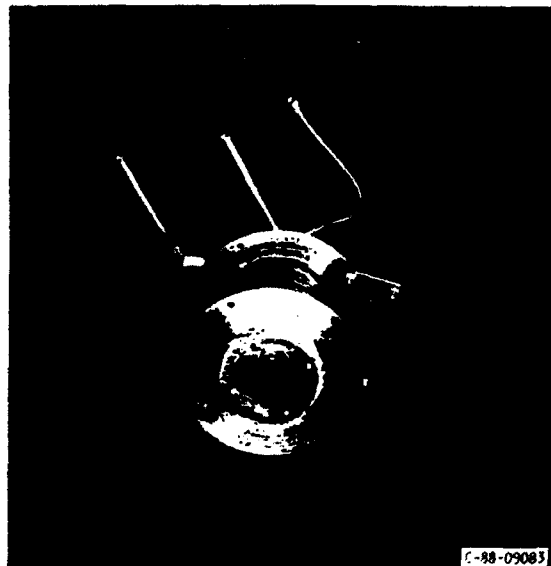
FIGURE 7. - PENNINGTON TYPE PLASMA SOURCE.
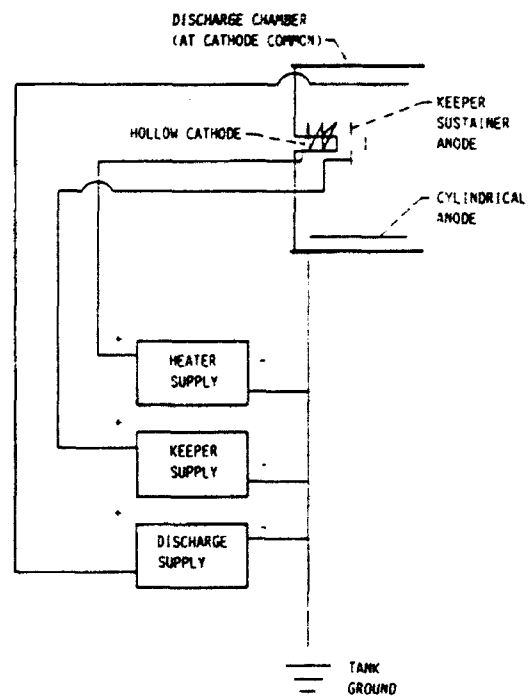
FIGURE 8. - DIVERGENT FIELD TYPE PLASMA SOURCE SCHEMATIC.

344
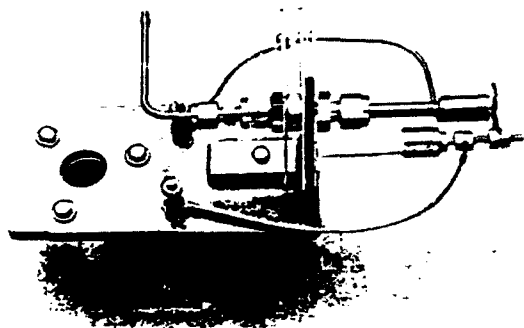
FIGURE 9. - HOLLOW CATHODE PLASMA SOURCE.
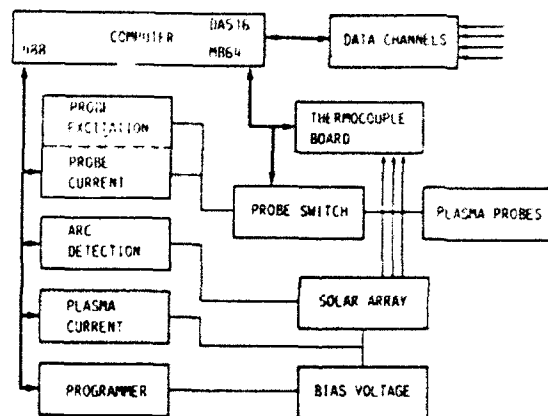
FIGURE 10. - DATA SYSTEM DIAGRAM.
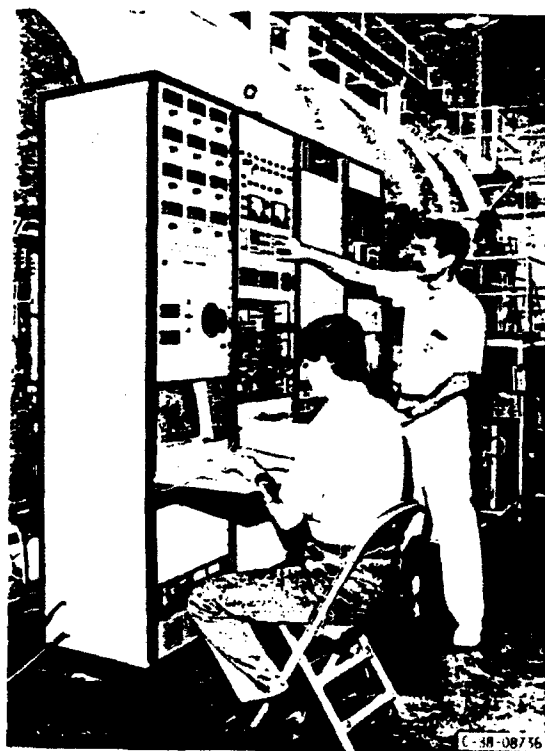
FIGURE 11. - DATA SYSTEM.

345

SAMPIE - A SHUTTLE-BASED SOLAR ARRAY ARCING EXPERIMENT

Dr. Dale C. Ferguson
Principal Investigator
NASA Lewis Research Center

Abstract:

SAMPIE (the Solar Array Module Plasma Interaction Experiment) is a joint NASA/ESA Shuttle flight experiment to investigate arcing thresholds and plasma collection currents for modern solar array designs in low Earth orbit (LEO). Previous ground and space flight tests have shown that anomalous current collection ("snapover") at high positive voltages and arcing at high negative voltages may be expected for solar arrays in LEO. New, high power solar arrays being considered for use in LEO use new materials and construction techniques, which may change arcing thresholds and collection currents. SAMPIE has been manifested for launch aboard the Shuttle in late calendar year 1994. The experiment will be justified on the basis of previous ground test results and the results of flight experiments PIX and PIX-II, and on the new materials and construction techniques for modern, high power solar array designs. Phase B design and definition are now in progress. Considerations which influence the experiment design w :l be discussed, and objectives and constraints will be identified.

I. Background and Justification for SAMPIE

Numerous ground experiments and two flight experiments (PIX I and PIX II, Grier and Stevens, 1978, and Grier, 1983) have shown two ways that solar arrays interact with the plasma. First, they collect current from the plasma. Because the mass of an electron is much smaller than the mass of a positive ion, the electron current collected at positive bias relative to the plasma is much greater than the ion current collected at comparable negative biases. At positive biases greater than about two hundred volts relative to the plasma potential, insulating surfaces surrounding exposed conductors behave as if they were themselves conductors, due to the phenomenon called "snapover", greatly enhancing electron collection. On an operating solar array, the currents collected from the plasma appear as losses in the array operating current and in the efficiency of the array. Furthermore, the currents collected from the plasma determine the potential at which different parts of the array will "float". It is important to determine the manner in which solar arrays collect current from the space plasma, in order to evaluate array operating efficiency and to predict and control spacecraft potentials.

Secondly, at high negative biases relative to the surrounding plasma, solar arrays arc into the plasma, causing disruptions in the current produced, electromagnetic interference, and large discontinuous changes in the array potentials. Both ground tests and flight tests have indicated that for arrays having silver-coated interconnects a threshold potential relative to the plasma exists, below which no arcing occurs, at about -230 volts (Ferguson, 1986). There are theoretical reasons and some indications from ground tests (Jongeward et al, 1985, Snyder, 1986) that different conducting materials exposed to the plasma have different arcing threshold potentials. It is

important to determine the arcing threshold, arc strengths, and arc rates for solar arrays operating at high negative potentials in the space plasma.

High power level solar arrays now being considered for space applications will operate at high end-to-end voltages to minimize the array current. A major driver toward higher operating voltages is the mass of cabling which must be lofted into orbit to transmit the electrical power from the arrays at high efficiencies. Because the resistance of the cable is a strongly decreasing function of the cable mass per unit length, and because the cable losses are proportional to the current squared, it is advantageous to operate at high voltages, where the currents will be low, and a larger resistance per unit length (less cable mass per unit length) may be employed. A further factor in operating at high voltage and low current is that magnetic interaction effects (such as magnetic torques and magnetic drag) are minimized with minimum current operation.

To save weight and manufacturing cost, new solar arrays being considered for NASA and ESA missions are of a new design and utilize new materials, which may change the currents collected and the arcing threshold. In particular, new arrays being considered for NASA missions have solar cells with interconnects in the back, bonded to lightweight flexible substrates, employing copper traces which may become exposed to the space plasma. All of the solar arrays which have been flown in space to-date have had silver-coated interconnects exposed to the plasma between cells on the front of a rigid substrate.

A full panel of new array technology solar cells planned for Space Station Freedom application have been shown to arc at biases as small as -210 V, relative to the plasma, in ground tests at the Lewis Research Center (Nahra, Felder, and Staskus, this session). No in-space tests of these arrays have been done, or are planned. The Space Station Freedom array nominal operating voltage of 160 V is uncomfortably close to the 210 V arcing threshold found in these ground tests and may be exceeded when the arrays come out of eclipse.

Comparison of ground tests and flight tests of the old-technology solar arrays have shown many differences between their behavior in vacuum tanks and in the real space plasma. On PIX II, for example, the shape of the collection current versus voltage curves were quite different in space than on the ground, and two different types of curves were obtained, depending on whether the arrays were in the ram (forward facing) or wake (backward facing) orientation. Although the same arcing threshold seems to obtain for the PIX II cells in orbit and in the ground plasma, the arc rate versus potential above the threshold potential was quite different (and much higher at voltages less than about 1000 V) in the space plasma than on the ground. The origin of the discrepancies is not known, due to inadequacies in the theory of the arcing phenomenon (Jongeward et al, 1985, and Hastings et al, 1989). Thus, while ground tests may give us information about the arcing threshold potential, they will not give us the detailed information necessary to allow confident design of large future NASA and ESA solar arrays.

For these reasons, it is important to determine the dependence of plasma collection currents, arc rates and strengths on potential relative to the plasma, and arcing potential thresholds for new technology solar arrays in a real space plasma through one or more space flight experiments. The relevant

plasma parameters, such as electron density and temperature, and spacecraft factors, such as orientation relative to the velocity vector, and potential relative to the plasma, must be concurrently measured along with the array performance, in order to understand the interactions which take place, and to enable confident and reliable design and operation of future NASA and ESA space power systems. SAMPIE will help enable the design of such systems.

II. SAMPIE Objectives

The objectives of SAMPIE are to:

1) Determine the voltage thresholds at which arcing occurs on the NASA and ESA solar array test modules and the arc rates and strengths.
2) Determine the plasma current collection characteristics of the solar array test modules.
3) Measure a basic set of plasma parameters to aid in data analysis.

III. Description of SAMPIE

SAMPIE will consist of two small solar arrays, individually biased to high potentials relative to the plasma, mounted on the end of a collapsible tube mast (CTM) which may be extended up to 15 meters from the payload bay of the Space Shuttle (see Figures 1 and 2). The CTM is of ESA design and construction, and will impose operational and design constraints on SAMPIE. One of the solar arrays will be of NASA chosen design and construction, and the other will be of ESA design and construction. The arrays will be biased by a power supply to LC voltages as high as -700 V and +700 V with respect to the array structure ground, so that the arrays will be at high potentials with respect to the space plasma. While the arrays are biased, instruments will detect the occurrence of and measure the strength of any arcs from the arrays to the plasma, and will measure the amount of current being collected from the plasma. To characterize the plasma and other test conditions, other instruments will measure the degree of solar insolation and the plasma electron density and temperature, as well as the potential of the solar array structure ground with respect to the plasma, this being a minimum set of conditions to be measured. The orientation of the solar arrays with respect to the Shuttle velocity vector will be known at all times, as well as the times and conditions of Shuttle reaction control thruster events. This information will be obtained from Shuttle operations logs or tapes.

SAMPIE will be performed with the CTM at full extension and at two or more intermediate extensions, including zero extension, to derive information about the influence of the large Shuttle Orbiter body on the ram and wake conditions seen by the arrays, and on the plasma surrounding the Orbiter. While at full extension, the maneuvering capability of the Shuttle will be limited to the use of the vernier thrusters only, for structural dynamics reasons. A further limitation on Shuttle operations is imposed by the fact that the experiment ground will be tied to Shuttle Orbiter ground, which is tied to the plasma potential mainly through about 30 m^2 of exposed metal on the Shuttle Main Engines (Sasaki et al, 1986). When the arrays are biased to positive voltages higher than about 100 volts, the orientation of the Orbiter will be restricted such that the Main Engine nozzles are not in the vehicle wake, for large vehicle potential excursions would occur at those times, due to the low collectible ion density in the Orbiter wake. An operational constraint may also be imposed on the conduct of the experiment by the

prospect of the Orbiter charging to high potentials. The maximum desirable positive array bias will be considered under IV. Scientific and Technological Constraints.

SAMPIE will be mounted on a Hitchhiker attachment plate within the Orbiter payload bay, and will use the standard Hitchhiker data recovery systems. Because of limitations on the size and number of wires for power and data transmission which may be extended with the CTM, as much as possible of the electronics necessary to perform the experiment and diagnose experiment conditions will be placed on the end of the mast along with the solar arrays. Mass limitations on the package at the end of the CTM are imposed by structural dynamics, and a maximum mass of 15 kg on the end of the mast has been agreed to by NASA and ESA.

SAMPIE's operational mode will be to bias one array segment to a certain voltage for a certain length of time, measuring the current collected and the times and strengths of arcs as they occur, and simultaneously to measure the diagnostics of solar insolation, plasma conditions, and vehicle potential, and then to move on to another bias voltage, measuring all of the same things, repeating until all of the design bias voltages have been covered. Then the other array segment will be tested in a similar fashion. The arrays will be tested at each CTM extension in a wide variety of vehicle orientations with respect to the sun and the vehicle velocity vector in order to determine effects on collection currents due to solar insolation, ram and wake conditions at different distances from the Orbiter body, and aspect with respect to the Earth's magnetic field. SAMPIE will have control of the Orbiter orientation.

Because the solar arrays at high negative potentials relative to the plasma will produce arcs, which are known to emit broadband electromagnetic interference (Leung, 1985), the capacitance of the arrays to space will be tailored to produce arcs of acceptable size and EMI production. Also, a waiver of the EMI specs for Orbiter payload bay experiments will be necessary.

SAMPIE will benefit from the prior experience gained at the Lewis Research Center in design and construction of the SPHINX, PIX, PIX-II, and VOLT-A plasma interaction space flight experiments.

IV. Scientific and Technological Constraints

SAMPIE will be placed in an orbit which keeps it from entering the auroral oval, for occasional strong high energy electron fluxes and low thermal electron fluxes there make conditions hard to measure, unpredictable, and therefore not ideal for this experiment. The Orbiter orbital inclination during SAMPIE will be restricted to less than about 58° to the equator.

SAMPIE is now manifested for flight in 1994, shortly after the maximum of the solar activity cycle, in 1992, but there is a possibility that it will fly in 1993. The plasma density in low Earth orbit depends on the level of solar activity, peaking at times of solar maximum. Recent estimates of the level of solar activity expected at the peak in 1991 or 1992 place the level unusually high, with some estimates of the averaged sunspot number as high as 200. Runs of the IRI-86 computer model for the ionosphere (Rawer and Bradley, 1987) place the maximum daytime electron density for such high solar activity levels as high as 3.8×10^6 electrons per cubic centimeter, at electron temperatures

between 1100 K and 2300 K. Nighttime electron densities are predicted to be as low as 1.6×10^5. Under these conditions, the plasma will be capable of maintaining electric fields at low potentials over a distance of approximately one Debye length, which is given by equation (1),

$$\text{lambda}_d = (kT_e/4\pi \, ne^2)^{1/2} = 7.43 \times 10^2 \, (T_e/n)^{1/2},$$

where T_e is the electron temperature in eV, k is the Boltzmann constant, pi = 3.14159..., e is the charge of the electron, and n is the electron density in cm^{-3}. Placing representative values from runs of the IRI model in the above equation, one finds a minimum Debye length from 0.12 cm at 1100 K to 0.17 cm at 2300 K. Openings in the experiment electronics enclosure will be smaller than the minimum Debye length to prohibit plasma interactions with the experiment electronics.

It is be desirable for SAMPIE to place its plasma diagnostic instruments outside the plasma sheath (the sheath being the region where the plasma is significantly disturbed by the applied electric fields) of the array being biased. For large potentials, using orbit-limited collection (see Galofaro, this session) the plasma sheath radius may be taken as the radius of a sphere with the same area as the area of the collecting array segment, multiplied by the square root of the quantity, the applied bias in volts divided by the electron energy in eV. Under ram conditions, the ion sheath may be somewhat smaller than this (perhaps 1/4 the radius), because the flux of ram ions is greater than the thermal flux. For a voltage of 700 V, this implies a sheath radius of more than a meter under all reasonable plasma densities. At even moderate voltages, such as two hundred volts, the sheath will extend for a distance of more than 45 cm, using orbit-limited theory.

Alternatively, one may assume that the flow of charged particles to the solar arrays is limited by a build-up of space charge around the collecting array. In this case, calculations indicate that at 200 V, the sheath radius will be at least 30 cm for electron collection and/or ion collection without ram ion impingement, and at least 9 cm collecting ions in the ram direction. In the case of electron and non-ram ions, this indicates that the sheath radius is much greater than the array dimensions discussed below, so that orbit-limited theory will apply. Recent experiments of Thiemann and Bogus (1986 and 1988), indicating much smaller plasma sheaths, may have been influenced by electron ionization of the dense background gas, or by ram ion impingement in their high energy streaming plasma. The discrepancies will be investigated as part of SAMPIE by means of NASCAP/LEO.

A preliminary mechanical design of the array package to be placed on the end of the CTM is shown in Figures 3, 4, and 5. It may not be possible to have the Langmuir probe or other instruments measure the undisturbed plasma density and temperature and "ground" potential on the array structure when an array segment is being biased to significant voltages because the plasma sheath will have dimensions exceeding the dimensions of the array structure. Between array bias voltages the array bias will be switched off for a short time, to allow sensors mounted on the structure to measure the undisturbed plasma, before going on to the next bias voltage.

Calculations of the rate of change of plasma parameters in the IRI model of the ionosphere show that within 5 degrees of orbit, the plasma densities and temperatures may change by 25%. Since it is desired to measure the plasma

conditions to within about 50%, each bias voltage interval will be restricted to less than about 10 degrees in the orbit, or about 3 minutes of time.

Of great interest to SAMPIE is a calculation of the floating potential of the Shuttle Orbiter when the array segments are biased to high voltages. Not only do the true potentials of the array segments with respect to the plasma depend on the potential of the spacecraft "ground" relative to the plasma, but it may be possible to charge the Orbiter up to potentials where non-array material junctions could arc into the plasma. As this is clearly undesirable, I will perform a calculation of the expected Orbiter floating potential. In this first calculation, I will assume that the plasma sheath dimensions greatly exceed the collecting surface dimensions, so that current collecting surfaces collect current according to the spherical orbit-limited collection law,

$$I = J_o A (1 + eV/kT),\qquad (2)$$

where A is the area of exposed conductor, e is the electron charge, V is the applied potential relative to the plasma, k is the Boltzmann constant as before, and T is the temperature of the collected species (Chen, 1965). Here, J_o is the so-called "thermal current density", given by the expression

$$J_o = (ne/4)(8\ kT/pi\ m)^{1/2},\qquad (3)$$

where n is the density of the charged species, k and T are as defined before, and m is the mass of the charged species. Evaluating J_o for electrons at the maximum density of 3.8×10^6 cm^{-3}, it may be seen that

$$J_o = 3.1 \times 10^{-6}\ \text{amps/cm}^2\ \text{at 1100 K, or}$$
$$4.5 \times 10^{-6}\ \text{amps/cm}^2\ \text{at 2300 K.}$$

Because of the difference in atomic oxygen ion mass and electron mass, for ions,

$$J_o = 1.8 \times 10^{-8}\ \text{amps/cm}^2\ \text{at 1100 K, or}$$
$$2.1 \times 10^{-8}\ \text{amps/cm}^2\ \text{at 1400 K.}$$

There is evidence from ground tests that the plasma current collection characteristics of solar arrays depends on the potential of the surrounding material, and also on the speed with which the bias is applied (Carruth, 1987). The surrounding material may alter the orbits of the electrons to be collected, and thus change the currents reaching the exposed biased conductors. For this reason, to simulate a large solar array, where large adjacent areas are at about the same potential, it is best to bias up both array segments when measuring the electron collection current of either of them, to give a surrounding potential nearly the same as that of the array segment being measured.

Setting the electron and ion currents equal, and approximating the distribution of voltages on the Orbiter as a high negative voltage area at one negative potential and one high positive voltage area at one positive potential, equation (3) yields

$$V_+/V_- = -(A_-/A_+)(J_i/J_e)(T_e/T_i),\qquad (4)$$

where the subscript e refers to electrons, i to ions, and + and - to negative and positive potential collecting areas. At low voltages, the array collecting areas will be the areas of exposed conductor, which for solar arrays even of the old technology comes out about 5% of the array area. However, under snapover conditions, at positive array potentials of more than about 150 volts, the entire biased array area starts to behave as if it were exposed conducting material, and the effective collecting area of the array is greatly increased over the interconnect area. Taking the electron and ion temperatures equal, and the ratio of $J_-/J_+ = 171$, as it is for an atomic oxygen plasma in LEO, and assuming a biased array electron collecting area of 1000 cm^2 and an area of 30 m^2 for the Shuttle Orbiter, under snapover conditions,

$$V_+/V_- = -1.75.$$

Thus, under snapover conditions on the array segment, the Orbiter is likely to charge up to a potential comparable to the potential on the array segment. Quantitatively, if the array segment is biased to +300 V with respect to the plasma, V_-, the Orbiter potential, becomes -171 V, a potential where it is unknown whether arcing could occur from the Orbiter to the plasma. Laboratory measurements made by the late J. Staskus, of LeRC, on new technology solar arrays (Staskus, 1988), show that at a potential of +200 V relative to the plasma, only about 30% of the cell area acts as collecting area, but at +300 V, nearly all of the cell area acts as a collector. In practical terms, this implies that to keep the Orbiter potential, V_-, lower than about -75 V, the Skylab proven "safe" operating potential to avoid arcing, the array potential relative to the plasma must be limited to about +260 V, and the array bias relative to the Orbiter must be limited to below about +335 V.

A somewhat more realistic calculation takes account of the fact that the main engine nozzles of the Shuttle, where the ion collection takes place, are much larger in dimension than the ion sheath will be at realistic Shuttle potentials. The currents collected at this end will then be space charge limited, rather than orbit limited, as they will be at the electron collecting array end. Also, the flux of ions onto the Main Engine nozzles due to the Orbiter velocity will exceed the thermal flux, modifying the size of the ion sheath and the currents collected. A preliminary calculation indicates that the Shuttle may float at -75 V when the array is at +240 V relative to the plasma, putting a possible limit on the maximum positive array bias voltage of 315 V. This calculation depends sensitively on the ion density hitting the nozzles, however. Further calculations using NASCAP/LEO are required to place realistic constraints on the experiment.

A possibly more serious limitation on the positive bias of the arrays will be current limitations on practical power supplies. Again, using Staskus's measurements, the thermal current is collected at a potential of about +150 V. This corresponds to about 3 mA, for a SAMPIE 1000 cm^2 array at 3.7×10^6 cm^{-3} and a temperature of 1100 K. At about +200 V, the current in Staskus's experiments increased to about 3/10 the full snapover current, or about 1.8 A in terms of SAMPIE. At +300 V, full snapover was reached, implying currents of several amps and power levels of over 1000 W, clearly impractical for the mass and power constraints on the SAMPIE power supply. One might expect that at about +175 V potential, the array may sometimes be drawing as much current as a 100 mA power supply (for example) could provide.

Using equation (4), and assuming that at this potential, the effective array current collecting area is about 300 cm^2, gives $V_- = -30$ V. Then V_+-V_-, the bias voltage, is 205 V.

From these considerations, it appears that a positive bias of from +205 V to +335 V is the maximum practical for the bias voltages which may be used in SAMPIE. This will restrict the ability of SAMPIE to explore the snapover regime fully, but under ordinary conditions, voltage limitations on arrays imposed by the possibility of arcing on the negative end may make snapover unreachable on the positive end, so that space measurements of full snapover may not be as immediately important as measurements of arcing thresholds. Ground tests may help further illuminate the snapover voltage for the new technology solar cells, and computer modeling may help to specify the maximum usable bias voltage in SAMPIE. On SAMPIE, since instruments will be measuring the "ground" potential V_- relative to the plasma, it may be possible to design so as to stop increasing the array positive bias when the Shuttle Orbiter goes a specified number of volts (such as -75 V), away from plasma potential.

On the negative bias side, constraints on the experiment are imposed by the expected arc rate of the solar panels. In the only quantitive, large scale ground tests of new technology, welded-through interconnect solar panel arc rates to date, Norman Grier's (1984) measurements may be interpreted to yield an arc rate versus voltage law of

$$R = 6.6 \times 10^{-27} \, V^{8.1} \, n \, T^{0.5} \, m^{-0.5},$$

where T is the plasma temperature in eV, V is negative potential in volts, n is the plasma density in cm^{-3}, and m is the ion mass in amu (Ferguson, 1986). Taking $n = 3.8 \times 10^6$, the maximum expected in orbit, $T = 5$ eV (the ram ion energy), and $m = 16$ (atomic oxygen), one finds that the expected arc rate at -700 V is 1552 arcs per second! Because of the strong dependence of arc rate on voltage, the expected arc rate drops to 0.06 arcs per second at -200 V, and 0.00022 arcs per second at -100 V.

Ground experiments done by David Snyder, of LeRC, have shown (Snyder, 1986) that for simulated silver solar cell interconnects, the potential after arcing drops to about -230 V, the same as the arcing voltage threshold found from PIX II and ground tests. Similar tests done for copper, the material likely to be exposed to the plasma in the new technology solar cells, show that the potential after arcing drops to a much lower voltage, on the order of -100 V, suggesting that the arcing threshold for copper may be as low as -100 V. Thus, it is desirable for SAMPIE to be able to measure arc rates as low as they may be at -100 V in orbit.

For a single arc at -100 V at the arc rates calculated above, SAMPIE would need to dwell at -100 V for 76 minutes, the greater part of a complete orbit, even at the maximum predicted plasma density. This seems to be impractical, given the time constraints on any experiment in orbit. Because of the strong dependence on voltage, however, a dwell time of only about 20 minutes would be necessary to expect one arc at -120 V. Thus, an experiment timeline has been set up which allows at least a twenty minute dwell time at -120 V, and correspondingly shorter times at higher voltages. SAMPIE will not to test for arcs at a voltage greater than -600 V. At this voltage, the arc counter may be filled up at the end of two seconds, and it may be impractical to reset the high voltage power supply on a time scale shorter than a few

milliseconds, as will be seen below. To follow the plasma density during the long dwell times it may be necessary to break them up into increments of 3 minutes or less, with Langmuir probe sweeps in between.

To keep the solar arrays from being damaged by large arcs powered by the high voltage power supply, a large impedance will be placed in the bias voltage circuit, between the high voltage power supply and the biased array segment. This will isolate the array segment from the power supply during the short duration arcs. To tailor the size of the arcs to something that the transient detector can comfortably detect, the capacitance of the array segment to the Orbiter will be specified. These considerations limit the ability of circuit to recover rapidly after an arc takes place, and may limit the highest negative voltage to be used in arcing studies because of the expected high arc rates at high negative voltages. Because the arcs are likely to last for about 20 microseconds at the most, SAMPIE will have an RC time constant in the bias circuit of at least 100 microseconds.

There is evidence that the arc rate of a solar array in a plasma decreases to a steady state value on a time scale of a few hours (Miller, 1983, Ferguson, 1986). Also, outgassing from the Orbiter payload bay may make neutral densities abnormally high for a matter of many hours after the Orbiter is in orbit. Under such conditions, electron ionization of the neutral gas may make collection currents and arc rates and strengths uncharacteristic of the values obtained in a long-lived solar array in orbit. For these reasons, the start of SAMPIE will be delayed for at least 24 hours after the Orbiter is in orbit with the payload bay doors open.

In order to compile good statistics and to cover an adequate range of plasma conditions, Orbiter attitudes and CTM extensions, the one orbit voltage bias sequence will be done for at least six times with each array segment, for a total of at least twelve orbits (18 hours).

Finally, arcing may be exacerbated by the presence of strong electric fields in the vicinity of the arc site. For this reason, when one of the array segments is being biased negative, the other segment will be grounded, to strengthen the local fields. This also will help simulate the possible adjacency of different parts of the large area array string in future large space power systems. In ground experiments, arcs sometimes have also occurred between adjacent conductors at high relative potentials. The arc detector on SAMPIE will be capable of discriminating these two types of arcs, based on characteristics found in ground experiments.

V. SAMPIE Arrays to be Tested

Part of the SAMPIE flight project is a ground-based testing effort, to evaluate array arcing and collection models, and to determine the most informative samples to flight test. Dr. G. Barry Hillard will be conducting this ground-test effort in laboratories at Lewis Research Center. Dr. Hillard presents his plans as another paper in this session, so I won't go into them further here. However, it is interesting to note that SAMPIE is being designed so that which the flight samples are tested may be determined as late as possible, to allow ground-based testing to help optimize the information to be gained in flight.

VI. Conclusions

SAMPIE is a Shuttle-based flight experiment which will investigate the currents collected by, and the arcing behavior of, new technology solar arrays in LEO. It is in the Phase B design and definition stage of development, but is manifested for launch in 1994. Design and construction of modern high power, high voltage, solar arrays for use in LEO require the information that a flight experiment such as SAMPIE may obtain.

References

Carruth, M.R. Jr. 1987. "Plasma Electron Collection Through Biased Slits in a Dielectric", J. Spacecraft and Rockets, 24, pp. 79-85.

Chen, F.F. 1965. "Electric Probes", Plasma Diagnostic Techniques, Ed. R.H. Huddlestone and S.L. Leonard - Pure & Applied Physics, 21, Academic Press, New York, pp. 113-200.

Ferguson, D.C. 1986. "The Voltage Threshold for Arcing for Solar Cells in LEO - Flight and Ground Test Results", NASA TM-87259.

Grier, N.T. 1983. "Plasma Interaction Experiment II (PIX II): Laboratory and Flight Results", Spacecraft Environmental Interactions Technology 1983, NASA CP-2359, pp. 333-347.

Grier, N.T. 1984. "Dilute Plasma Coupling Currents to a High Voltage Solar Array in Weak Magnetic Fields", 19th IECEC Conference, San Francisco.

Grier, N.T. and Stevens, N.J. 1978. "Plasma Interaction Experiment (PIX) Flight Results", Spacecraft Charging Technology 1978, NASA CP-2071, pp. 295-314.

Hastings, D.E., Weyl, G., and Kaufman, D. 1989. "A Simple Model for the Threshold Voltage for Arcing on Negatively Biased High Voltage Solar Arrays", Journal of Spacecraft and Rockets, submitted.

Jongeward, G.A. et al 1985. "The Role of Unneutralized Surface Ions in Negative Potential Arcing", IEEE Trans. Nucl. Sci., vol. NS-32, no. 6, Dec., pp. 4087-4091.

Leung, P. 1985. "Characterization of EMI Generated by the Discharge of a 'Volt' Solar Array", JPL D-2644, Jet Propulsion Lab, California Institute of Technology, Sept. 1985.

Miller, W.L. 1983. "An Investigation of Arc Discharging on Negatively Biased Dielectric-Conductor Samples in a Plasma", Spacecraft Environmental Interactions Technology 1983, NASA CP-2359, pp. 367-377.

Rawer, K., and Bradley, P.A., eds. 1987. International Reference Ionosphere-Status 1986/87, The Committee on Space Research, Pergamon Press, New York.

Sasaki, S., Kawashima, N., Kuriki, K., Yanagisawa, M., and Obayashi, T. 1986. "Vehicle Charging Observed in SEPAC Spacelab-1 Experiment", J. Spacecraft and Rockets, 23, pp. 194-199.

Snyder, D.B. 1985. "Characteristics of Arc Currents on a Negatively Biased Solar Cell Array in a Plasma", NASA TM- 83728.

Snyder, D.B. 1986. Private communication.

Staskus, J.V. 1988. Private communication.

Stevens, N.J. 1978. "Interactions Between Spacecraft and the Charged-Particle Environment", Spacecraft Charging Technology 1978, NASA CP-2071, pp. 268-294.

Thiemann, H. and Bogus, K. 1986. "Anomalous Current Collection and Arcing of Solar-Cell Modules in a Simulated High-Density Low-Earth Orbit Plasma", ESA-Journal, 10, pp. 43-57.

Thiemann, H. and Bogus, K. 1988. "High Voltage Solar Cell Modules in Simulated Low-Earth-Orbit Plasma", Journal of Spacecraft and Rockets, 25, pp. 278-285.

POWER TECHNOLOGY DIVISION

SOLAR ARRAY MODULE PLASMA INTERACTION EXPERIMENT
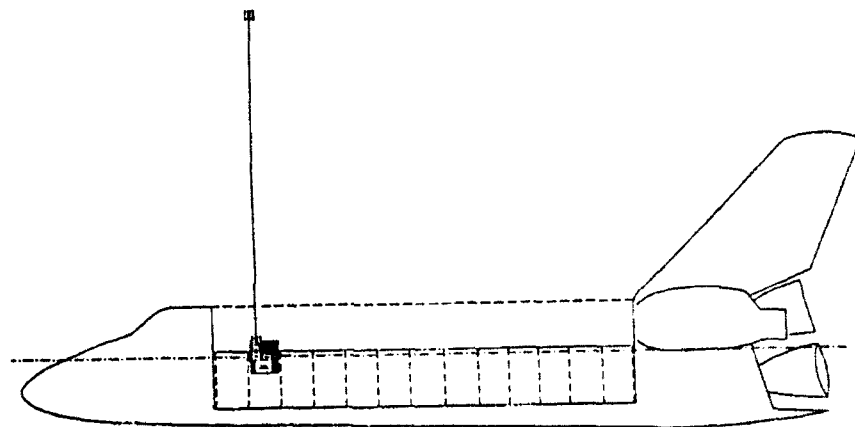
Accomodation of CTM/SAMPIE (side view)

Figure 1

IFCE Payload
Interface

Payload/Mast
I/F Flange

CTM Mast
Size 3

Payload
Latch

Latch Support
Structure

CTM Size 3
Mechanism

Figure 5.1-1

CTM - TDP
Configuration
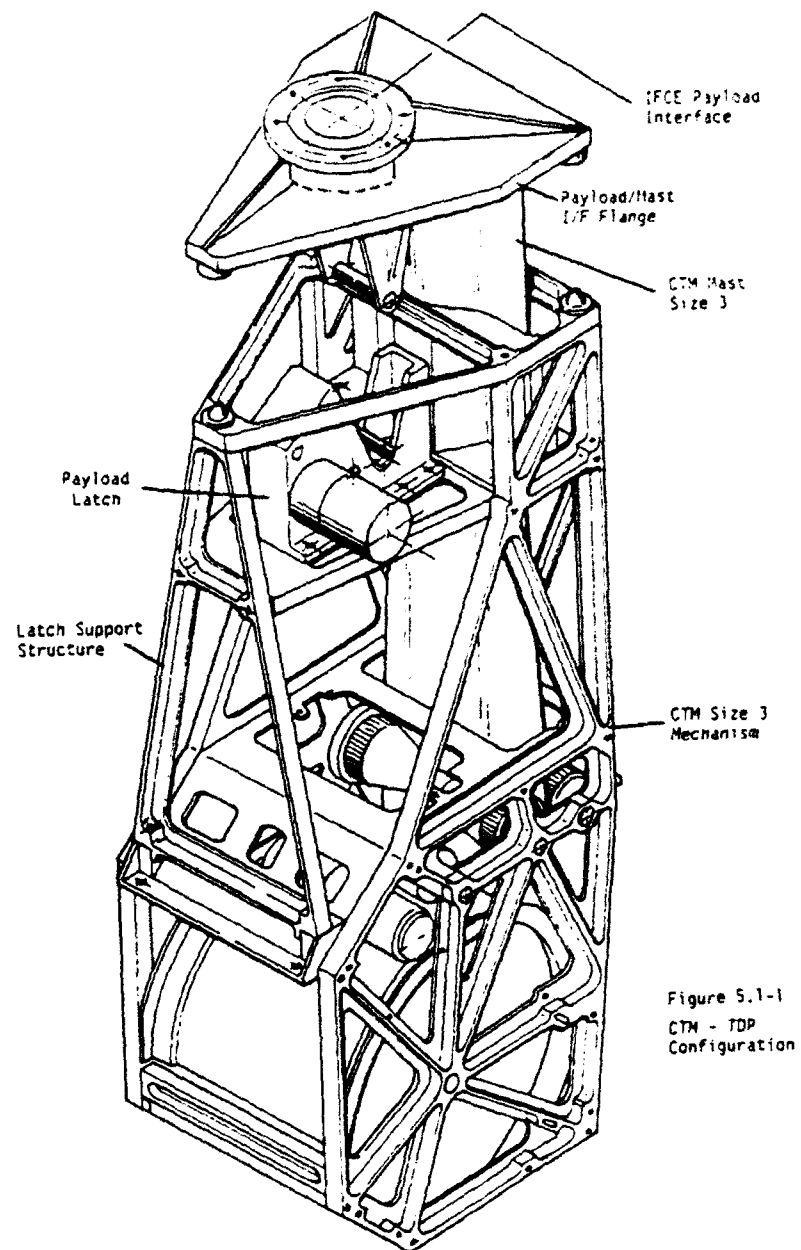
Figure 2: CTM Mast Deployment Unit (MDU)

358

SIDES WITH PCB GUIDES

TOP

PC BOARDS (7 Total)
(1) Microcontroller Board
(1) Electrometer Board
(1) Power Control Unit Board
(1) Transient Current Detector Board
(1) Memory Board
(1) Diagnostics Board
(1) Interface Board

FRONT & REAR SIDES

ELECTRONIC MODULES
(1) HV Power Supply
(1) Langmuir Probe Unit

NOTES

1. SOLAR PANEL REMOVED FOR CLARITY

BASE

REVISIONS			
REV	DESCRIPTION	DATE	APPROVED

CONTRACTOR	NASA LeRC Cleveland, Ohio	
Sverdrup Technology, Inc. Contract No. NAS3-25266	TITLE SAMPIE - EXPLODED VIEW	
DATE: 18 OCT 88	SIZE FSCM NO.	DWG NO. SK201001	REV
DRAWN BY: J. PETROSKI	SCALE NONE	SHEET

Figure 3

TOP VIEW
Cover Removed

HV Power Supply

Langmuir Probe Unit

Microcontroller Board
Electrometer Board
Power Control Unit Board
Transient Current Detector Board
Memory Board
Diagnostics Board
Interface Board

REVISIONS

REV	DESCRIPTION	DATE	APPROVED

CONTRACTOR	NASA LeRC Cleveland, Ohio		
Sverdrup Technology, Inc. Contract No. NAS3-25266	TITLE	SAMPIE ASSEMBLY (PARTIAL)	
Date: 25 Oct 89	SIZE FSCM NO.	DWG NO. SY20-003	REV
Drawn by: J. Petroski	SCALE none	SHEET	

Figure 4

360

Figure 5

Optical signatures of the beam-plasma interaction during the ECHO 7 sounding rocket experiment

R C Franz and J R Winckler (Both at: School of Physics and Astronomy, University of Minnesota, Minneapolis, MN 55455)

INTRODUCTION

Electron beams injected during the ECHO 7 sounding rocket experiment were used to investigate the large scale properties of the interaction of the beams with a neutral magnetized-plasma environment. This interaction, known as the beam-plasma interaction (BPI), can under certain conditions, modify or even destroy the adiabatic character of the initially injected beam. The characteristics of the BPI have been recently reviewed by Papadopoulos and Szuszczewicz (1988). Of fundamental importance is the determination of the conditions under which these collective beam-plasma effects would dominate especially in rocket experiments such as the ECHO series (Winckler, 1980) in which beams of electrons are also used to probe the distant magnetosphere. During the BPI, ambient electrons can be energized to suprathermal energies which can collisionally interact with the neutral atmosphere to produce luminosity. Measurement of this luminosity can then reveal information about characteristics of the electrons producing the light, and ultimately yield information about the BPI. This paper will show optical measurements of the luminosity made during the ECHO 7 experiment. The results presented will show images obtained by onboard low-light television camera, and photometric observations measuring the luminous manifestations of the BPI over an altitude range from 200 km to about 95 km.

EXPERIMENTAL CONFIGURATION

The ECHO 7 experiment was launched February 8, 1988 from Poker Flat Research Range. The scientific payload consisted of a 'MAIN' accelerator payload, and three free-flying subpayloads: Nose, Plasma Diagnostic Package (PDP) and Energetic Particle Package (EPP) carried aboard a Terrier Black-Brant I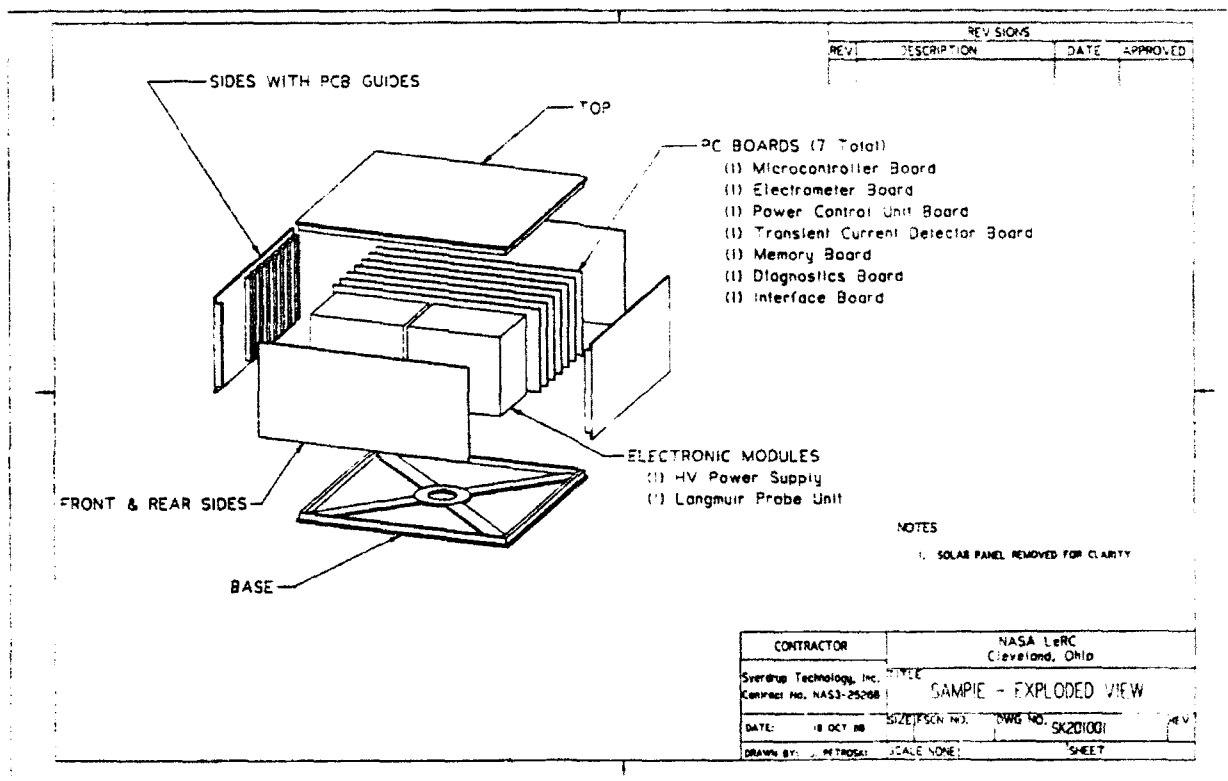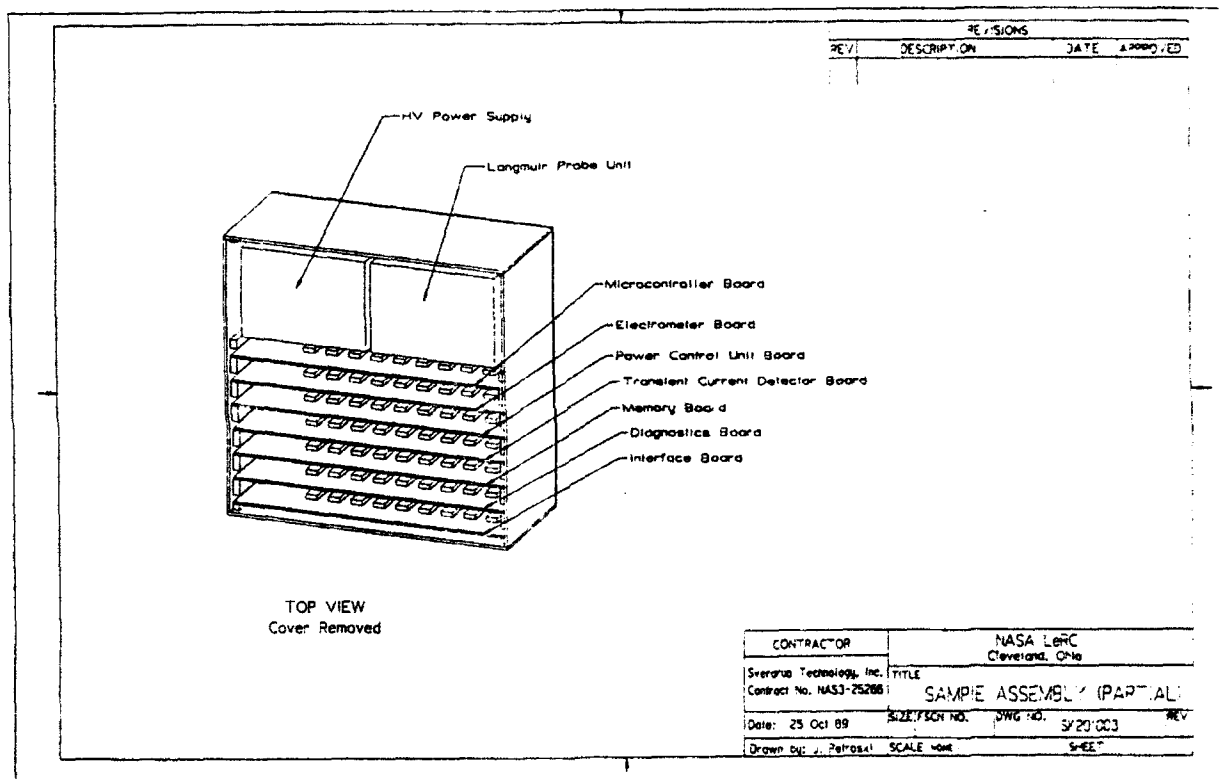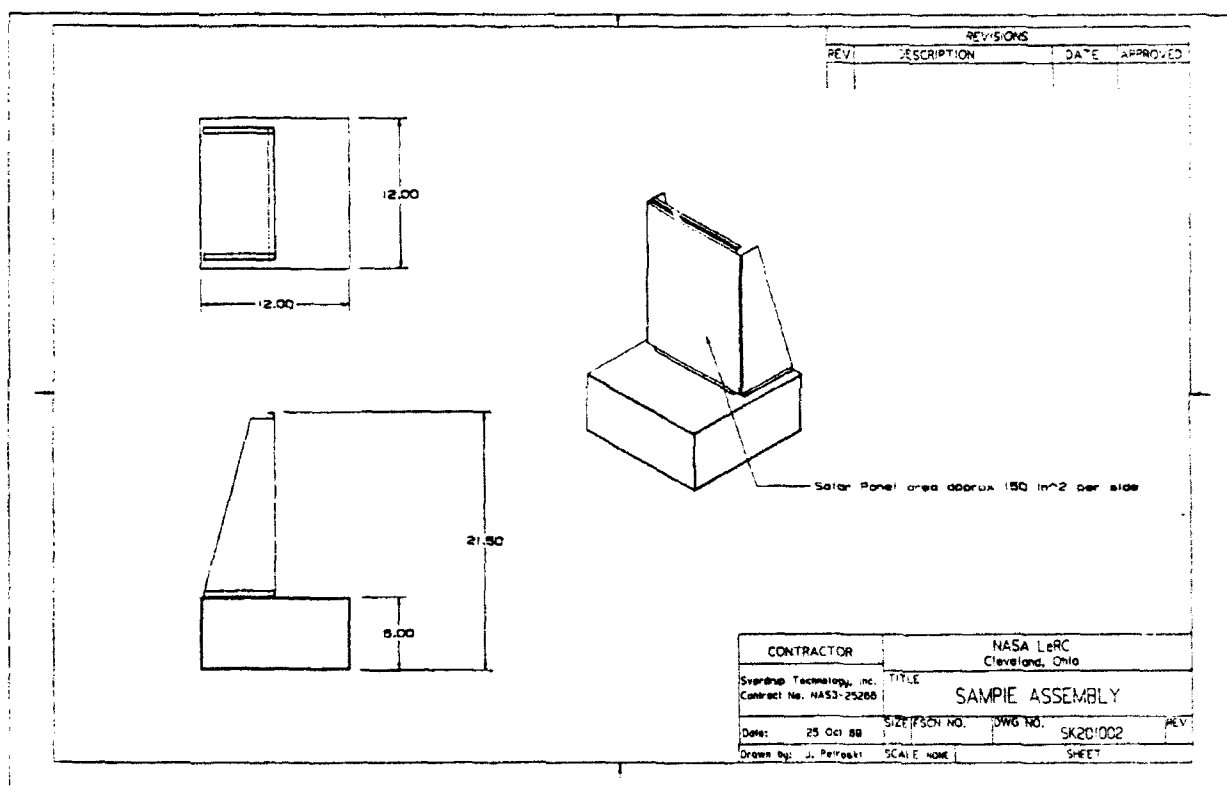X sounding rocket. The rocket travelled on an eastward trajectory reaching an altitude of 291 km at apogee. The subpayloads were deployed from the MAIN while it was spinning at 0.6 rps. The NOSE was deployed at 4 m/s directly up the field, the PDP at 1.75 m/s towards magnetic south at an angle of 16 degrees to the field, and the EPP at 2 m/s at 25 degrees to the field in a westerly direction. Figure 1 is an illustration of the deployment geometry of the subpayloads with respect to the MAIN and injected beam. After subpayload deployment, the accelerator payload was completely despun and oriented north-south in a magnetic horizontal plane.

The MAIN payload contained a single diode electron gun, of a similar design as those used on previous ECHO missions (Winckler,

1982). The gun was capable of injecting electrons in two possible modes: a 'continuous' or swept energy mode (40 KeV to 8 KeV every 1 ms), and a 'discrete' or quasi-dc mode, injecting at 10 KeV (26 mA) or 36 KeV (180 mA). The continuous beam, injected at a pitch angle of 110 degrees, was used primarily for the conjugate echo portion of the experiment (Nemzek et al., 1989). The discrete beams, injected at pitch angles varying from 40 to 175 degrees, were used for the purpose of plasma heating, wave generation, and creating luminosity around the beam and MAIN payload. The gun was programmed to inject a sequence of pulses of 50, 100, and 150 ms, with similar duration off times, forming a pattern that repeated every 10 seconds. The gun was turned on at 180 seconds into the flight at an altitude of 250 km and operated until 499 seconds at an altitude of less than 90 km. Further details about the ECHO 7 mission can be found in Winckler et al., 1989.

OPTICAL INSTRUMENTATION

An Intensified Charge Injection Device (ICID) low-light-level television camera, manufactured by ITT, model 4562 was used to obtain images during the ECHO 7 flight. It was placed on the PDP and oriented along the spin axis back toward the MAIN (Figure 1) to view the light surrounding the MAIN and beam during gun operation. The camera operated in a standard video mode, capturing frames at 1/30 per second, which were telemetered in real-time to ground. A Fujinon F1.4, 25 mm lens was used, giving the camera a field of view of 15 x 20 degrees. The camera had a rated sensitivity of 10^{-6} footcandles, and was capable of discerning stars of magnitude 6.5.

In addition to the camera, a total of nine photometers were placed on the MAIN, PDP and EPP. Six photometers were filtered at 391.4 nm with a 10 nm bandpass, and two were filtered at 380.5 nm with a 5 nm bandpass, measuring the First Negative and Second Positive bands of molecular Nitrogen. One additional photometer measured white light (350 nm to 650 nm).

RESULTS

The photometers and television camera measured luminosity throughout the flight. At high altitudes, from 250 km on the upleg to about 215 km on the downleg, the large scale features of the beam were essentially invisible to the camera except during the injection of Attitude Control System (ACS) gas. Results reported in this paper are concerned with the variation of the large scale beam features during the downleg from 200 km to 95 km. The observations can be divided into three categories (A, B, C), depending on the altitude region and physical appearance of the beam. Region A extended from 200 km to 145 km, region B from 145 to 110 km, and region C from 110 to 95 km. A survey of these regions will follow.

During beam injection in region A, a column of luminosity surrounded the beam, and extended up and down the magnetic field

line. A typical view of the beam injection is shown in Figure 2 at an altitude of 175 kr for a 36 Kev injection at 110 degree pitch angle. The local time "23:24:12" or 443.85 flight seconds is shown at the bottom of the photograph. In the figure, the beam was propagating upwards along the field line, originating from the MAIN which is surrounded by the bright luminosity. The tail on the bright spot extending to the right-hand side of the photograph is an artifact of the camera due to the extreme brightness of this luminosity near the MAIN. The column of luminosity was initiated at gun turn-on and persisted the entire 100 ms beam injection. The intensity of the luminous column was uniform both up and down the field line and out to the full width of the 25 meter gyro-diameter. An analysis of the intensity of the light made during a number of similar injections as the rocket moved to lower altitudes is shown in Figure 3. The lower panel shows the relative intensity of the video output measured in portions of the beam column above and below the MAIN as indicated in the legend. The intensities of the luminosity measured in the different parts of the column have been determined by digital image processing techniques. In the upper panel, the neutral N_2 density is plotted versus altitude, and is seen to vary by five orders of magnitude between 200 km to 90 km. In region A, in which Figure 2 belongs, the luminosity in the portion of the beam column above the MAIN increased about a factor of two, while the altitude decreased from 190 to 150 km. The luminosity in the beam below the MAIN remained constant. The neutral density shown in the upper panel increased about a factor of 10 during this time. It is clear that the variation in the luminosity with altitude was not tied directly to the ambient neutral density, as would be the case if the luminosity were produced by collision of the primary beam with the neutrals.

During the transition from region A to B, a transient enhancement in portions of the beam column was observed. The region of unstable light production is denoted with an arrow as shown in Figure 3. This indicates that the luminosity in portions of the beam column appear to jump between two levels for successive images 1/30 s apart during the same 100 ms injection. The magnitude of the upper level saturated the video output, at a level greater than five times the normal intensity. Figures 4(a) and 4(b) show an example of this effect. Figure 4(a) shows a luminous column five seconds after the image shown in Figure 2, at an altitude of 165 km. The column in Figure 4 appears slightly rotated from that shown in Figure 2 due to the rotation of the camera on the PDP. The next image obtained 1/30 second later is shown in Figure 4(b). During this frame, a large enhanced region of luminosity developed in a portion of the beam column. The region extended about 300 meters up the field line from the MAIN. The part of the beam affected seems to be localized along the direction of the column in which the beam is propagating, and on the side of the beam column which is on the same field line as the MAIN. The intensity level in the enhanced region saturated the video output, as seen in Figure 3. A sharp demarcation between the normal diffuse column and the enhanced column is seen. Outside the enhanced region,

the appearance of the column is the same as in the previous images. The enhancement at this time persisted only one TV frame (1/30 s). The light appears to be bi-modal, as if the production mechanism responsible for the light were being turned on and off in that portion of the beam column. The transient enhancements in the column are first seen at 443 s (175 km), and continue during the discrete injections until 458 s (150 km) as noted in Figure 3.

As the payload moved to lower altitudes, into region B, the enhancements change from transient (lasting 30 ms) to persistent, lasting throughout the gun pulse (100-150 ms). The appearance of the beam in region B is very similar to the transient enhancement shown in Figure 4(b). The only difference between the luminosity in region B, and that shown in Figure 4(b) is entirely due to increased duration and radial extent of the enhanced portion of the beam. The change in the duration and extent of the enhanced luminosity is first evident in the 36 KeV Out pulse at an altitude of about 145 km. The enhanced luminosity extends to the full width of the beam column, and is spread out along the field line engulfing the MAIN.

As the payload moved from region B to region C, the light level in the column decreased. Figure 5 shows a view at 98 km in which the larmor spiral of the beam is clearly visible. At this time, the beam was injected at 36 KeV with a pitch angle of about 130 degrees. The beam maintained its coherent spiral over a distance greater than 300 m. In addition to the 17 m wide larmor spiral there is a faint field aligned glow similar to that seen at higher altitudes.

Region C, extending from 110 to less than 90 km, is also the region where downward beams injected at higher altitudes deposit their energy creating artificial auroral streaks. However, the ground based television camera observations of these streaks from previous ECHO missions, (Hallinan et al., 1975), did not show any evidence of a larmor spiral structure. This may be due to the limited resolution of the camera. These streaks can be explained in terms of collisional processes in which luminosity is produced by primary and secondary electrons. The production mechanism of the helix also in region C is most likely tied directly to the interaction of the primary beam with the ambient neutrals.

The intensity of the luminosity produced at 98 km is comparable with that produced at higher altitudes (Region A) even though the neutral density has changed four to five orders of magnitude. It is clear that if the production mechanism of the light at 98 km is related directly to the primary flux of the beam, then it is doubtful the same mechanism could be responsible for the Region A light. The diffuseness and lack of larmor structure also points away from a luminosity production mechanism involving the direct excitation by collisions with primary beam with the neutrals. The luminosity is most likely produced by suprathermal electrons having been energized in a beam-plasma interaction.

A similar constant light intensity-altitude profile made during the Polar V experiment support the premise that the light around the payload at high altitudes is produced by suprathermal electrons

energized in a BPI. (Grandal et al., 1980). Photometric measurements of luminosity made near the accelerator payload, observed a near constant light level from 215 km to 140 km. The intensity was inconsistent with luminosity produced either by primary or secondary electrons and were attributed to a flux of suprathermal electrons energized during a beam-plasma interaction.

Features of the beams in Figures 2, 4 (a,b) and 5 are similar to observations made during the Zarnitsa 2 experiment (Dokukin et al, 1981). Photographs taken by ground based cameras of the payload at an altitude of 150 km show a bright near-payload region extending 200 m to 300 m along the field line around the accelerator, and near rocket ray extending one to seven km below the rocket as the 7 keV beam was injected downward. The interaction region on Zarnitsa was attributed to the beam-plasma discharge (BPD) which was excited during beam injection.

The optical characteristics of the beam-plasma-discharge (BPD) as studied in the laboratory are very similar to the ECHO 7 results. The BPD is characterized by a dramatic increase in light at some critical threshold, determined by the beam parameters, neutral density and magnetic field strength (Hallinan et al., 1984). The enhanced luminosity displayed in Figure 4(b), and also in Region B, was most likely produced during a BPD. The critical threshold was attained as the neutral density increased during the downleg of the flight. The transition from region A to region B in the ECHO 7 observations occur in the neighborhood of 145 km, an altitude consistent with the Zarnitsa results, and also with theoretical predictions of BPD onset (Papadoupolos, 1982).

TRANSIENTS AND OSCILLATIONS

In Region A, from 190 km to 145 km, large periodic and random flucuations in the light were observed by photometers placed on the free-flyers. Figure 6 shows 1.4 s of data during which the beam injected in both continuous (CON) and discrete modes at pitch angles of 40 degrees (DOWN), 110 degrees (OUT) and 175 degrees (UP). During an UP injection at 448.2, a large oscillation was seen in the light near the MAIN by photometer PHP1 (See Figure 1 for photometer identification). In addition, PHP3 and PHP4 which intercepted the beam at about 650 m up the field line from the MAIN also recorded the fluctuations, which were found to be directly in phase with oscillations found near the MAIN. The variation in the luminosity during the oscillation event approaches 100 % of the total value, as if the light production mechanism were turning on and off. The frequency of the oscillation at this time was about 30 Hz. An analysis of several events during the downleg show that the frequency varied from 23 Hz to 42 Hz depending on the type of injection.

Large oscillations in the luminosity have been observed on previous ECHO flights. During the ECHO 4 experiment (Israelson and Winckler, 1979) a large 22 Hz oscillation in the light measured by photometers developed during the downleg of the flight. The ECHO 5 flight produced similar low frequency oscillations (Arnoldy

366

et al., 1985). Laboratory measurements of the beam-plasma discharge also show numerous low frequency oscillations preceeding the onset of the BPD (Hallinan et al., 1984; Sivjee et al., 1989). The low frequency oscillations measured in flight preceeded the region B luminosity, and are most likely precursors to the BPD initiated in region B.

In addition to the low frequency oscillations, large transient flashes at gun turn on were observed during the downleg of the flight. Figure 6 shows a transient lasting 10-20 ms during the start of the OUT injections. The shape of the transients resemble one period of the oscillation events shown during the UP injection. The transient at 448.9 has a number of small oscillations following the main event which appear to be damped out. It is possible that the oscillation events were BPI unable to sustain themselves. Similar large scale transients were also observed by photometers onboard the accelerator payload during the ECHO 6 experiment (Franz et al., 1984). The transients reached as much as 10 times the steady state level, and involved the entire beam column, measured in a similar configuration as shown in Figure 1 (Franz and Winckler, 1989).

SUMMARY

This paper has shown some of the observations of the luminosity surrounding an electron beam-emitting rocket during the ECHO 7 experiment. It is clear that the observations of the luminosity *cannot be explained by* considering the light to originate from direct ionization of the neutral gas by the beam alone. The complex and non-linear behavior of the luminosity suggest that the beam interacted with the plasma (BPI) to produce a large population of suprathermal electrons which were responsible for the enhancment in the luminosity. In addition, the BPI transitioned into a BPD from about 145 km to about 115 to 120 km. The observations of the luminosity which are direct indications of these effects are:

1. A nearly constant intensity of luminosity produced in and around the beam which shows little variation with altitude.

2. The appearance of a bi-modal intensifications in the light, including both intensifications in small areas of the beam column, and large scale photometric transients, observed at gun turn-ons.

3. Large scale oscillations in the light of the beam column similar to those observed proceeding the onset of laboratory BPD.

ACKNOWLEDGEMENTS

BIBLIOGRAPHY

Arnoldy, R. L., C. J. Pollock, and J. R. Winckler, The energization of electrons and ions by electron beams injected in the ionosphere, J. Geophys. Res., 90, 5197, 1985.

Bernstein, W., H. Leinback, P. J. Kellogg, S. J. Monson, T. Hallinan, Further Laboratory Measurements of the Beam-Plasma Discharge, J. Geophys. Res. 84, 7271, 1979.

Dokukin, V. S., V. N. Ivchenko, A. K. Markeev, G. P. Milinevshy, E. V. Mishin, R. I. Moisya, Ju. Ja. Ruzhin, R. Z. Sagdeev, V. V. Fomichev, and I. A. Zhulin, Results of Zarnitsa-2, A rocket experiment on artificial electron beam injection in the ionosphere, Adv. Space Res. 1, 5-15, 1981.

Franz, R. C., J. R. Winckler, J. E. Steffen, and R. L. Swanson, Studies of the luminosity around and electron beam emitting rocket in the ionosphere, EOS, 65, 1062, 1984.

Franz, R. C., and J. R. Winckler, The transient and Oscillatory Behavior of Luminosity Surrounding An electron beam-Emitting Rocket: Echo 7, EOS, 70, 440, 1989.

Galeev, A. A., Mishin, E. V., Sagdeev, R. Z., Shapiro, V. D. and Shevchenko, V. I., Discharge in the region around a rocket following injection of electron beams into the ionosphere, Soviet. Phys. Dokl. 21, 641, 1979.

Grandal, B., Thrane, E. V. and Troim J., Polar 5 An electron accelerator experiment within an aurora. 4. Measurements of the 391.4 nm light produced by an artificial electron beam in the upper atmosphere, Planet. Space Sci. 28, 309, 1980.

Hallinan, T. J., H. C. Stenbaek-Nielson, and J. R. Winckler, The ECHO 4 Electron Beam Experiment: Television Observation of Artificial Auroral Streaks Indicating Strong Beam Interactions in the High Latitude Magnetosphere, J. Geophys. Res., 83, 3709, 1975.

Hallinan, T. J., H. Leinback, G. Mantjoukis, and W. Bernstein, Measurements of the optical emissions produced during the laboratory beam plasma discharge, J. Geophy. Res. 89, 2335, 1984.

Israelson, G. A., and J. R. Winckler, Effect of a neutral N2 cloud on the electrical charging of an electron beam-emitting rocket in the ionosphere: Echo IV, J. Geophys. Res. 84, 1442, 1979.

Nemzek, R. J., and J. R. Winckler, Immediate and delayed High-Energy electrons due to ECHO 7 accelerator operation, -- These proceedings

Papadopoulos, K. Theory of the Beam Plasma Discharge, in Artificial Particle beams in Space plasma Studies, Edited by B. Grandal, Plenum Press, New York, 1982.

Papadopoulos, K., and E. P Szuszczewicz, Current Understanding and issues on electron beam injection in space, Adv. Space Res, 8, 101, 1988.

Winckler, J. R., The application of artificial electron beams to magnetospheric research, Rev. of Geophys. and Space Phys., 18, 659, 1980.

Winckler, J. R., The use of artificial electron beams as probes of the distant magnetosphere, in Artificial Particle Beams in Space Plasma Studies, edited by B. Grandal, Plenum Press, New York, 1982.

Winckler, J. R., P. R. Malcolm, R. L Arnoldy, W. J. Burke, K. N. Erickson, J. Ernstmeyer, R. C. Franz, T. J. Hallinan, P. J. Kellogg, S. J. Monson, K. A. Lynch, G. Murphy, and R. J. Nemzek, ECHO 7: An Electron beam experiment in the Magnetosphere, EOS, 70, 657, 666-668, 1989.

ELECTRON BEAM →

$\vec{B}$

EPP

PHE1
PHE2

PHP3
PHP4

PHP5

PDP

PHOTOMETER PHP1
AND TV CAMERA
FIELD OF VIEW

MAIN
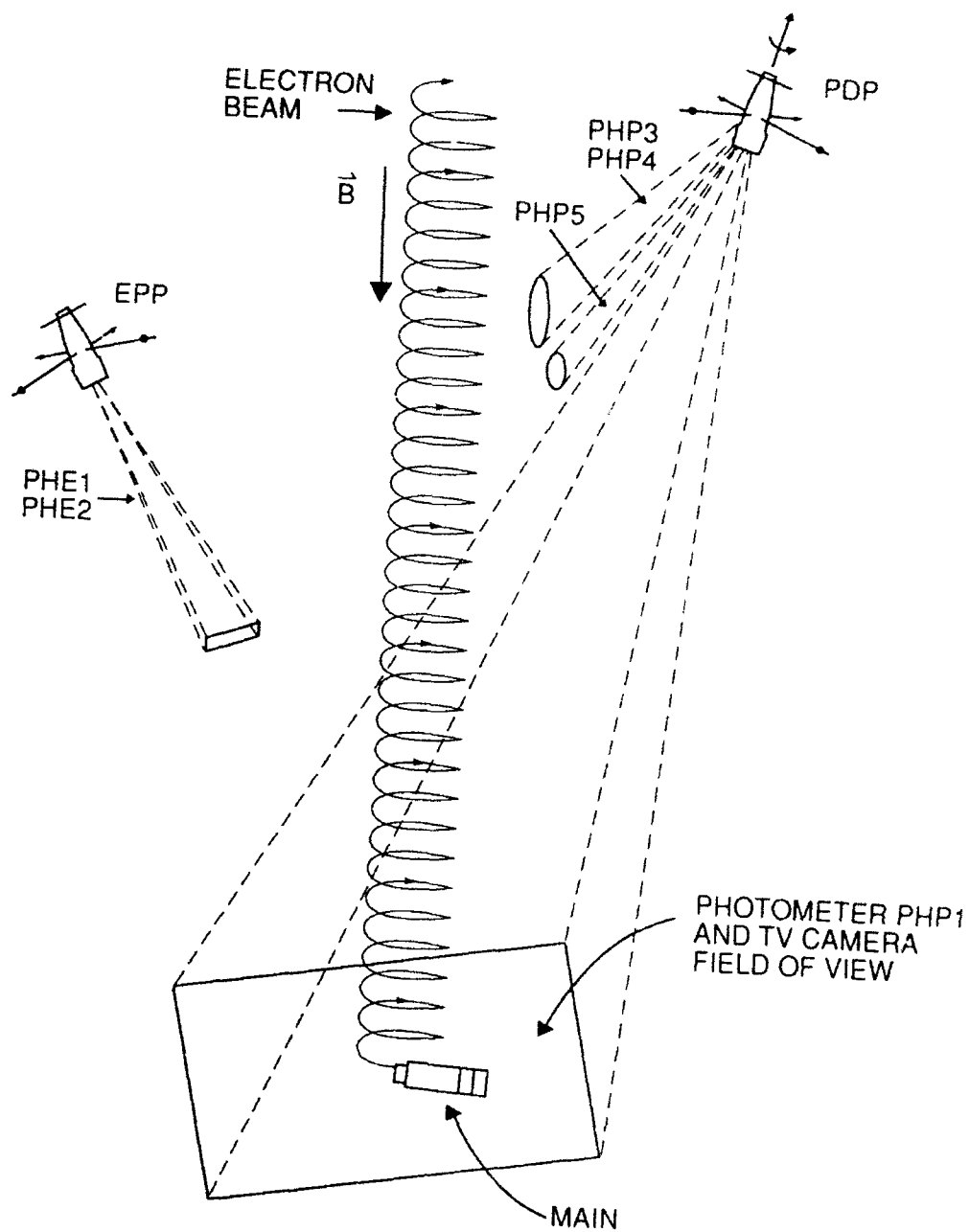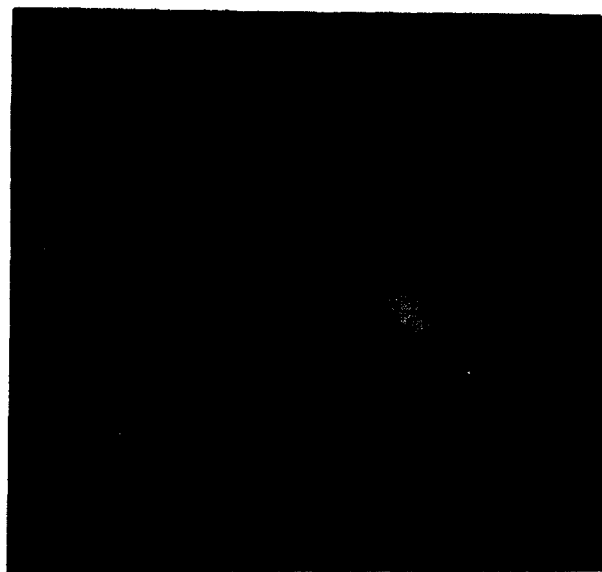
FIGURE 1

FIGURE 2

FIGURE 3

(a)

(b)

FIGURE 4

FIGURE 5

FIGURE 6

375

Neutral Gas Effects on the Charging of ECHO-7

P. R. Malcolm
Department of Physics
USAF Academy, CO 80840

and

W. J. Burke and G. P. Murphy
Geophysics Laboratory (AFSC)
Hanscom AFB, MA 01731-5000

ABSTRACT

Electron beams reaching 40 KeV in energy and 220 milliamperes in current were emitted during the ECHO-7 sounding rocket flight. In order to measure the potential of the beam emitting MAIN payload, a high impedance probe (TETHER) was ejected from MAIN near apogee (292 km). During the flight, beam emission frequently occurred together with attitude control system (ACS) corrective maneuvers involving the ejec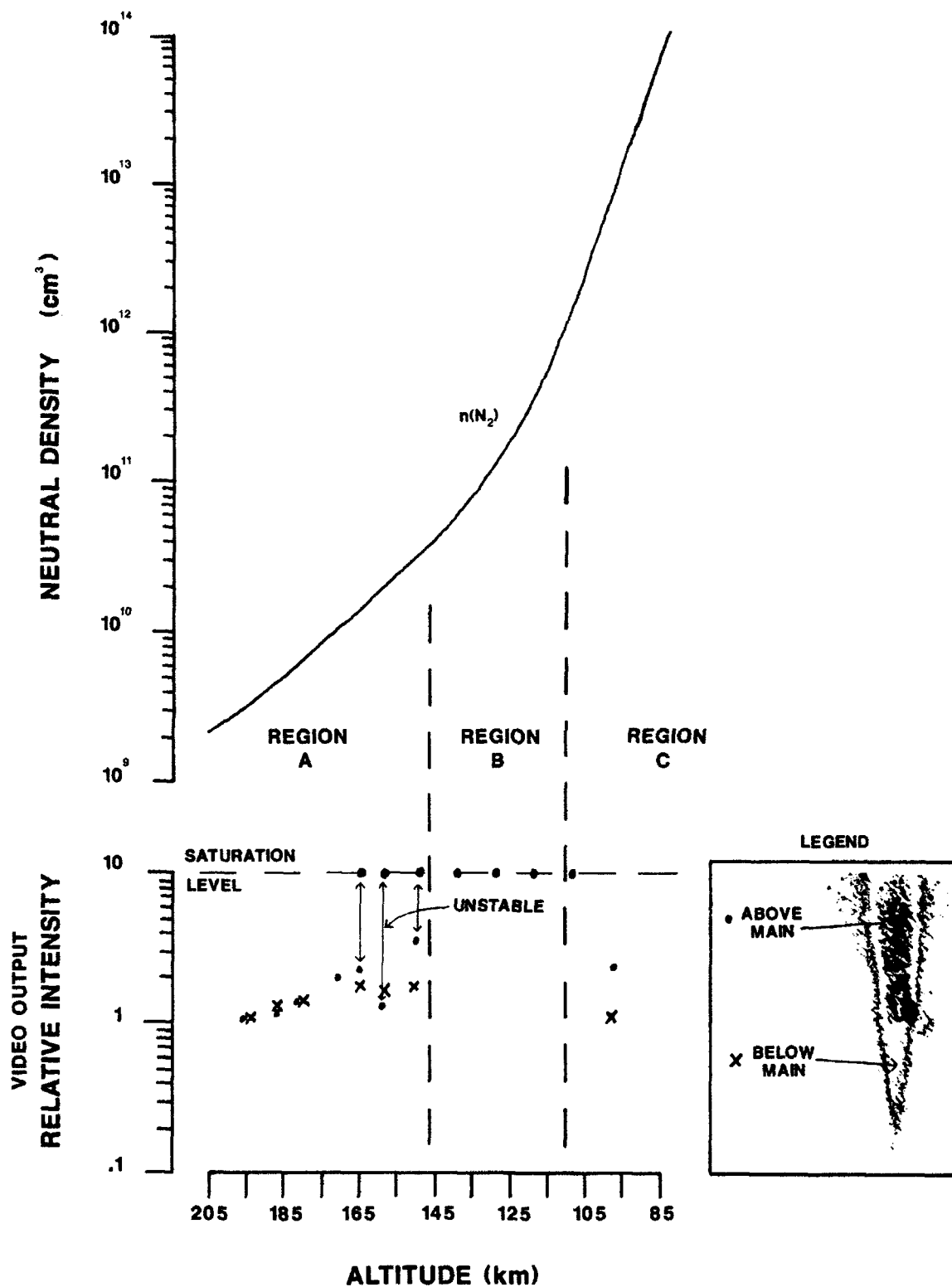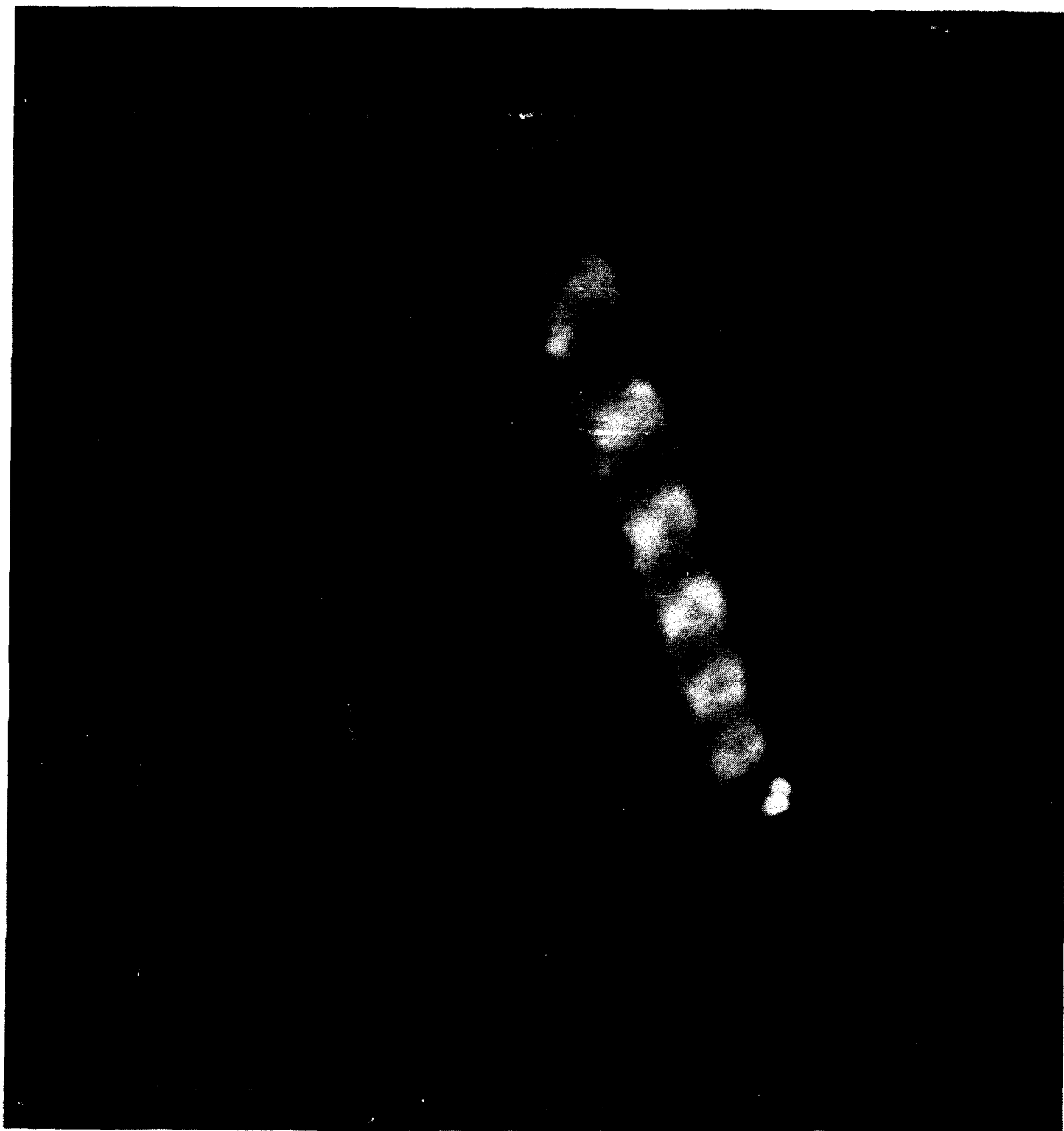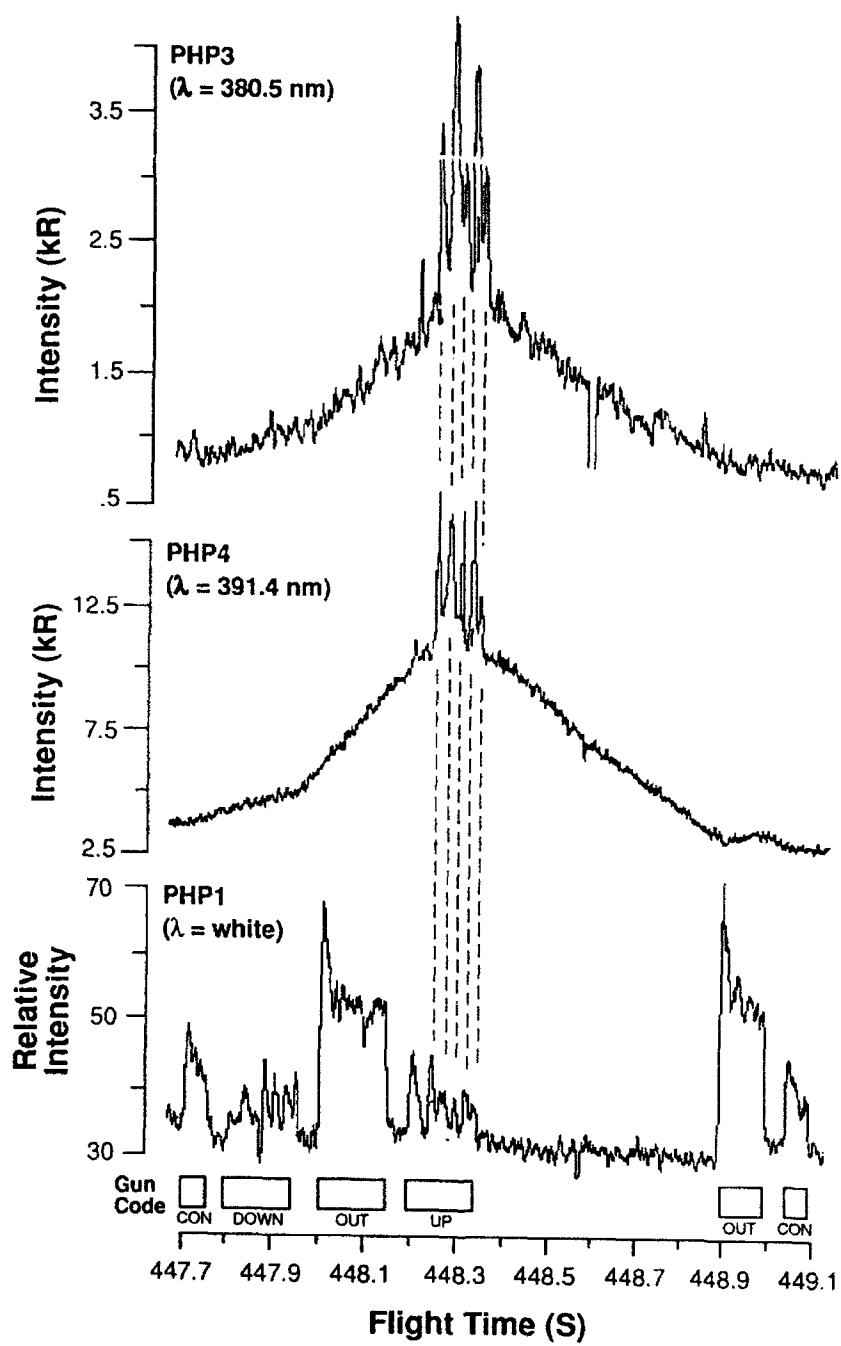tion of nitrogen gas. Four seconds of data from the tether and an upward looking surface current monitor (SCM), located at the gun end of the payload, show the effects of ACS neutral gas on the current/voltage characteristics of the MAIN payload.

During beam emission with no ACS gas ejection, the tether measured charging levels of 2-3 kilovolts while the SCM measured current densities of 8-10 microamperes/cm^2. Then during all simultaneous electron beam and ACS emission periods, the vehicle potential decreased to a few tens of volts and the SCM detected only background level return currents. When ACS gas ejection across magnetic field lines terminated, the vehicle potential and SCM current immediately returned to their original values (2-3 kV, 8-10 μA). In contrast, gas ejected with velocity components along the magnetic field lines continued to influence the vehicle potential for several tens of milliseconds after the flow was turned off. In this case, vehicle potentials were below while the SCM currents were above their original values with no ACS gas ejection. These results are consistent with the return current being localized to the immediate vicinity of the emitting ACS nozzles and show the strong influence of the earth's magnetic field on the motion of the return current electrons.

INTRODUCTION

On the evening of February 8, 1988, at 8:16:49 UT, the ECHO-7 sounding rocket payload was launched toward the east from the Poker Flat Research Range. ECHO-7 was a sophisticated experiment designed to study the complex interactions of artificial electron beams propagating great distances along magnetic field lines in space (Winckler et al., 1989). It is known that energetic electron beams interact with themselves, the space environment and their host vehicles. This report concentrates on the interactions in the immediate vicinity of the ECHO-7 beam-emitting MAIN payload during a four second period near its 292 km apogee. During this interval, we measured how the vehicle potential responded to several different types of beam operations by means of a high-impedance tethered probe. Of particular interest are the dynamics of the vehicle potentials and return currents following intermittent emissions of neutral gas from the payload's attitude control system (ACS). Unfortunately, the tether voltage measurements were prematurely terminated by a nearly catastrophic event that destroyed the power convertor for several diagnostic sensors and triggered a safety circuit that temporarily shut down beam emissions (Malcolm et al., 1989).

Beam-induced spacecraft anomalies are well known hazards of the trade. During an electron beam emission operation on the SCATHA (P78-2) satellite, severe arcing was induced, an energetic electron spectrometer was destroyed and the main telemetry system was temporarily impaired (Cohen et al., 1981). At the time of these upsets the beam energy and current were 3 keV and 13 mA (39 W), respectively. Data from the Norwegian rocket MAIMIK indicate that whenever currents from its 8 kV gun exceeded 84 mA (640 W) the vehicle charged to at least beam energy (Maehlum et al., 1988). During one MAIMIK charging event, a spurious command was induced causing a pyrotechnic device to detonate prematurely. During the BERT-1 sounding rocket flight, the main telemetry encoder and the experiment sequencer were destroyed when the payload's electron gun was turned on with beam energy and current of 2 keV and 20 mA (40 W). Most recently, when the SCEX-2 electron beam system was turned on, arcing from 170 volt battery packs to payload ground resulted in their destruction during flight (Massey et al., 1987).

None of these are cases of human carelessness. In all cases, the beams systems were tested in laboratories for many hours prior to flight. Rather, these failures testify to the inherently hazardous conditions that develop whenever energetic particle beams are emitted into space plasmas. Because particle beams offer powerful methods for actively

probing space plasmas, it is imperative to consider carefully the circumstances surrounding all beam-induced spacecraft interactions.

Recently Banks et al. (1988) reported on the results of the CHARGE-2 sounding rocket experiment, a tethered mother-daughter payload that emitted a 1 keV electron beam with currents up to 40 mA. The potential of the mother was normally high. However, whenever gas was released from the ACS on the tethered daughter vehicle, the potential of the mother decreased dramatically. This indicates that ionization of neutral gas during ACS releases increases the source for neutralizing current, thus reducing the required vehicle potential. Within certain environments this may provide a simple and safe technique for assisting energetic electron beams in escaping from emitting bodies in space with little energy degradation.

This report is divided into three main sections in which we first summarize the ECHO-7 mission and its payload complement. We next give a detailed presentation of vehicle potential and return current measurements acquired during a four second period which included a sequence of planned beam emissions and random neutral gas releases. Finally we discuss elements of a simple, empirical model that qualitatively helps us understand the interactions.

MISSION AND PAYLOAD

The main purpose of the ECHO-7 experiment was to study the propagation characteristics of energetic electron beams travelling great distances along magnetic lines of the earth (Winckler et al., 1989). During the experiment, electron beams were emitted from the MAIN payload flying over Alaska. Guided by the earth's magnetic field, the beams propagated to the southern ionosphere to the west of Antarctica. There, they either magnetically mirrored or were scattered off the atmosphere. Upon reflection to the northern hemisphere, the electrons were detected by sensors deployed on or near the beam-emitting vehicle (Winckler, et al., 1989, Nemzek, 1990 and Nemzek, et al., 1991). The time delay between beam emission and the detection of electron echoes has been used to calculate the shapes of field lines threading the distant magnetosphere (Nemzek, 1990 and Nemzek, et al., 1991). To understand the observations it is critical to know the energy of the electrons after they leave the immediate vicinity of the emitting payload.

Secondary objectives of the mission include the investigation of how charged particle beams interact with the ionospheric plasma environments and with their host

vehicles. Environmental effects include the ionization/excitation of atmospheric and host-vehicle neutrals, and collective interactions with charged particles in the beam or ionospheric plasma. Interactions with neutrals manifest themselves mostly through the emission of light. Beam plasma interactions lead to the emission of electrostatic and/or electromagnetic waves in the VLF and HF frequency bands. The most important interaction with the host vehicle involves surface charging and the development of high potential sheaths.

Figure 1 sketches the configuration of the ECHO-7 science payload. The instrumented nosecone section (NOSE), ejected within a few degrees of the magnetic field line, was primarily designed to detect waves generated in or near the beam. The Plasma Diagnostics Package (PDP) was ejected magnetically south while the Energetic Particles Payload (EPP) was ejected to the magnetic north-west cf the beam-emitting MAIN payload. They each carried sensors to detect echoing, energetic electrons and beam-related electromagnetic fields. The PDP also carried a low-light level television camera that pointed back along the PDP spin axis toward the position of the MAIN. Detailed descriptions of the NOSE, PDP and EPP complement of instruments have been written by Winckler et al. (1989) and are not needed for the present study. In what follows we concentrate on the MAIN payload's instrumentation and operations.

The MAIN payload consisted primarily of an electron accelerator, scientific instrumentation, a telemetry system and an attitude control system (ACS). The ACS used pressurized nitrogen with pitch, roll and yaw jet nozzles to maintain three-axis stability. The positions of the jets relative to the magnetic field direction are shown in Figures 2 and 3. They were located about 1.5 m aft (south) of the electron gun aperture. After initial payload deployments, gas emissions occurred randomly throughout the flight to keep the orientation of MAIN perpendicular to the earth's magnetic field.

The ECHO-7 9 kW electron beam accelerator is shown schematically in Figure 4. It functioned perfectly from turn-on at 179 sec (250 km) through reentry at 500 sec (90 km) while emitting beams reaching 40 keV in energy and 220 mA in current. The accelerator was similar to those flown on previous ECHO missions, but incorporated several design changes to increase program flexibility and reliability. It had five basic components: a battery power system, power converters, a diode electron emitter or gun, beam focusing and deflection magnets, and a programmer to control functions during flight.

Primary power was supplied by four silver-zinc battery packs capable of delivering up to 100 volts at 100 amperes when connected in series. Power was taken from one of two battery taps selected by the programmer. The high voltage tap was connected to the top of the 100 volt (loaded) pack while the low tap connected to a point capable of delivering 25 volts under load. This power fed the primary side of a DC-DC converter that stepped the 100 volts up to 40 kV with a maximum current of 250 mA. This produced a DC output with < 10 percent ripple (see Figure 5, "Discrete Mode"). No attempt was made to filter the output because of the hazards involved in using large capacitors charged to high voltages.

A second, or "continuous", accelerator mode used the converter drive to charge and discharge a 500 μF capacitor during each drive cycle. When the transformed output was full wave rectified, the resultant output decayed exponentially from 40 kV to 8 kV during each millisecond half-cycle (see Figure 5, "Continuous Mode"). This mode is called "continuous" because it results in an electron beam continuously spread in energies between 40 and 8 keV. Continuous mode beams were used to enhance the probability of echo detection (Winckler et al., 1989).

The electron gun was a space-charge limited diode with a geometry described by Pierce (1949). The source of electrons was a tantalum ribbon filament heated to incandescence with a floating power supply. The filament and cathode focusing element were biased by the negative high-voltage output of the accelerator convertor while the gun anode was grounded to the payload skin. Since the gun was not emission limited within its operating range, it was capable of producing a beam current of 220 mA with a -40 kV bias and 30 mA with a -10 kV bias, following the $V^{3/2}$ relation for a space-charge limited diode.

The accelerator was placed in the payload so that when the MAIN was stabilized perpendicular to the earth's magnetic field, with the long axis parallel to the magnetic north-south direction, the electron beam injection pitch angle with no magnetic deflection was 110°. In the "continuous" accelerator mode the beam always emitted at a pitch angle of 110°. With the deflection magnet turned on, other injection pitch angles were possible when the accelerator was in the "discrete" mode. These were downward at a pitch angle of 40°, upward at a pitch angle of 170° and a continuous sweep from 40° to 175°.

All the accelerator emission modes and beam-deflection angles were controlled by a simple programmer interfaced to the accelerator drive circuits through fiber-optic links for maximum noise immunity. A 200-step accelerator program was

burned into EPROMs that were read every 50ms in a program of 10 second duration. Figure 6 shows that the program consisted of "discrete" injections at two different energies and four series of coded pulses in the "continuous" mode. The code consisted of a mix of 50, 100 and 150 ms duration pulses that allowed identification of exactly which pulses were detected as conjugate echoes.

Care was taken to prevent catastrophic damage to the power convertor system if high-voltage breakdown in the gun should occur. A safety circuit was designed to monitor the battery current and to inhibit the accelerator convertor for 300ms if the primary current exceeded 100 amperes. It did not, however, affect the precise 10 second repetition rate of the programmer. The safety circuit saved the drive system from three potential failures during flight when breakdowns occurred within the gun (Malcolm et al., 1989).

Besides the electron accelerator, the MAIN payload carried a tethered probe (TETHER) to measure the potential of the MAIN during beam operations, a set of photometers, a set of scintillator electron detectors, a complement of Geiger-muller tubes, two electrostatic analyzers (ESA) and a bipolar, 1 cm^2 surface-current monitor (SCM). The SCM and the ESAs were located at the top (north) end of the MAIN and looked directly up the magnetic field lines. This paper makes extensive use of simultaneous data from the TETHER and the SCM whose measurements were sampled 625 times per second.

The time-altitude plot in Figure 7 shows the TETHER being ejected near apogee (279 seconds, 292 km). It was spring ejected with a velocity of about 1.5 meters per second in the magnetic north direction. Sixty meters of Teflon insulated wire, stored on a fishing reel inside the probe, played out as the probe moved northward. Images from the PDP television camera showed that the probe succeeded in reaching its full 60 meter separation distance and rebounded back towards the MAIN near the end of the flight. The TETHER probe itself was an Aerodag coated aluminum cylinder with a total surface area of 544 cm^2. The probe was electrically connected to an isolation amplifier in the MAIN through a 10^9 Ohm resistor (see Figure 8). The circuit was designed to measure potential differences at three levels of sensitivity up to 5kV. To provide an in-flight calibration of the TETHER current collection system, the reference of the isolation amplifier was tied to stepping power supply that periodically biased the system at 100, 200, 300, 400 and 500 volts.

PAYLOAD POTENTIAL AND RETURN CURRENT VARIATIONS

In this section we consider the vehicle responses to various combinations of beam emissions and ACS maneuvers during the period in which the tethered probe was operating. An overview of measurements retrieved during the period from 278.5 to 283.5 seconds is given in Figure 9. The top three panels of the figure give the on/off status of the pitch, roll and yaw ACS jets. The next two panels give the potential between the MAIN and the TETHER on scales of 0 - 5000 volts and 0 - 1000 volts, respectively. The sixth panel indicates negative biases between 0 and 500 volts applied to the TETHER in 100 volt increments. The bottom two panels show the energy and pitch angles of the emitted beams.

Due to the impulse associated with the ejection of the TETHER at 279 seconds, a large number of ACS ejections occurred in the following 1.5 seconds. A cursory glance at the TETHER voltage measurements during the first sequence of continuous beam operations (when ACS activities were frequent) and the second sequence (when ACS activities were infrequent) reveals significantly different responses. Exact details are examined below. We note that during the early phase (280.35-280.75 sec) of the 10 keV emission, the vehicle potential was approximately 350 volts. Except at the time of the pitch maneuver near 281.1 sec, the potential difference between the TETHER and the MAIN increased with the applied biases. We also note that during the 36 keV operations the TETHER potential was generally in excess of the 5 kV measurable potential. During the downward emission near 282.85 sec the TETHER potential hovered very close to 5 kV.

A comparison of the actual with the planned operations (Figure 6) shows that the 110°, 36 keV beam emission near 283.1 sec terminated early and the planned upward injection never occurred. This beam turn-off was associated with an ejection of gas from one of the pitch ACS jets during which the power convertor for the TETHER and the surface current monitor was destroyed. The beam turn-off was caused by the activation of the safety circuit when the primary of the beam power drive tried to draw current in excess of 100 amperes. Malcolm et al. (1989) showed that this demand for high currents was caused by a breakdown due to the presence of positive ions within the gun. We note that all three cases of safety circuit activation coincided with ACS releases and occurred when the deflection magnetic field was either off or weak. The latter point suggests that the damaging ions were created outside of the gun aperture. This is also supported by pre-flight vacuum chamber tests of the accelerator system. During those tests, breakdown

occasionally occurred within the gun when the beam
deflection magnet was turned off or was at a low field
strength.

Before considering detailed responses of the vehicle to
gas releases during continuous operations, it is useful to
consider first the situation when no gas releases occurred.
Figure 10 gives data acquired during a 50 ms continuous beam
emission beginning at 282.353 sec. The top three panels
show that all jet nozzles were closed. The vehicle
potential, measured at three levels of sensitivity are given
in the panels marked HVM3, HVM2, and HVM1 with full range
deflections of 0 to 100 volts, 1000 volts and 5000 volts,
respectively. The panel marked HVM4 gives the current
measured by the 1 cm^2 surface current monitor. This sensor
measured background electron current densities (toward the
vehicle) of about 4×10^{-8} amperes/cm^2. Note that this
"background" level is about 40 times higher than that
provided by the natural, diffuse auroral precipitation in
which the payload flew. The voltage monitor shows that in
the 15 ms after gun turn-on the MAIN acquired a potential of
3.8 kV that gradually decreased to 2.5 kV. The current
measured by the surface current monitor was about 8 μA. This
was typical of measurements during other continuous beam
operations with no ACS activity.

The estimated return current density for the continuous
injections was estimated by dividing the average current
during continuous injections (I_{ave} = 64 mA) by the effective
area of the MAIN payload perpendicular to the magnetic field
($Aperp$ = 0.9 m^2). The estimated current density is about 4
μA/cm^2. If the return current had access to only one side
of the payload, the current density would obviously be 8
μA/cm^2, nearly the same as the measured current.

The mean and standard deviations of the potential and
the SCM measurements during discrete emissions with no ACS
gas or biases are listed in Table 1.

TABLE 1

Beam Operation	MAIN Potential (volts)	Surface Current (μA/cm^2)
10 keV, 30 mA	347 +/- 38	3.2 +/- 0.4
36 KeV, 185 mA, up	~ 5,000	8.4 +/- 1.4
36 keV, 185 mA, out	> 5,000	11.6 +/- 4.8

The first example of the effects of ACS gas releases,
during a 100 millisecond continuous electron gun operation
beginning at 279.533 sec, is given in Figure 11. The beam

ejection was preceded by bursts from the pitch jets, beginning at 279.507 sec and ending at 279.550 sec. After beam turn-on, the MAIN potential only went to 35 V and the current measured by the SCM remained at its background level. When the pitch jets turned off, the potential of the MAIN quickly increased to more than 2 kV and the SCM detected currents in the 8 to 10 μA range. The roll jet opened at 279.565 and closed at 279.600 sec. Again the vehicle potential decreased to about 30 V and background currents at SCM. However, after the gas turned off, the potential and currents remained at depressed levels for 33 ms until the gun operation terminated.

Figure 12 provides a second example, this time with gas coming from the upward pointing yaw jet. While the beam and jet were both turned on, the vehicle potential was about 60 volts and SCM measured background level currents. In the 25 ms after the yaw jet nozzle closed, the vehicle potential and SCM current increased to 600 volts and more than 10 μA, respectively.

The final example, Figure 13, is designed to show the persistence of gas from ACS roll maneuvers. After the first beam turn-on at 279.233 sec, the potential and current monitors measured values > 2 kV and 10 μA. When the nozzles opened they decreased to 45 volts and background, respectively. After a 50 ms gun-off interval, the beam turned on for a 100 ms operation. Lingering effects of the gas are evident. We see that the potential of the MAIN slowly increased to 1.5 kV, a full kilovolt below the average charging level for continuous emissions with no ACS gas. The current collected at SCM reached values of 16 μA, almost twice the amount collected in the example shown in Figure 10.

For the sake of comparison we have plotted in Figure 14 the current measured by the SCM as a function of vehicle potential. The circled dots represent all of the data points measured subsequent to the turn-off of the yaw jets (Figure 12). The "x" points were measured in the 100 msec period after 279.333 sec (Figure 13). Measurements taken during the discrete operations, summarized in Table 1, and the continuous operation (C) shown in Figure 10 are also plotted. The lowest voltages and currents were detected after nozzle turn offs. Although the vehicle potentials did not recover to the levels without gas, the highest currents measured by SCM occurred after gas ejections. The straight lines in Figure 14 representing $I \propto V^{n/2}$, where n = 1, 2, 3 are meant as guides for the eye to which we attribute no physical significance at this time.

DISCUSSION

The results of the previous section can be summarized in terms of three empirical conclusions:

(1) During all types of ACS releases, the vehicle potential decreased to between 30 and 60 volts and the SCM measured currents at background levels.

(2) Immediately after pitch ACS maneuvers the vehicle potential and the SCM measurements returned to levels associated with no gas near the MAIN.

(3) For several tens of milliseconds after yaw and roll maneuvers the vehicle potential remained depressed but return current at the SCM exceeded unperturbed values.

In the following paragraphs we discuss the significance of these results for our understanding of beam vehicle interactions during and after ACS gas releases at ionospheric F-layer altitudes.

The decreased potentials of MAIN with respect to TETHER during ACS operations agrees with the results from CHARGE 2 reported by Banks et al. (1988). This general result was theoretically anticipated by Linson (1983), although he had the case of outgassing from the Shuttle in mind. The consistent measurement of low return-current readings by SCM at first appears counter intuitive. With the vehicle potential lowered from 2 - 3 kV to several tens of volts, the beam more easily escapes through the sheath surrounding the MAIN. Thus, total return currents equivalent to the full beam current must be collected on the surface of MAIN. These return currents are made up of electron extracted from the nearby atmosphere and newly produced ionization from the ACS gas plumes. The non-detection of return current electrons by the SCM provides a critical clue about the nature of plume-vehicle interactions.

We recall that the SCM was a 1 cm^2 patch that looked upward along the magnetic field and located on the north end of MAIN, close to the location of the electron gun aperture. The ACS jets were on the south end of the payload, about 1.5 meters aft of the gun and SCM. During ACS releases, most of the return current was not collected at the beam end of the vehicle. The surface collecting area of MAIN was approximately 3 m^2. During discrete 10 and 36 keV operations the gun emitted 30 and 180 mA, respectively. If current was uniformly collected on the surface of MAIN, SCM would have detected 1.6 and 7.2 μA, about a factor of two lower than levels in Figure 14. We attribute this to the

control of electron motion exerted by the earth's magnetic field.

Scaling the "c" data points in Figure 14, we estimate a root mean squared current of approximately 100 mA during continuous emissions. During ACS releases, N_2 molecules were released at the rate of ~ 10^{23} per second. Providing a return current of 100 mA required the ionization of only one molecule in 10^5. The several tens of volts detected during gas emissions is sufficiently above the 15.5 eV ionization potential of N_2 to generate the required current.

The fact that currents detected at the location of SCM remained at background levels during gas releases is consistent with the bulk of the return current being collected close to the locations of the ACS jets. The probability of producing ionizing collisions between ambient electrons and neutral molecules is greatest close to the jet where the densities of emitted, neutral molecules and the kinetic energies of impacting electrons are highest. Also, for an electron to contribute to the return current it must be allowed access to the surface by the earth's magnetic field. At auroral latitudes the gyroradius of a 10 eV electron is about 20 cm.

The influence of the earth's magnetic field explains the varied current/voltage responses of the MAIN after gas emissions from the different jets terminated. Figures 2 and 3 show that the pitch nozzles ejected gas across the magnetic field, while the gas from the roll and yaw jets had significant components along the earth's field. Data in Figure 11 show that as soon as the pitch jet turned off the vehicle potential and the return current collected by the SCM returned to their unperturbed values. Electrons created in the N_2 cloud after it magnetically separated from the MAIN could not return in large numbers to the vehicle's surface. In the cases of roll and pitch ejections the gas remained in magnetic contact with the vehicle for relatively long periods of time after gas turn-off. Significant fractions of the electrons created in ionizing interactions within these clouds (with accelerated ambient or beam electrons) maintained access to the vehicle's surface, but now in the vicinity of SCM.

CONCLUSIONS

We conclude that in the light of our experience with ECHO 7, the suggestion of Banks et al. (1988) that neutral gas emissions provide a safe method for ensuring that energetic beam particles get away from the emitting vehicle should be qualified. First, if possible, use continuous gas emissions to protect the vehicle from very rapid changes in charging status. Second, if only intermittent gas releases are possible, deflection magnets can protect the gun from internal discharges. Third, the effects of intermittent gas releases can be enhanced by directing them with a thrust component in the direction of the magnetic field.

REFERENCES

Banks, P.M., B.E. Gilchrist, T. Neubert, R.I. Bush, P.R. Williamson, N. Meyers and W.J. Raitt, Rocket observations of electron beam experiments with vehicle charging neutralized by neutral gas plumes, XXVII COSPAR, 18 - 29 July 1988, Espoo Finland, Topical Meeting on Active Experiments, 343, 1988.

Cohen, H.A., R.C. Adamo, T. Aggson, A.L. Chesley, D.M. Clark, S.A. Dameron, D.E. Delroy, J.F. Fennell, M.S. Gussenhoven, F.A. Hanser, D. Hall, D.A. Hardy, W.B. Huber, Katz, H.C. Koons, S.T. Lai, B. Ledley, P.F. Mizera, A.G. Rubin,G.W. Schnulle. N.A. Saflekos, M.F. Tautz and E.C. Whipple, P78-2 Satellite and Payload Responses to Electron Beam Operations on March 30, 1979, in Spacecraft Charging Technology 1980, NASA CP 2182; AFGL-TR-81-0270, ed. by N.J. Stevens and C.P. Pike, 509-559, 1981. ADA114426

Linson, L.M., (1983) The Importance of Neutrals, Transient Effects and the Earth's Magnetic Field on Sheath Structure, in Proceedings of the Air Force Geophysics Laboratory Workshop on Natural Charging of Large Space Structures in Near Earth Polar Orbit: 14-15 September 1982, AFGL-TR-83-0046, ed. by R.C. Sagalyn, D.E. Donatelli and I. Michael, pp. 283-292, 1983. ADA134894

Maehlum, B.N., J. Troim, N.C. Maynard, W.F. Denig, M. Friedrich and K.M. Torkar, Studies of the electrical charging of the tethered electron accelerator mother-daughter rocket MAIMIK, Geophys. Res. Lett., 15, 725-728, 1988.

Massey, D.E., C.P. Williams, E.D. Ransone T.E. EDDY and S.J. Monson, Black Brant 36.004 UE Final Failure Report, NASA Goddard Space Flight Center, Wallops Flight Facility, 1987.
Pierce, J.R., Theory and Design of Electron Beams, D. Van Nostrand Co., New York, 167 - 187, 1949.

Nemzek, R.J., ECHO 7 - Magnetospheric Properties Determined by Artificial Electron Beams, PhD thesis, University of Minnesota, Minneapolis, MN, 1990.

Nemzek, R.J., P.R. Malcolm and J.R. Winckler, Comparison of Echo 7 Electron Bounce Time Measurements to Magnetospheric Model Predictions, to be submitted to J. Geophys. Res., 1991.

Winckler, J.R., P.R. Malcolm, R.L. Arnoldy, W,J, Burke, K.N. Erickson, J. Ernstmeyer. R.C. Franz, T. J. Hallinan, P.J. Kellogg, K.A. Lynch, S.J. Monson, G.P. Murphy, and R.J. Nemzek, ECHO-7: An Electron Beam Experiment in the Magnetosphere, EOS: Trans. Am. Geophys. U., 70, 657-668, 1989.

ECHO-7

PAYLOAD CONFIGURATION

NOSE

PDP

PDP
TV CAMERA
FIELD OF VIEW

EPP

TETHER

MAIN
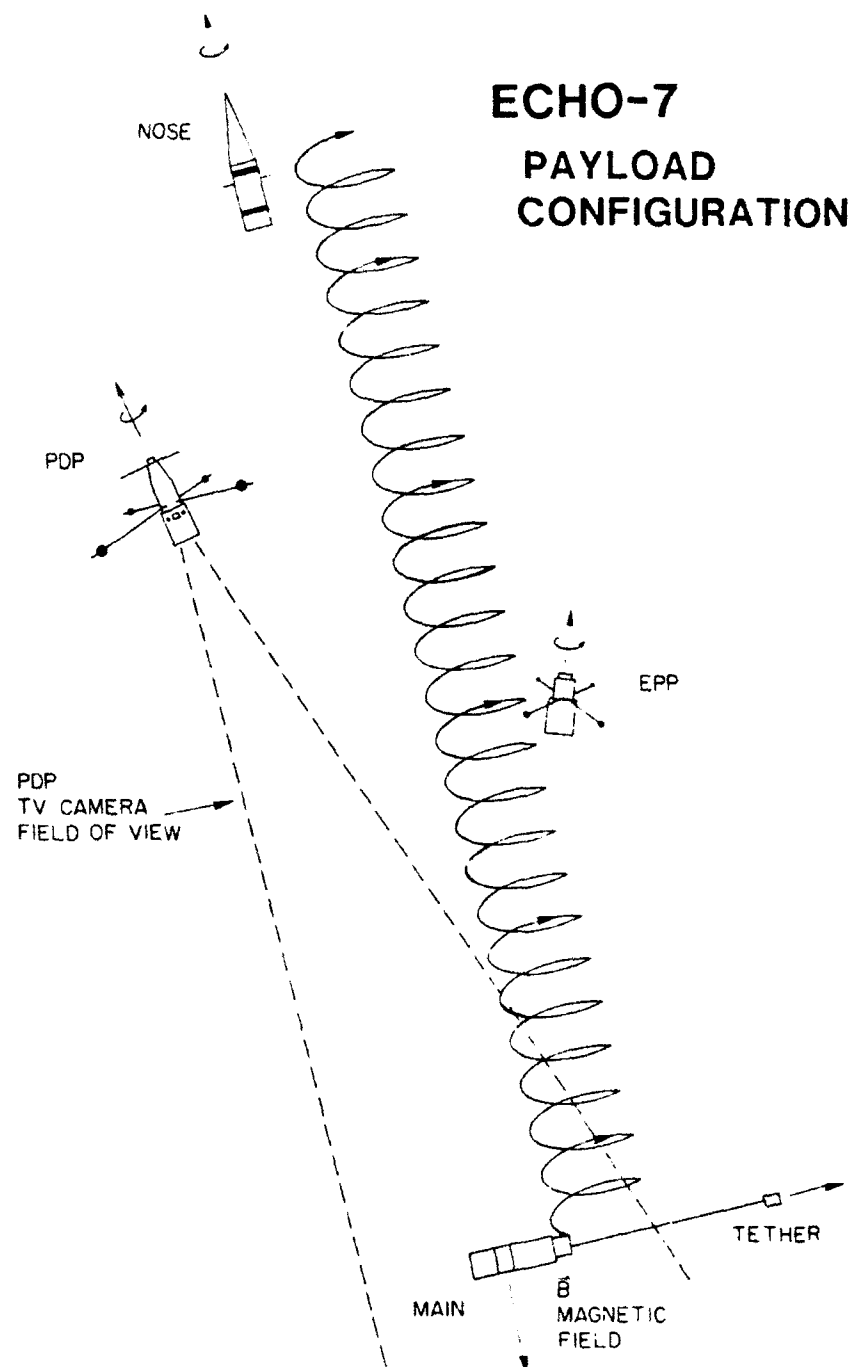
MAGNETIC
FIELD

Figure 1. Configuration of the four free-flying ECHO-7 payloads. NOSE was ejected straight up the magnetic field line, the Plasma Diagnostics Payload (PDP) 10° to the magnetic south and the Energetic Electron Payload (EPP) 25° to the magnetic west of the electron beam emitting MAIN payload.
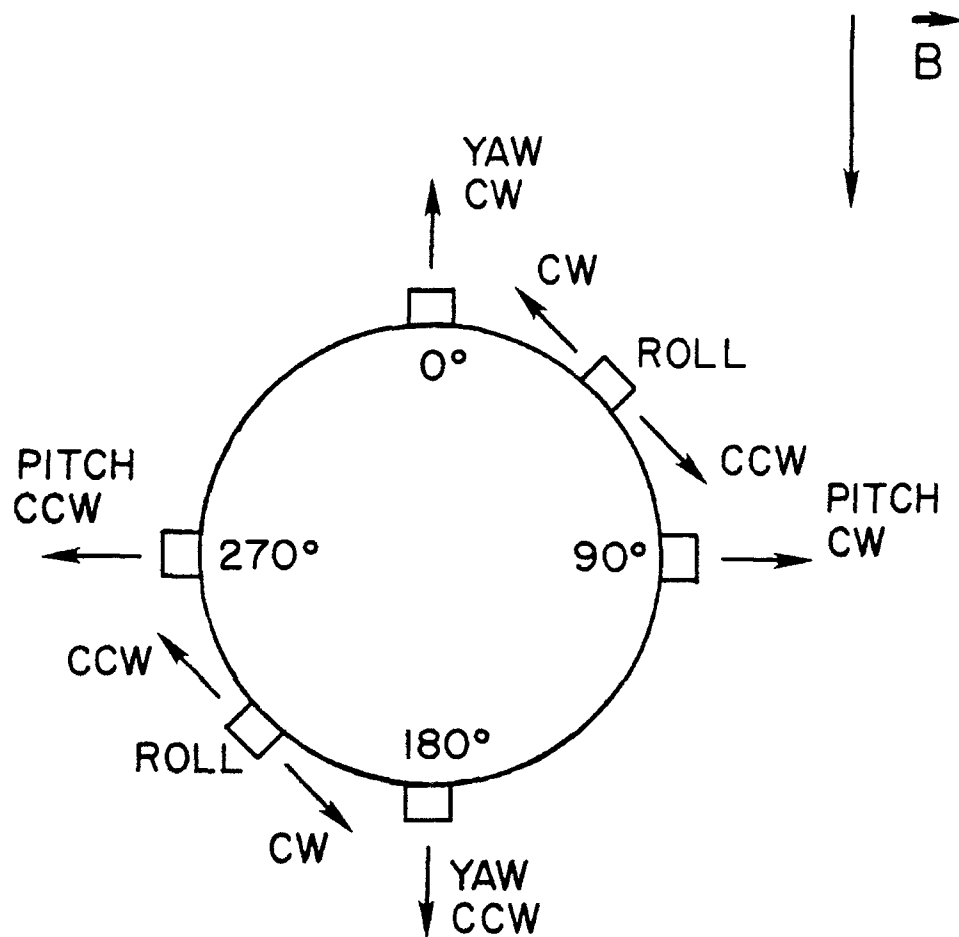
Figure 2. The relative positions of the pitch roll and yaw gas jet nozzles relative to the direction of the earth's magnetic field. The notations CW and CCW indicate clockwise and counter clockwise impulses applied to MAIN.
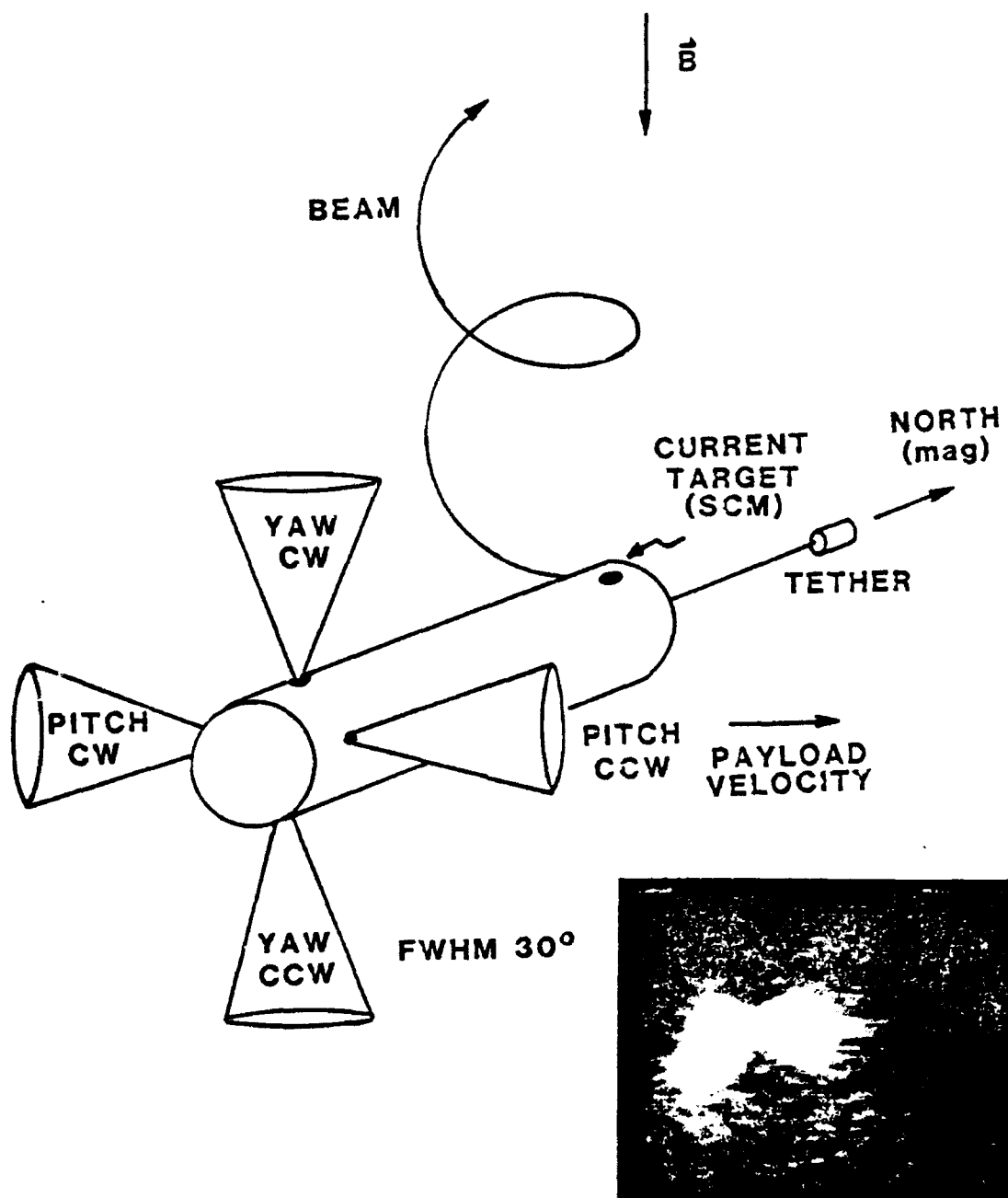
Figure 3. Configuration of the ECHO-7 MAIN payload, orientated perpendicular to the earth's magnetic field with the TETHER being ejected toward the magnetic north. The surface current monitor (SCM), or current target, was located on the top side of the payload near the electron gun. The attitude control system (ACS) was located on the south end of the payload with the orientations of pitch and yaw jets shown. The inset shows ACS roll jet nitrogen plumes, excited during beam emission, recorded by the PDP television camera.
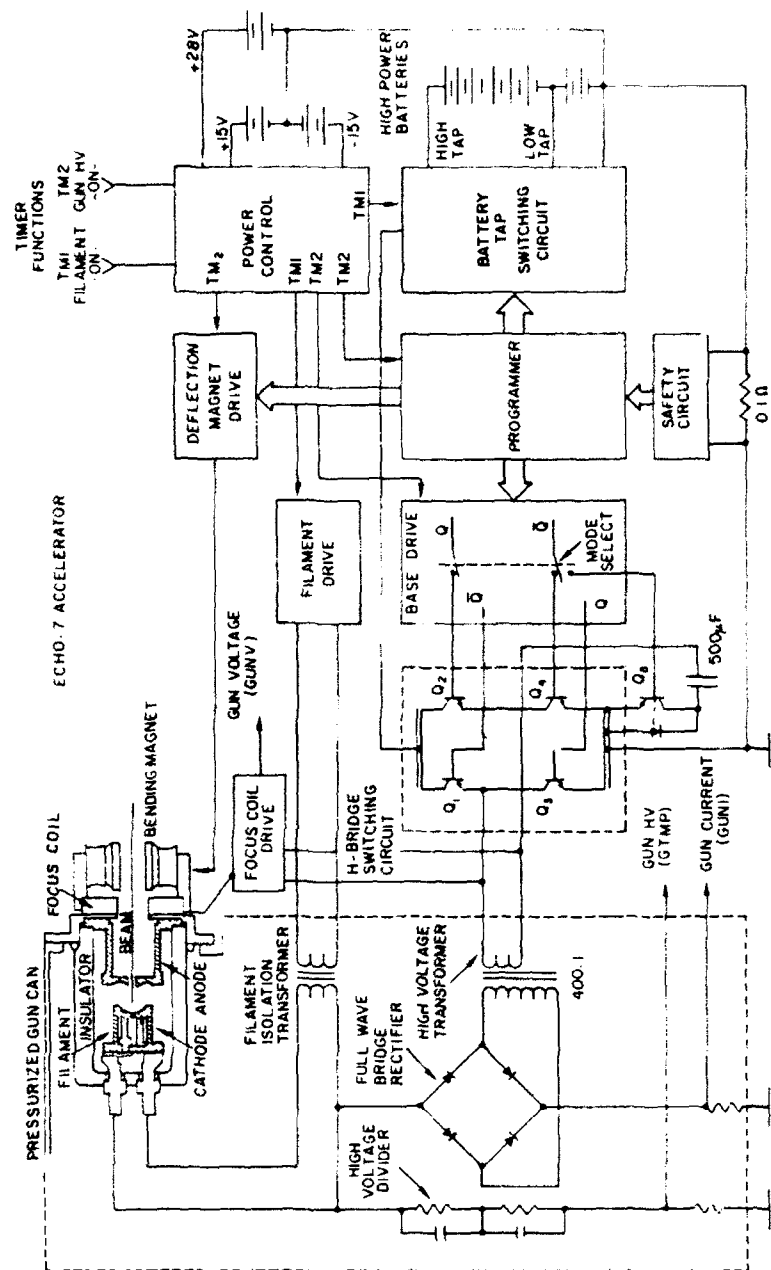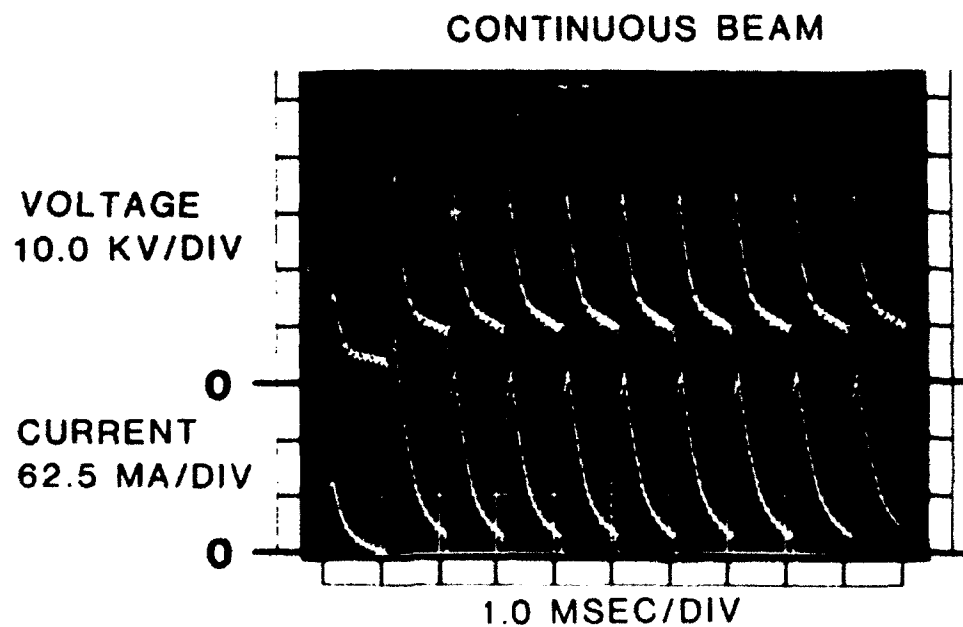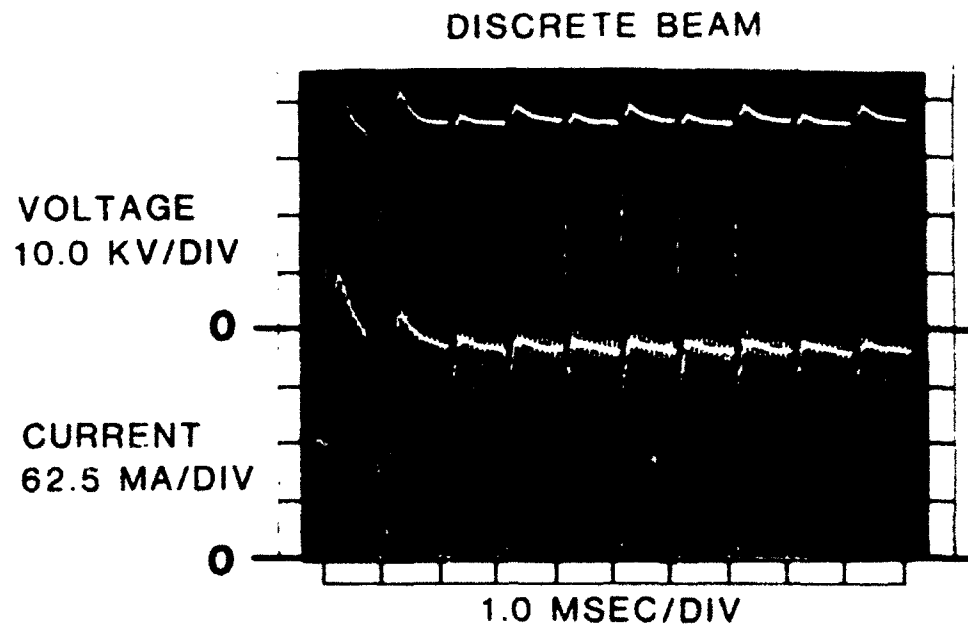
Figure 4. Diagram representing the main components of the ECHO-7 electron beam emission system.

ELECTRON GUN OUTPUT WAVEFORMS

DISCRETE BEAM

VOLTAGE
10.0 KV/DIV

CURRENT
62.5 MA/DIV

1.0 MSEC/DIV

CONTINUOUS BEAM

VOLTAGE
10.0 KV/DIV

CURRENT
62.5 MA/DIV

1.0 MSEC/DIV

Figure 5. Oscilloscope photographs of accelerator output voltages and currents while operating in the "discrete" and "continuous modes".
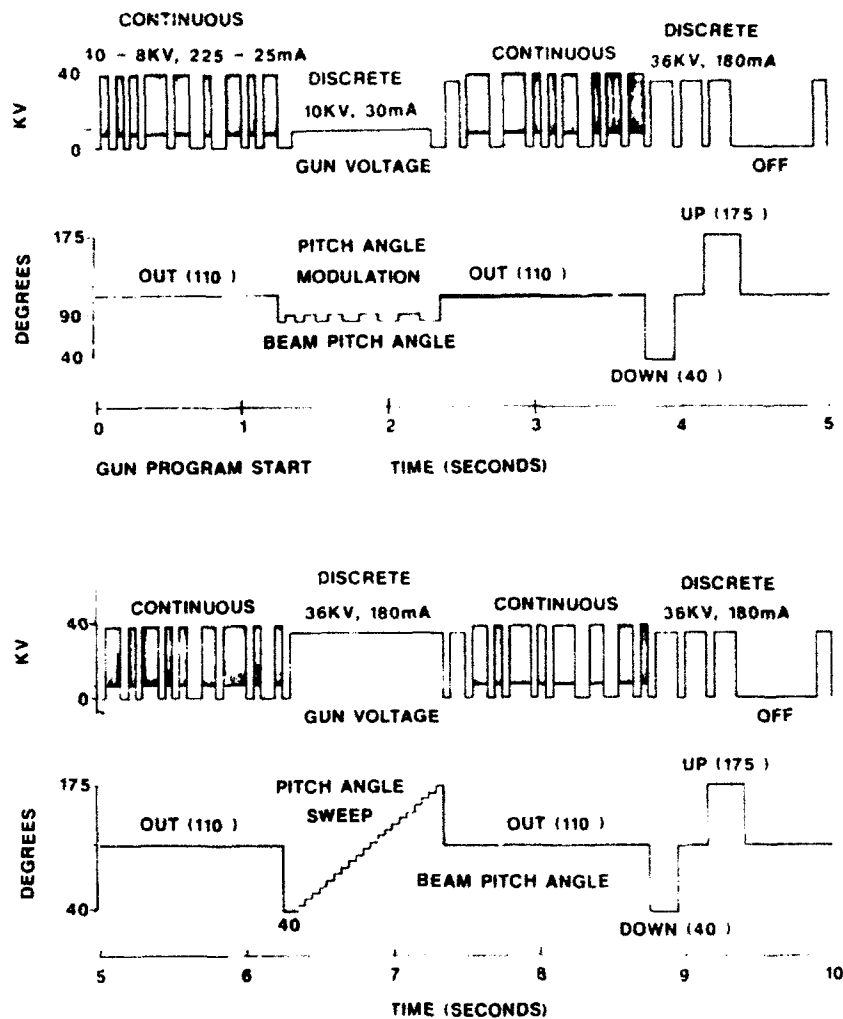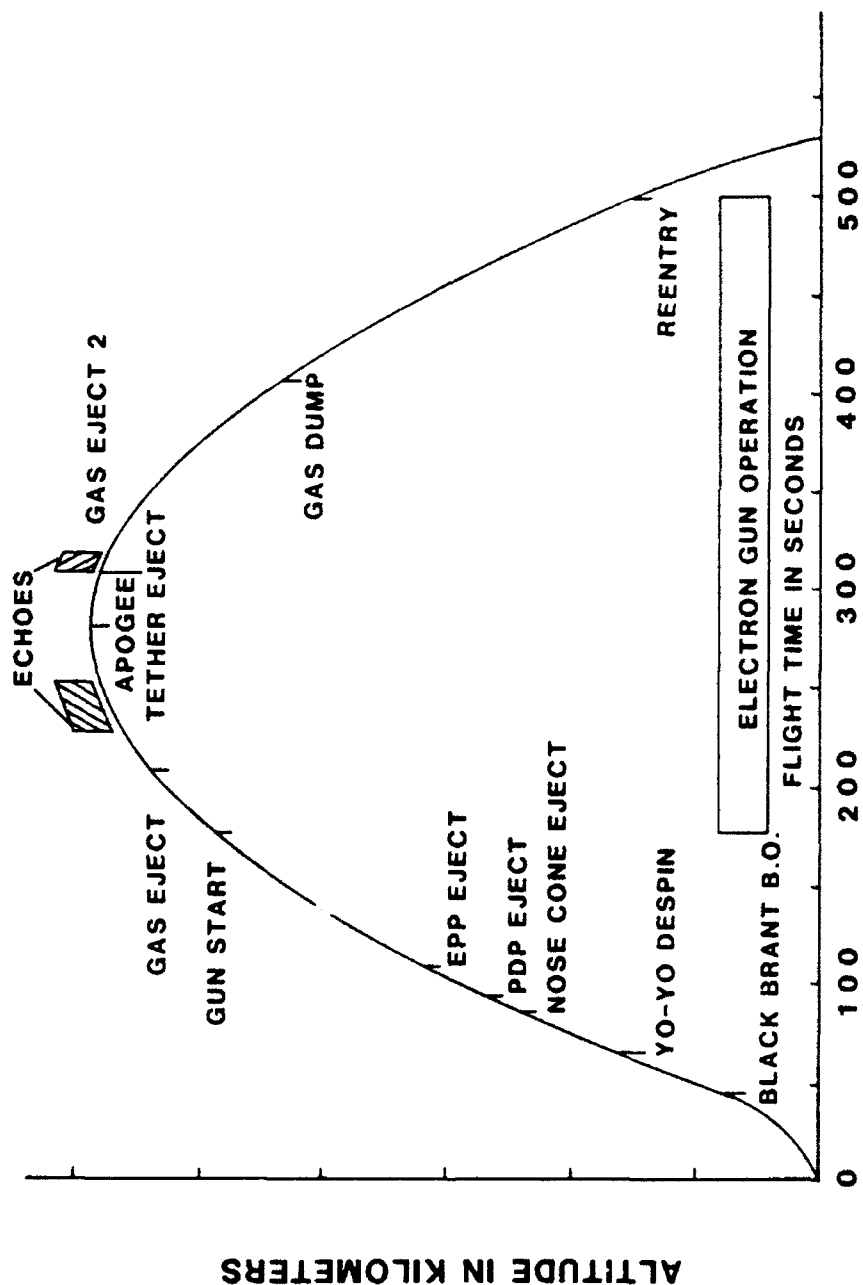
Figure 6. The ten-second, programmed electron beam emission sequence. This sequence was repeated from beam turn-on at 179 sec of the flight through re-entry at 500 seconds.

Figure 7. Time-altitude plot of ECHO-7 trajectory with time events labeled.
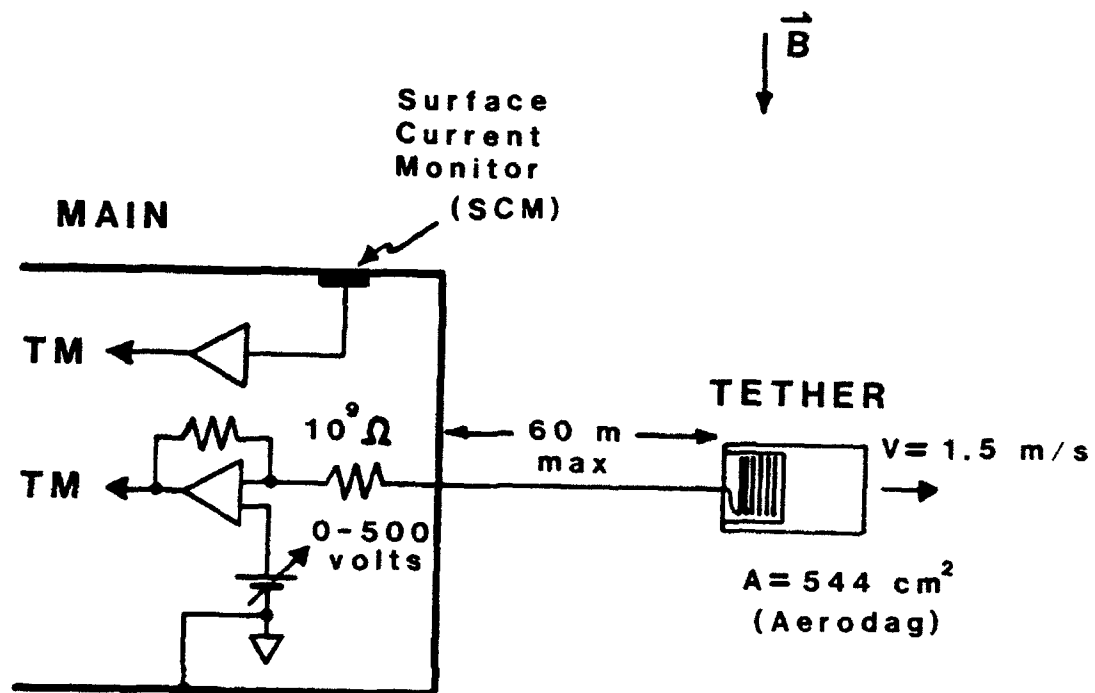
Figure 8. Schematic representing the TETHER deployment configuration and electronic circuitry.
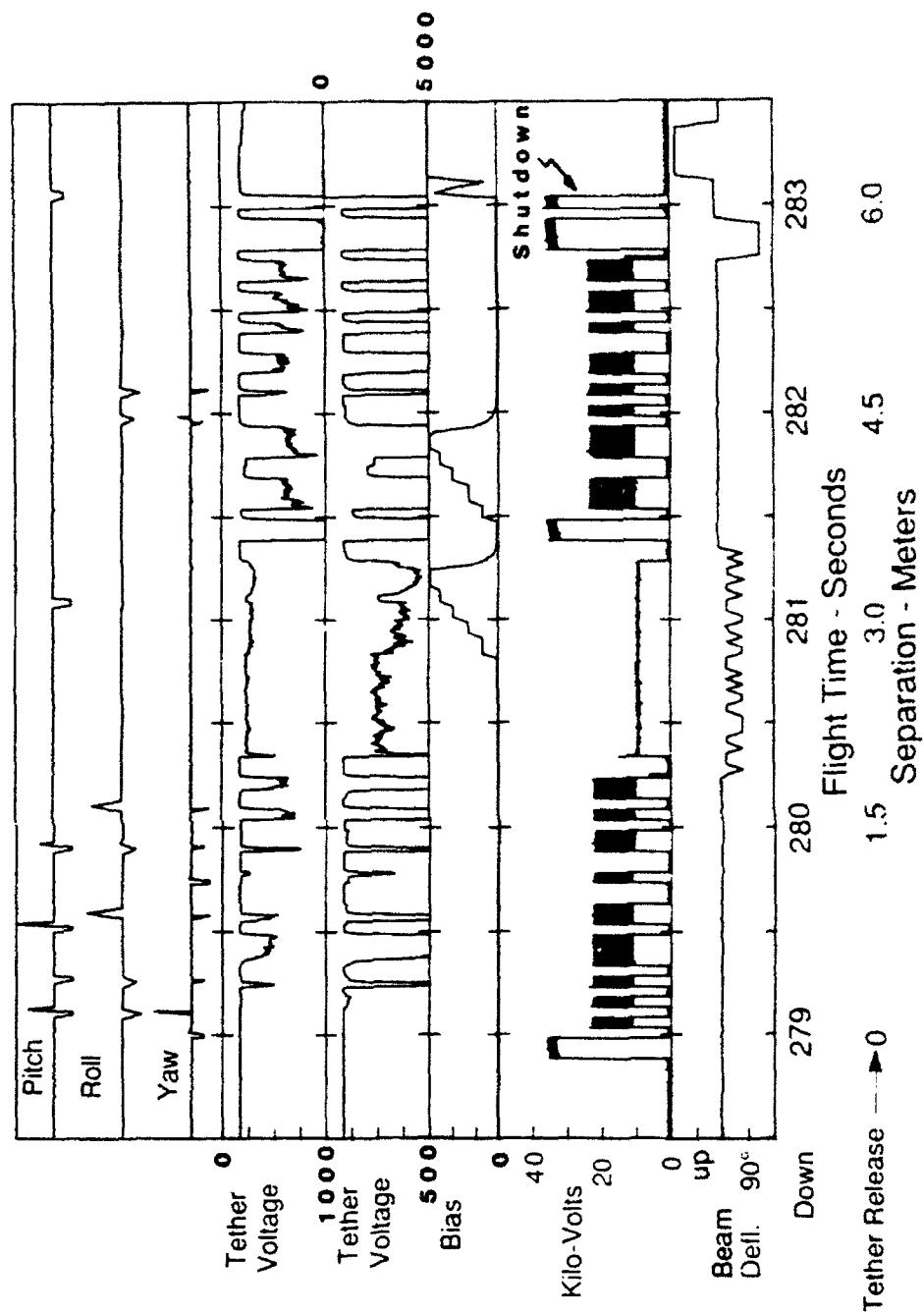
Figure 9. MAIN-Tether data acquired during the interval 278.5 - 283.5 sec after launch. The top three panels give the ACS status. The next two panels give the Tether potential with respect to MAIN at two levels of sensitivity. The fifth panel shows the bias voltage applied to TETHER. The bottom two panels represent the beam voltages and injection pitch angles.

398
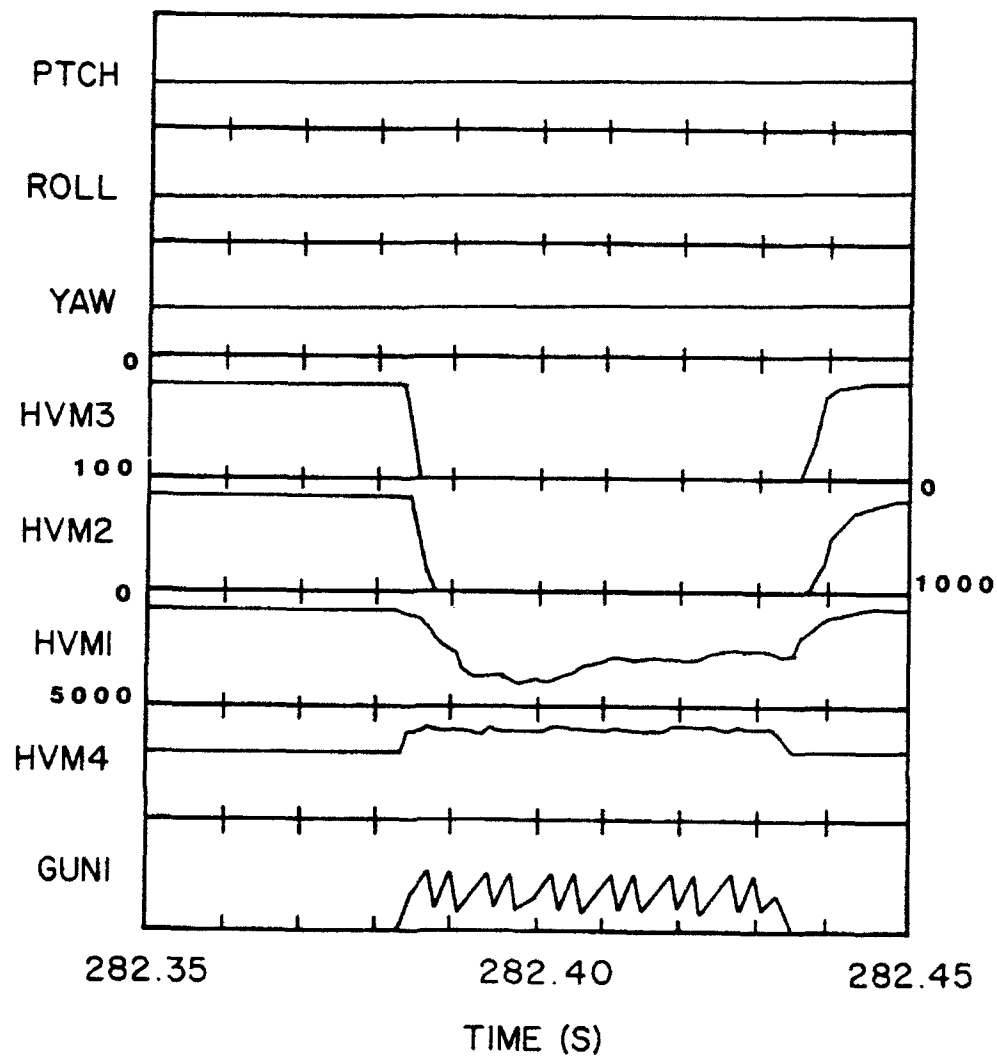
Figure 10. MAIN/TETHER measurements during a 50 ms continuous beam operation with no ACS ejection.

399

Figure 11. MAIN-TETHER measurements during a 100 ms continuous beam operation with a sequence of pitch and roll ACS ejections.

400

Figure 12. MAIN-TETHER measurements during a 50 ms continuous beam operation with a yaw ACS ejection.

401
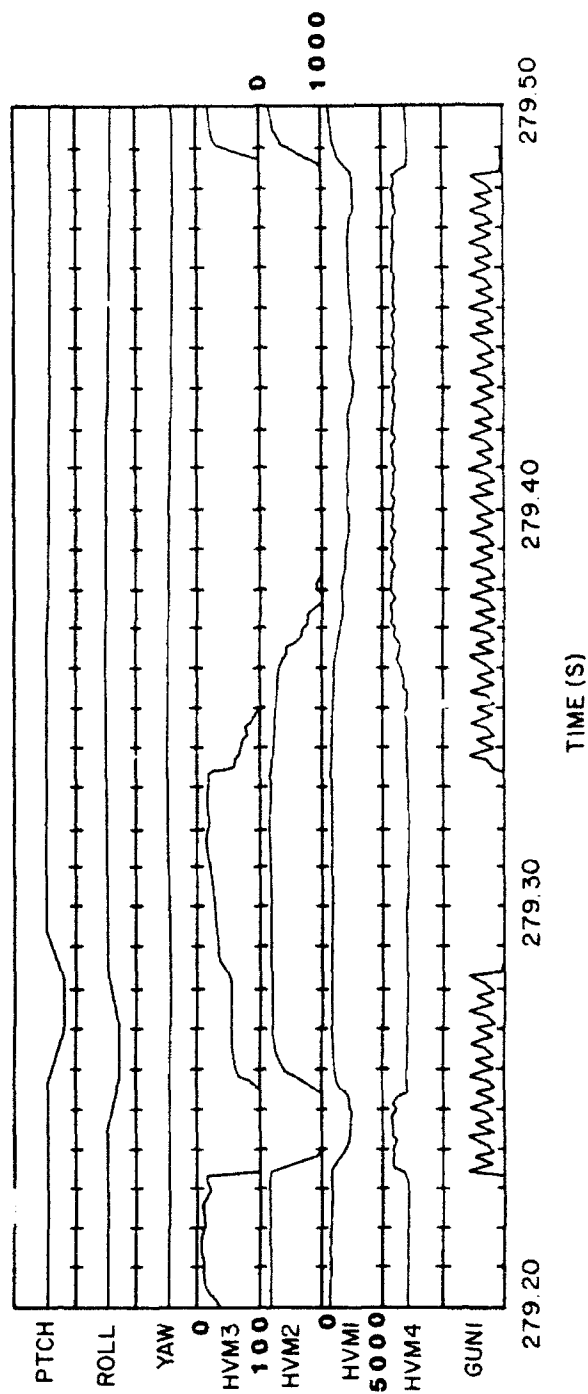
Figure 13. MAIN-TETHER measurements during a sequence of continuous operations with a pitch and roll ACS operation.
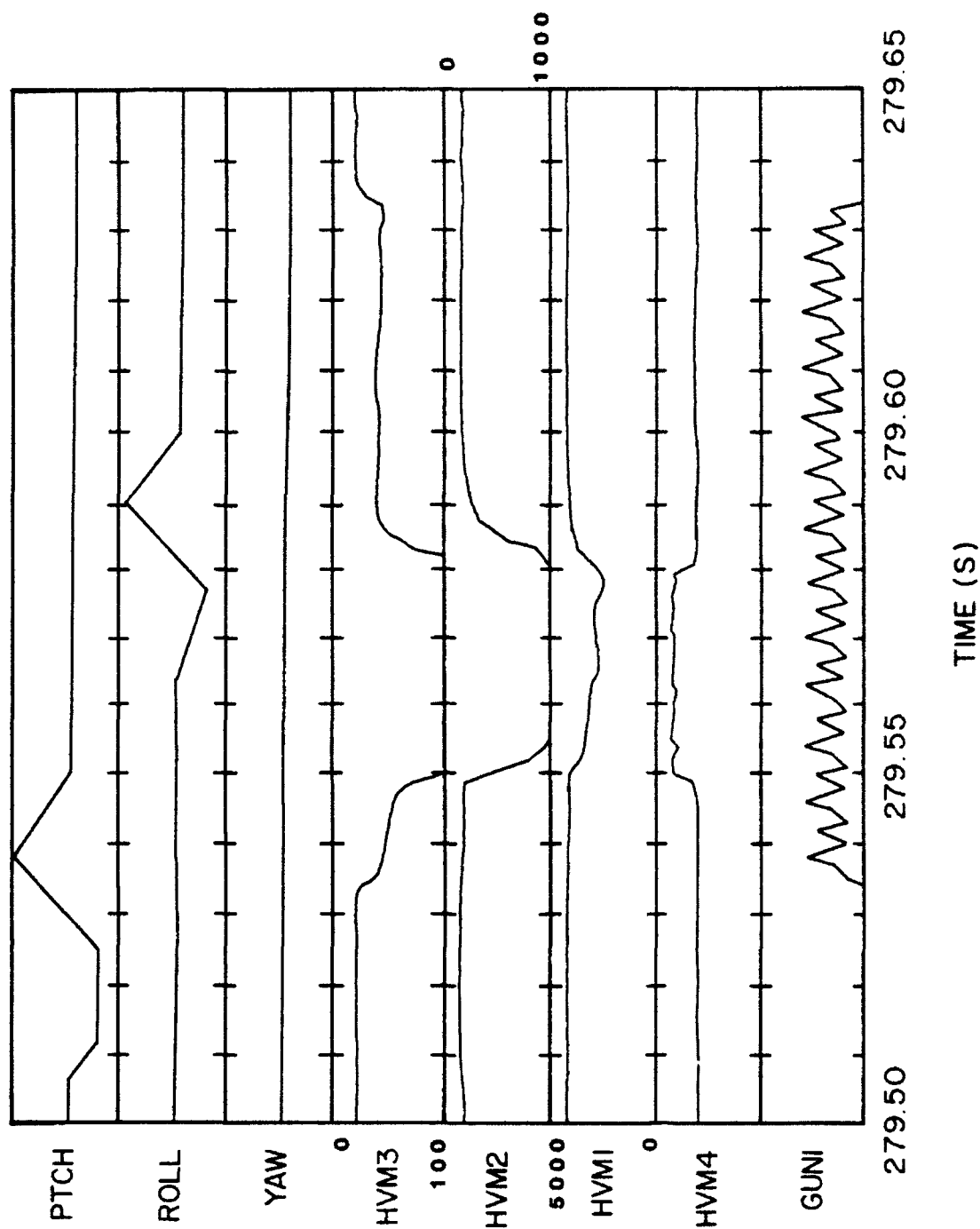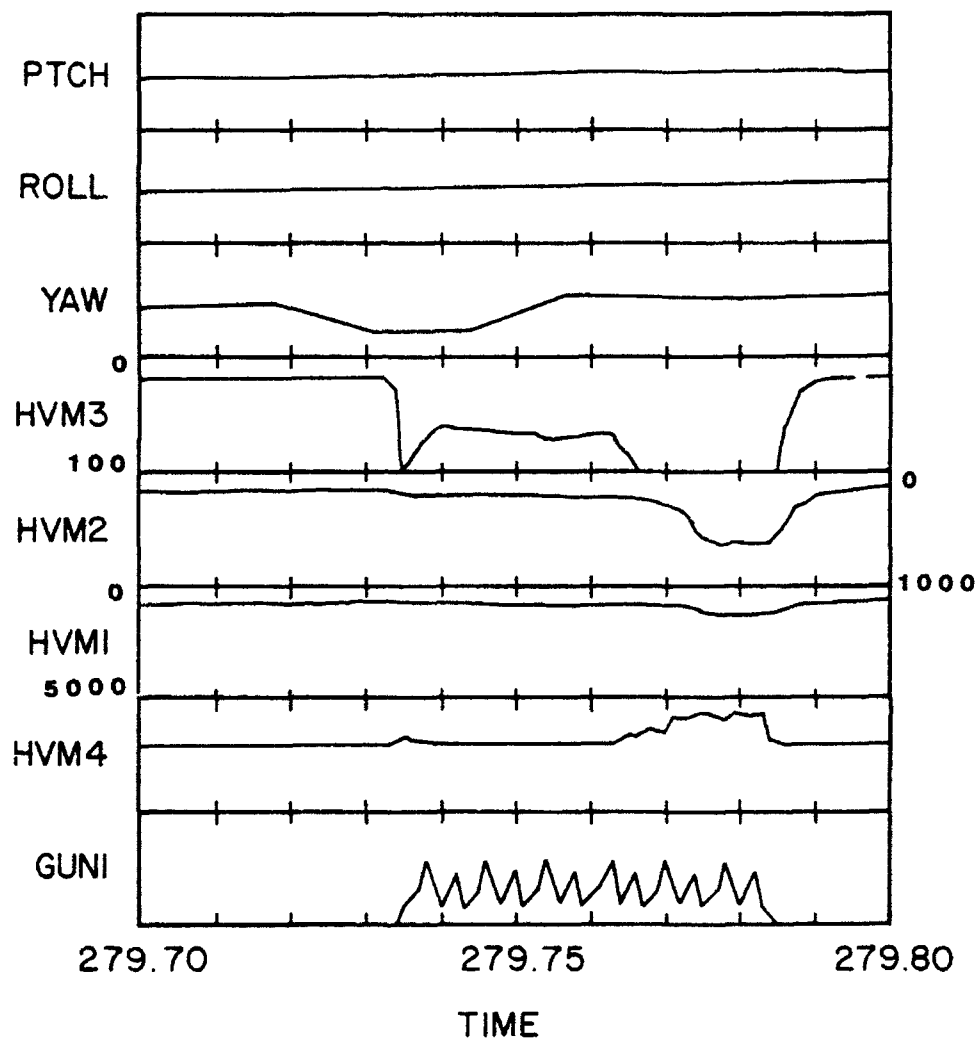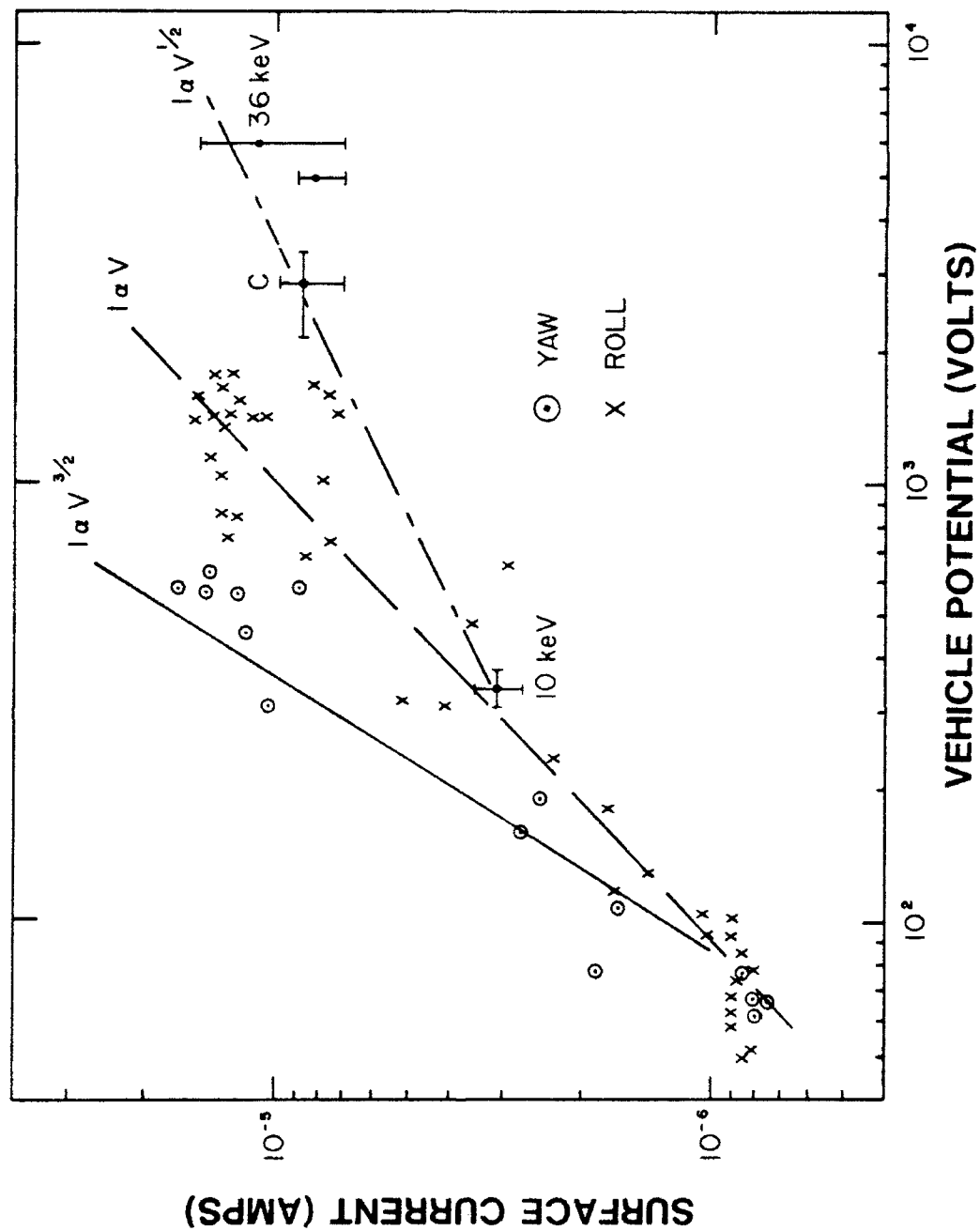
402

Figure 14. Surface current measurements as a function of
the vehicle potential. The circled dots (crosses)
represent measurements after the yaw (roll) gas ejections
shown in Figure 8.

403

Immediate and Delayed High-Energy Electrons due to Echo 7 Accelerator Operation

R J Nemzek and J R Winckler
School of Physics and Astronomy, University of Minnesota

Abstract:
Detectors on the Echo 7 sounding rocket measured a variety of >1 keV electron pulses resulting from injections of high-energy electron beams. The pulses came from directly-scattered beam electrons, stimulated precipitation of trapped radiation, beam-plasma interactions, and conjugate echoes. The different sources can be distinguished by their delays relative to gun injections- coincident, delayed by 10-100 milliseconds, or delayed by several seconds, respectively.

Introduction:

The Echo 7 sounding rocket, launched 0816:49 UT, 9 Feb. 1988 from Poker Flat, AK, carried a number of detectors designed to measure electrons with energy greater than 1 keV. Most of the instruments were intended to measure 'conjugate echoes'- artificial electron pulses that travel to the southern hemisphere conjugate point and back- but they actually observed a number of immediate and delayed responses to electron gun firing. These included scattered beam particles, ambient electrons accelerated or scattered toward the accelerator payload, particles energized in beam-plasma interactions, and conjugate echoes. Electrons from these different sources can be distinguished from each other by their delay relative to gun firing- the scattered beam electrons and natural particles were observed in coincidence with gun injections, Beam-interaction products were detected 10-100's of milliseconds after injections as they drifted in the payload wake, and the conjugate echoes were measured several seconds after gun pulses as required for their round trip to the southern hemisphere. We will treat each of these processes in turn. The conjugate echo discussion will emphasize payload charging and beam losses rather than the natural magnetospheric properties that can be deduced through the echo technique (see, e.g., Winckler, 1982).

Electron Gun and Instrumentation:

The Echo 7 electron gun operated in two modes: Continuous and Discrete. In Continuous mode, the beam voltage decayed exponentially from 42 kV to 8 kV each millisecond. The gun was a space-charge-limited diode, so the current was proportional to (gun voltage)$^{3/2}$. The current at 42 kV was 225 mA; at 8 kV, 20 mA. All Continuous injections were at 110 degrees pitch angle. Continuous injections were coded in unique groups of 50, 100, and 150 millisecond pulses, to aid in identifying conjugate echo bounce times. Discrete injections

were quasi-DC pulses at 36 keV, 180 mA or 10 keV, 27 mA. 36 keV pulses were 100 or 150 milliseconds long, and were designated by pitch angle as Down (45 degrees), Out (110 degrees) or Up (175 degrees). The 10 keV injections were .95 seconds long, at a pitch angle that was slowly modulated around 90 degrees. Winckler et al. (1989) gave a more complete description of the Echo 7 electron gun.

As explained in Winckler et al. (1989), Echo 7 consisted of a MAIN or accelerator payload and three free-flying subpayloads- NOSE, EPP and PDP. The data presented here will be from a combination of Geiger tubes, scintillation counters, and electron spectrometers flown on the MAIN, PDP, and EPP. A brief description of the instruments follows:

1. Geiger tubes: The Echo 7 Geiger tube experiment was provided by the Air Force Geophysics Lab. Two sets of 4 tubes were flown on the MAIN, one set looking down the magnetic field, the other perpendicular to it. Each set had mica windows with thicknesses resulting in low-energy electron cutoffs at 30, 38, 50, and 75 keV, where the cutoff is defined as half-maximum detection efficiency. The response function for the windows was fairly broad, as shown in Figure 1. The AFGL calibration apparatus only extended to 40 keV, so the upper part of the 50 keV edge and all of the 75 keV edge have been constructed assuming that all the windows had $dE/Eo = 25\%$, where Eo is the half-max energy. This was true for all the measured curves. The widths of the thresholds and the overlap between them complicate analysis somewhat. Each tube was collimated to 45 degrees half-angle and had a geometry factor of .78 cm^2sr. All the tubes accumulated counts with a sample time of 25.6 milliseconds, except the down-looking 30 keV tube, which was read out every 3.2 milliseconds. A roughly 50 microsecond deadtime after each count imposed an upper limit of about 20 kHz count rate. Count rates above about 300 cts/sample seriously underestimated the actual incident flux.

2. The Echo 7 scintillators were very similar to those flown on previous Echo flights. 4500 Å of aluminum on the scintillation crystal's front surface established an approximately 1 keV lower energy threshold. The phototube output was read as a current and sent through a 5-decade log amplifier. The scintillators were collimated to 13 degrees half-angle and had a .13 cm^2sr geometry factor. The absolute energy flux calibration of the scintillators has not been completed. Four scintillators were flown on the PDP and EPP, one every 90 degrees in azimuth. The MAIN held two scintillators, one looking up at electrons with 0 degrees pitch; the other looking parallel to the injected beam, detecting electrons at 70 degrees pitch angle. Scintillators on the PDP and EPP were sampled at 625 Hz, while the up-looking MAIN scintillator was read at 2500 Hz and the out-looking tube at 5000 Hz.

3. TED's: The Toroidal Electron Detectors (TED's) were curved-plate electron spectrometers with geometry factors of about 5×10^{-3} cm^2 sr keV. They measured electron energies to 7.5% resolution, from 2 keV to 40 keV. The detectors accumulated counts during 32, 1.6 millisecond steps, for a complete sweep time of 51.2 milliseconds. EPP and PDP each had two TED's, 180 degrees apart, perpendicular to the subpayload spin axis (EPP) or 80 degrees from the spin axis (PDP). Only EPP TED 2 and PDP TED 2 functioned properly.

Measurements:

The electron measurements made by the Echo 7 high-energy electron detectors can be separated into several categories: the natural trapped radiation background; "immediate responses," electrons observed by MAIN payload detectors in coincidence with accelerator operation; "prompt responses," apparent products of a beam interaction observed in the payload wake after a short time delay; and "conjugate echoes," electrons which returned to the payload after several seconds of travel through the magnetosphere.

Background:

Figure 2 shows the high-energy background measured by the Geiger tubes perpendicular to B during gun off times. The down-looking detectors measured <<1 ct/sample. The various Geiger tube channels showed similar temporal features. Counts in the >30 and >38 keV channels were approximately equal, while the >50 kev count rate was slightly lower and the >75 keV rate was only about .3x the rates in the lower-energy channels. This implies a spectrum with electrons primarily above 40 keV, trailing off above 50 keV. Main payload telemetry failed after 325 seconds flight time.

Immediate Responses:

During gun operation, all of the Geiger tubes showed an increased electron flux. Since most injections were at 36 kV or below 42 kV, the > 75 keV channel should not have been greatly affected by scattered gun electrons, although lower channels were probably severely contaminated by this source. Count rates began to increase simultaneously with injections, and built up to a maximum over a roughly 10 millisecond period. At the end of gun pulses, count rates declined to zero in the same length of time. Figure 3 shows the response of the out and down detectors to Continuous injections. Figure 4 is the same for Discrete Out injections, which produced the most intense response in the Geiger tubes. All channels in Figure 4 except the >75 keV curve were saturated. At 250 seconds the flux became so intense that the tubes went into a constant discharge and virtually stopped counting. The count rate at this time was likely >1 MHz. Down and Up injection responses were several times less intense than those from the Out pulses. 10 keV injections produced a slight but definite increase in all Geiger tube channels. This shows that at least some of the Geiger tube signals were

406

likely produced by electrons far above the beam energy. We are assuming that the Geiger tube responses all were due to electrons. If x-rays from beam electrons were present in sufficient numbers, the analysis of the Geiger tube data could be quite different. Even low energy x-rays could penetrate the high energy windows of the tubes.

Comparing Figures 3 and 4 to Figure 2, it is clear that several features are the same in each- e.g., the peaks at 260 and 310 seconds. This indicates that some of the high-energy electrons counted by the Geiger tubes were probably precipitated natural particles. The electron beam opened the loss cone above the rocket, allowing the formerly trapped radiation to propagate downward. This result would take a substantial change in pitch angle- electrons at 90 degrees pitch above the rocket would need their pitch angles reduced by 45 degrees in order to mirror and return within the solid angle of the down-looking detectors. A pitch angle of 70 degrees, however, would allow electrons to intercept the 100-km atmosphere; thus most of the upward-travelling electrons are likely backscattered from the atmosphere. Count rates in the 75 keV out- and down-looking channels were about equal, so the flux reaching the rocket must have been nearly isotropic. The count rate increases near 190 seconds and 310 seconds were relatively large compared to the corresponding change in the background rate. This may be the result of enhanced precipitation and beam scattering at lower altitudes; apogee was at 281 seconds.

The Trigger (Bering et al., 1982), Araks (bering et al., 1982) and G-60-S (Managadze et al., 1988) active experiments all measured precipitation of trapped electrons through electron beam perturbation. The Trigger and Araks precipitation, though, was delayed by several seconds with respect to the perturbation, pointing to an interaction occurring out in the magnetosphere. The Echo 7 precipitation and that during G-60-S was coincident with electron beam operation. The G-60-S precipitation was inversely related to payload potential. A similar dependence of precipitation on payload potential may be responsible for the 'altitude effect' resulting in the large flux increases near 190 and 310 seconds flight time as mentioned above.

At present we do not have a complete understanding of the physical process culminating in the precipitation. As discussed above, the precipitation began immediately upon electron injection but required some time both to build up to full intensity and to die away, so the bulk of the scattering probably occurred well above the payload, up to 100 km away. The ratios of the count rates in the >75 keV channels between various injection modes show that the precipitation was greater for high energy-high current gun pulses. This may not be a simple relationship, though. The precipitation during Discrete, 110 degree injections was up to several

hundred times that during Continuous, 110 degree injections, even though the Discrete gun current was only 2.3x the average Continuous injection current. Also, if the payload potential-precipitation connection found by G-60-S operated during Echo 7, the precipitation would have been favored during Continuous injections, which had payload potentials several times lower than Discrete injections (Winckler et al., 1989).

W.J. Burke (personal communication, 1988) has suggested that the loss cone might be opened, allowing precipitation, by the removal of a downward parallel electric field above the payload. The parallel field would be that associated with a local field-aligned current. The beam electrons plus the ambient electrons heated by the plasma might constitute enough downward current to eliminate the need for a parallel electric field to supply the Region 2 field-aligned current. If the beam-produced current was sufficient, an upward parallel electric field might even develop. The loss or reversal of the pre-existing field would then lower the mirror points of the trapped radiation to the payload altitude. A 20° change in pitch angle for a 50 keV electron would require a 5 kV field-aligned potential. We do not have any evidence for the existence of field-aligned currents or large parallel electric fields above the Echo 7 payload.

The MAIN payload scintillators also showed a response coincident with gun pulses. This was primarily composed of gun-energy and lower electrons. The scintillator signal oscillated with the gun drive frequency, 1 kHz. At gun turn on there was often a transient amplitude increase in the oscillations up to 100x the steady-state amplitude. This was also shown by the Geiger tubes (Figure 5). The transient had a harder spectrum than the precipitating radiation. So it appears that the payload initially charged to a significant fraction of the beam voltage and settled back to a steady-state value after about 15 milliseconds. The MAIN payload tether measured an average 2 kV potential during Continuous injections at apogee (Winckler et al., 1989).

Immediately following beam turn-off, the MAIN scintillators measured a short burst of electrons. As altitude increased, the maximum of the burst came progressively later than beam turn-off, being about 10 milliseconds after near apogee (Figure 6). The effect was present even in injections that were disturbed by ACS gas injections, which wiped out practically all other high-energy electrons. Some suprathermal electrons in the hot plasma region could be energetic enough to be counted by the scintillators, but the burst was only at 0 degrees pitch angle. Such a field-aligned pulse of electrons could occur if there was a parallel potential above the payload after beam turn-off. MAIMIK measured a positive payload potential occurring ≈10 milliseconds after a gun pulse (Maehlum et al., 1988), but

this was only about 10 V; the Echo 7 scintillator data require a potential of at least 1 kV to accelerate the electrons.

Prompt Responses

Detectors on the EPP, positioned to the west of the accelerator payload, measured electron pulses delayed by 10-180 milliseconds with respect to gun injections. The location of the EPP means that it was in the general direction of the payload plasma wake, as determined by the combination of ExB drift and the negative of the payload velocity vector. We have dubbed the delayed pulses "prompt responses," in keeping with terminology used for similar events observed during the SCEX I flight (Wilhelm et al., 1985). The best prompt response measurements came from EPP TED2, although the EPP scintillators also detected them. The prompt responses were composed of electrons covering the full 2-40 keV range of TED2, with a differential spectrum proportional to $E^{-3/2}$. The raw data, Figure 7, demonstrates that the responses were most intense for discrete injections near 90 degrees, and that the delay between gun pulse and prompt response increased with flight time- i.e., with increasing distance between the MAIN and EPP. The delay increased almost linearly with distance (Figure 8); the slope of the line in Figure 8 corresponds to a speed of about 1500 m/sec, comparable to the plasma drift velocity in the payload frame. The delays in Figure 8 were determined by measuring the time from the start of a gun pulse to the beginning of the response, regardless of what energy the analyzer was reading at that time. Obviously, there was little dispersion in arrival times between high and low energies.

Our model for creation of the prompt response events is this: when the gun fired, a beam interaction created a flux tube filled with electrons of a wide range of energies, even above the beam energy. This flux tube drifted back into the payload wake region. After some time, it intercepted the EPP, causing the measured prompt response. As the EPP moved away, the drift time increased. Since electrons of all energies drifted at the same speed- gradient-curvature drift was negligible at these low altitudes- there was no dispersion in arrival times. High and low energies would, however, have had to start from different altitudes. The longest measured delays were 180 msec (for 100 and 150 msec injections!). It would be difficult to trap a 40 keV electron near the payload for that amount of time, so the particles must have come from very high altitudes. A 40 keV electron would have to start near 2000 km altitude to be part of a response delayed by 180 msec. The full range of electron energies would be created at these high altitudes, but only the high energies would be able to propagate back down to the payload in time. The delays in Figure 8 go to zero at a perpendicular distance of 60 m; this is the approximate lateral size of the flux tube.

409

As the 2000 km-tall flux tube moved back into the payload wake, its particle population diminished. Figure 9 shows this exponential decay expressed in the flux of 1C keV electrons. The flux dropped off with a 1/e time of about 50 msec. This lifetime and the size quoted above are comparable to those measured for near-rocket 'halos' on Echo 3 (Arnoldy and Winckler, 1981) and Polar 5 (Maehlum et al., 1980). The halos may be the part of the prompt response flux tube nearest the accelerator payload.

The "Out" prompt responses were usually 50-60 msec longer than gun pulses. The responses existed in any one location for the length of the gun pulse plus the time for the flux tube to drift over the subpayload after gun operation ceased. If we assume a nominal 1500 m/sec plasma drift speed, the extra 50 msec is equivalent to a flux tube 75m across, similar to the size derived from the 0-drift-time intercept. When the response amplitude dropped to near zero- around 260 seconds and after 400 seconds in Figure 9- the responses were only as long as gun pulses. At these times the subpayload must have been just grazing the flux tube edge. So it appears that the EPP was in the plasma wake at gun turn-on, moved out of it by 260 seconds flight time, then moved back into it until the prompt responses died away after 400 seconds.

If the ionospheric convection electric fields were nearly constant, as they appear to have been (K.N. Erickson, personal communication, 1989), the EPP should have crossed the flux tube during a single time interval. The movement of the flux tube across the EPP twice may indicate that large-scale, beam-produced electric fields were affecting the flux tube's motion. This might also explain why the drift speeds for prompt responses from Down and Up injections were significantly lower than Out drift speeds: 1000 m/s and 600 m/s, respectively, vs. 1500 m/sec.

The prompt responses appear to have been a major beam power loss mechanism. If we take the prompt response amplitude closest to the payload and assume that it was constant over a 60 m radius, 2000 km tall cylinder, the integrated flux is equivalent to 1000x the total beam power. This is a serious problem. In our mechanism the prompt response power should have come from the injected beam. This discrepancy might be resolved in two ways: by limiting the height of the interaction region, or by reducing the effectiveness of the interaction with height. The 2000 km height came from the very long delay times combined with high-energy electrons; if some trapping mechanism was functioning, the electrons would not have to come from such high altitudes. Trapping could be accomplished by parallel electric fields, but they would have to be on the order of 5 kV total potential. The calculation above assumed that the prompt response amplitude was constant along the entire flux tube. This was certainly not the case.

The relative prompt response intensities during injections at different pitch angles show that the prompt response interaction was maximized for injections near 90 degrees. As the beam propagated to higher and higher altitudes, its pitch angle would have decreased, so the prompt response mechanism would have become less effective with altitude. If the prompt response intensity decreased with altitude, it would change the interpretation of Figure 9. If the power calculation is correct, then the energy for the prompt responses must have come from a non-beam source- perhaps the trapped radiation or the diffuse auroral flux.

The prompt responses likely were caused by an interaction of the beam with the trapped radiation. This source would not only alleviate the prompt response power dilemma but also would present a natural way of providing electrons with very high energies without having to energize ambient plasma electrons to greater than beam energy. Most of the high-energy electrons in the responses probably were not beam particles since their spectrum had no hint of a peak at beam energy. The spectrum was likely not the true trapped radiation spectrum either, but rather the trapped energy distribution modified by the interaction.

One may ask whether the prompt responses were identical to the stimulated precipitation measured by the MAIN Geiger tubes. They apparently were somewhat different phenomena. The prompt responses had an intensity that continually decayed with distance from the MAIN payload, with none of the structure evident in the Geiger tube data. Still, they do both appear to be expressions of stimulated precipitation. The Geiger tubes may have been responding primarily to electrons with energies far above the TED energy range. The prompt responses should have been energetic enough to be counted by the Geiger tubes. The prompt responses probably contributed to a constant count rate in the Geiger tubes, especially during the discrete injections, when the prompt responses were most intense. The MAIN payload would have been on the southern edge of the prompt response region, and the generally westward plasma drift would drag the region away from the MAIN. Therefore any prompt responses measured on the MAIN would only be as long as gun pulses, not longer as the EPP prompt responses usually were.

Conjugate Echoes
Conjugate echoes occur when an electron beam injected in the ionosphere spirals out into the magnetosphere, mirrors or scatters at the conjugate point, and returns to the injecting payload. Whether an echo pulse returns to the payload position exactly or just to the vicinity depends on a vector cancellation between payload velocity perpendicular to B and bounce-average particle drift (gradient-curvature drift and ExB drift). A complete examination of conjugate echo theory can be found in Winckler (1982).

The detection of conjugate echoes was the main purpose behind all flights in the Echo program. Echoes resulting from artificial electron injection can be used to elucidate several properties of the magnetosphere- field line geometry, ionospheric electric field mapping, and equatorial pitch angle diffusion. In the present context, echo measurements can put limits on payload charging and beam power loss.

All Echo 7 particle instruments designed for electron energies greater than a few keV measured echoes, although the scintillators and Geiger tubes on the MAIN were practically useless for conjugate echo work because of interference from the intense immediate electron fluxes that resulted from gun operation. Most of the echo instrumentation was on the free-flying PDP and EPP, which drifted well outside the region of serious gun disturbances. Fortunately the prompt responses described in the previous section did not greatly interfere with echo measurements.

One of the best sequences of conjugate echoes is shown in Figure 10a. The timing and widths of the scintillator pulses match almost exactly with the sequence of gun pulses shown below them- but the electrons arrived at the scintillators about 2.8 sec after they left the accelerator. This means that the time for a complete bounce to and from the conjugate point was 2.8 seconds. Figure 10b shows the energy measurement for two individual pulses from 10a- they were nearly monoenergetic at about 18 keV. This was expected due to the spectrometer action of the magnetosphere. The gradient-curvature drift is energy dependent, so the initial continuous-energy pulses were spread out into a kilometer-long east-west oriented sheet, high energies to the east and low energies to the west. This effect increased the area over which echoes could be detected, and was the motivation behind the use of Continuous injections. The energy measured at the payload position depended on the values of eastward payload velocity and ExB drift present at the time of injection. The measured echo energy changed during the flight, probably due to changing northward electric fields, and so we were able to construct a bounce time-energy diagram (Figure 11). The solid line in the Figure was calculated by numerically tracing electron trajectories through the Olson-Pfitzer quiet time magnetic field model (Olson and Pfitzer, 1977). This demonstrates both that the Olson-Pfitzer model is a reasonable fit to the real magnetosphere during the Echo 7 flight, and that the echoing particles travelled adiabatically.

Echo energy/bounce measurements should not have been affected greatly by moderate levels of payload charging. The initial beam had a continuous energy spectrum; a payload potential would have shifted the spectrum as a whole. As long as payload charging did not slow the entire beam below the adiabatic echo energy, echoes would still return. If the energy change occurred less than an Earth radius or so from the

payload, it would not have a large effect on the total bounce time. The free flyers were far enough away from the MAIN that charging did not alter the energy of returning echoes.

Payload potentials must have been less than the difference between the maximum beam energy and the echo energy. For the data in Figure 11, this puts an upper limit of 20 kV on payload charging. There are many echoes that could not be shown in Figure 11 because they did not have easily determined bounce times. They probably came from Continuous injections. The highest energy echo found as yet was at 34 keV, giving a payload potential upper limit of 8 kV. The MAIN payload tether measured an average potential of 2 kV during continuous injections (Winckler et al., 1989). The tether indicated payload potentials of >5 kV during 36 kV Discrete injections. Unfortunately, the one echo known to have come from a Discrete injection apparently underwent some non-adiabatic process during its bounce (Nemzek and Winckler, 1989) and so can't be used in a simple analysis of payload charging.

The echoes prove that a fraction of the beam escaped to "infinity," in a steady-state fashion. Fast pulsed emission such as theorized by Winglee and Pritchett (1987) would appear to be identical to continuous emission in the echo measurements. We have estimated the total fraction of beam current returning to the rocket altitude in conjugate echoes. We assumed that an echo occupied an area 2 gyrodiameters on a side. This is justified by Echo 4 measurements, which demonstrated that an echo retains a size on the order of a gyrodiameter (Winckler, 1982). We have also assumed that the echoes were monoenergetic and isotropic over the upper hemisphere; Echo 7 echoes had electrons with pitch angles from >90 degrees down to at least 45 degrees. With these assumptions, the intensities measured by the TED's for the echoes shown in Figure 10 were equivalent to a current 1.3 x 10^{15} electrons/second. This current is integrated across the entire area occupied by the 18-keV echoes. This is about 20% of the average beam current at the echo energy. If there was significant payload charging then the echo current should be compared to the gun current at a higher voltage, corresponding to the energy of the echoing electrons when they left the gun. For 2 kV charging during continuous injections, this gives an echo current equal to 17% of the initial beam current. The lack of optically-observed echoes put an upper limit of 8% on the returning beam current in Discrete injections, which had much more power than the Continuous injections (Winckler et al., 1989). The discrepancy between the fraction of the beam returning for the two types of injections indicates that the Discrete injections underwent an increased interaction that the Continuous beams did not. The prompt response mechanism had this behavior: Discrete beams resulted in much higher fluxes than did Continuous pulses. The amount of beam returning to

413

the rocket also appears to be dependent on the level of geomagnetic activity (Winckler et al., 1988).

Conclusion:

This paper presents only a fraction of the phenomena measured by the Echo 7 electron detectors. While these data cover diverse topics, there is a common thread linking several explanations: a natural or beam-induced parallel electric field above the payload. Still, we have no direct evidence to confirm the existence of such a field, and the speculation about a parallel electric field in this paper does not even constitute circumstantial evidence. Indeed, if there was an upward field with ≈ 5 kV total potential above the payload, many of the conjugate echoes would not have escaped the payload region at all. More detailed examination of the echo bounce times and energies will allow us to put an upper limit on the total parallel potential above the payload.

References:

Arnoldy, R.L., and J.R. Winckler, The hot plasma environment and floating potentials of an electron-beam-emitting rocket in the ionosphere, J. Geophys. Res., 86, 575-584, 1981.

Bering, E., J. Benbrook, J. Roeder, and W. Sheldon, Evidence for beam-stimulated precipitation of high-energy electrons, in Artificial Particle Beams in Space Plasma Studies, B. Grandal, ed., 147-157, Plenum, 1982.

Maehlum, B.N., B. Grandal, T.A. Jacobsen, and J. Troim, Polar 5- An electron accelerator experiment within an aurora. 2. Scattering of an artificially produced electron beam in the atmosphere, Planet. Space Sci., 28, 279-289, 1980.

Maehlum, B.N., J.Troim, N.C. Maynard, W.F. Denig, M. Freidrich, and K.M. Torkar, Studies of the electrical charging of the tethered electron accelerator mother-daughter rocket MAIMIK, Geophys. Res. Lett., 15, 725, 1988.

Managadze, G. G., V.M. Balebanov, A.A. Burchudladze, T.I. Gagua, N.A. Leonov, S.B. Lyachov, A.A. Martinson, A.D. Mayorov, W.K. Riedler, M.F. Friedrich, K.M. Torkar, A.N. Laliashvili, Z. Klos, and Z. Zbyszynski, Potential observations of an electron-beam emitting rocket payload and

other related plasma measurements, Planet. Space Sci., 36, 399-410, 1988.

Nemzek, R.J. and J.R. Winckler, Non-adiabatic conjugate electron echoes due to Echo 7 accelerator operation (abstract), EOS trans., in press, 1989

Olson, W.P. and K.A. Pfitzer, Magnetospheric magnetic field modeling, McDonnel-Douglas Astronautics Co., Annual Science Report, AFOSR Contract F-44620-75-C-0033, 5301 Bolsa Ave., Huntington Beach, CA, 92647, 1977.

Wilhelm, K., W. Bernstein, P.J. Kellogg, and B.A. Whalen, Fast magnetospheric echoes of energetic electron beams, J. Geophys. Res., 90, 491, 1985.

Winckler, J.R., R.J. Nemzek, R.L. Arnoldy, and T.J. Hallinan, ECHO electron beam experiments in the diffuse aurora (abstract), EOS trans., 69, 1368, 1988.

Winckler, J.R., The use of artificial electron beams as probes of the distant magnetosphere, in Artificial Particle Beams in Space Plasma Studies, B. Grandal, ed., 3-34, Plenum, 1982.

Winckler, J.R., P.R. Malcolm, R.L. Arnoldy, W.J. Burke, K.N. Erickson, J. Ernstmeyer, R.C. Franz, T.J. Hallinan, P.J. Kellogg, S.J. Monson, K.A. Lynch, G. Murphy, and R.J. Nemzek, ECHO 7: An electron beam experiment in the magnetosphere, Eos, 70, 657,666-668, 1989

Winglee, R.M., and P.L. Pritchett, Space charge effects during the injection of dense electron beams into space plasmas, J. Geophys. Res., 92, 6114-6126, 1987.

Figure Captions:

Figure 1. Echo 7 Geiger tube thresholds: Relative detection efficiency was measured for low energies (solid curves) and reconstructed for high energies (dashed curves). Energies of Discrete and Continuous accelerator pulses are marked.

Figure 2. Geiger tube background: The Geiger tubes oriented at 90° to B measured trapped radiation >40 keV during gun off times. Measurements are plotted every 5 seconds.

Figure 3. Geiger tube response to continuous injections: During Continuous injections, both 90 degree (top) and 180 (bottom) Geiger tubes measured enhanced count rates. The peak at 260 seconds is also found in Geiger tube background measurements. Data are plotted once every 10 seconds.

Figure 4. Geiger tube response to Out injections: 36 kV, 180 mA discrete injections at 110 degrees produced the largest Geiger tube count rates. Only the >75 keV channels were not saturated. The notch at 250 seconds was caused by extremely high count rates shutting down the Geiger tubes.

Figure 5. Transient particle flux increase at start of gun pulse: Scintillator and Geiger tube responses to injections often started with a sharp increase which died away to a steady-state value after about 15 msec.

Figure 6. Field-aligned electron bursts after injections: At the end of gun pulses, the scintillator looking parallel to B measured a pulse of electrons. As the payload approached apogee, the bursts separated from the injections.

Figure 7. Prompt Responses: EPP TED2 measured a broad spectrum of electrons produced by gun firing. The prompt responses delay increased as the EPP moved away from the MAIN.

Figure 8. Prompt Response delays: The delay between gun pulse and prompt response increased nearly linearly with perpendicular distance between the EPP and MAIN.

Figure 9. Prompt Response decay: The prompt response amplitude for 10 keV electrons decayed exponentially as the EPP moved away from the MAIN. Near 260 seconds and after 400 seconds the amplitude dropped to 0.

Figure 10 a. Scintillator echoes: Pulses measured by the PDP scintillators matched gun pulses emitted 2.8 seconds earlier.
b. PDP TED2 measurements of individual scintillator echo pulses show that the echoes were monoenergetic at 18 keV.

Figure 11. Energy-bounce time plot: The various echo energy-bounce time pairs match well with calculations made by tracing field lines in the Olson-Pfitzer field model.

416

ECHO 7 GEIGER TUBE THRESHOLDS
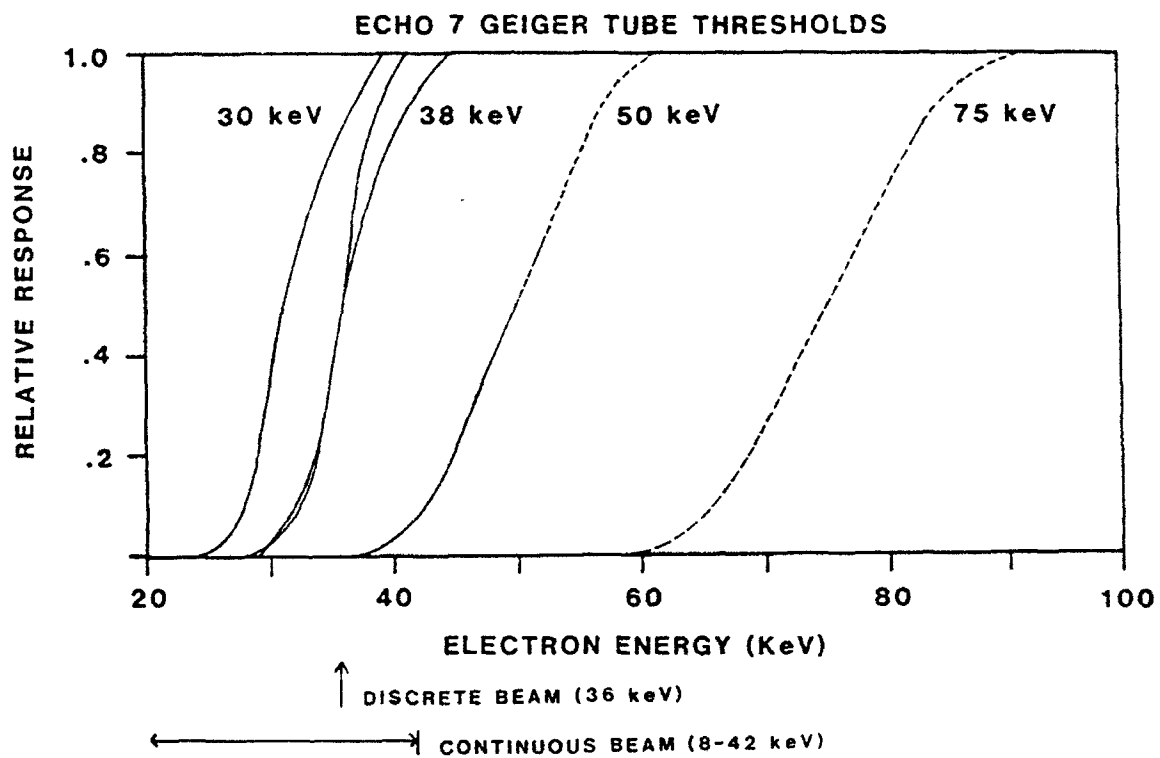
FIGURE 1

GEIGER TUBE RESPONSE TO BACKGROUND

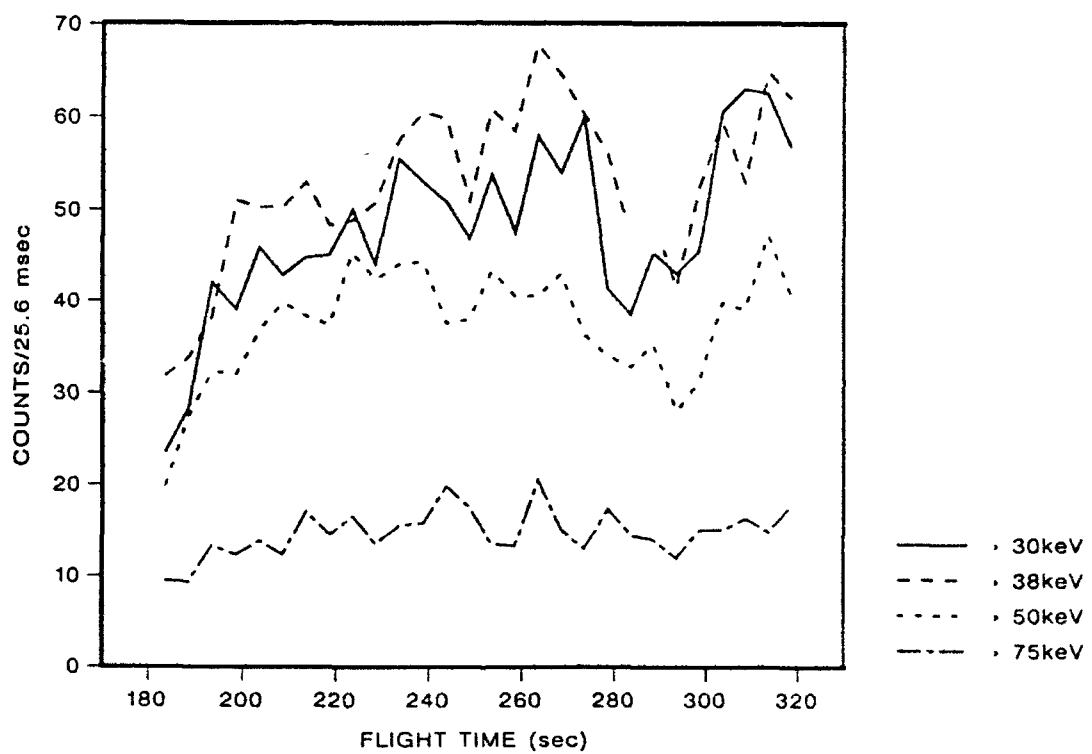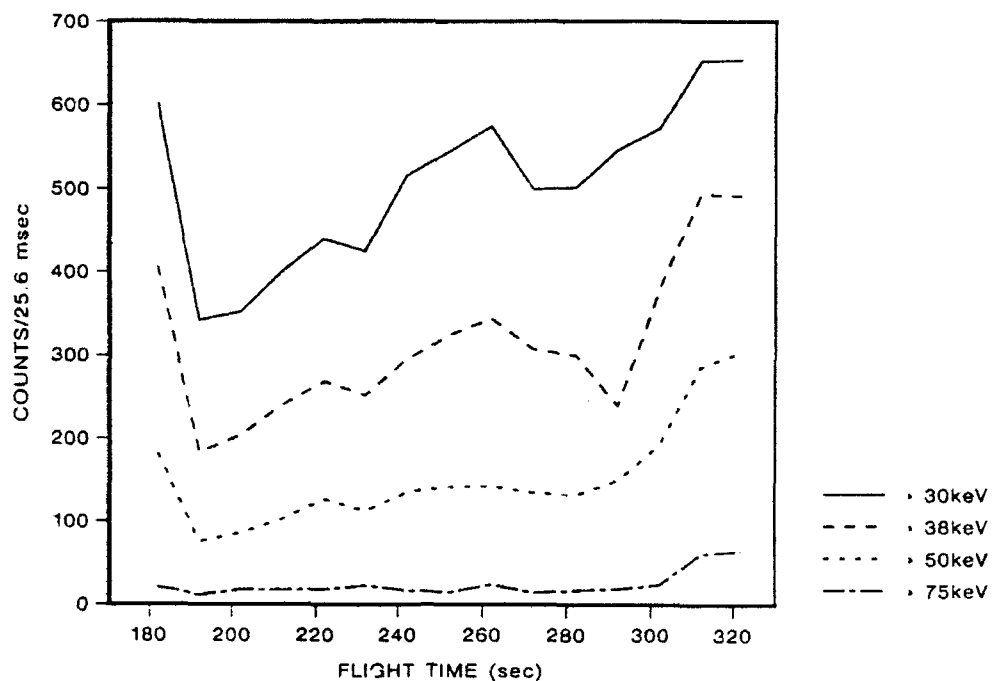## ELECTRONS AT 90 DEGREES PITCH ANGLE

FIGURE 2

GEIGER TUBE RESPONSE TO CONTINUOUS INJECTIONS

ELECTRONS AT 90 DEGREES PITCH ANGLE

GEIGER TUBE RESPONSE TO CONTINUOUS INJECTIONS

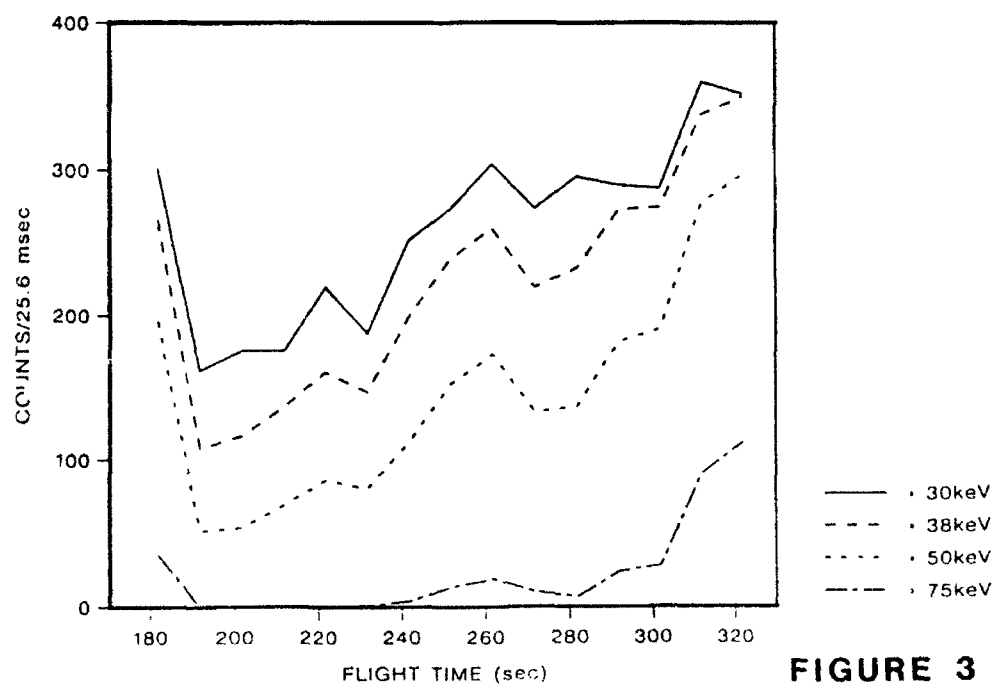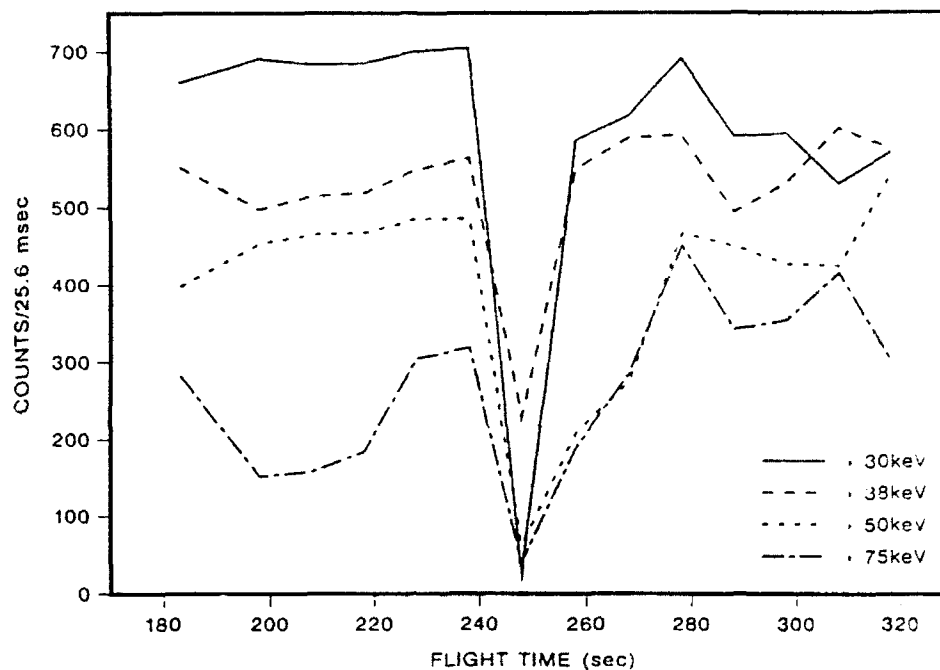## ELECTRONS AT 180 DEGREES PITCH ANGLE

FIGURE 3

GEIGER TUBE RESPONSE TO OUT INJECTIONS
ELECTRONS AT 90 DEGREES PITCH ANGLE

GEIGER TUBE RESPONSE TO OUT INJECTIONS
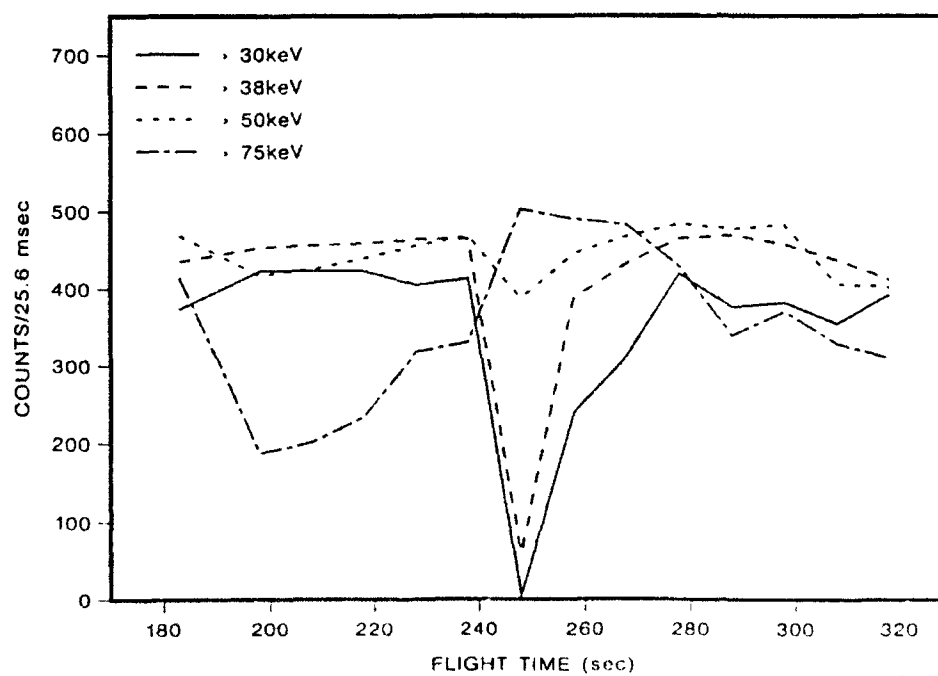## ELECTRONS AT 180 DEGREES PITCH ANGLE
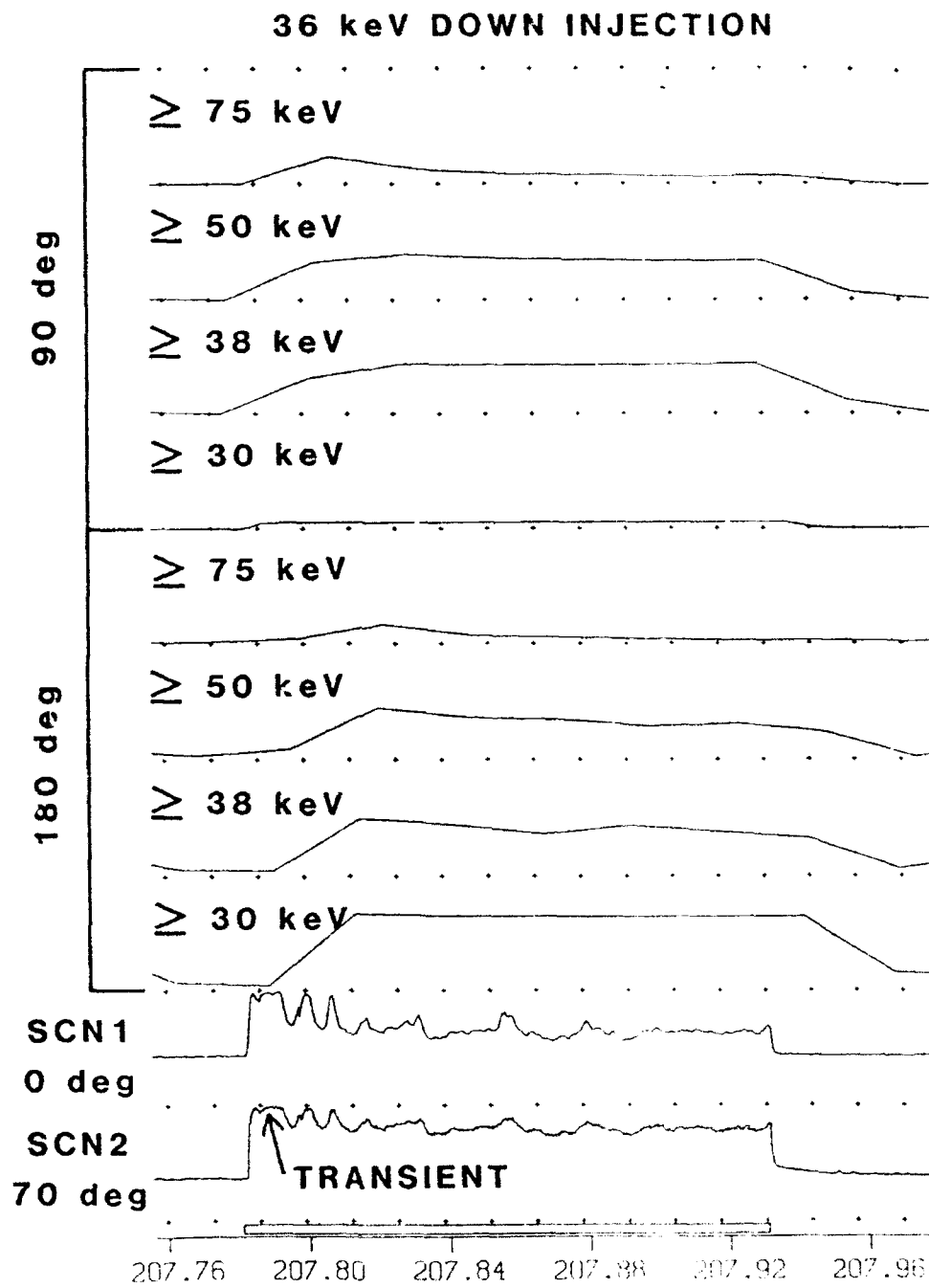

FIGURE 4

FIGURE 5

50 msec CONTINUOUS INJECTIONS

SCINTILLATOR 1

0 deg ELECTRONS

LOG

SCINTILLATOR 2

70deg ELECTRONS

LOG

GUN I
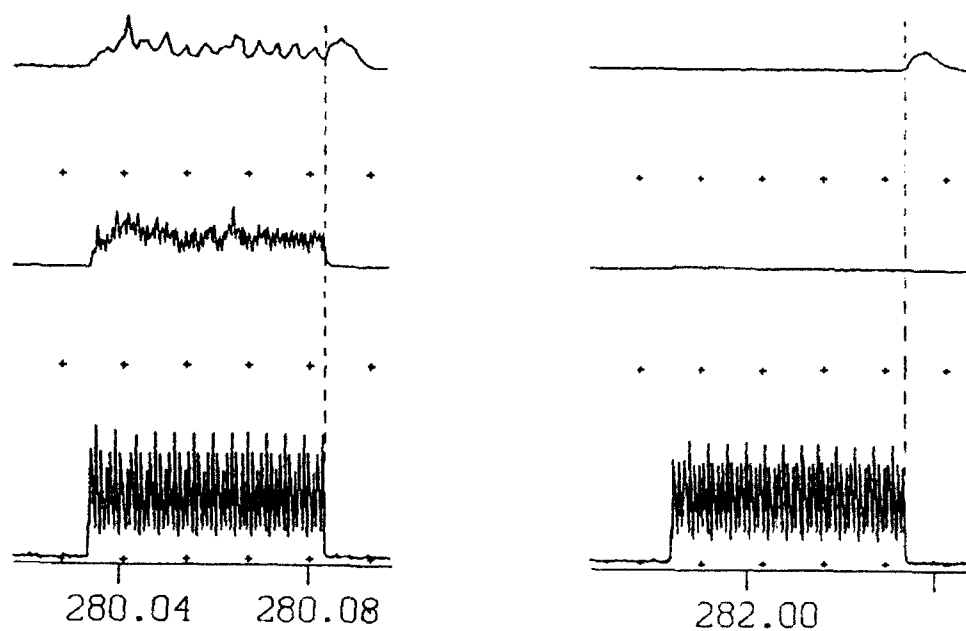
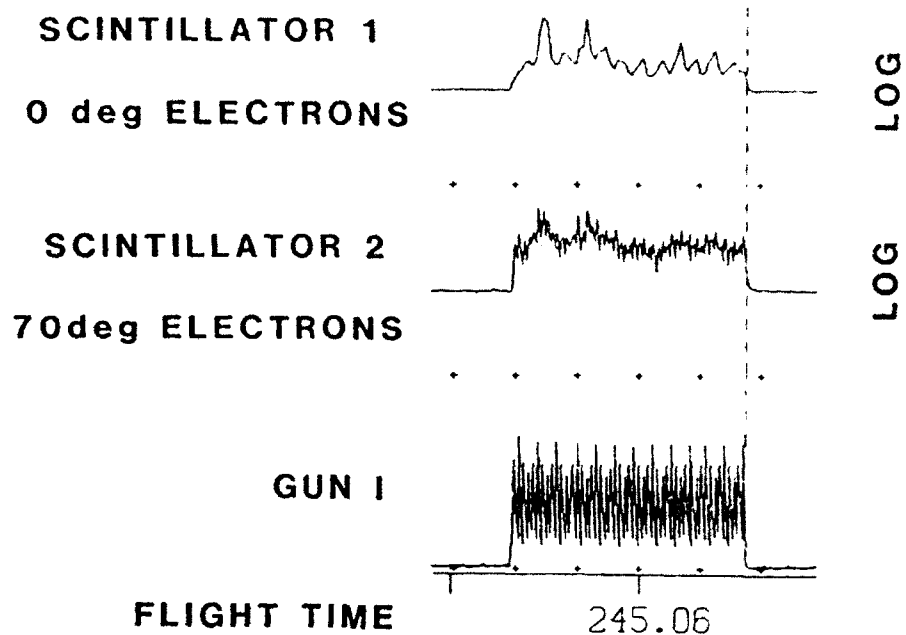FLIGHT TIME   245.06

280.04   280.08

282.00

FIGURE 6   WITH ACS GAS
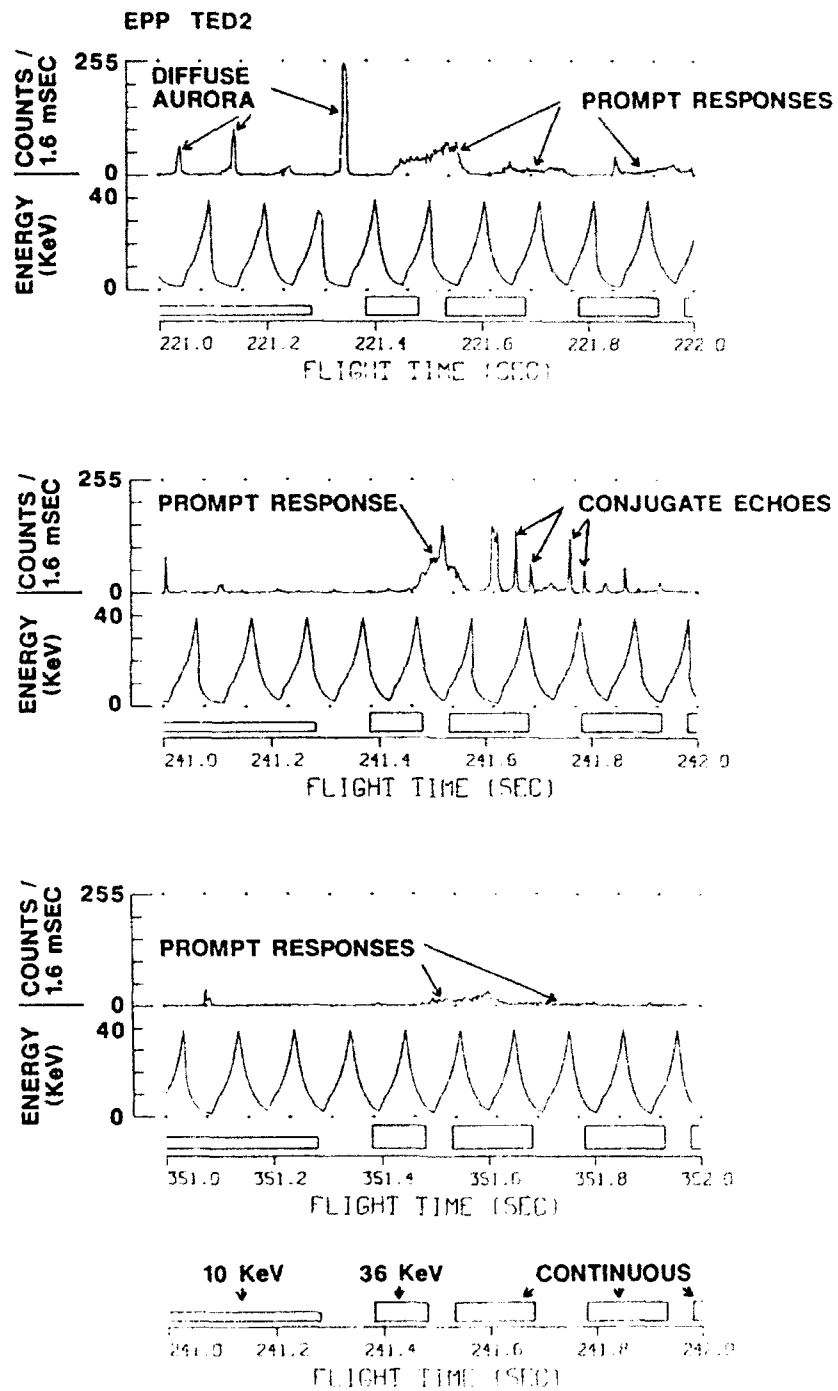
FIGURE 7

PROMPT RESPONSE DELAY FOR OUT INJECTIONS

EPP TED2

FIGURE 8

PROMPT RESPONSE AMPLITUDE FOR OUT INJECTIONS

AMPLITUDE AT 10 keV   EPP TED2

FIGURE 9

FIGURE 10

BOUNCE TIME (SEC)

4

3

2

1

5
6

3
4

2
1

ECHOES:

1. EPP, 235 SEC
2. PDP, 242 SEC
3. PDP, 245 SEC
4. PDP, 247 SEC
5. EPP, 330 SEC
6. PDP, 393 SEC

BOUNCE TIME CALCULATED FROM
OLSON-PFITZER QUIET TIME MODEL

10   20   30   40

ENERGY (KeV)

FIGURE 11

ALTITUDE EFFECTS ON HIGH-TIME RESOLUTION MEASUREMENTS OF VEHICLE CHARGING DUE TO ELECTRON EMISSION AT LEO ALTITUDES
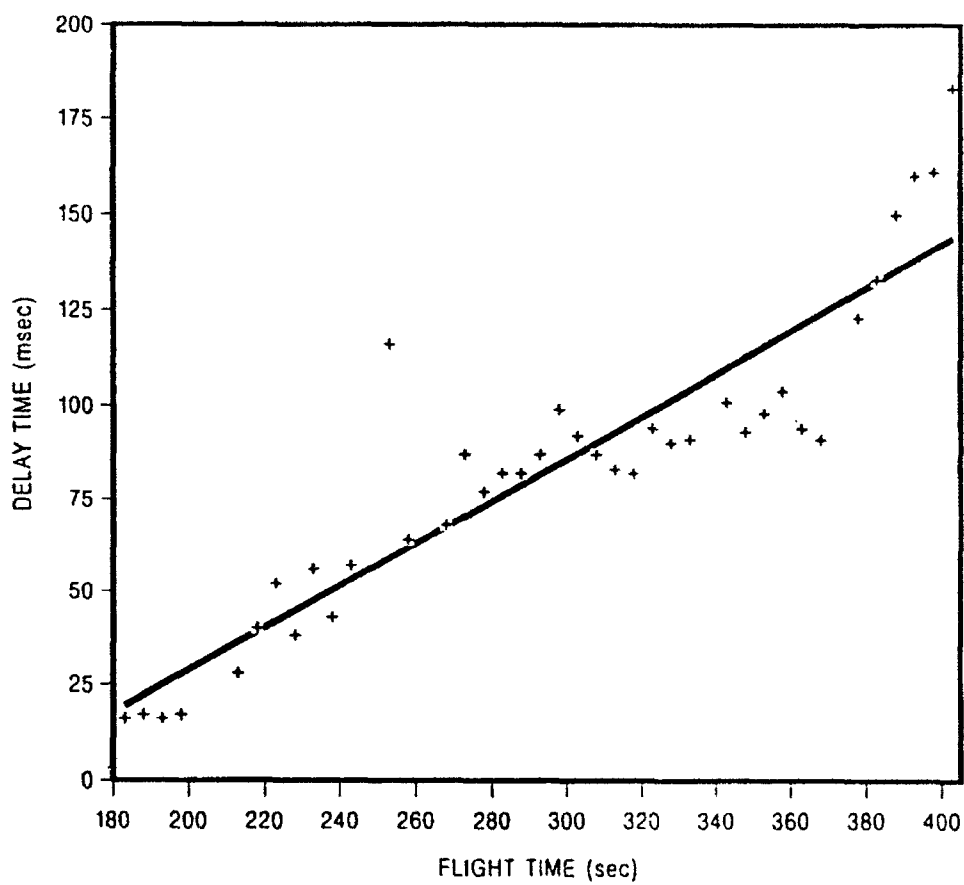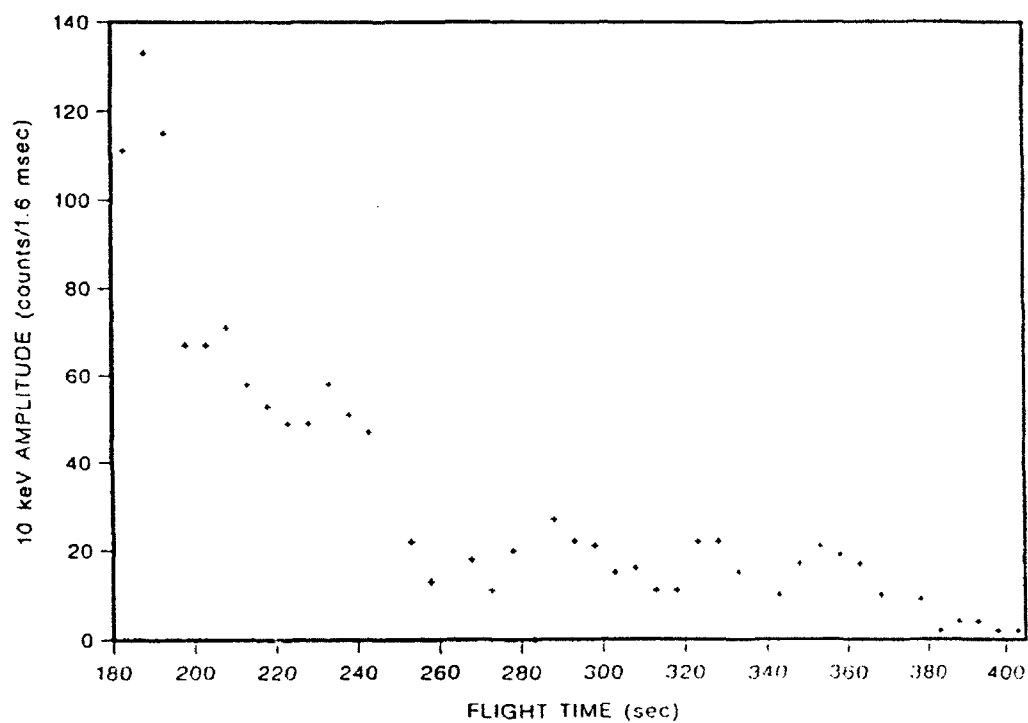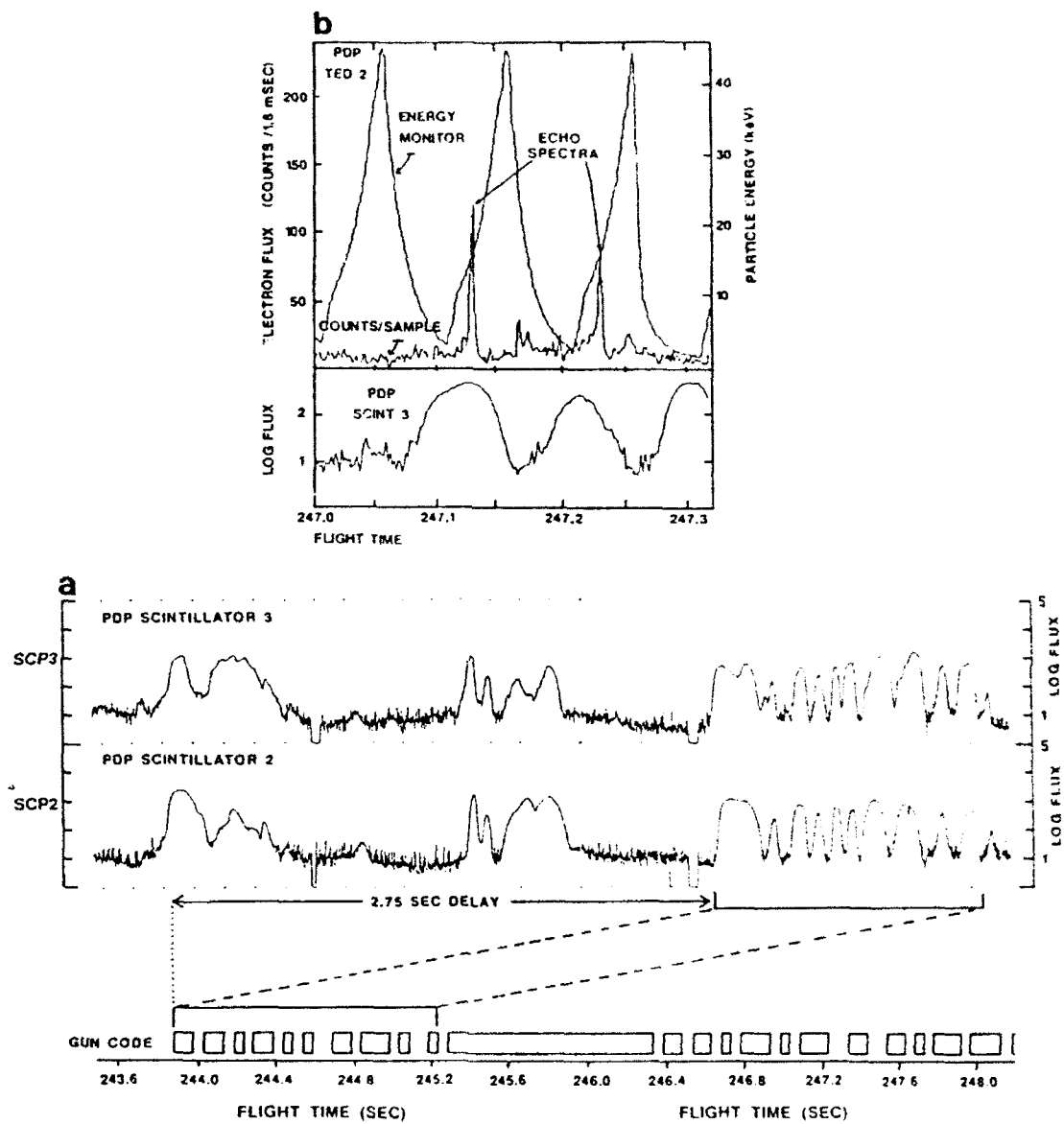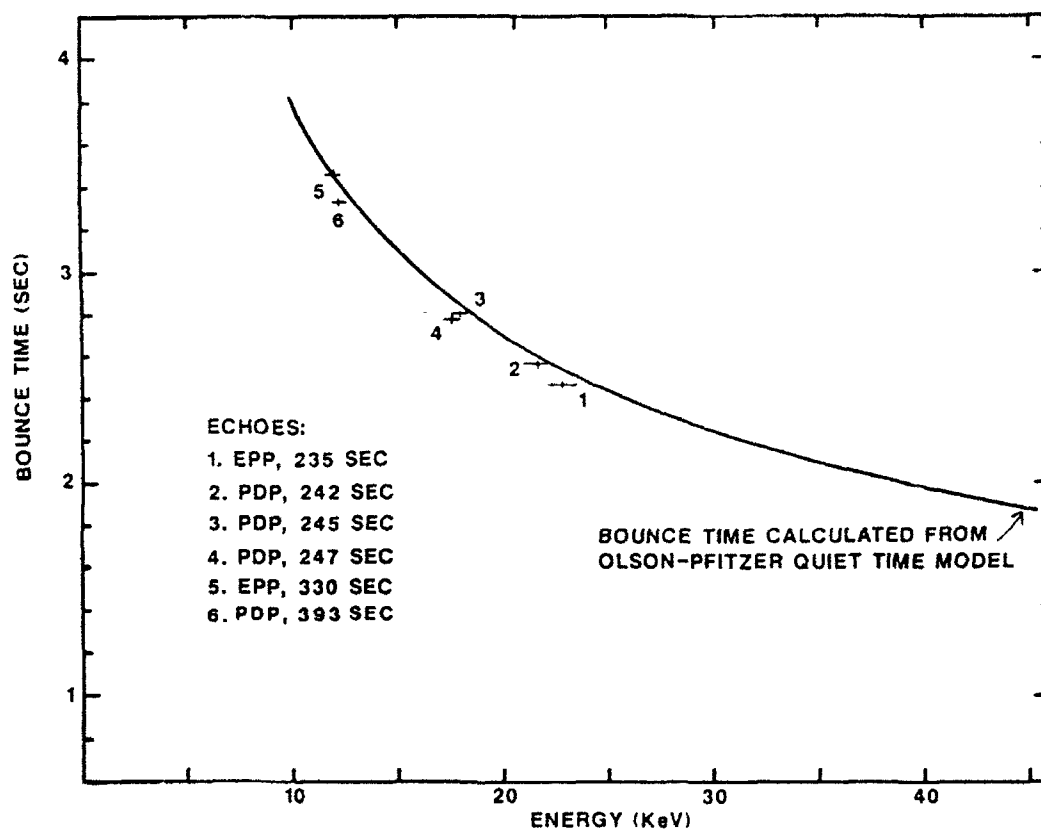
Neil B. Myers* and W. John Raitt
Center for Atmospheric and Space Sciences
Utah State University

*now at Rome Air Development Center
Hanscom AFB, MA

Abstract. Transient vehicle potential was measured during the CHARGE-2 electron beam experiment using a tethered payload as an electrical reference. Measurements of transient vehicle potential were obtained at sample intervals as short as 100 ns. Above 220 km transient potentials increased monotonically. Below 220 km the transient potential reached a maximum 50 μs after initiation of beam emission and then decreased. Beam-neutral and beam-plasma interactions are thought to be responsible for the decrease in vehicle potential below 220 km.

Introduction

Electron beam experiments have been performed in the ionosphere using sounding rockets since 1969 [Hess et al., 1971]. The success of these experiments in emitting electron beams contradicted the predictions of some models that predicted severe restrictions on the amount of current that could be collected from the ionosphere [Parker and Murphy, 1961]. According to the models, a vehicle which emitted too large of a current (depending on the area of the vehicle) would not be able to collect a sufficient current to balance the emitted current and the potential of the vehicle would rise to that of the accelerating potential of the electron gun preventing further emission. The successful emission of currents larger than the theoretical limitations stimulated interest in understanding the processes that occur during electron beam emission that provide the return current to the vehicle. A large number of electron beam experiments were performed using sounding rockets [Winckler, 1980], but unambiguously measuring both the vehicle potential and the collected current proved difficult. The Cooperative High Altitude Rocket Gun Experiment

428

(CHARGE) series was designed to compare the current collection of a vehicle in the ionosphere at high potential both with and without electron beam emission. During the successful flight of the CHARGE-2 experiment it was found that without electron beam emission the collected current was magnetically limited as predicted by Parker and Murphy [*Myers et al.*, 1989]. However the electron emission process greatly enhanced the current collection at low altitude (below 240 km). Measurements of vehicle potential with high time resolution were performed to aid in understanding the processes that allow the electron beam to generate sufficient electron return current and will be the subject of this paper.

Experiment

The CHARGE-2 experiment was launched December 14, 1985 just after local midnight from White Sands Missile Range, New Mexico. The main payload carried the electron beam and most of the diagnostic instrumentation and was referred to as the mother. A portion of the vehicle was deployed up to 426 m from the mother, connected by a conducting insulated tether, and was referred to as the daughter. The 1-kV electron gun emitted beam currents from less than 1 mA to 48 mA. The electron beam was successfully emitted from altitudes of 115 to 262 km. The daughter payload served as a reference electrode for the mother potential during beam emission. A high time resolution data capture system was used to measure the beam current and vehicle potential with sample intervals as short as 100 ns. Many other instruments were flown as part of the experiment as can be seen in Figure 1. The scope of this paper is limited to the high time resolution measurements. Results from some of the other instrumentation have been reported by *Myers et al.*, (Vehicle charging effects during electron beam emission from the CHARGE-2 experiment, in press *J. Spacecraft and Rockets*, 1990) and *Sasaki et al.*, [1987].

During electron emission a sheath is formed around the beam-emitting vehicle. In addition, the region surrounding the vehicle is disturbed by the beam-emission process. This complicates the interpretation of vehicle potential by a probe inside of the sheath and the disturbed region. To avoid this complication the daughter was deployed outside of the sheath in a direction perpendicular to the geomagnetic field to remove it from the disturbed region. The mother potential was then measured referenced to the daughter potential during beam emission. The mother-to-daughter potential is equal to the mother potential with respect to the plasma if the daughter potential is small, as seen in Figure 2. This was the method used to make the high time resolution measurements of the mother vehicle potential during electron beam emission. The beam current was measured using a Rogowski coil with the same time resolution as the potential measurements. The tether current, which equals the current collected by the daughter, was measured at a sample

rate of 1250 s^{-1}. Thus the current collected by the mother was determined by subtracting the tether current from the beam current.

Results

Measurements using the high time resolution system were limited to capturing 1024 points, which filled the cache memory. Thus at a sample interval of 100 ns data were captured for a total window of 102 μs. The cache memory then took 0.82 seconds to dump to the telemetry system so further data could not be obtained for 0.82 seconds. The sample interval could be varied from 100 ns to 25.6 μs. Measurements of the electron beam current using the high time resolution system are shown in Figure 3. Beam current is shown versus time in microseconds after the triggering of the cache memory for a sample interval of 100 ns. The beam current rose to a fairly constant value after 400 ns. This demonstrates the fast rise time of the electron beam current.

Figure 4 shows beam current and mother potential versus time in microseconds using a sample interval of 100 ns, at an altitude of 260 km. The data in the panels on the left were obtained at the initiation of beam emission and show the beam current and potential for the first 100 μs of beam emission. The data in the panel on the right shows the second capture of data during the same beam emission obtained 0.82 s after initiation of beam emission and shows 100 μs of data after steady-state conditions prevailed. No beam current data can be obtained for steady state conditions since the Rogowski coil is an AC coupled current measuring device. The beam current rose quickly to a value of about 23 mA. The vehicle potential rose to 40 V within a few microseconds and then continued to increase to 60 V by the end of the 102 μs window for data capture. The potential must have continued to rise since the second panel of potential measurements indicates a value of 160 V for the potential difference between the mother and the daughter payloads. The potential measurements of the second panel do not represent the potential of the mother with respect to the plasma since the daughter has obtained a large potential with respect to the plasma within 0.82 s after the initiation of beam emission due to the low resistance between the mother and daughter (approximately 40 kΩ in this case). The first panel of potential measurements does represent the mother potential with respect to the plasma since the daughter cannot change potential quickly due to the capacitance of the tether (calculated to be 10^{-7} F). Thus the daughter could not obtain large potentials due to the mother's positive potential for times much less than 4 ms. The measurements of the second panel were obtained much more than 4 ms after the beam turn-on, so the daughter has had time to charge to a high positive potential. Measurements from the floating probe array 1 m from the mother skin indicate a steady-state mother potential of about 440 V with respect to the plasma at this time. This indicates that the

430

daughter obtained a potential of about 280 V with respect to the plasma during steady state.

Two separate beam emissions with a beam current of 3 mA are shown in Figure 5. Potential is shown versus time in microseconds after the beginning of beam emission. The data in the top panel were obtained with a sample interval of 1.6 μs while the data of the lower panel were obtained with a sample interval of 100 ns. The two beam operations occurred within one second of each other at 235 km. The potential was very small during the first 100 μs as seen in the lower panel but rose to about 40 V within 500 μs (upper panel). Low transient potentials were typical for the data above 200 km where the plasma density was relatively large (greater than 10^{10} m^{-3}). This is to be expected for low beam currents on the order of the thermal current to the vehicle.

A comparison of similar beam operations at different altitudes is shown in Figure 6. The mother-daughter potential is shown versus the time in microseconds after the start of the beam operation. The data obtained at 156 km were from a 2-mA beam emission, while the data obtained at 235 km were from a 3-mA beam operation. Both data sets were obtained with a 100-ns sample interval. The vehicle potential was larger for the low altitude data as would be expected due to the lower plasma density. The potential obtained at the lower altitude also showed a maximum value about 50 μs after the start of the beam operation, and then decreased for the remaining 50 μs of the data capture window.

A similar comparison of vehicle potential obtained at different altitudes is shown in Figure 7. In this case the data were obtained with a sample interval of 1.6 μs, allowing a data window of 1.6 ms. Both data sets were from a 1.5-mA beam operation. The high altitude data were obtained at 237 km and show a steadily increasing potential until 1 ms after the start of the beam emission. The low altitude data were obtained at 155 km and exhibits the same potential maximum about 50 μs after the start of the beam operation followed by a decreasing potential as seen the low altitude data from Figure 6.

High time resolution vehicle potential data were also obtained during pulsing beam operations, but only at low altitude. An example of this is shown in Figure 8 with beam current versus time in microseconds after the start of the beam pulsing operation in the top panel and potential versus time in the lower panel. The beam pulsed on for 4 μs and off for 4 μs. The sample interval was 200 ns and the data were obtained at 125 km. The 48-mA beam current was much larger than the previous examples using DC beam emissions. The vehicle potential shows the same maximum at 50 μs after the start of the pulsing operations followed by decreasing potentials for each successive beam pulse as seen in the previous examples of low altitude potential measurements. This same behavior was seen in other pulsing operations at low altitude regardless of the beam pulsing frequency.

Discussion

The measurements of the transient potential between the mother and daughter payloads due to electron beam emission were lower than the steady state measurements of the mother potential using the floating probes on a 1-m boom. Thus steady-state conditions were ot reached for over 100 μs. This is much longer than it takes electrons to travel the meter-length sheath distance of the *Langmuir and Blodgett* [1924] type. This indicates that current collection in the ionosphere is more complicated than the simple space-charge-limited models. As shown by *Myers et al.*, [1989] current collection by a passive vehicle at high potential follows closely the magnetically limited model of *Parker and Murphy* [1961] which allows for the collection of electrons from large distances along the magnetic field lines. The large time until steady-state conditions were achieved supports this conclusi n.

It was also shown by Myers that the process of electron beam emission can drastically affect the current collection of a high potential vehicle at altitudes below 240 km. The results of the transient measurements also support the conclusion that a different process becomes important at altitudes below 220 km. The small plasma density at these low altitudes prevents a large current from being collected in the vicinity of the vehicle, and initially the potential rises to large values until a subsequent decrease in potential 50 μs after the initiation of beam emission. Although the maximum potential occurs consistently at 50 μs for the low altitude data it is unlikely that this is due to charging of the daughter since this behavior is not seen for the high altitude data and the tether time constant should be on the order of milliseconds. The contribution due to ionization of neutrals by the sheath-accelerated electrons does not explain the decrease of potential because of the large amount of time involved. It is possible that E x B trapped electrons could continually increase to the point where they ionize a significant number of neutrals. However the pulsing beam operations would not be explained by this since the vehicle potential returned to plasma potential between pulses and would continually turn off the E x B process, preventing such a build up of density. Also a large number of trapped electrons would yield a different signature from the monotonic sheath which the sheath floating probes measured [*Myers et al.*, 1989]. The most likely explanations for this behavior at low altitude are the beam-plasma and beam-neutral interactions. Beam-plasma interactions should not be important initially since the decrease of potential at 50 μs occurs only at the low altitudes where plasma density is small. Neutral density is larger at the lower altitudes providing a greater probability that beam electrons will ionize the neutrals. The long time for the vehicle potential to decrease indicates that the neutrals are ionized at great distances from the rocket. The interaction of the electron beam with the neutral atmosphere at large distances is discussed by *Neubert et. al.*, (The interaction of an artificial electron beam with the

432

Earth's upper atmosphere: Effects on spacecraft charging and the near-plasma environment, submitted to *J. Geophys. Res.*, 1990) and in a paper in this proceedings. It is possible that beam-plasma interactions play an increasing role in providing a return current once the beam electrons create a significant number of low energy electrons in the beam column.

References

Hess, W.N., M. G. Trichel, T. N. Davis, W. C. Beggs, G. E. Kraft, E. Stassinopoulos and E. J. R. Maier, Artificial auroral experiment: Experiment and principal results, *J. Geophys. Res., 76*, 6067, 1971.

Langmuir, I. and K. Blodgett, Current limited by space charge flow between concentric spheres, *Phys. Rev., 24*, 49, 1924.

Myers, N.B, W.J. Raitt, B.E. Gilchrist, P.M. Banks, T. Neubert, P.R. Williamson, S. Sasaki, A comparison of current-voltage relationships of collectors in the Earth's ionosphere with and without electron beam emission, *Geophys. Res. Lett.,16*, 365, 1989.

Parker, L. W. and B. L. Murphy, Potential buildup on an electron-emitting ionospheric satellite, *J. Geophys. Res., 72*, 1631, 1967.

Winckler, J. R., The application of artificial electron beams to magnetospheric research, *Reviews of Geophysics and Space Physics, 18,* 659, 1980.

Sasaki, S., W. J. Raitt, K-I. Oyama, N. Kawashima, P. R. Williamson, W. F. Sharp, A. B. White, P. M. Banks, T. Yokota, Y. Watanabe, K. Hirao, and T. Obayashi, Results from a series of tethered rocket experiments, *AIAA Journal of Spacecraft and Rockets*, 24, 444, 1987.

Figure Captions

Figure 1. The CHARGE-2 payload configuration.

Figure 2. Potential distribution during electron beam emission.

Figure 3. High time resolution measurements of electron beam current.

Figure 4. High time resolution measurements of beam current and mother-daughter potential for two successive data captures during one DC beam operation at 260 km.

Figure 5. High time resolution measurements of vehicle potential for two separate 3-mA beam operations at 235 km. Sample interval is 1.6 μs (top panel) and 0.1 μs (lower panel).

Figure 6. High time resolution measurements of vehicle potential for a 2-mA beam operation at 156 km and a 3-mA operation at 235 km with a sample interval of 0.1 μs.

Figure 7. High time resolution measurements of vehicle potential for 1.5-mA beam operations at 155 km and 237 km with a sample interval of 1.6 μs.

Figure 8. High time resolution measurements of beam current (top panel) and vehicle potential (lower panel) for a pulsing beam operation at 125 km with a sample interval of 0.2 μs. The beam was on for 4 μs and off for 4 μs.
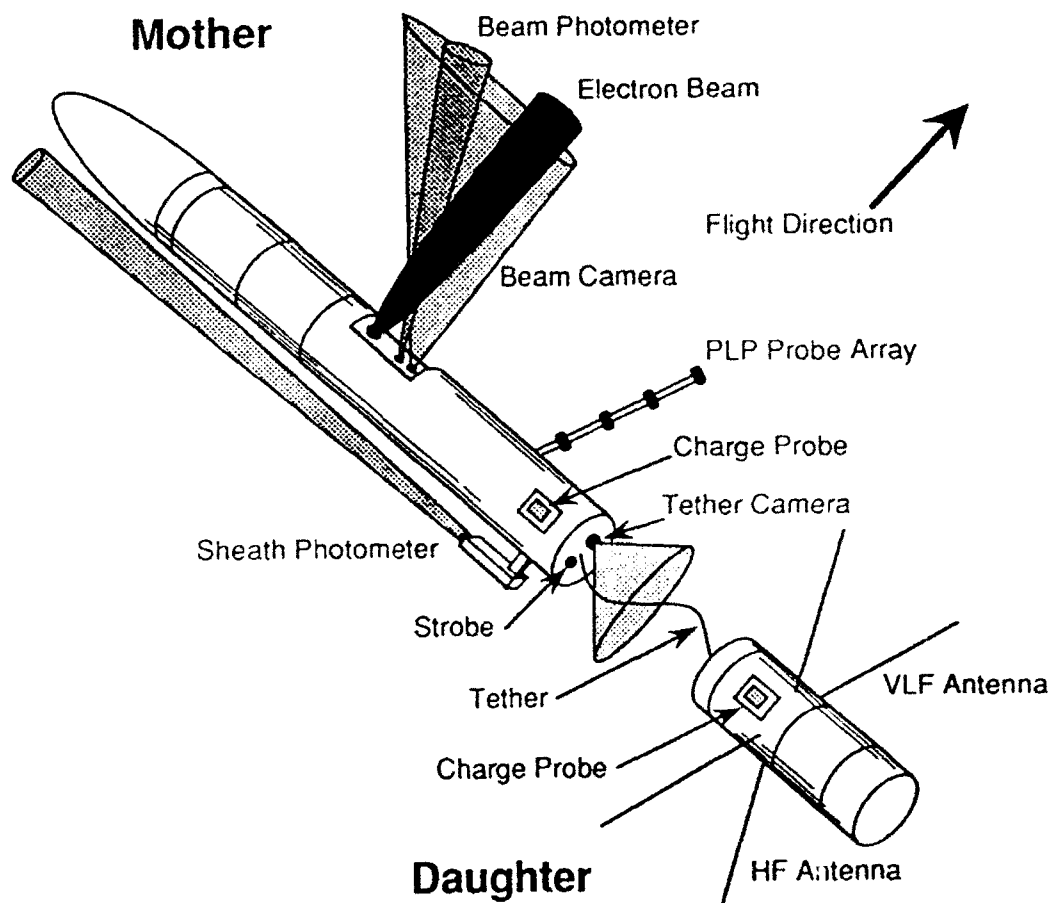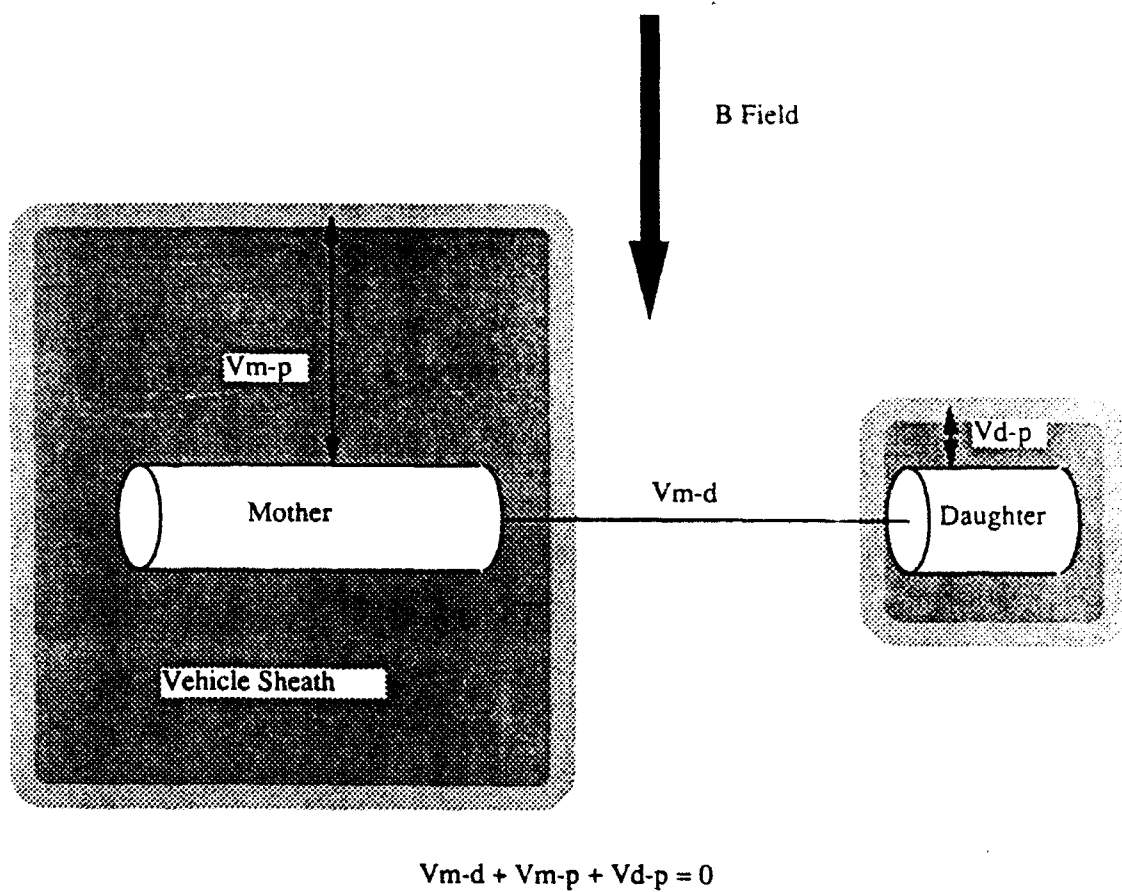
Figure 1

B Field

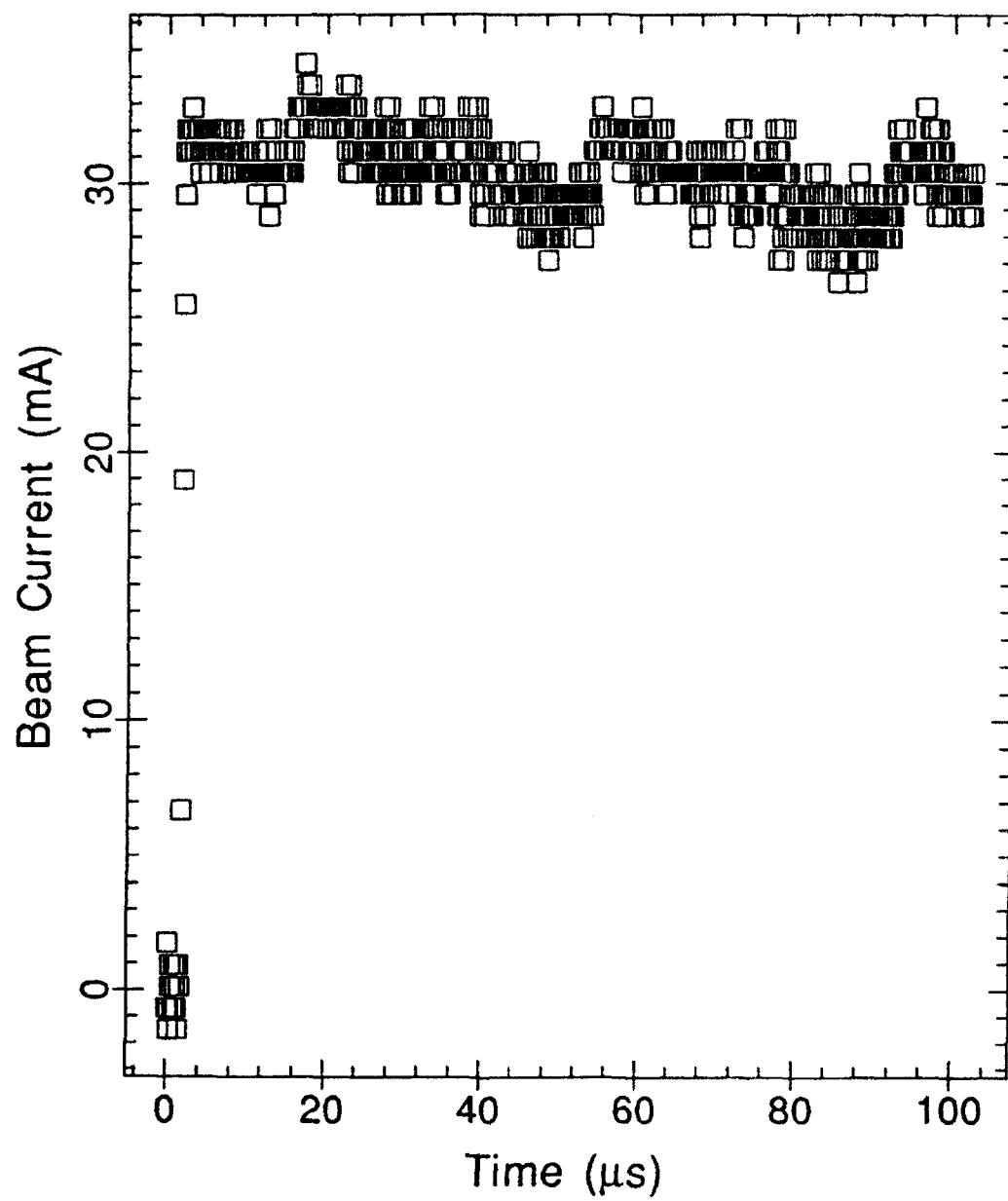Vm-p

Mother

Vm-d

Vd-p

Daughter

Vehicle Sheath

$$Vm\text{-}d + Vm\text{-}p + Vd\text{-}p = 0$$

Figure 2

Figure 3

437

No Data

Figure 4

438

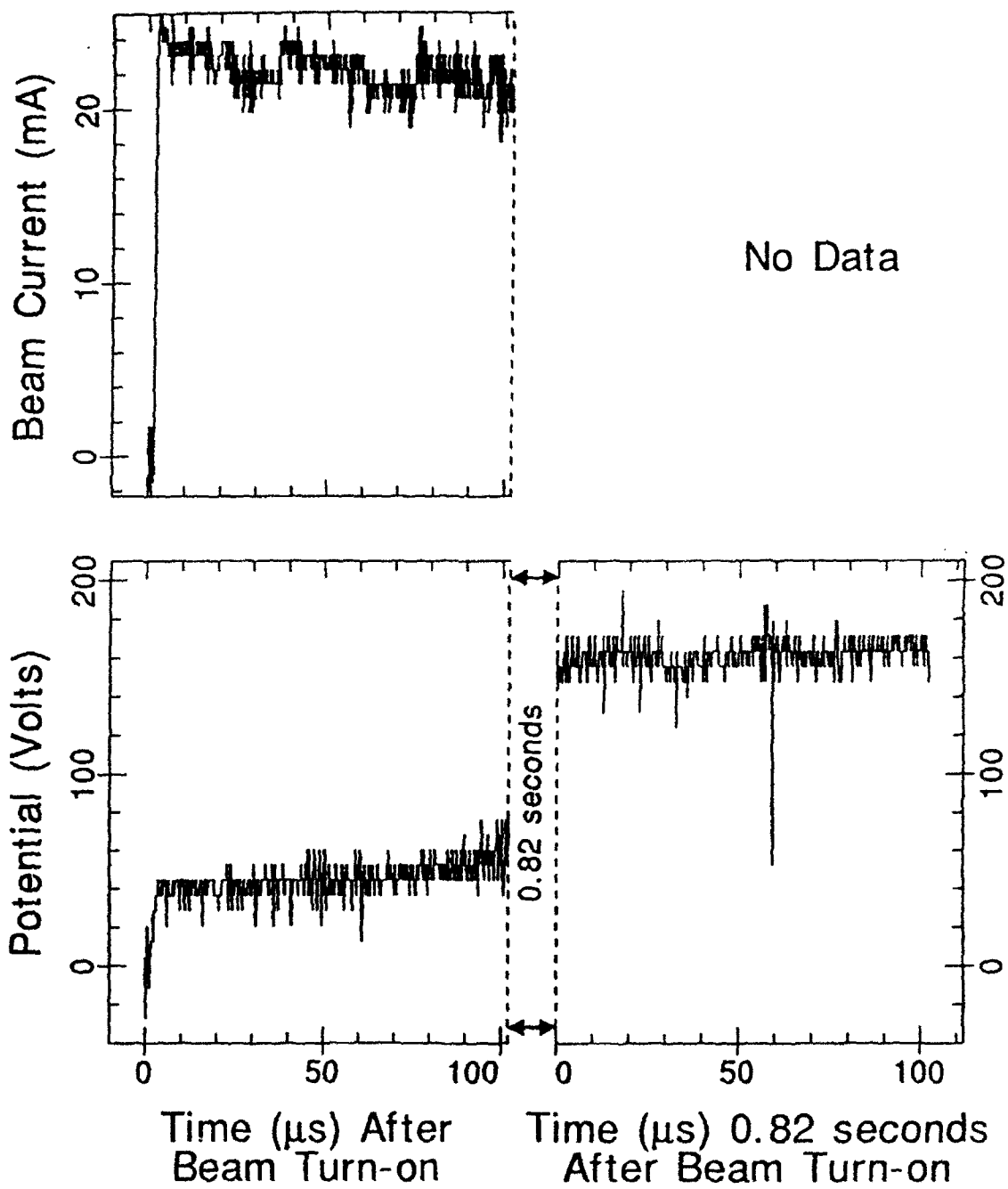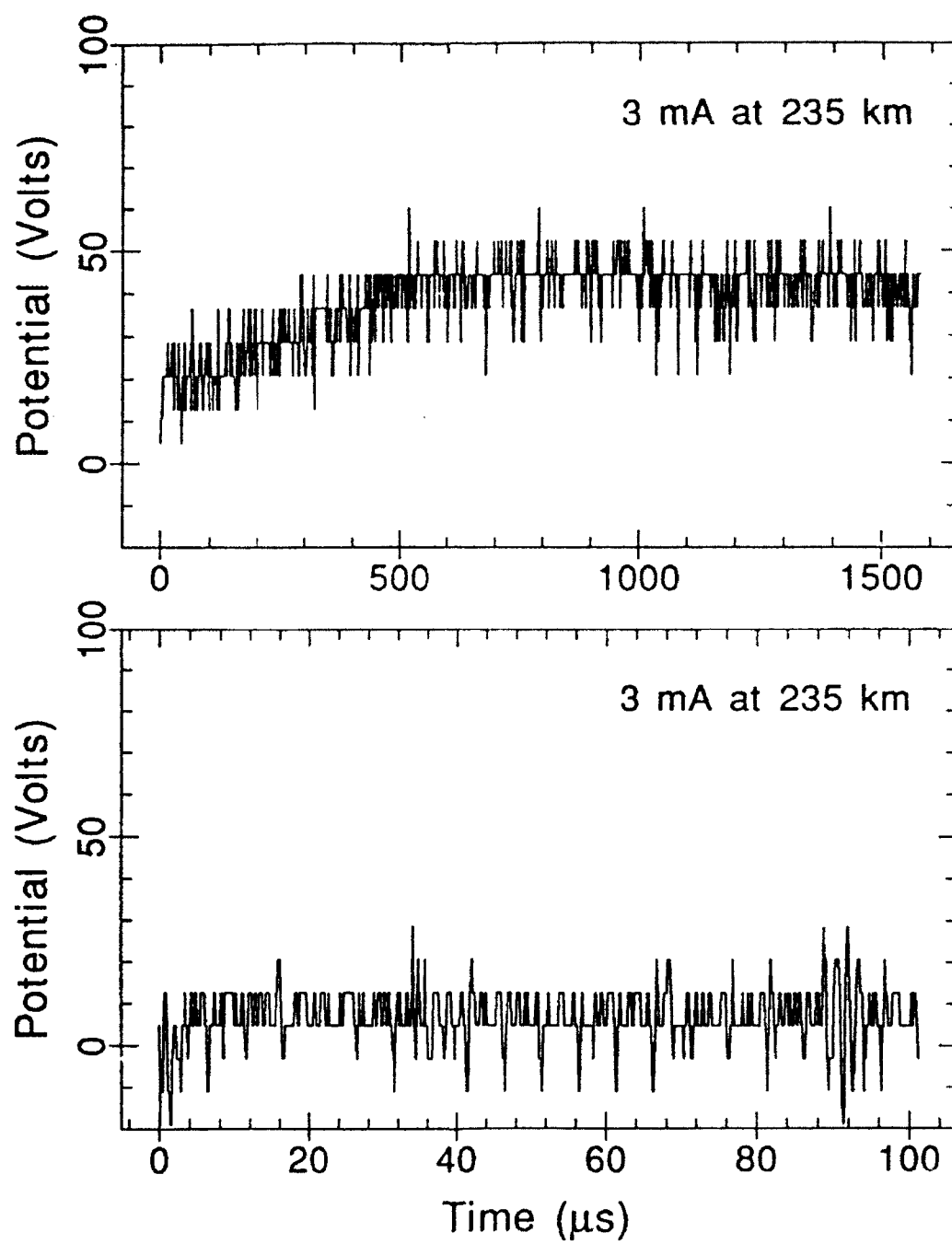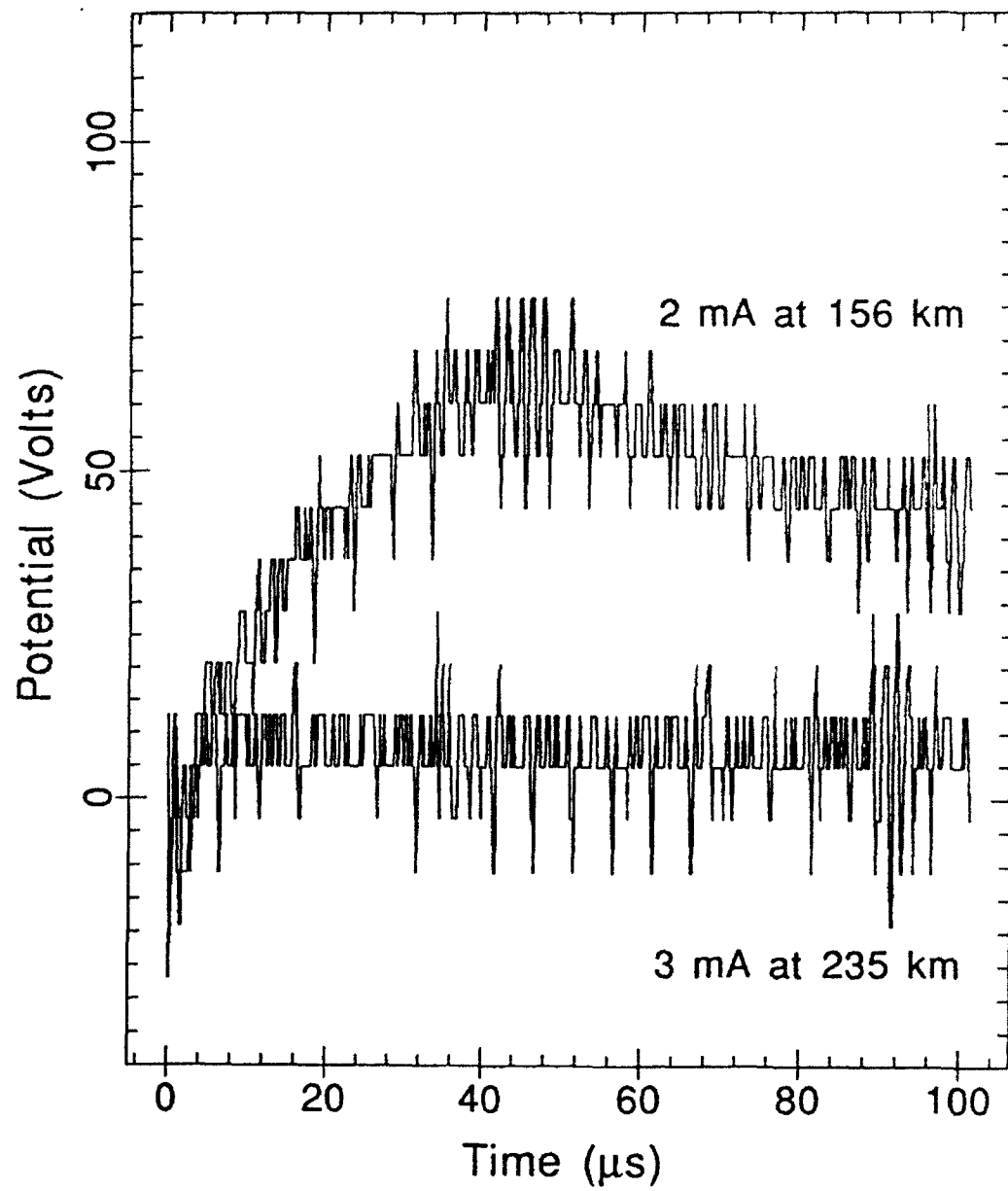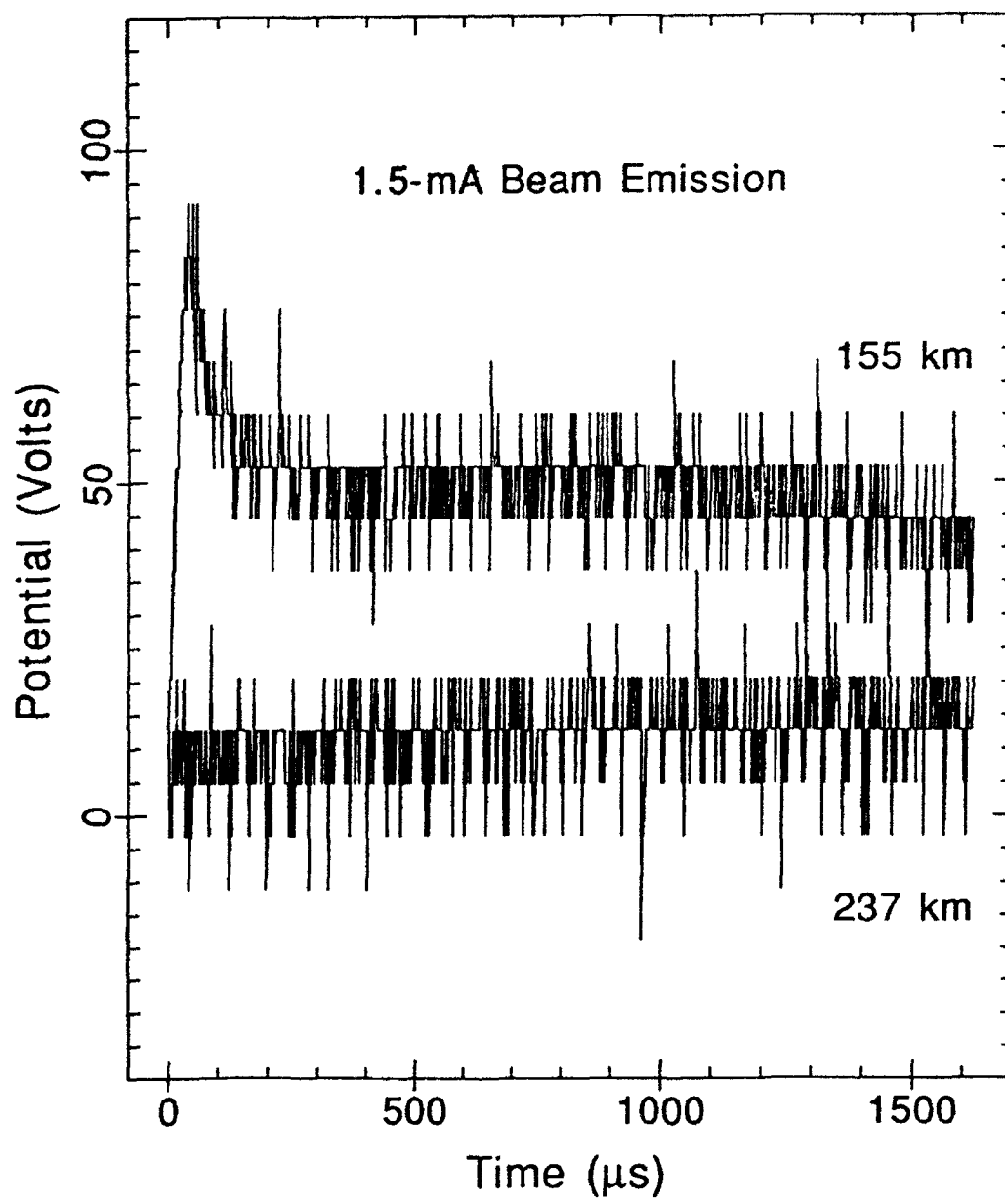Figure 5

Figure 6

Figure 7

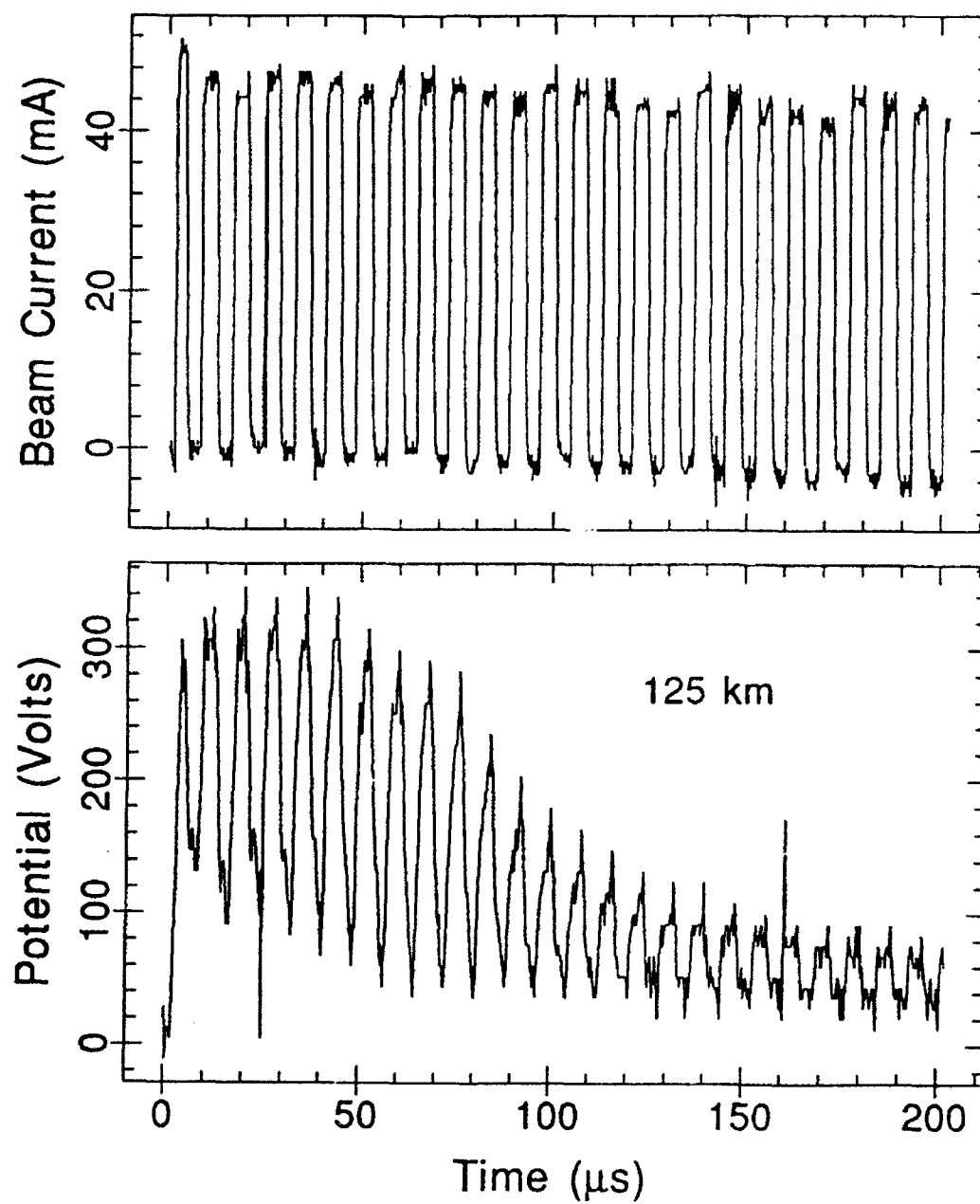Figure 8

A REVIEW OF THE MAIMIK ROCKET EXPERIMENT

W. F. Denig
Geophysics Laboratory (AFSC)
Hanscom AFB, MA 01731-5000
and
B.N. Maehlum and K. Svenes
Norwegian Defense Research Institute (NDRE)
N-2007, Kjeller, NORWAY

ABSTRACT

The MAIMIK Mother-Daughter sounding rocket experiment has provided documented evidence of significant vehicle overcharging by an accelerator payload in the ionosphere. The instrumentation on the daughter included an electron gun system which injected 8-keV beams ranging from 20 mA to 800 mA into a low-density ionospheric plasma. The daughter and mother payloads were separated in-flight and electrically tethered during the early electron gun operations. The measured daughter potentials for the larger currents, at times, exceeded by 50% the nominal 8-keV beam energy. The effects of the beam-plasma interaction and the extreme vehicle charging were evident in the plasma and DC electric field instrumentation on the mother. The energy transfer from the beam to the ionospheric plasma, evidenced by an enhancement in the local electron temperature, maximized at 80 mA with no obvious indication of an anomalous ionization discharge mechanism. The transient electric fields measured at beam turn-on were consistent with the rapid charging of the daughter and the resulting ionospheric response. The three-fold purpose of the present report is to present an overview of the MAIMIK rocket experiment, review the evidence for the overcharging phenomenon, and discuss the relevent plasma and electric field observations.

INTRODUCTION

The MAIMIK experiment was a mother-daughter tethered sounding rocket originally conceived to address a number of crutial issues related to the electrodynamic behavior of an electron-emitting spacecraft in the ionosphere. The rationale for the experiment was based in part on the results of the earlier POLAR rocket series (Maehlum et al., 1980) as well as other investigations using artificial electron beams in space (Hess et al, 1971; Cambou et al., 1975; Winckler; 1980). These experiments had demonstrated the non-classical behavior of the interaction between the charged beam and the ionosphere which resulted in enhanced ionization production rates, extreme heating of the background plasma, and the generation of intense plasma waves. Although important contributions to the basic understanding of the beam-plasma interaction were made by a number of labo atory experiments (Bernstein et al., 1979; Grandal, 1982) the applicability of these studies to the space

environment had not been well established (and still isn't). The specific issues proposed for further investigation by the MAIMIK rocket experiment were; 1) the energy transfer mechanism from the beam to the background plasma and its dependence on varying beam currents and changing atmospheric density, 2) measurement of the time constants for the relaxation of the ionosphere following the termination of the beam, 3) determination of the physical dimensions of the disturbed ionospheric region, and 4) an investigation of the charging processes for a beam-emitting spacecraft and a tethered companion payload.

The MAIMIK rocket experiment was conducted under the auspices of the Royal Norwegian Council for Scientific and Industrial Research (NTNF) and the National Aeronautics and Space Administration (NASA). Payload integration was conducted by the Norwegian Defense Research Establishment (NDRE) and launch activities coordinated at the Andoya Rocket

Range (69°17'39" N, 16°01'15"). The project scientist for the MAIMIK rocket experiment was Dr. B.N. Maehlum (NDRE) with participating scientists from Norway, the USA, Sweden, and Austria. Supporting ionospheric measurements at the time of the flight were made by the European Incoherent Scatter (EISCAT) radar facility.

The principal findings from the MAIMIK rocket experiment have been the observations of an overcharging condition by the beam-emitting payload, a current dependent peak in the beam to plasma energy transfer rate in the absence of an anomalous ionization source, and impulsive electric fields well outside of the heated plasma region which were driven by ion dynamics. This report is a summary of the important MAIMIK results which have been separately reported elsewhere (Maehlum et al., 1988; Svenes et al., 1988; Denig et al., 1989). However, we have also endeavored in the preparation of this report to combine these separate analyses by showing the interrelationships among the various topics.

INSTRUMENTATION

The MAIMIK sounding rocket was launched in a northwesterly direction into a quiet sub-auroral ionosphere at 18:56 UT on 10 November 1985. The payload section of the Terrier/Black Brant two-stage vehicle consisted of separate mother and daughter sections which were detached 62 s after launch with the aft-mounted mother remaining attached to the second stage motor. Following separation the velocity of the daughter relative to the mother payload remained a constant 0.8 m-s^{-1} at 23° to the local magnetic field. Attitude stability for both the mother and daughter payloads was maintained by their respective spin rates of 0.3 Hz and 3.3 Hz. The coning half-angle for the mother was 35° with a coning period of 300 s. The coning half-angle for the daughter was much less severe, being about 5°. The MAIMIK mother and daughter payloads reached an apogee of 381 km at 320 s.

During the interval between separation and 113 s, the mother and daughter payloads were electrically tethered through a 10 Megohm impedance. This time interval overlapped the initial electron gun operations which commenced at 101 s and

continued throughout the remainder of the flight. The purpose of the tether was to provide a "mother" ground reference during
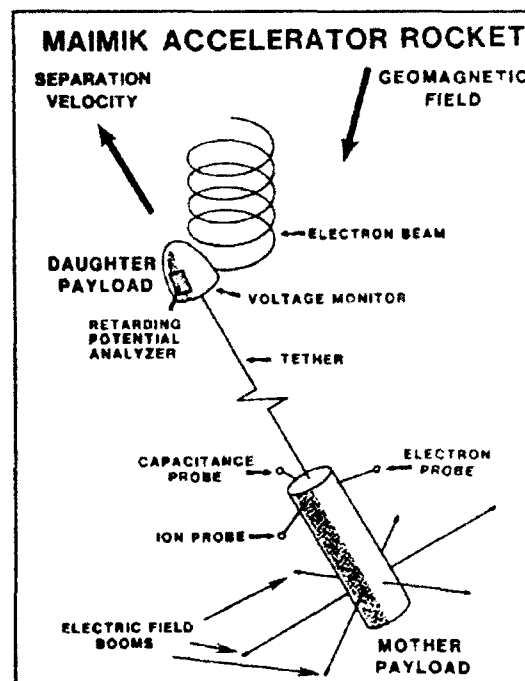

Figure 1. Schematic Illustration of the MAIMIK Rocket Experiment.

electron beam operations when the daughter was actively charged relative to the background plasma. The accuracy of the ground reference was futher maintained by keeping the conducting surface area of the mother (9.7 m^2) large compared to that of the active daughter (1.1 m^2). Although the mission plan was to keep the two payloads tethered until 130 s, the premature disconnection of the tether wire at 113 s limited the total amount of tether data available to 17 beam pulses over a full range of emission currents. The full complement of scientific instruments included in the MAIMIK rocket program is listed in Table 1. Unfortunately, the failure of a PCM encoder within the mother payload early in the flight had a catastrophic effect on the downlink data from the particle spectrometer, the VLF wave receivers, and the television camera. On the other hand, the analysis of the data from the HF

444

transmitter and receiver is presently ongoing but has little bearing on the present subject (K. Torkar, private communication, 1989). Figure 1 is a simplified schematic of the MAIMIK rocket payload detailing the instrument geometry for several of the experiments relevant to the present study. On the daughter payload the experiments included the electron accelerator, a set of electron retarding potential analyzers, and a tether voltage monitor. A daughter magnetometer was used to determine the beam injection pitch angle and to estimate the vehicle's instantaneous attitude. The mother instrumentation included a set of plasma probes and a three-axis electric field instrument. The MAIMIK mother attitude was determined by the NASA-Wallops Flight Facility (Reference: BB1X 36005) using the available gyro data and the higher time resolution data from an onboard magnetometer.

The electron accelerator system on the daughter payload consisted of a set of five identical gun units operated in an emission-limited diode configuration at a fixed accelerator voltage of 8 keV. Sequential 11-ms pulses of 320 mA, 80 mA,

Table I. Scientific Instrument Complement for the MAIMIK Rocket.

Daughter Payload

Electron Accelerator
Return Current Monitor
Voltage Monitor
Retarding Potential Monitor
HF Transmitter
Photometer Array

Mother Payload

DC E-field detector
TV Camera
Capacitance Probe
Ion Probe
Electron Temperature Probe
Fast Particle Spectrometer
VLF/HF Wave Receivers

---

40 mA, 20 mA, 40 mA, 80 mA, 160 mA, and 800 mA were injected into the ionosphere at a pulse repetition frequency of 1.2 Hz. For currents in the range 20 mA to 160 mA only a single gun head was used to generate the beam. However, the 320 mA and 800 mA current pulses required the simultaneous operation of two and five heads, respectively. The nearly DC beam operated at a high voltage chopper frequency of 1.2 kHz with a voltage ripple of less than 2 kV below the nominal accelerator voltage. The injection pitch angles ranged from 65° to 115° with an unfocused beam spread of less than 10°. Although the electron gun was instrumented to monitor the accelerator voltage and current, these data were carried on the telemetry channel that failed during the flight. The values used in the present analysis were from pre-flight calibrations.

The daughter's potential was measured using the tether voltage monitor (VM) and the electron retarding potential analyzers (RPA's). The tether connecting the mother and daughter payloads was an insulated stainless steel wire having a cross section of 0.2 mm². The differential voltage between the payloads was measured across a 10 Megohm resistor located in the active daughter payload. The VM output was linear between +10 V and -10 V and logarithmic between -10 V and -15 kV. Note that a negative VM signal indicated a positive daughter potential relative to the mother. The RPA consisted of an array of eight separate analyzer grids having fixed retarding potentials of 0 V, -12 V, -85 V, -180 V, -400 V, -800 V, -1.6 kV, and -3.2 kV relative to the daughter. The collecting area of each detector was 6.6 cm² and the minimum detectable current was 2 nA. The observed energy cut-off during positive charging of the daughter provided a redundant measure of the payload charging level. Although the RPA operated only over a limited energy range, the instrument did provide a continuous monitor of the daughter potential throughout the entire rocket flight well past tether disconnect at 113 s.

The set of mother plasma probes consisted of an electron temperature probe (ETP), an ion probe (IP), and a capacitance probe (CAP) each mounted on a separate 80-cm boom and deployed at 60 s. The ETP was a

Langmuir-type probe consisting of a spherical grid, 5 cm in diameter, surrounding a collector at a bias at +10V. The outer grid was swept both up and down between -1.9V and +4.9V relative to spacecraft ground with a "sweep" time of 13.1 ms. The general theory of gridded spherical sensors and their application for sounding rocket measurements has been discussed by Sagalyn et al. (1963). The IP was a 4-cm diameter solid spherical sensor held at a fixed bias voltage of -2V. The measurements included both the AC and DC components of the incoming ion flux. The CAP measured the capacitance of a 4.2 cm diameter floating probe immersed in the background plasma. During periods when the payload and plasma were not greatly disturbed the CAP was surrounded by a classic Debye sheath having a radial dimension proportional to the square root of the ratio of the electron density and temperature. The capacitance of this RF probe formed part of an LC-oscillator circuit which operated at a fixed frequency of 1 MHz (Balmain; 1966). Although the plasma probes had a nominal performance during the entire flight, prior to tether disconnect at 113 s the probe data was adversely affected by the mother charging during electron gun operations.

Vector electric fields at the location of the MAIMIK mother payload were measured using an orthogonal, three-axis set of double probes. Each double probe consisted of a cylindrical boom pair having 61 cm of bare wire at the extremes which contacted the plasma and whose potential was monitored through a 10^{12} ohm preamplifier impedance and referenced to the rocket body. The inner portion of each boom was insulated from the plasma by a coating of Kapton. As depicted in Figure 1, two of the boom pairs were mounted at 45° to the rocket spin axis while the third pair was in a plane perpendicular to the spin axis. The 45° booms were constructed of rigid stainless steel whose active elements had a nominal separation of 5.7 m. The third pair had a separation length of 8.8 m and were fabricated from a flexible Beryllium-Copper alloy. The electric field booms were deployed between 70 s and 100 s and were fully operational prior to the first gun pulse. Thereafter, the instrument had a nominal operation until re-entry. The components of the local electric field were derived in a straight-forward fashion as the negative of the potential difference between each boom pair divided by the boom length. The sensitivity of the vector instrument ranged from 3 mV-m^{-1} (limited by the 8-bit telemetry system) to greater than 1 V-m^{-1} at a maximum sampling frequency of 2.44 kHz. The measurements were corrected for motion-induced electric fields and for contact potential variations. During the main part of the flight the systematic errors associated with the data were determined to be no greater than 5 mV-m^{-1}. However, prior to 130 s major changes in the measured background field were caused by contact potential variations partially caused by outgassing of the rocket payload and energetic electron bombardment.

DATA

The MAIMIK launch criteria specified a darkened subauroral ionosphere and geomagnetic quiet conditions. The sounding rocket was launched in the absence of any visible auroral activity. Figure 2 is the background electron density and figure 3 is the ionospheric electric field measured by MAIMIK. The electron density profile for the ascent and descent phases of the flight was normalized to the EISCAT radar which measured an electron density of 4×10^4-cm^{-3} and a temperature of 1500 °K near the
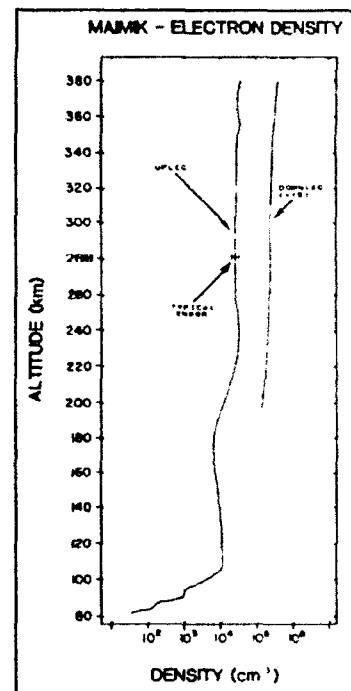

Figure 2. Measured electron densuty profile during rocket ascent and descent.

446

250-km F-region peak (T. Hanson, private communication, 1984). The MAIMIK measurements indicated that the density profile between 240 km and apogee was fairly constant with only a modest increase (50%) at the F-region peak. A 3-hour averaged $K_p=3$ level persisted for the 24 hours preceding the flight (Coffey, 1986) and overflights by the Defense Meteriological Satellite Program (DMSP) F7 satellite indicated that the Field-Aligned Currents (FAC) within the eveningside northern hemisphere were weak and consistent with a northward Interplanetary Magnetic Field (IMF). Although the main portion of the rocket flight was at subauroral latitudes it is likely that MAIMIK entered the auroral oval towards the end of the mission when

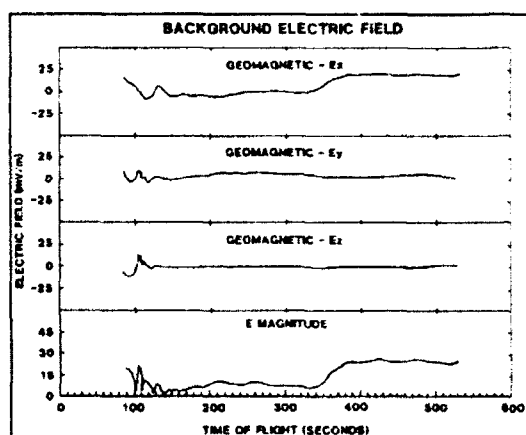Figure 4. Tether voltage monitor.

Figure 3. Measured ionospheric electric field for the MAIMIK flight.

the measured northward component of the ionospheric electric field sudden increased from near 0 to 26 $mV\text{-}m^{-1}$ at 340 s. At the time of this transition, the rocket was situated at a geomagnetic latitude of 56° and at 19.6 MLT closely corresponding to the statistical location of the low-latitude auroral boundary for a $K_p=3$ (Hardy et al., 1985).

Figure 4 is a summary plot (lower curve) of the tether voltage monitor for the period between 100 s and 110 s which included the initial twelve electron beam pulses. The indicated 8-kV voltage level refers to the nominal energy of the beam electrons. Also shown in the top panel of figure 4 are the corresponding currents for each beam pulse. The sense of the tether voltage was the
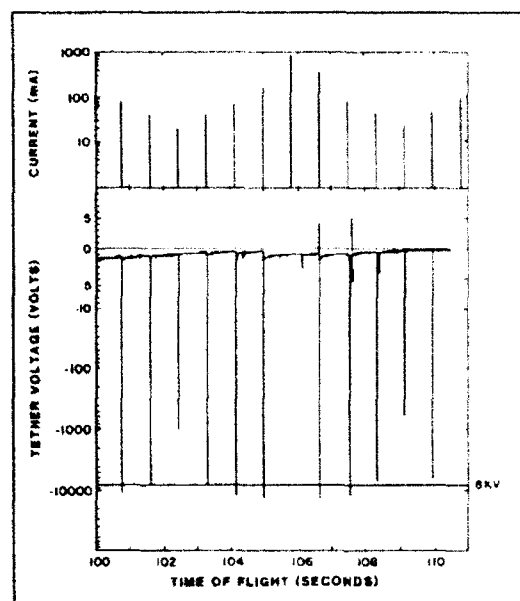
potential of the "floating" daughter relative to the "grounded" mother where negative tether voltages indicated the positive charging of the active daughter payload. A comparison of the tether voltages with the daughter RPA confirm the proper operation of the tether system at least within the 0-to-3.2 keV energy range of the RPA (Maehlum et al., 1988). The tether measurements indicated that the daughter potential at times exceeded the energy of the beam by as much as 50% for beam currents greater than 40 mA. At 40 mA and below, the daughter charging was less than the beam energy although the charging level was still significant. Finally, we note that although the indicated 800-mA current pulse did occur, the tether voltage monitor data was lost due to an onboard telemetry system anomaly.

A more detailed look at the characteristics of the tether voltage during a sample 160-mA beam pulse is provided in figure 5. Note that the sudden change in the tether voltage corresponds to the start of the beam pulse and that high potentials were achieved within a telemetry sample period of beam turn-on. For the remainder of the beam the daughter potential oscillated at the 1.2 kHz frequency of the gun high voltage chopper

447

circuit. The maximum potential during the pulse reached about 14 kV or some 6 kV above the nominal beam energy. At beam termination, the daughter potential remained positive but dropped rapidly to within 10 eV of the mother and then decreased more gradually to zero over the next several milliseconds.
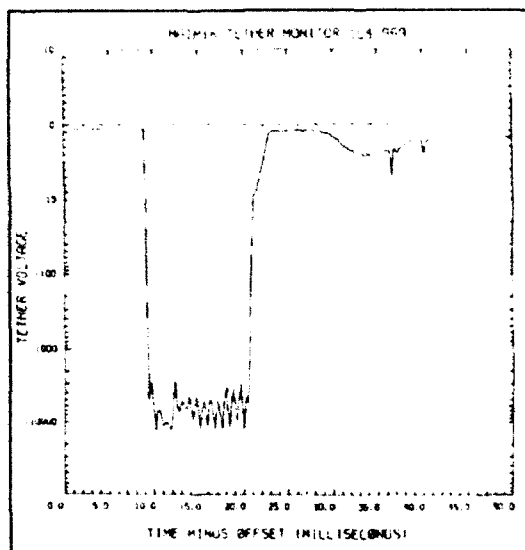

Figure 5. High time resolution VM measurements for a 160-mA beam.

Figure 6. High time resolution RPA measurements for a 160 mA-beam

The RPA measurements shown in figure 6 for the same 160 mA pulse sample confirm the rapid charging of the daughter payload at the initiation of the gun pulse and the persistent high charging level throughout the 11-ms pulse. The variations seen in some of the energy channels were perhaps associated with the oscillations in the daughter potential although the limited sampling frequency of the RPA channels does complicate the association. Following the termination of the beam and the rapid return towards zero of the daughter potential, the vehicle remained enveloped in a low density cloud of energetic electrons, up to 800 eV, which persisted for several tens of milliseconds. Although the daughter was moving out of the interaction region during these measurements the residual signal placed a lower limit on the relaxation
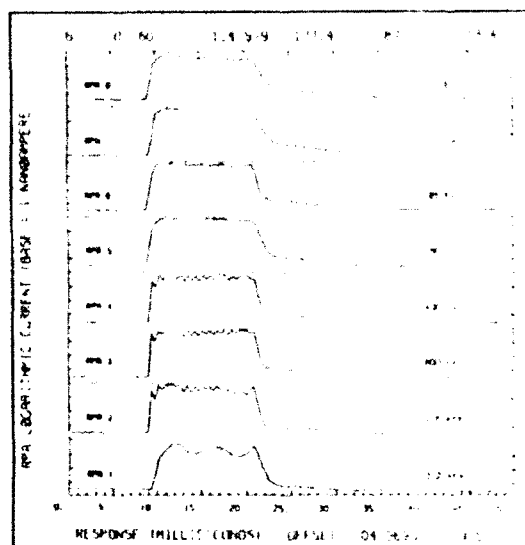
time of the cloud.

The residual effects of the heated plasma region could also be seen in the tether monitor observations. The sample data in figure 5 indicates that the relative voltage between the mother and daughter had a broad but distinct peak centered several tens of milliseconds after the termination of the beam pulse. Note that there was no corresponding aftereffect in the RPA data of figure 6 suggesting that the signal was due to local effects near the mother. At the time of the broad voltage signature the mother was traversing the region of space formerly occupied by the beam-emitting daughter. The small negative charging of the vehicle must have been due to the mother moving into the residual hot plasma cloud.

The spatial and temporal characteristics of the heated plasma region were examined in more detail using the MAIMIK set of plasma probes on the mother payload (Svenes et al., 1988). The beam-induced effects were evident both during the injection pulses and as pulse aftereffects. There were also significant differences in the responses of the plasma probes relating to the tether and the analysis was therefore separated into observations made before and

448

after the tether disconnect.

Prior to the electrical separation at 114 s, the beam-induced responses in the plasma probes were adversely affected by the high charging of the daughter which tended to draw the mother payload somewhat positive. At the maximum charging level of 14 keV the tether current through the 10 Megohm impedance was 1.4 mA. On the other hand, the thermal flux at the mother for an ionospheric density and electron temperature of 4×10^4 cm^{-3} and 1500 °K, respectively, was 8.5 nA-cm^{-2} resulting in a total available thermal current of 0.8 mA to the mother payload (9.7 m^2 surface area). The slight charging of the mother payload was necessary to draw the additional current from the ionosphere.

The plasma probe pulse responses during the tether measurements were increases in the electron flux to the ETP and CAP probes and a decrease in the positive ion flux to the IP. Immediately after the termination of the beam pulse the potential of the mother decreased and the ETP returned to a more normal operation. ETP measurements made during the first Langmuir sweep after the beam showed enhanced electron temperatures well above background that were proportional to the current of the beam. A separate population of suprathermal electrons were also detected at these times. The pulse aftereffects persisted for approximately 15 ms before the plasma returned to its pre-pulse quiet state.

Following tether disconnect the dominant probe responses were due to the hot plasma environment. Enhanced electron temperatures associated with the electron beam were detected by the mother payload out to 8? m from the active daughter corresponding to a perpendicular separation of 34 m. In addition, clearly defined aftereffects were also evident within a 61 m, or 24-m perpendicular, separation. Figure 7 is a plot of the current-dependent temperature enhancements measured by the ETP soon after tether separation. The dominant heating effect of the 80 mA emission is clearly evident in the plot. Similar responses were observed at larger distances although the magnitude of the responses were decreased.

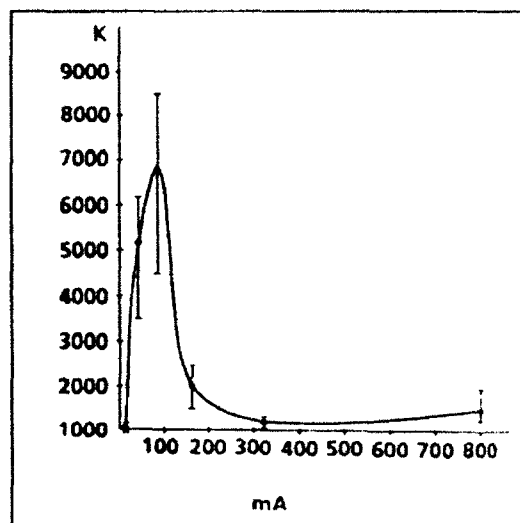The electric fields measured in the vicinity of the daughter payload produced systematic responses to the pulsed beam which could be detected out to radial distances exceeding 60 m. Figure 8 is a representative sample of the electric field responses measured for different mother-daughter separation distances at a fixed current level of 160 mA. The data has been plotted in an instrument-centered coordinate system with no corrections for vehicle motion or contact potential variations. The legend accompanying each beam pulse specifies the time of flight (TOF), the pulse number, the injection pitch angle, the mother-daughter cross-field separation, and the altitude. The pulse signature within a radial distance of about 30 m was a onset impulse field of 1-to-2 ms followed by a persistent field lasting for at least the remainder of the pulse. In general the persistent electric fields could be measured at all beam current above 20 mA within the region of enhanced electron temperatures as measured with the ETP. Also, these persistent electric fields often could be measured for several milliseconds following beam termination. The impulse fields, on the other hand, were consistently measured only for currents greater than 80 mA but were detected well

Figure 7. Electron temperature enhancements versus beam current during the pulse aftereffects.

449

outside the hot plasma region. The amplitude of the impulse field decreased with increasing radial distance and could not be detected beyond 65 m. For the remainder of this section, we restrict our attention to the impulse response features found during beam injections of 160 mA. In addition, for simplicity we will consider here only the perpendicular components of the electric field and ignore the complications introduced by the parallel component.

In order to present a synoptic view of the perpendicular electric field data from the MAIMIK experiment, a field-aligned coordinate system has been adopted which places the active daughter at the origin and fixes the azimuthal injection angle of the beam. Figure 9 is a plot of the 160-mA pulse data presented in this fixed coordinate system. Note the location of the daughter at the origin and the nominal trajectory of the 8-keV beam electrons injected along the positive Y axis. Beam electrons spiral in a clockwise direction with a nominal gyroradius of 6.2 m due to the downward pointing geomagnetic field. Changes in the gyroradius of the beam due to variations in the injection pitch angles and slight changes in the magnetic field strength during the course of the flight have been neglected in the plot. Also, the effects that a changing coordinate system might have on the mor-

phology of the strong sheath can be neglected due to the small amplitude of the background field. Due to the increasing mother-daughter separation length and the spinning of the active payload between successive gun pulses the locus of points representing the mother's position during the successive 160-mA beam injections traces out a spiral in this coordinate system. The perpendicular projection of the corrected electric fields were then rotated into this normalized coordinate system and plotted at the determined locations of the mother. The advantage of this coordinate system is the clarity that it permits for representing the full set of field data on a single plot where the disturbance source is fixed at the origin.

The 160-mA response data in Figure 9 indicate that the impulse fields had outward-pointing radial components and tangential, or azimuthal, components. The MAIMIK results make it clear that the tangential components produced a systematic pattern of counterclockwise deflections from the radial direction. Similar patterns were obtained for the 320 mA and 800 mA beam cases. Although the wave nature for the radial components is not immediately obvious in the data, the consistent counterclockwise deflections in the tangential fields strongly suggests that the azimuthal component must have been of electromagnetic origin. The similar time responses for the radial and tangential components further suggests that they were either part of the same wave train or were responding to the same driving source.

DISCUSSION

The analysis of data from the MAIMIK rocket experiment has so far concentrated on the observations of high charging, particularly the overcharging, of the daughter payload, the current-dependent heating of the background plasma, and the impulsive electric fields driven by the pulsed electron beam. These separate topics are, of course, quite interrelated although it is the overcharging mechanism which we believe is responsible for the unanticipated plasma heating effect (Svenes et al, 1988) and the generation of the impulsive electric fields (Denig et al., 1989). In this section, we carefully consider the experimental
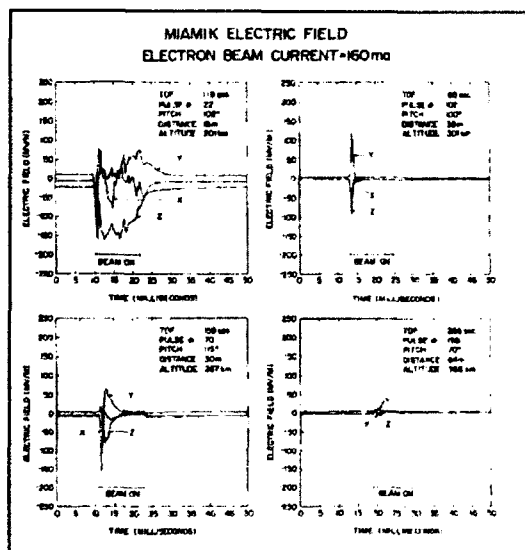

Figure 8. Uncorrected electric field responses versus separation distance for 160-mA beam pulses.
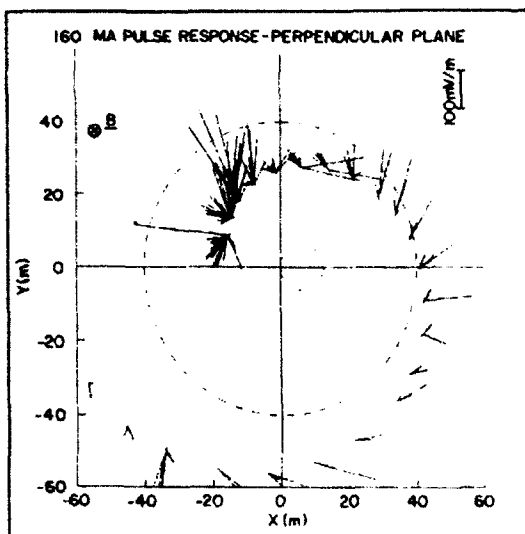
450

Figure 9. Summary plot of the corrected electric field signatures in a daughter centered coordinate system for 160-mA beam injections.

observations and formulate a physical description of the interaction among the active payload, the electron beam, and the background plasma.

The observation of extreme potential charging by the active daughter payload was not entirely anticipated prior to the MAIMIk flight. There had been an earlier indication that modest charging by a rocket-borne accelerator was possible (Jacobsen and Maynard, 1980) but the overcharging condition was a new and surprising result. MAIMIK was the first experiment to successfully test the tethered rocket concept during active electron emission although the technique had been demonstrated earlier for lower payload potentials (Williamson et al. (1982). Paramount in the use of a tether for potential measurements is the reliability of the ground reference. In the case of the MAIMIK experiment, there were several compelling reasons to suggest that the reference did not significantly deviate from the potential of the undisturbed background plasma. Specifically, the electric field measurements indicated that the vehicle was outside the region of intense potential gradients and that the integrated radial electric field beyond the mother was only a minor contributor to the daughter payload potential. Second, it was unlikely that the

tether upset the ground reference since the 1.3 mA of current which flowed through the 10 Megohm tether during the largest potentials was easily drawn from the surrounding ionospheric plasma by the large surface area of the mother payload. Most conclusive, however, was the rather strong agreement between the tether voltage measurements and the energy distribution of the returning electron flux within the instrument capabilities of the RPA. For these reasons we believe that the high charging observations from the MAIMIK experiment were real.

A detailed examination of the active daughter payload was possible only for the initial gun operations occurring prior to tether disconnect at 113 s. However, the limited data set provided measurements over the full range of beam currents and was used to identify a current threshold in the overcharging mechanism. The experimental observations indicate that for the MAIMIK experiment this threshold occurred somewhere between 40 mA and 80 mA. We believe that this threshold represents the formation of a virtual cathode; that is, a turbulent region of negative space charge, near the electron gun aperture (Denig et al., 1987; Maehlum et al., 1988).

A virtual cathode is a naturally occurring phenomenon in the (near) vacuum propagation of intense electron beams when the injected current exceeds the space-charge limit defined by the system geometry (Miller, 1982). The existence of a virtual cathode has been suggested from laboratory space simulation experiments (Kellogg et al., 1982) and in space (Managadze et al., 1988).

The experimental conditions responsible for the formation of the virtual cathode during the MAIMIK rocket flight were the high beam-to-plasma density ratio and the small physical size of the daughter (Maehlum et al., 1988). The limited return current available from the ionosphere caused the initial high charging of the beam payload. Once the space-charge limit for the system was exceeded the virtual cathode formed and reflected the bulk of the beam back to the payload. The turbulent behavior of the cathode stocastically accelerated, via wave particle interactions, a portion of the primary electrons allowing a small percentage of the beam to escape the system and to thereby drive the payload into the

451

overcharged state.

The RPA data indicated that the daughter payload continued to charge to high potentials during beam operations until the rocket entered the mesosphere near the end of the flight (J. Triom, private communication, 1987). In most cases the vehicle potential exceeded the 3.2 kV maximum energy of the RPA but the instrument quickly recovered at the termination of the beam. During the post-pulse interval the instrument measured a suprathermal population of electrons near the gun-emitting payload which persisted for 10-to-20 ms. A suprathermal electron population was also measured by the ETP within a heated plasma region around the daughter.

The ETP measurements show that maximum electron heating occurred for the 80 mA beams and that the radial size of the disturbed plasma region was limited to within 34 m from the central body. The heated plasma near beam emitting payloads has been extensively studied using sounding rockets and supporting data from laboratory experiments (Grandal, 1982). The measured electron energy distribution within the interaction region of beam-plasma experiments shows the increased heating effect and the suprathermal acceleration of the background plasma by the beam (Jost et al., 1980). The sources of free energy available to create the suprathermal electrons and to heat the background electrons are the collisional effects of the beam and instability processes such as the two-stream instability (Arnoldy et al., 1985; Winckler and Erickson, 1986). The radial size of the heated region in space has been found to scale with the gyroradius of the primary beam and with the magnitude of the injected current (Duprat et al., 1983). The radial dimension of the heated plasma region on MAIMIK was about 6 gyro radii wide which scales well to some previous rocket results (Winckler and Erickson, 1986).

The observed current threshold in the electron heating efficiency by the MAIMIK electron beam was the direct result of the overcharging condition. Since the major portion of the electron beam was immediately reflected by the virtual cathode its effective reaction length with the local plasma was reduced and the local plasma heated to a lesser degree.

The measured recovery time of the background plasma following the termination of the beam pulse was much quicker than expected from collisional cooling effects and recombination. This suggests that the plasma thermalization occurred via some wave-particle interaction (Okuda and Abhour-Abdulla, 1988). This also implies that the beam-plasma interaction did not lead to significant background ionization during the pulse. It may be that the critical parameters for the onset of the Beam-Plasma Discharge (Bernstein et al., 1979) were not achieved during the MAIMIK flight.

The persistent electric fields measured within 30 m of the central body corresponded to the region of enhanced electron temperatures and were perhaps the residual effects of the outer sheath of the highly charged daughter payload. Although the persistent fields existed for all currents above 20 mA they were generally small and not very amenable to detailed analyses. The beam signatures of greater interest were the impulsive fields measured at the initiation of the beam pulses for currents above the overcharging threshold. Similar impulse fields were observed during the active POLAR 5 (Jacobsen and Maynard, 1980) and ECHO 6 (K. Ericksen, private communication, 1989) rocket experiments during periods when the payloads are believed to have charged to some high potential. However, the details of the impulse fields and the vehicle charging for these other rocket experiments were not fully addressed due to instrument limitations.

The MAIMIK impulse fields were consistent with the expected effects of ion dynamics driven by the sudden increase in the potential of the daughter at the beam initiation. A calculation of the equivalent vacuum capacitance for the daughter; that is, about 33 pF for the 30-cm sphere, shows that the excess charge needed for the daughter to reach 14 kV was accumulated within several microseconds of beam turn-on. On the other hand, the time scale for the formation of the high potential sheath was on the order of several ion plasma periods (Borovsky, 1988) or a fraction of a millisecond during which time the ions were expelled from the inner sheath region near the daughter. The ion blast wave was a

452

local source of spacecharge which generated the radial impulse fields. The momentary radial field then caused the local electrons to **ExB** drift well before the background ions could respond. The transient Hall current generated by the flowing charge in turn generated a time varying magnetic field which coupled into the azimuthal field via Faraday's Law. The magnitude and orientation of the calculated azimuthal field are consistent with the MAIMIK impulse electric field measurements (Denig et al., 1989).

CONCLUSIONS

The scenario which we feel describes the set of MAIMIK data described here is the following. The overcharging of the daughter payload during active electron emission was due to the combined effects of the low ionospheric plasma density and the small size of the payload. The physical mechanism responsible for the overcharging was virtual cathode formation near the gun aperture which reflected the major portion of the beam. On the other hand, the highly turbulent nature of the cathode energized a small fraction of the beam which then escaped the system and thereby sustained the discharged. Due to the reduced beam propagation above the current threshold for virtual cathode formation the beam-plasma interaction was greatly reduced and a minimum heating effect observed. The rapid charging of the daughter payload at beam initiation accelerated the local ions outward which, in turn, created a radial E-field at distant locations. This momentary field caused the background electrons to **E** x **B** drift azimuthally during an interval when the ions were fixed by their larger inertia. The time response of the induced current coupled into an azimuthal E-field via Faraday's Law.

ACKNOWLEDGEMENTS

REFERENCES

Arnoldy, R.L., C. Pollock, and J.R. Winckler, The energization of electron beams injected in the ionosphere, J. Geophys. Res., 90, 5197-5210, 1985.

Balmain, K.G. Impedance of a radio-frequency plasma probe with an absorptive surface, Radio Science, 1, 1-12, 1966.

Bernstein, W., H. Leinbach, P.J. Kellogg, S.J. Monson, T. Hallinan, Further laboratory measurements of the beam-plasma discharge, J. Geophys. Res., 84, 7271-7278, 1979.

Borovski, J.E., The dynamic sheath: Objects coupling to plasmas on electron-plasma-frequency time scales, Physics Fluids, 31, 1074-1100, 1988.

Cambou, F., V.S. Dokoukine, V.N. Ivchenko, G.G. Managadze, V.V. Migulin, O.K. Nazarenko, A.T. Nesmyanovich, A. Kh. Pyatsi, R.Z. Sagdeev, and I.A. Zhulin. The Zarnitza rocket experiment on electron injection, Space Research, XV, 491-500, 1975.

Cartwright, D.G., S.J. Monson, and P.J. Kellogg, Heating of the ambient ionosphere by an artifically injected electron beam, J. Geophys Res., 83, 16-24, 1978.

Coffey, H.E., Geomagnetic and solar data, J. Geophys. Res., 91, 3328, 1986.

Denig, W.F., N.C. Maynard, W.J. Burke, and N.C. Maynard, E-field measurements during electron beam emissions on MAIMIK, EOS, Trans. AGU, 68, 1400, 1987.

Denig, W.F., N.C. Maynard, W.J. Burke, and B.N. Maehlum, Electric field measurements during supercharging events on the MAIMIK Rocket Experiment, submitted to J. Geophys. Res., 1989.

Duprat, G.R., B.A. Whalen, A.G. McNamara, and W. Bernstein, Measurements of the stability of energetic electron beams in the ionosphere, J. Geophys. Res., 88, 3095-3108, 1983.

Grandal, B., Artificial Particle Beams in Space Plasma Studies, 704 pp., Plenum, New York, 1982.

Hardy, D.A., M.S. Gussenhoven, and E.

Holeman, A statistical model of auroral electron precipitation, J. Geophys. Res., 90, 4229-4248, 1985.

Hess, W.N., M.C. Trichel, T.N. Davis, W.C. Beggs, G.E. Kraft, E. Stassinopoulos, and E.J.R. Maier, Artificial auroral experiment: experiment and principal results, J. Geophys. Res., 76, 6067-6081, 1971.

Jacobsen, T. A. and N. C. Maynard, POLAR 5 - An electron accelerator experiment within an aurora. 3. Evidence for significant spacecraft charging by an electron accelerator at ionospheric altitudes, Planet. Space Sci., 28, 291-307, 1980.

Jost, R.J., H.R. Anderson, and J.O. McGarity, Electron energy distributions measured during electron beam/plasma interactions, Geophys. Res. Letts., 7, 509-512, 1980.

Kellogg, P.J., H.R. Anderson, W. Bernstein, T.J. Hallinan, R.W. Holzworth, R.J. Jost, H. Leinbach, and E.P. Szuszczewicz, Laboratory simulation of injection particle beams in the ionosphere, in Artificial Particle Beams in Space Plasma Studies, edited by B. Grandal, pp. 289-329, Plenum, New York, 1982.

Maehlum, B.N., K. Maseide, K. Aarsnes, A. Egeland, B. Grandal, J. Holtet, T.A. Jacobsen, N.C. Maynard, F. Soraas, J. Stadsnes, E.V. Thrane, and J. Troim, POLAR 5 - An electron accelerator experiment within an aurora. 1. Instrumentation and geophysical conditions, Planet. Space Sci., 28, 259-278, 1980.

Maehlum, B.N., W.F. Denig, A.A. Egeland, M. Friedrich, T. Hansen, G. K. Holmgren, K. Maseide, N.C. Marnard, B.T. Narheim, K. Svenes, K. Torkar, J. Troim, and J.D. Winningham, MAIMIK - A high current electron beam experiment on a sounding rocket from Andoya Rocket Range, In Proc. 8th ESA Symposium on Rockets and Balloons, ESA SP-270, 261-265, 1987.

Maehlum, B.N., J. Troim, N.C. Maynard, W.F. Denig, M. Friedrich, and K.M. Torkar, Studies of the electrical charging of the tethered electron accelerator mother-daughter rocket MAIMIK, Geophys. Res. Lett., 15, 725-728, 1988.

Maehlum, B.N., M. Friedrich, W.F. Denig, G. Holmgren, N.C. Maynard, W.J. Burke, K. Svenes, K.M. Torkar, and J. Troim, MAIMIK -A tethered "mother-daughter"

electron accelerator rocket, Space Research, in press, 1989

Managadze, G.G., V.M. Balebanov, A.A. Burchudladze, T.I. Gagua, N.A. Leonov, S.B. Lyakov, A.A. Martinson, A.D. Mayorov, W.K. Reidler, M.F. Friedrich, K.M. Torkar, A.N. Laliashvili, Z. Klos, and Z. Zbyszynski, Potential observations of an electron-emitting rocket payload and other related plasma measurements, Planet. Space Sci., 36, 399-410, 1988.

Maynard, N. C., D. S. Evans and J. Troim, Electric field observations of time constants related to charging and charge neutralization processes in the ionosphere, in Artificial Particle Beams in Space Plasma Studies, edited by B. Grandal, pp. 627-644, Plenum, New York, 1982.

Miller, R.B., An Introduction to the Physics of Intense Charged Particle Beams, 351 pp., Plenum, New York, 1982.

Okuda, H. and M. Ashour-Abdulla, Ion acoustic instabilities excited by injection of an electon beam in space, J. Geophys. Res., 93, 2011-2015, 1988

Sagalyn, R.C., M. Smiddy, and J. Wisnia, Measurement and interpretation of ion density distributions in the daytime F region, J. Geophys. Res., 68, 199-211, 1963.

Svenes, K., J. Triom, M. Friedrich, K.M. Torkar, and G. Holmgren, Ionospheric plasma measurements from the accelerator rocket MAIMIK, Planet. Space Sci., 36, 1509-1522, 1988.

Williamson, P.R., W.F. Denig, P.M. Banks, W.J. Raitt, N. Kawashima, K. Hirao, K.I. Oyama, and S. Sasaki, Measurements of vehicle potential using a mother-daughter tethered rocket, in Artificial Particle Beams in Space Plasma Studies, edited by B. Grandal, pp. 645-653, Plenum, New York, 1982.

Winckler, J.R., The application of artificial electron beams in magnetospheric research, Rev. Geophys. Space Phys., 18, 659-682, 1980.

Winckler, J.R. and K.N. Erickson, Plasma heating, plasma flow and wave production around an electron beam injected into the ionosphere, in Space Technology Plasma Issues in 2001, ed. H. Garrett, J. Feynman, and S. Gabriel, JPL Publication 86-49, pp. 295-306, 1986.

Current Saturation of Electron Beam Emission from the SCATHA Satellite

S.T. Lai

Geophysics Laboratory, Hanscom AFB, 01731

ABSTRACT

Data taken from SCATHA show that when the satellite is charged to near electron beam energy, saturation behavior in the current-voltage curve occurs. We analyse SC10 data of boom-satellite potential difference to obtain the satellite potential as a function of electron beam current emitted. As the satellite rotates in sunlight, a fraction of the photoelectron current generated on the long booms is received by the satellite body. The satellite potential is governed by the balance of currents of outgoing electron beam, incoming photoelectrons, and ambient plasma. The SC10 data are modulated at a frequency of twice per satellite rotation in sunlight. By means of a simple model of partial return of photoelectrons and beam electrons, we explain the saturation behavior of the modulating SC10 data obtained during high current electron beam emissions resulting in the charging of the satellite to near beam potential. The returning electron beam current as a function of emitted beam current is deduced.

INTRODUCTION

The SCATHA satellite was launched in 1979 for investigating problems of spacecraft charging at geosynchronous altitudes. Descriptions of the experiments on board SCATHA have been given by *Stevens and Vampola* [1978] and *Fennell* [1982]. The satellite, about 1m long and 1.6m in diameter, spins at about once per 60s, and is equipped with two 50m booms (SC10) deployed oppositely in the equatorial plane (Figure 1). The SC10 booms are electrically isolated from the satellite. The outer 20m of each boom is a copper beryllium (CuBe) alloy. The inner segment is coated with Kapton, an insulating material. The SC10 data ϕ represent the difference between the potential ϕ_{CuBe} of the tip of a boom and that ϕ_s of the satellite body (ground) [*Aggson et al*, 1983]. That is

$$\phi = \phi_{CuBe} - \phi_s \tag{1}$$

An electron beam (SC4-1) can be emitted from SCATHA with various energies and currents. During quiet days, the satellite is normally charged positively to a few Volts in sunlight. The emission of an electron beam tends to raise the satellite potential, depending on the ambient condition, beam energies and currents. When the satellite is rotating in sunlight, the amount of sunlight received by boom surfaces vary sinusoidally, and therefore the photoelectron current from the booms varies likewise.

When the satellite body is charged positively as a result of electron beam emission, there is a tendency for the photoelectrons from the booms to be attracted by the satellite body [*Lai et al*, 1987]. The booms form part of the satellite body's environment. In this case, the satellite body not only interacts with its ambient plasma environment but also with the booms which are electrically isolated from the body. This is a case of *Multi-body Interaction* in spacecraft charging.

Electron current saturation in diode tubes is well known [*Child*, 1911; *Langmuir*, 1912]. In a diode tube, the distance and potential difference between the electrodes are controlled parameters. As the current density increases, so does the space charge. Beyond a critical current density, the

space charge tends to return part of the current; only a fraction of the emitted current arrives at the anode. This is known as current saturation. The space charge limiting current is given by the famous *three-halves power* law [*Child*, 1911; *Langmuir*, 1912].

In space, however, the situation of an electron beam is different from that in a diode. The distance between the cathode and the anode in space is ill-defined, because, unlike a diode, it is not clear where the anode is in space. Furthermore, the beam emitted into space is not well collimated because the beam space charge tends to make the beam divergent. Therefore, it is interesting to ask whether current limitation can occur in beams emitted into space, and, if it does, whether there is a critical current under given experimental conditions.

Observations of current limitation in beam experiments on satellites have been reported. Olsen [1985] has presented ATS-5 results. Lai et al [1987] have presented SCATHA Day 89 results. The Day 89 data span a wide range of beam currents and energies and the data points are widely separated. To follow the development of current saturation and to pin point the sudden appearance of a critical current, it is necessary to choose a day in which the beam current increases continuously.

In the following sections, we will briefly discuss SCATHA SC10 data taken on Day 89, 1979. A theoretical model of photoelectron current modulation during electron beam emissions is presented. The SC10 data of Day70 are particularly interesting because they feature a continuous increase in electron beam current while the beam energy is held constant and the environment is quiet. This gives a rare opportunity to observe spacecraft charging in response to a known driving factor: the beam current. The purpose in this case study is to compare theoretical and experimental results and to determine the critical current for the onset of current limitation.

SCATHA CHARGING DURING ELECTRON BEAM EMISSIONS

Due to the high secondary emission coefficient of CuBe, the outer section of a SC10 boom is not expected to be charged to high potentials, except in unusually energetic ambient conditions. When the potential ϕ_s is high compared with ϕ_{CuBe}, the SC10 data ϕ represents a good approximation of ϕ_s with the sign reversed. There are other instruments measuring spacecraft potential on SCATHA. They show that SC10 data often give good approximate measurements of the satellite potential. We will assume that SC10 data ϕ is $-\phi_s$ approximately, since we consider quiet days only.

When SCATHA is in sunlight, with or without beam emission, SC10 data show oscillations at twice the satellite rotation frequency [*Lai et al*, 1986, 1987]. When the satellite is entering eclipse, the amplitude of oscillation decreases gradually [*Cohen et al*, 1981]; this evidence supports the contention that the oscillation is due to the effects of photoelectrons.

In total eclipse, SC10 data still show some insignificant but noticeable oscillation with a small amplitude, which, with its low signal to noise ratio, correlates weakly with the boom sun angle. The reason of this barely noticeable oscillation in eclipse is unknown. Some plausible reasons are (1) the sun in UV is bigger than what it appears to be, (2) there is a weak ambient magnetic field effect, or (3) there are anisotropic ambient currents. This property, however, is outside the scope of this paper.

In sunlight without electron beam emission, several aspects of SC10 data resemble those with electron beam emission. Sinusoidal oscillations are present, with the same frequency and boom sun angle correlation. The amplitude of oscillation is about 4 to 5 volts typically on quiet days [*Lai et al*, 1986].

As the electron beam current increases from zero, the spacecraft potential increases. And, not only the magnitude of SC10 data but also that of the oscillation increases. The extrema of the oscillation correlate well with the sun angle of the booms [*Lai et al*, 1987]. The minima occur at $\theta=0°$ and $\theta=180°$ and the maxima at $90°$ and $270°$. Another instrument, SC2, also measures the potential of the spacecraft body. The oscillation frequency and phase of SC2 data are identical with those of SC10; this evidence shows that the oscillations are due to the variations of the potential of the spacecraft body.

The amplitude $\Delta\phi$ of the SC10 data variation is a function of beam current and beam energy. The ratio of amplitude $\Delta\phi$ to the satellite potential θ shows nonmonotonic behavior as a function of beam current. The ratio first increases with the beam current until a maximum is reached and then it decreases as beam current further increases. When the beam current is large, the satellite is

charged to near beam energy, while the variations almost cease. Our contention is that, at large beam currents, the beam does not leave completely because of some current limiting mechanism, a saturation behavior.

Despite the wide range of combinations of beam current and energy on Day 89, 1979, the data are widely separated. In order to show the response of the satellite potential ϕ_s to continuously increase in beam current, we present the Day 70, 1981 data (Figure 2). The beam energy is controlled at 300 eV constantly. The electron beam current increases continuously from near zero to about 90μA. There are several 30sec periods of dropouts (for calibration purposes) at regular intervals; the data in these periods are ignored in our study. The oscillation in the Day70 data correlates with boom sun angle θ in the same manner as in Day 89, the maxima of spacecraft potential occur when the booms are parallel or antiparallel to sunlight, and minima occur when the booms are perpendicular to sunlight. Starting from zero current, the oscillation amplitude increases monotonically with beam current until a critical current (about 60 μA) is reached; then it decreases slightly with further increase in beam current. Unlike the Day 89 data, the continuous nature of the increasing beam current enables the critical current to be determined with better accuracy.

THEORY OF PHOTOELECTRON CURRENT MODULATION

The photoelectron current from the booms depends on the sun angle θ. Depending on the potential ϕ_s of the satellite body, a fraction f of this current is received by the body. In a self-consistent manner, the satellite potential ϕ_s depends on the photoelectron current I_{ph} received. In the low density plasma environment at geosynchronous altitudes, the orbit-limiting Langmuir plasma probe model is applicable for the collection of ambient current. The current balance equation for the satellite body is

$$I_e(0)(1+e\phi_s/kT_e)^\alpha + I_{ph}(\phi) = I_{beam}(\phi) - I_{return}(\phi)$$ (2)

and

$$I_{ph}(\phi) = 2d\int_0^{50m} dr\ f\ [\phi(r)]\ j_{ph}\ \sin\theta$$ (3)

where $I_e(0)$ is the ambient current collected if the spacecraft potential ϕ_s is zero without photoelectron or beam emission. I_{beam} is the electron beam current emitted. If the beam energy is high and the beam current density low, the whole beam leaves. However, if the beam energy is low and the beam current density is high, part of the beam may return and the return current I_{return} becomes nonzero. For a spherical body, the power α of the orbit-limiting current collection term in eq(1) equals unity; for an infinite cylinder, α equals 1/2. However, for SCATHA, the geometry of the satellite body resembles a sphere more than a cylinder. Thus, the power α of the Langmuir orbit-limiting current collection term for SCATHA should be near unity; the exact value of α is not needed for our purposes in this paper. The photoemissivity of the copper beryllium boom surface material on a rotating satellite (at about 1 AU) has been estimated to be 2×10^{-9} to 4×10^{-9} amp.cm^{-2} [Kellogg, 1980]. The photoemissivity j_{ph} of the CuBe surfaces on the SC10 booms of SCATHA is considered as a parameter to be determined in this paper.

To model $I_{ph}(\phi)$, it is necessary to assume a photoelectron energy spectrum and a satellite sheath potential profile. Both laboratory and space experiments have shown that a Maxwellian distribution is a good approximation to describe the photoelectron energy spectrum [Hinteregger et al, 1965; Whipple, 1982]. Our model assumes energy partition of the spectrum.

$$f\ [\phi(r)] = \frac{\int_0^{e\phi(r)} dE\ E\ \exp(-E/kT_{ph})}{\int_0^\infty dE\ E\ \exp(-E/kT_{ph})}$$ (4)

where the satellite sheath potential $\phi(r)$ is often modeled by the Debye form [Godard and Laframboise, 1973].

457

$$\phi(r) = \frac{\phi_s R}{r + R} \exp(- r / \lambda_D) \qquad (5)$$

The Debye length λ_D of the ambient plasma is about 45m [Aggson, et al, 1983]. The photoelectron temperature T_{ph} is about 2 eV [Whipple, 1982; Lai et al, 1986]. Using ths model, we compute the total photoelectron current going towards the satellite body (Figure 3).

The maxima and minima of the SC10 data of Figure 2 are plotted in Figure 4 as emitted beam current versus satellite potential. The data with photoemission (minimum $|\phi|$ with $\theta=90^\circ$ or 270°) are plotted in Figure 5, and those without photoemission (maximum $|\phi|$ with $\theta=0$ or 180°) in Figure 6. At low beam currents, each set of data follows a smooth trend. Each trend deviates suddenly at a critical current. Without photoemission, the critical current is about 60 μA with the spacecraft potential at about 220 Volt. With photoemission, the critical current is higher (about 70 μA) with the spacecraft at a lower potential (about 140 Volt). Using the maximum $|\phi|$ ($\theta=0$ or 180°) data curve (without photoelectrons), the total photoelectron current $I_{ph}(\phi)$ is computed for a given photoemissivity j_{ph}. The total photoelectron current I_{ph} is then added to the maximum $|\phi|$ ($\theta=0$ or 180°) curve. The theoretical curve obtained fits fairly well with the experimental data points of minimim $|\phi|$ (with $\theta=90^\circ$ or 270°). We determine that the photoemissivity j_{ph} of the CuBe surfaces on the SC10 booms of SCATHA is about 3 nanoamp.cm^{-2}, which agrees with the values (2 to 4 nanoamp.cm^{-2}) estimated by Kellogg [1980] for the CuBe surfaces on a different spacecraft (Helios at 1 AU).

The satellite potential $\phi_s(\theta)$ oscillates as the satellite and booms rotate in sunlight. The amplitude of potential oscillation is given by $\Delta\phi = \phi_s(\theta=0$ or $180^\circ)-\phi_s(\theta=90^\circ$ or $270^\circ)$. As the beam current I_{beam} increases, so does the potential oscillation amplitude $\Delta\phi$. When the satellite is charged to near beam potential, the beam current ceases to leave completely. A non-monotonic behavior of the SC10 oscillation amplitude $\Delta\phi$ ensues [Figure 7].

ELECTRON BEAM SATURATION

When the beam current is saturated, the beam current leaving is less than the beam current emitted. Part of the beam returns (i.e. $I_{return} \geq 0$). When saturation occurs, the data points on the current-voltage curves (Figures 5,6) deviate from the smooth trend set by the unsaturated points. Physically, when saturation occurs, the net current leaving the system is less than the emitted beam current. Mathematically, when saturation occurs, the net current $I_{net} = I_{beam} - I_{return}$ (eq.2) should be used as the ordinate variable in place of I_{beam}. If I_{net} is used, the data points should again satisfy the same function, or curve, extrapolated from the unsaturated regime. Conversely, if the data points satisfy the extrapolated function, then the net current I_{net}, and hence the return current I_{return}, can be determined. Thus, this method allows one to determine the magnitude of return current I_{return} during beam saturation. The return current I_{return} are shown in Figures 5 and 6.

Also shown in Figure 5 and 6 are three regimes I, II, and III. In regime I and II, the beam current I_{beam} is unsaturated, and the return current I_{return} is zero. In regime I, photoelectron current from the satellite body can leave because the satellite positive potential ϕ_s is low. The amount of photoelectron current leaving is a function of satellite potential ϕ_s. An extrapolation of the regime II curve intercepts the y-zxis (zero ϕ_s) at about 10 μA (Figure 5); this determines the $I_e(0)$ term in eq(2). Using the typical ambient current [Purvis et al, 1984] at geosynchronous altitudes on quiet days and the dimension of SCATHA, one obtains a result of the same order of magnitude for $I_e(0)$, the ambient current intercepted by SCATHA. With photoelectrons leaving the spacecraft body, the data points in regime I deviate from the curve extrapolated from regime II. With an estimated photoelectron current of about 30 μA (which depends on the photoemissivity of the surface materials) leaving the spacecraft body at $\phi_s=0$, the data points (circles) are expected to intercept the y-axis at $I_e(0)-30$ μA, i.e. at -20 μA. In regime I, very little of the photoelectron current from the booms can reach the spacecraft body because of the low attraction offered by the low spacecraft potential ϕ_s. In regime II, the multi-body interaction between the satellite body, the booms, the

electron beam, and the ambient plasma is in action. In regime III, beam saturation occurs and part of the beam current returns. Schematically, the physical processes in the three regimes are shown at the bottoms of Figure 5 and 6.

The details of the physical mechanism leading to the electron beam saturation are not known at this time. Space charge limitation [Lai et al, 1980], beam energy broadening [Katz, et al, 1986] and spacecraft differential charging [Olsen, 1985] are plausible mechanisms to be studied. The results of this study may be useful for obtaining new insights into beam saturation mechanisms in space.

REFERENCES

Aggson, T.L., B.G. Ledley, A. Egeland, and I. Katz, Probe measurements of DC electric fields, ESA-SP-198, pp.13-17, 1983.

Cohen, H.A., et al, P78-2 satellite and payload responses to electron beam operations on March 20, 1979, NASA CP-2182, 1981.

Fennell, J.F., Description of P78-2 (SCATHA) satellite and experiments, in IMS Source Book, Am. Geophys. U., Washington, D.C. 1982.

Godard, R. and J.G. Laframboise, A symmetrical model for the current collection of a spherical electrotatic probe in a flowing plasma, EOS, 54, 392, 1973.

Hinteregger. H.E., L.A. Hall, and G. Schmidtke, Solar XUV radiation and neutral particle distribution in July 1963 thermosphere, Space Physics, Vol.5, 1175, 1965.

Katz, I., G.A. Joneward, D.E. Parks, D.L. Reasoner and C.K. Purvis, Energy broadening due to spacecharge oscillations in high current electron beams, Geophys. Res. Lett., Vol.13, 64, 1986.

Kellogg, P.J., Measurements of potential of a cylindrical monopole attenna on a rotating satellite, J. Geophys. Res., A85, 5157, 1980.

Lai, S.T. and H.A. Cohen, Space charge in electron and ion beams emitted from P78-2 satellite, EOS, Vol.61, No.17, p.1090, 1980.

Lai S.T., H.A. Cohen, T.L. Aggson, W.J. McNeil, Boom potential on a rotating satellite in sunlight, J. Geophys. Res., Vol.91, No.A11, pp.12137-12141, Oct., 1986.

Lai S.T., H.A. Cohen, T.L. Aggson, W.J. McNeil, The effect of photoelectrons on boom-satellite potential differences during electron beam ejections, J. Geophys. Res., Vol.92, No.A11, pp.12319-12325, 1987.

Langmuir, I., The effect of space charge and residual gases on thermionic currents in high vacuum, Phys. Rev., Vol.2, 450, 1913.

Olsen, R.C., Experiments in charge control of geosynchronous orbit - ATS5 and ATS6, J. Spacecraft & Rockets, Vol.22, pp.254-264, 1985.

Purvis, C.K., H.B. Garrett, A.C. Whittlesey, and N.J. Stevens, Design guidelines for assessing and controlling spacecraft charging effects, Rep. NASA-TP-2361, N84-33452, 44pp., 1984.

Stevens, J.R., and A.L. Vampola (Eds), Description of the space test program P78-2 spacecraft and payloads, Rep.SAMSO-TR-78-24, ADA 061 324, Air Force Sys. Command, Los Angeles, CA, 1978.

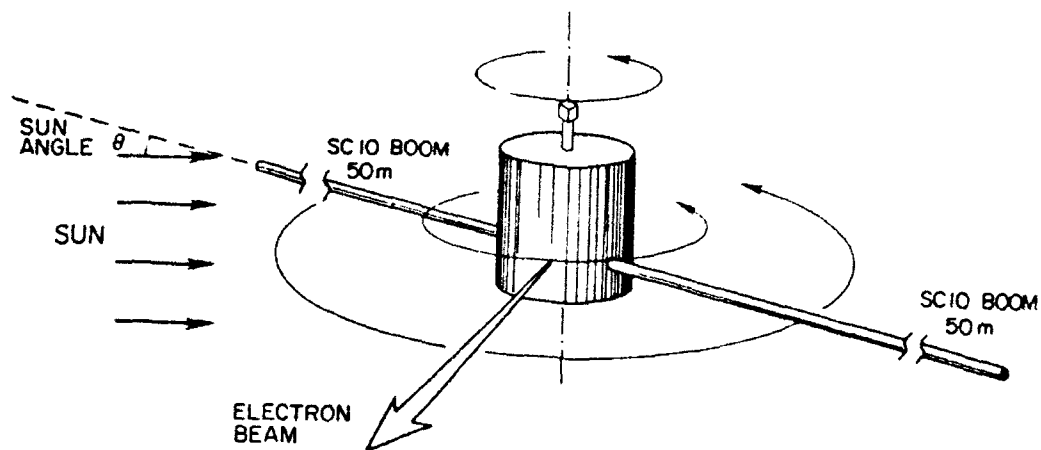Whipple, E.C., Potentials of surfaces in space, Rep. Prog. Phys., Vol.44, 1197, 1981.

Figure 1. Schematic diagram of the SCATHA satellite with beam emission (from *Lai et al*, 1987).

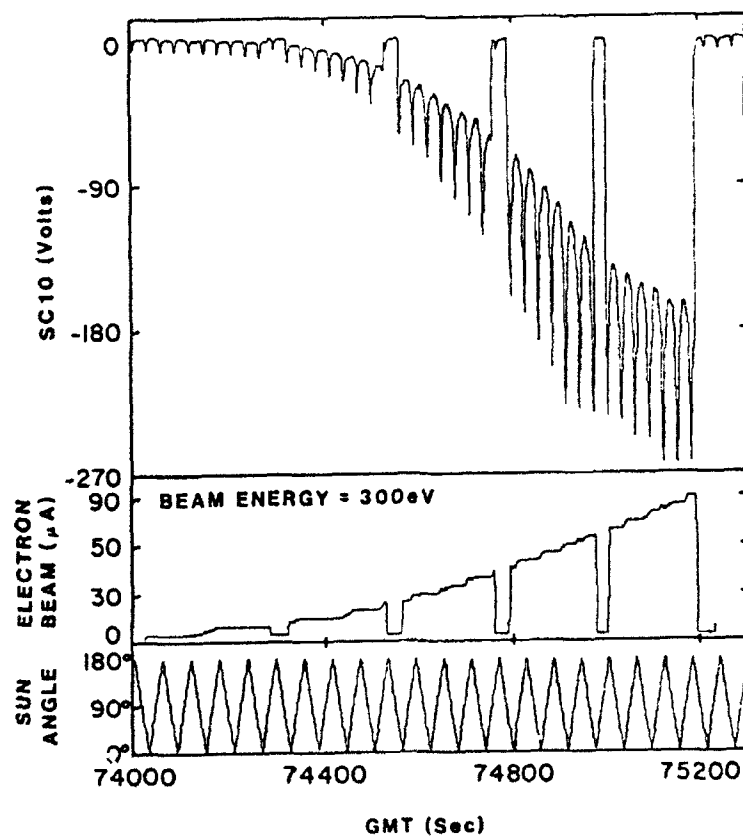

Figure 2. Day 70 SC10 ϕ data (Volts), electron beam current I_{beam} (μA), and SC10 boom sun angle θ (degrees) as functions of time. The electron beam energy is 300eV. The drop outs at regular intervals are for calibration.
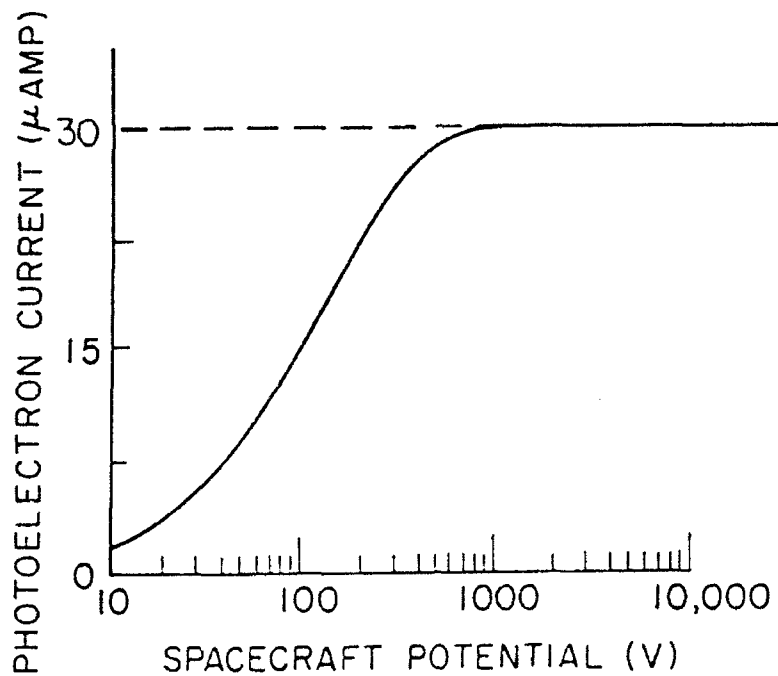
460

Figure 3. Total photoelectron current $I_{ph}(\phi_s)$ arriving at the spacecraft body as a function of spacecraft potential ϕ_s. The photoemissivity j_{ph} used is 3 nanoamp.cm^{-2}.
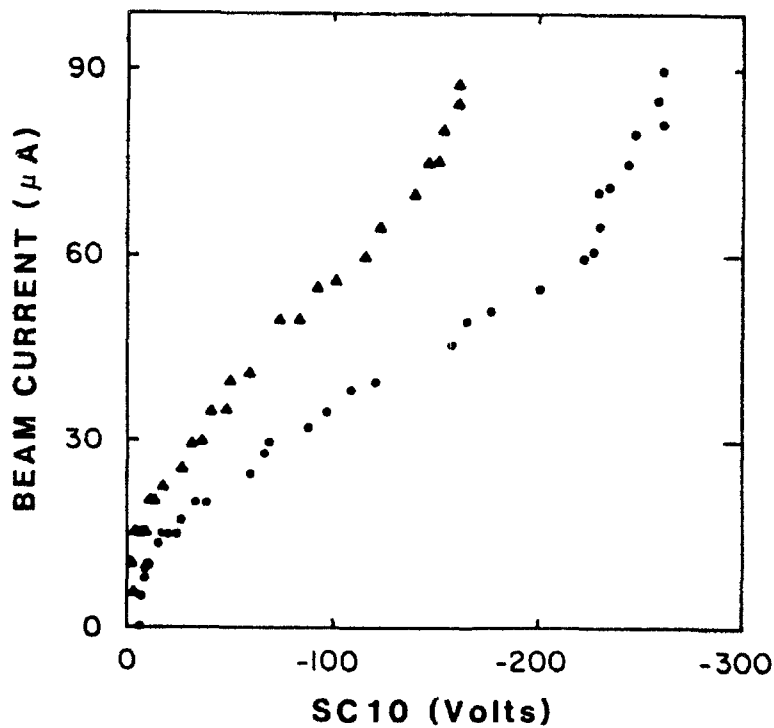
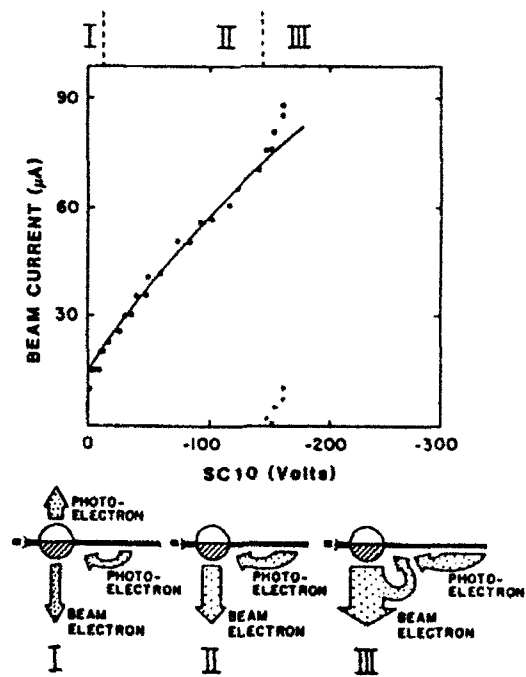Figure 4. The maxima and minima of SC10 data (from Figure 2) as functions of emitted beam current.

461
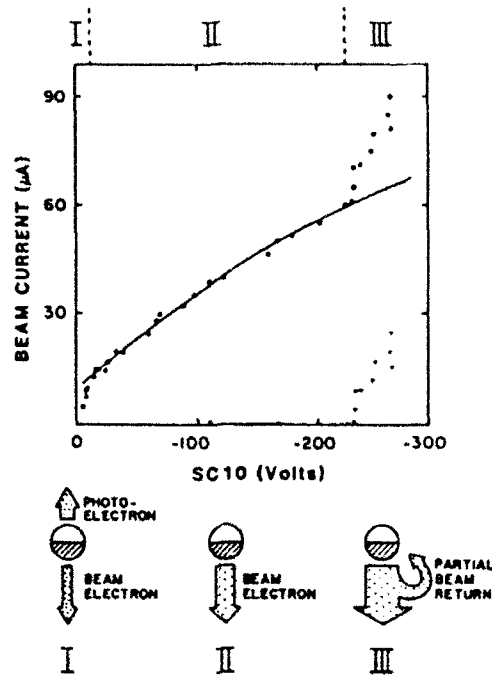
Figure 5. The emitted beam current I_{beam} and the SC10 data without photoemission (maximum $|\phi|$ with $\theta=0$ or $180°$). The three regimes are discussed in the text. The cartoons below the x-axis show schematically the physical processes in the regimes.

Figure 6. The emitted beam current I_{beam} and the SC10 data with photoemission (minimum $|\phi|$ with $\theta=90°$ or $270°$). The three regimes are discussed in the text. The cartoons below the x-axis show schematically the physical processes in the regimes.
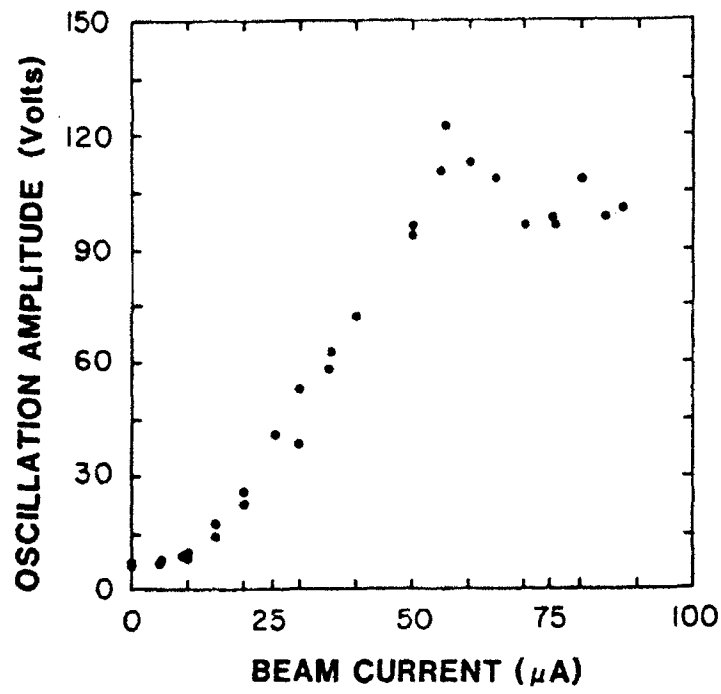
462

Figure 7. Non-monotonic behavior of the oscillation amplitude $\Delta\phi$ of SC10 as a function of emitted beam current I_{beam}. Saturation occurs when the beam current exceeds a critical value.

Dynamics of Spacecraft Charging by Electron Beams

M. J. Mandell and I. Katz

S-CUBED Division of Maxwell Laboratories, La Jolla, California

When a spacecraft or rocket emits an electron beam into an underdense plasma, it can charge to potentials in excess of the beam energy. We show calculations in which 8 keV beams are emitted along and across the earth's magnetic field, with parameters appropriate to the MAIMIK rocket. As was observed on MAIMIK, the spacecraft charged to potentials in excess of the beam potential due to energization of beam electrons by beam-generated electrostatic oscillations. This is in contrast to the low levels of charging often seen in denser environments, where higher plasma currents, coupled with ionization of neutrals, hold spacecraft potentials below a few hundred volts.

The beam structure and the spacecraft potential oscillate at a frequency corresponding to the mean lifetime of the beam electrons. These oscillations energize the beam electrons, and also pump energy into the ambient plasma, which exhibits lower frequency oscillations. The peak spacecraft potential is over 1 kV in excess of the beam energy. For the cross-field case, the oscillation frequency is proportional to the beam current for sufficiently intense beams.

Following beam turn-off, there is an immediate return of unscattered beam electrons and a longer term dissipation of scattered beam electrons. Analytic estimates are presented for the decay and overshoot of the spacecraft potential.

INTRODUCTION

A number of electron beam experiments have measured results that apparently violate conservation of energy. The SEPAC experiment (Reasoner *et al.*, 1984) measured a spectrum of returning electrons extending to energies well above that of the emitted beam, and the MAIMIK rocket (Maehlum *et al.*, 1988; Denig, Maehlum and Svenes, this conference) was charged by an 8 keV electron beam to potentials as high as 14 keV. Katz *et al.* (1986) performed a planar calculation that showed that oscillations of the beam electrons led to the spectral broadening seen in the SEPAC experiment. In this paper, we show 2-dimensional calculations, with parameters appropriate to MAIMIK, illustrating that space charge oscillations associated with the electron beam lead to rocket potentials in excess of the beam energy.

The electron beam on MAIMIK was directed nearly across the earth's magnetic field. The geometry of an intense beam directed across a magnetic field is shown in Figure 1a. If the spacecraft is near the beam energy, the beam electrons will be slowest at their farthest excursion from the spacecraft and will form a space charge maximum. This space charge maximum breaks the azimuthal symmetry of the problem, so that electrons may be scattered from their original gyro-orbits and leave the vicinity of the spacecraft. Unfortunately, this is a truly 3-dimensional situation and, therefore, very difficult to model.

Two beam configurations that can be modeled in 2-dimensional axisymmetric geometry are shown in Figures 1b and 1c. Figure 1b shows a beam directed along the magnetic field. An intense virtual cathode is formed. Most of the beam electrons move outward

from the virtual cathode and are attracted back to the spacecraft, which they impact from behind. A few of the beam electrons continue along the magnetic field line and escape the vicinity of the spacecraft. Figure 1c illustrates an "equatorial" beam, in which electrons are directed across the magnetic field from the entire spacecraft circumference. A ring of maximum space charge appears around the spacecraft. Because the space charge maximum is a full ring rather than a localized region, we expect it to be less intense than would be the case for a physical beam of the same current. Also, the space charge maximum is less effective at scattering because it does not break azimuthal symmetry.

The calculations described here were performed using an S-CUBED-developed, finite-element, electrostatic particle-in-cell code named Gilbert. Gilbert is a flexible, multi-purpose code with many special features. For these calculations, the space around the spacecraft was gridded with biquadratic elements of variable resolution to a distance of ten meters. Each element represents a volume of space corresponding to its area revolved in a full circle about the symmetry axis. For the "equatorial" beam, the calculation took advantage of mirror symmetry about the equatorial plane. The computational grids for the two cases are shown in Figure 2.

PHYSICAL PARAMETERS

Table 1 shows the physical parameters used in the calculation. The parameters listed in the "current collection" category are calculated for a spherical spacecraft at the beam potential of 8,000 volts.

Table 1. Problem Parameters

Geometrical Parameters

Inner (spacecraft) Radius	0.3 m
Outer Radius	10.0 m
Magnetic Field	0.4 gauss

Beam Parameters

Beam Current	0.16 amperes
Beam Energy	8000 eV

Plasma Parameters

Electron/Ion Density	3×10^9 m^{-3}
Electron Temperature	1 eV
Ion Mass	16 amu
λ_D	13.6 cm
ω_{pe}	3.1×10^6 sec^{-1}
ω_{ce}	7.0×10^6 sec^{-1}
J_{th}	8.0×10^{-5} A-m^{-2}

Current Collection

Langmuir-Blodgett Radius	10 m
Parker-Murphy Radius	1.54 m
Parker-Murphy Current	0.0025 amperes
Probe Charge	2.7×10^{-7} coulombs

The plasma surrounding the spacecraft is "underdense", in the sense that the Parker-Murphy bound (Parker and Murphy, 1967) on the plasma return current is only a few percent of the beam current. Also, the electron plasma frequency is below the electron cyclotron frequency and, as we shall see, well below the oscillation frequency of the beam.

The radius of the computational space is taken equal to the radius of a space-charge-limited spherical sheath in this plasma, which is far larger than the Parker-Murphy radius for current collections. The effect of the plasma external to this radius is represented by a zero potential condition on this boundary. In retrospect, this approximation appears adequate to represent the beam dynamics, the ion dynamics, and the collection of ambient electrons but omits long-range transient effects on the ambient electron density.

CALCULATION FOR BEAM ALONG FIELD

The calculation begins with the grid of Figure 2a filled with electron and ion macroparticles (Figure 3a). The beam is projected along the magnetic field (Figure 3b) and initially exits the computational space. The negative beam charge and the positive charge left behind on the spacecraft produce a dipole potential (Figure 3c) that expels ambient electrons from the beam region (Figure 3d).

The spacecraft reaches beam potential about 2.5 microseconds after beam turn-on (Figure 4a), and the potential exhibits persistent oscillations (at 2×10^6 Hz) for the duration of the calculation (Figure 4b). During this time, the spacecraft remains always above the beam potential and has a peak potential of about 9,100 volts.

The beam conformation oscillates along with the spacecraft potential. Figure 5a shows the beam conformation when the spacecraft potential is fairly high. The bulk of the beam electrons are far from the spacecraft, having been emitted when the potential was low. Figure 5b shows beam conformation at a fairly low potential. In this case, the bulk of the beam electrons are close to the spacecraft, having been emitted at high potential. However, a pulse of energized electrons can be seen escaping along the field line.

Figures 6a and 6b show the electrostatic potential structure about the spacecraft. The sheath is elongated along the magnetic field due to quasi-trapping of ambient electrons that cannot be collected. The contours are distorted along the axis by the beam electron space charge (Figure 6a). At times, a negative potential well forms in the cross-field region (Figure 6b).

Figure 7a shows the amount of beam electron charge in the computational space, and Figure 7b shows the time dependence of the dipole moment of the beam electrons, defined as

$$\text{Dipole Moment} = \int \rho \, z \, d^3 r$$

where ρ is the charge density of beam electrons. Since the dipole moment is oscillating at 2 MHz, we expect to see strong electromagnetic radiation at this frequency.

Figures 8abc show spectral analysis of some of the oscillating quantities. The potential (Figure 8a) shows a sharp peak at 2 MHz, with well-defined second and third harmonics. The beam dipole moment (Figure 8b) shows a sharp peak at 2 MHz, as well as a broad peak at the ambient electron plasma frequency (0.5 MHz). The dipole moment of the

ambient electrons (Figure 8c) shows little evidence of the 2 MHz oscillations but has a strong, broad peak near the ambient plasma frequency.

The beam charge (Figure 7a) varies from 0.04 to 0.08 μcoul. Dividing this by the beam current of 0.16 amperes shows that beam particle lifetimes fall mainly in the range 0.25 - 0.5 μsec. Noting also that the upstrokes in Figure 7a (strong return current) are steeper than the downstrokes (steadily emitted current) leads to the following interpretation. Most of the beam electrons return to the spacecraft in a short burst. Electrons emitted during the return burst see relatively weak retarding fields, travel far from the spacecraft, and have lifetimes of approximately a full oscillation period. Electrons emitted while the potential is rising see stronger retarding fields, travel smaller excursions, and return to the spacecraft at the same time as the long-lived electrons, producing the return current bunching. This bunching is similar to that seen by Katz *et al.* (1986).

Figure 9 shows the ion positions at the conclusion of the calculation (20 μsec). The ions have cleared a region of about two meters around the spacecraft. Thus the run time of this calculation is too short to approach the formation of an equilibrium "sheath".

CALCULATION FOR BEAM ACROSS FIELD

A similar calculation was performed for an equatorial beam directed across the magnetic field in the grid of Figure 2b. (Note that in this calculation we have taken advantage of mirror symmetry about the z = 0 plane. Values for current and charge will be quoted at double the computed values, so that they are characteristic of a complete sphere.)

The beam electrons at the conclusion of the calculation are shown in Figure 10. The figure shows a main stream of electrons emitted from the spacecraft, slowed by the electric field and turned by the magnetic field, then returning to the spacecraft. In addition, there is a column of beam electrons extending in the magnetic field direction. The mechanism for populating this column is that a beam electron in its initial orbit gains enough momentum along the magnetic field to miss the spacecraft on its first return passage, and while passing near the spacecraft receives a substantial impulse along the field. Electrons leave the column by either impacting the spacecraft or escaping the grid.

Figures 11ab show the time history of the spacecraft potential. Four different current values were used. From Figure 11b we see that, while doubling the current led to some increase in the mean potential and its oscillation amplitude, the main effect is to double the frequency.

Figures 12ab show the potential contours about the spacecraft at two different times. As in the previous case, the sheath is elongated along the field line, and a negative potential well is sometimes seen in the cross-field region.

Figure 13 shows the ambient electron macroparticles. The ambient electron population was maintained by generating the plasma thermal current at the spherical problem boundary out to a radius of eight meters. A low density region is seen to extend along the field line from the spacecraft; electrons in this region are allowed by the theory of Parker and Murphy (1967) to be collected by the spacecraft. A high-density cloud of electrons is seen in the cross-field region, as these electrons cannot be collected by the spacecraft and have low probability of escaping the grid. This ambient electron charge density structure is the cause of the elongated potential contours shown in Figures 12ab and 6ab.

467

Table 2 shows the range of beam charge, range of beam electron lifetime, and oscillation period for the different values of emission current. As with the field-aligned beam, the oscillation period is near the maximum beam particle lifetime. Except for the lowest current value, the beam charge increases only slightly when the current is doubled. This is because the maximum beam charge is approaching the charge on the sphere. When the current is doubled, a modest increase in mean spacecraft potential is sufficient to reduce the particle excursion distance and cut the beam particle lifetime by half. This point is further illustrated by Figure 14, which plots the quantity

$$\int \rho \, r \, d^3 r$$

The average and oscillation amplitude of this quantity varies slowly as the sheath is being formed, but shows no abrupt changes as the current is altered, leading to the conclusion that the system rapidly adjusts so that the beam charge times its excursion distance is independent of current.

Table 2. Beam Charge, Lifetime, and Oscillation Period for Equatorial Beam

Current (Amperes)	Charge (μcoul)	Lifetime (μsec)	Period (μsec)
0.16	0.07 - 0.1	0.44 - 0.62	0.62
0.32	0.12 - 0.2	0.38 - 0.62	0.47
0.64	0.13 - 0.21	0.20 - 0.33	0.28
1.28	0.14 - 0.25	0.11 - 0.19	0.18

BEAM TURN-OFF

Several papers at this conference discussed beam turn-off, showing that the spacecraft potential tends to overshoot and achieve a negative value. This led us to investigate the behavior of the equatorial beam system after turn-off of the 0.160 ampere beam.

Figure 15 shows the behavior of the spacecraft potential and the beam charge following beam turn-off. Most of the beam charge is promptly collected, dropping the spacecraft potential to 7,200 volts. Approximately 0.03 μcoul of charge remains in the field-aligned column of scattered beam electrons, which decays with a time constant of 2.1 μsec. About three-quarters of this depopulation rate results from electrons escaping the grid, and about one-quarter from electrons recaptured by the spacecraft. (When the spacecraft is at elevated potential, the escape rate must balance the Parker-Murphy collected current, leading to a 12 μsec time constant for escape.)

If the spacecraft discharges by collecting the Parker-Murphy current, its potential will follow the equation

$$dV/dt = (I_0/C) (V/V_0)^{1/2}$$

where I_0 is the Parker-Murphy current at potential V_0 (- 0.0025 amperes at 8,000 volts) and C is the spacecraft capacitance (3.4×10^{-11} farads). The solution is

$$t_2 - t_1 = -2.4 \times 10^{-6} (V_2^{1/2} - V_1^{1/2})$$

which gives a discharge time of about 200 μsec. Since the thermal ion speed is only a few thousand m-sec^{-1}, it will take about a millisecond for the ions to repopulate a sheath a few meters in radius. Assuming a thermal electron distribution, the spacecraft will charge negatively during this time according to

$$dV/dt = 4\pi a^2 J_{th} e^{V/\theta} / C$$

whose solution is

$$V/\theta = - ln(1 + t/\tau)$$
$$\tau = C \theta / (4\pi a^2 | J_{th} |)$$

For our parameters, τ is about 0.4 μsec, and we expect an overshoot to about -8 volts. However, if the electron distribution has an elevated thermal tail, as is likely due to turbulence associated with the nonuniform, nonequilibrium ion distribution, the negative overshoot will be much greater.

CONCLUSIONS

Electron beams emitted from spacecraft in the ionosphere exhibit complex behavior. We have analyzed here the case of a beam emitted into an underdense plasma, with parameters appropriate to the MAIMIK rocket. The beam was emitted both along the magnetic field and across the field in an "equatorial" fashion.

The beam-emitting system exhibits oscillations at a few megahertz. These oscillations are associated with bunched return of the beam electrons and cause electron energization so that the spacecraft can achieve potentials in excess of the beam energy. At least for the field-aligned beam case, these oscillations are dipolar in character and should be observable as electromagnetic radiation. For sufficiently intense beams, the oscillation frequency is proportional to the beam current.

The dynamics of the ambient plasma is largely independent of the beam dynamics. The ambient electrons show a broad peak at their own plasma frequency and form an elongated sheath.

Even in this very underdense plasma, the relaxation of spacecraft potential following beam turn-off is rapid compared with the time for ions to thermally fill in the sheath. If the nonuniform plasma that exists during this time causes electron heating, a substantial negative overshoot of the spacecraft potential can occur.

REFERENCES

Denig, W. F., B. N. Maehlum, and K. Svenes, A review of the MAIMIK rocket experiment, (this conference, 1989).

Katz, I., G. A. Jongeward, D. E. Parks, D. L. Reasoner and C. K. Purvis, Energy broadening due to space-charge oscillations in high current electron beams, *Geophy. Res. Lett.*, *13*, 64, 1986.

Maehlum, B. N., J. Troim, N. C. Maynard, W. F. Denig, M. Friedrich, and K. M. Torkar, Studies of the electrical charging of the tethered electron accelerator mother-daughter rocket MAIMIK, *Geophy. Res. Lett.*, *15*, 725, 1988.

Parker, L. W., and B. L. Murphy, Potential buildup on electron-emitting ionospheric satellites, *J. Geophys. Res.*, *72*, 1631, 1967.

Reasoner, D. L., J. L Burch, and T. Obayashi, Analysis of electron spectra produced by SEPAC electron beams on Spacelab-1 - evidence for strong beam plasma interactions, *EOS, Trans. Am. Geophys Union*, *65*, 1042, 1984.

$\vec{B}$ ⊙

$\vec{B}$ ⊙

(a) Beam Across $\vec{B}$

(b) Beam Along $\vec{B}$
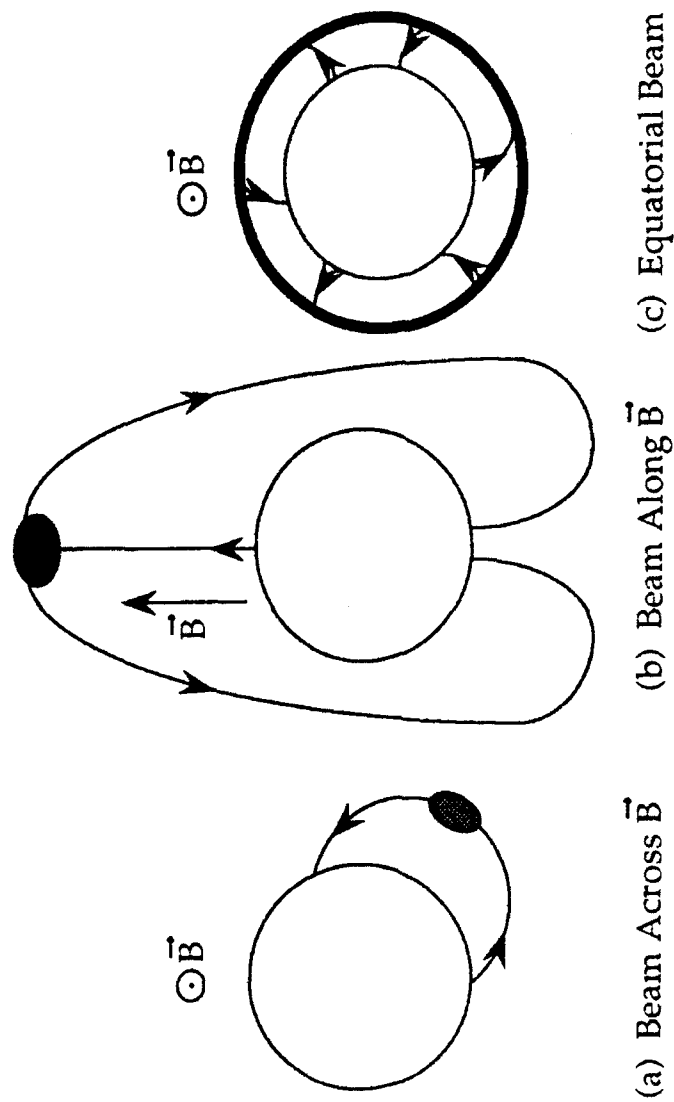
(c) Equatorial Beam

Fig. 1. Three beam configurations from a spherical spacecraft: (a) physical beam across magnetic field; (b) physical beam along magnetic field; (c) "equatorial" beam across magnetic field.
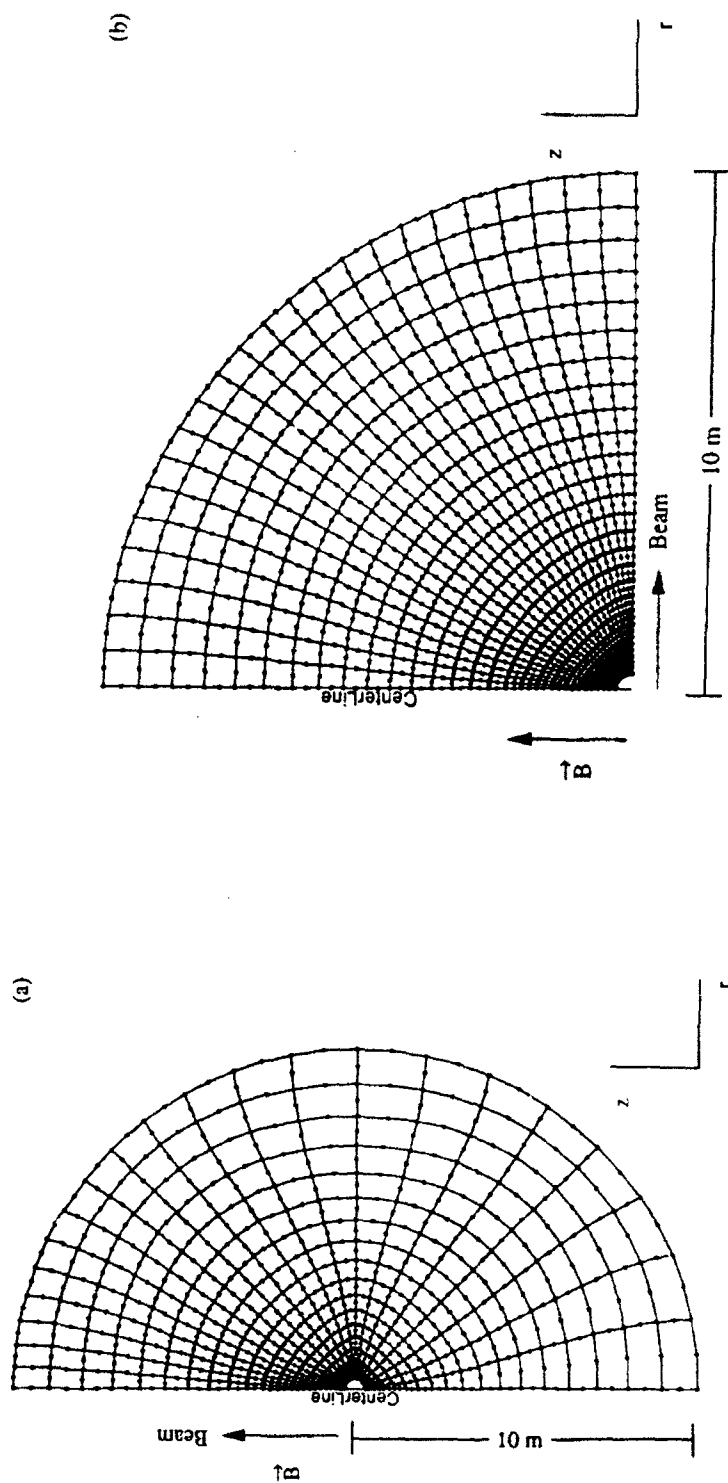
Fig. 2. Axisymmetric grids of biquadratic elements used in these calculations: (a) grid used for calculation of beam along magnetic field (fig. 1a); (b) grid used for calculation of "equatorial" beam (fig. 1b) using mirror plane.
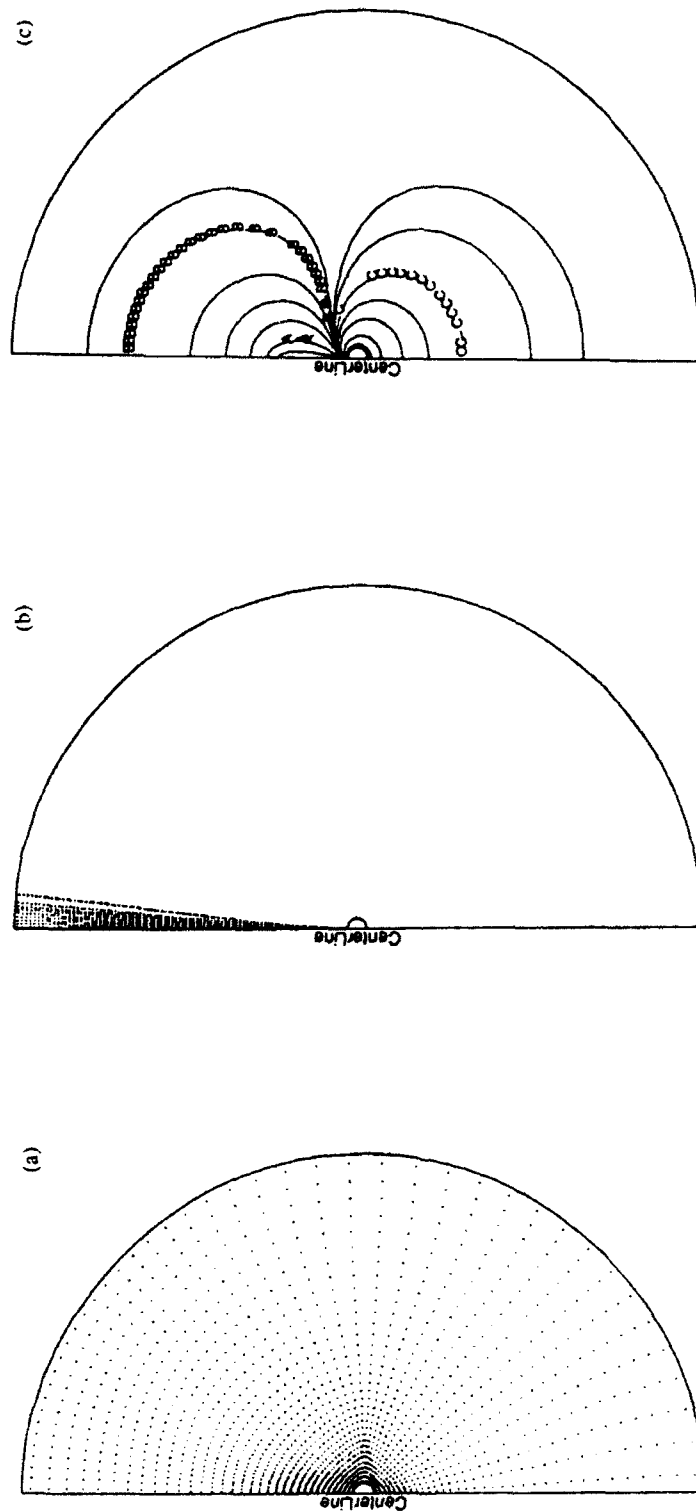
Figure 3. (a) Initial electron or ion macroparticles in grid of fig. 2a; (b) beam electron macroparticles at 0.2 µsec; (c) dipolar potential at 0.04 µsec, with contours marked A, B, and C at -50, -2, and +5 volts.
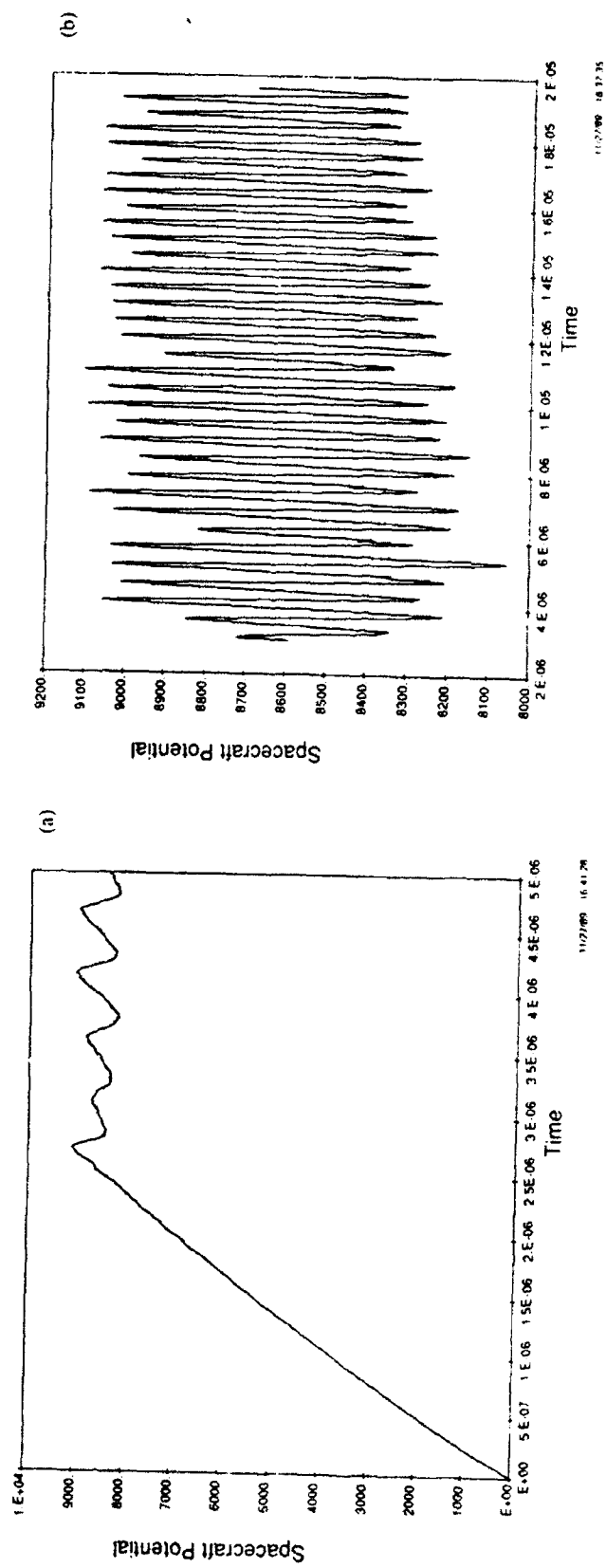
Fig. 4.   Time dependence of spacecraft potential for field-aligned beam: (a) initial transient; (b) persistent oscillations.

474
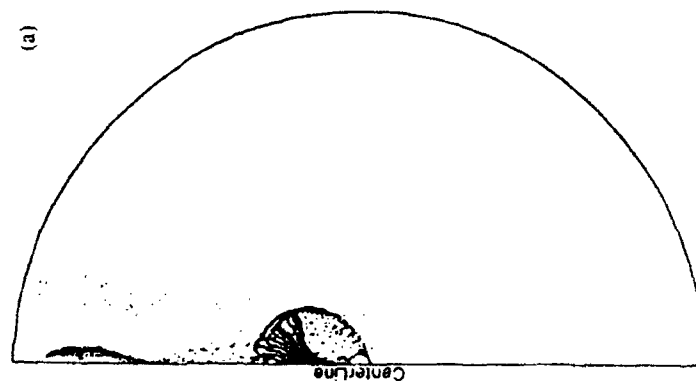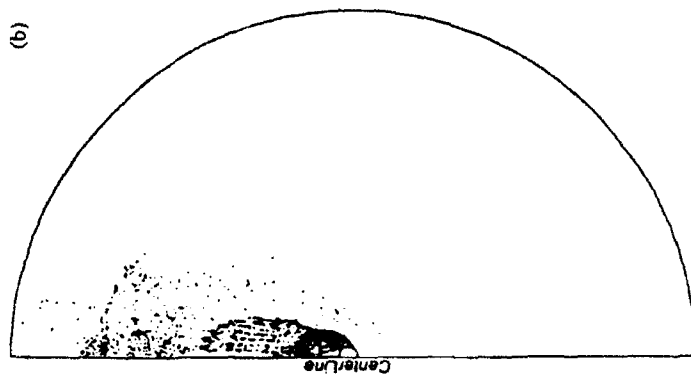
Fig. 5.   Beam conformation (a) at high potential; (b) at low potential.
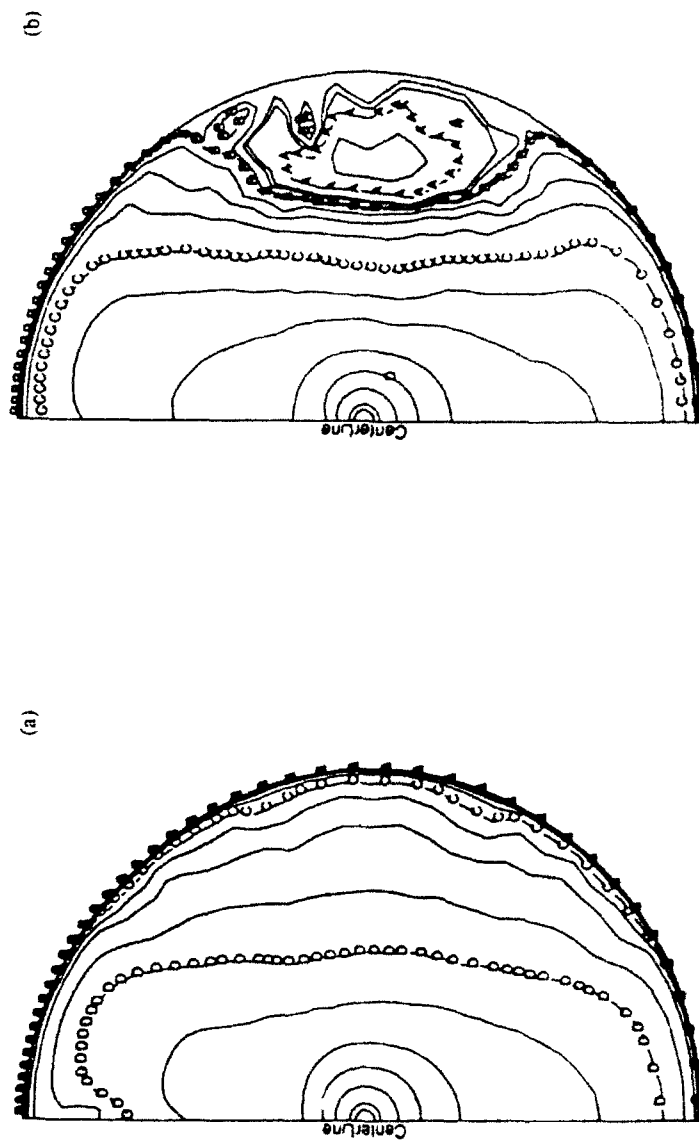
Fig. 6.   Electrostatic potential structure (logarithmically spaced contours) about the spacecraft (a) without and (b) with negative potential well in the cross-field region.
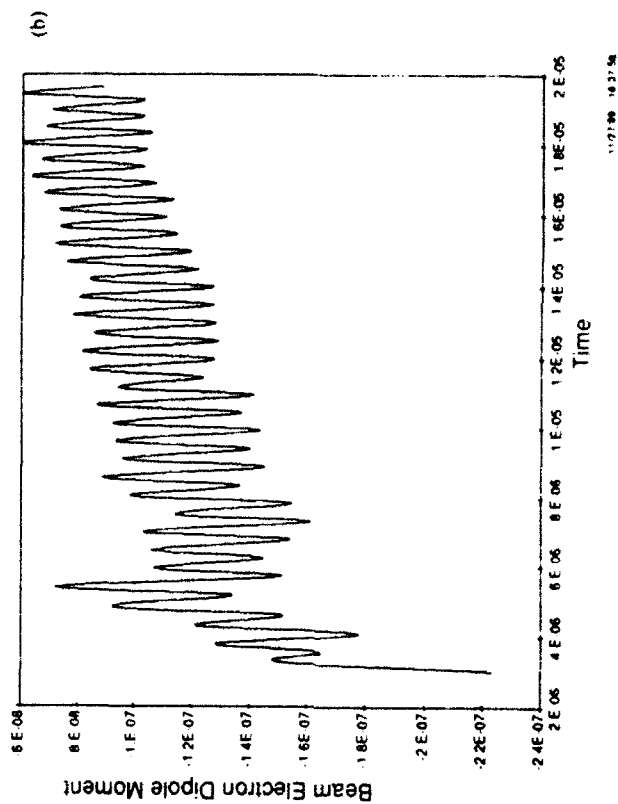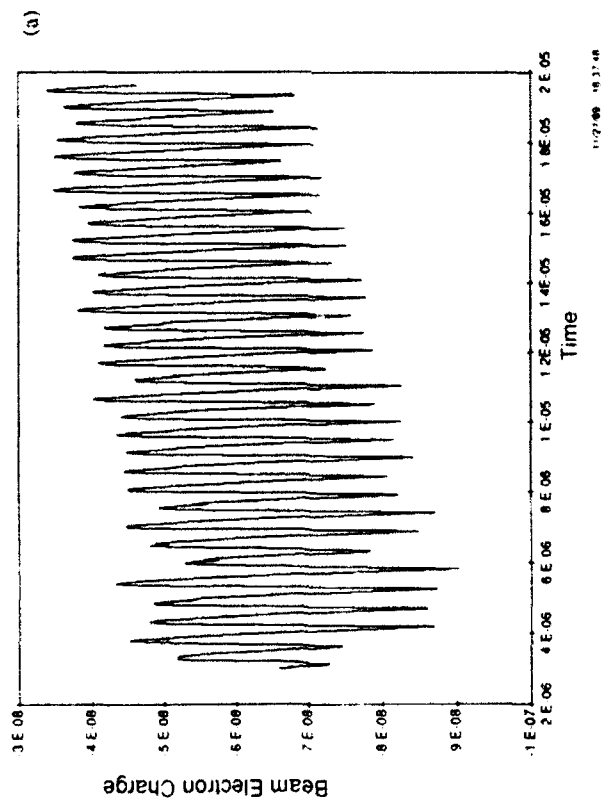
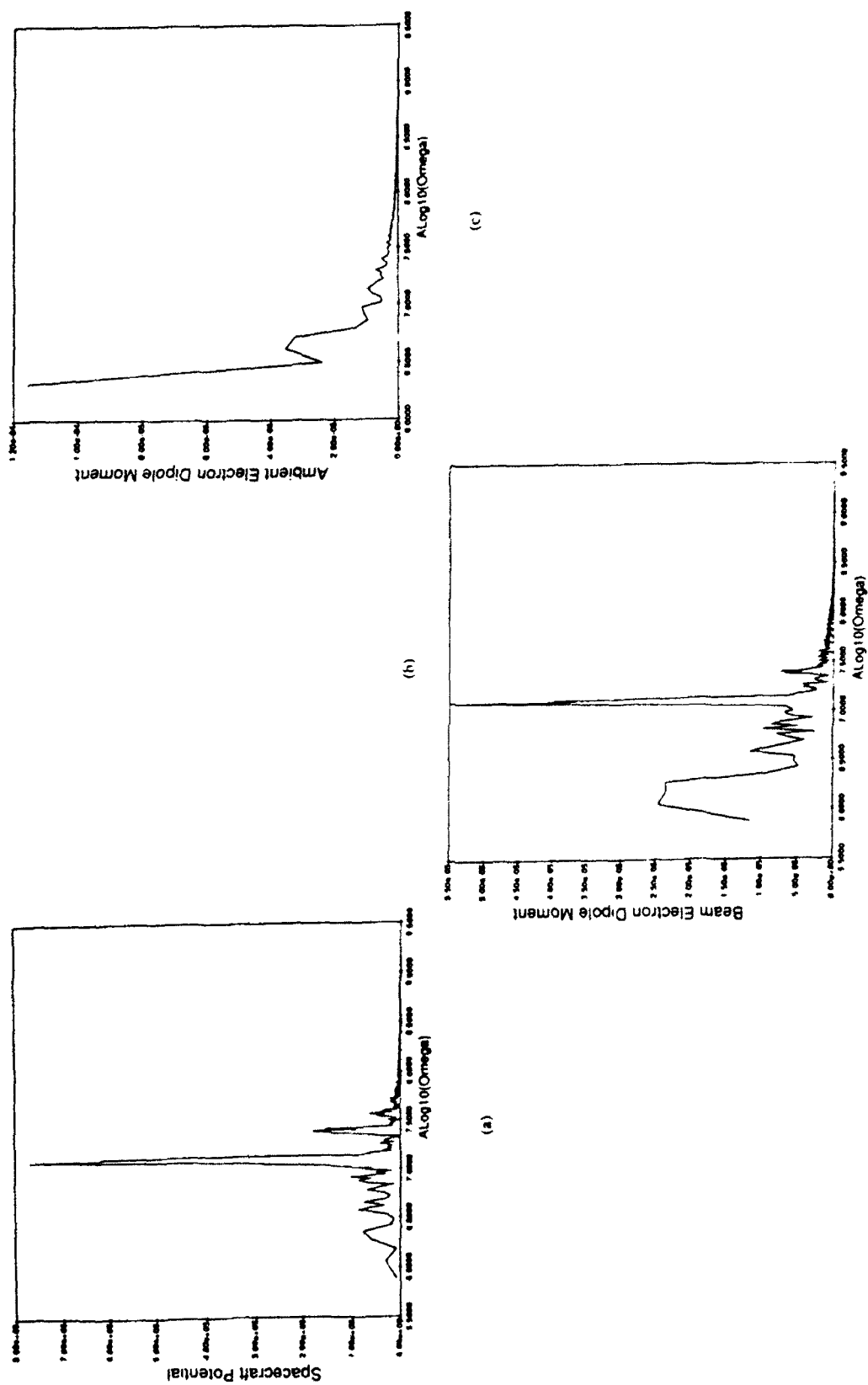Fig. 7. Time dependence of (a) beam electron charge; and (b) beam electron dipole moment.

477

Fig. 8. Spectral analysis of (a) spacecraft potential; (b) beam electron dipole moment; (c) ambient electron dipole moment.
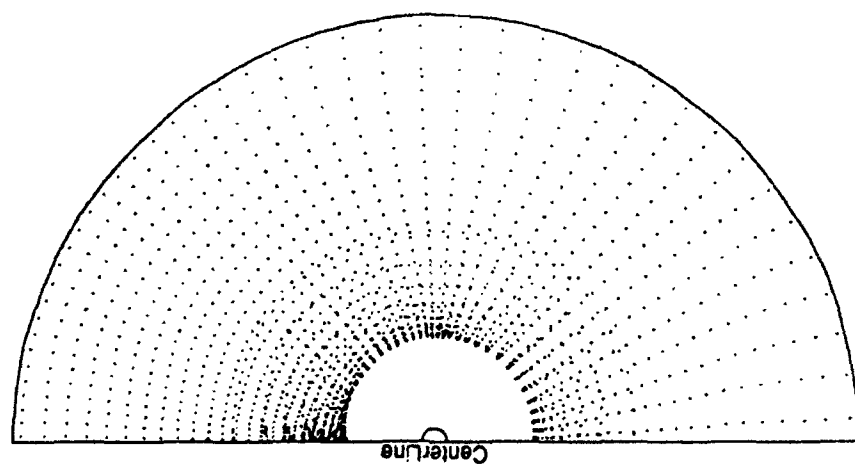
478

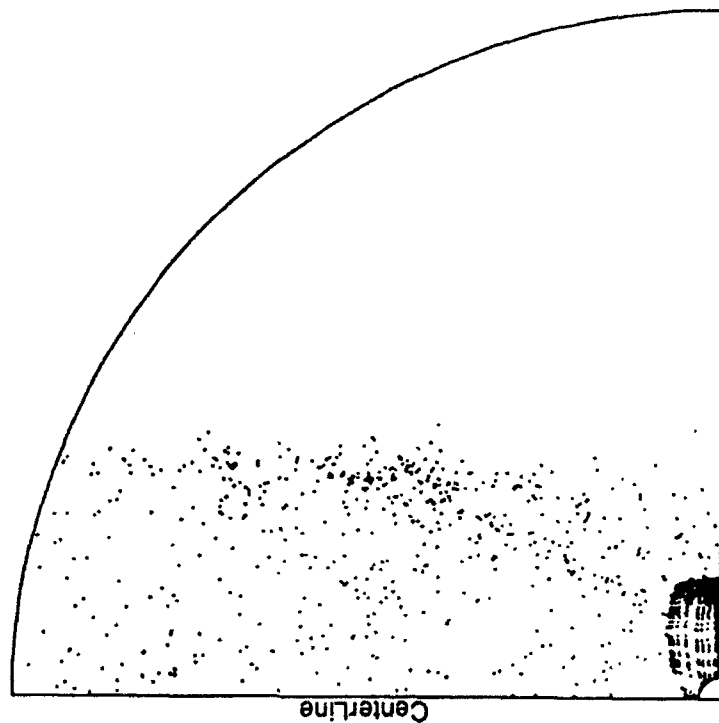Fig. 9. Ion positions after 20 μsec.

Fig. 10. Beam electrons at conclusion of equatorial beam calculation, showing circulating beam of unscattered electrons, and field aligned column of scattered electrons.
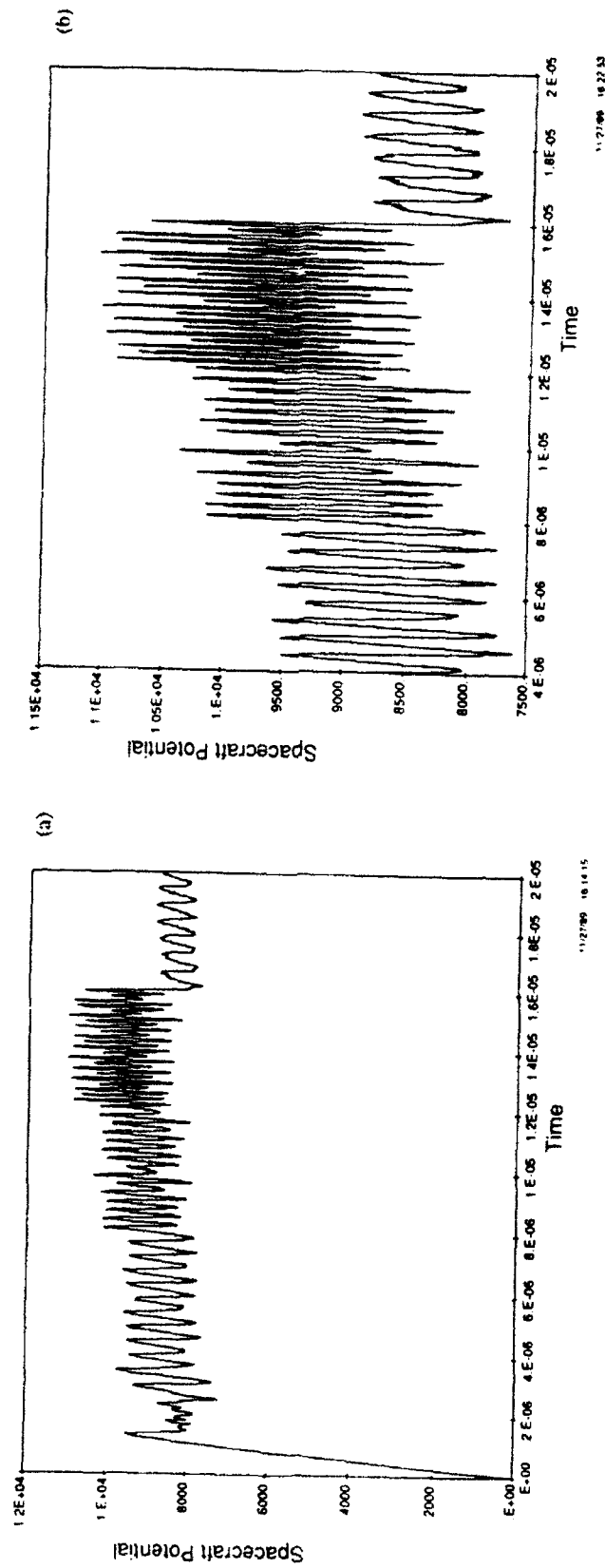
Fig. 11. Time dependence of spacecraft potential for equatorial beam: (a) initial transient; (b) persistent, current-dependent oscillations.
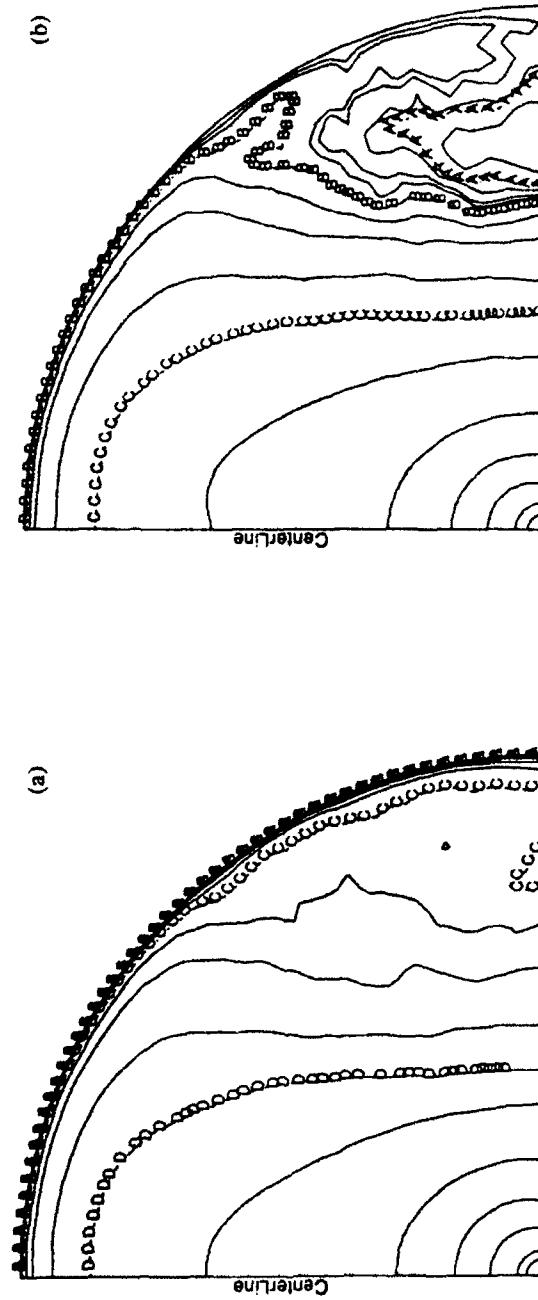
481

Fig. 12. Electrostatic potential structure (logarithmically spaced contours) about the spacecraft (a) without and (b) with negative potential we'l in the cross-field region.
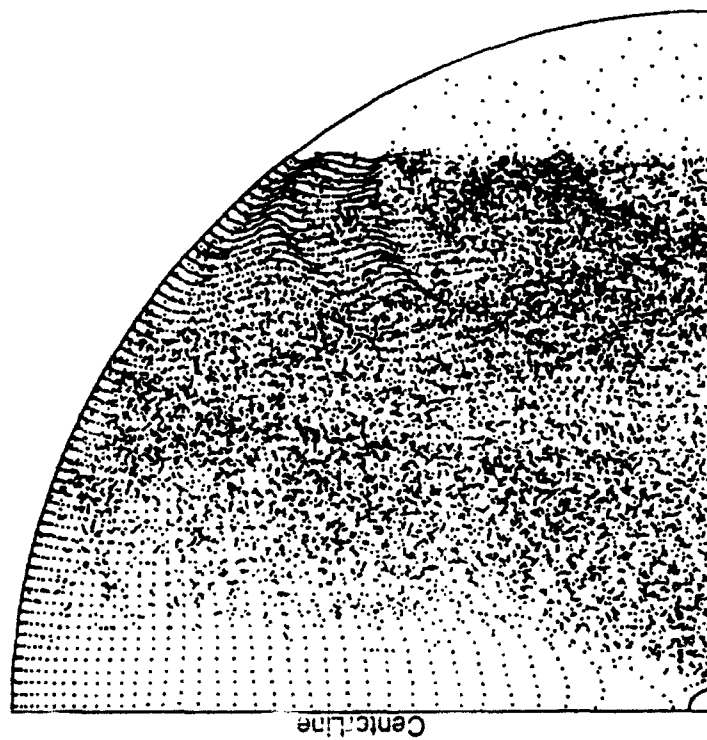
Fig. 13. Ambient electron macroparticles, showing low axial density and high cross-field density.
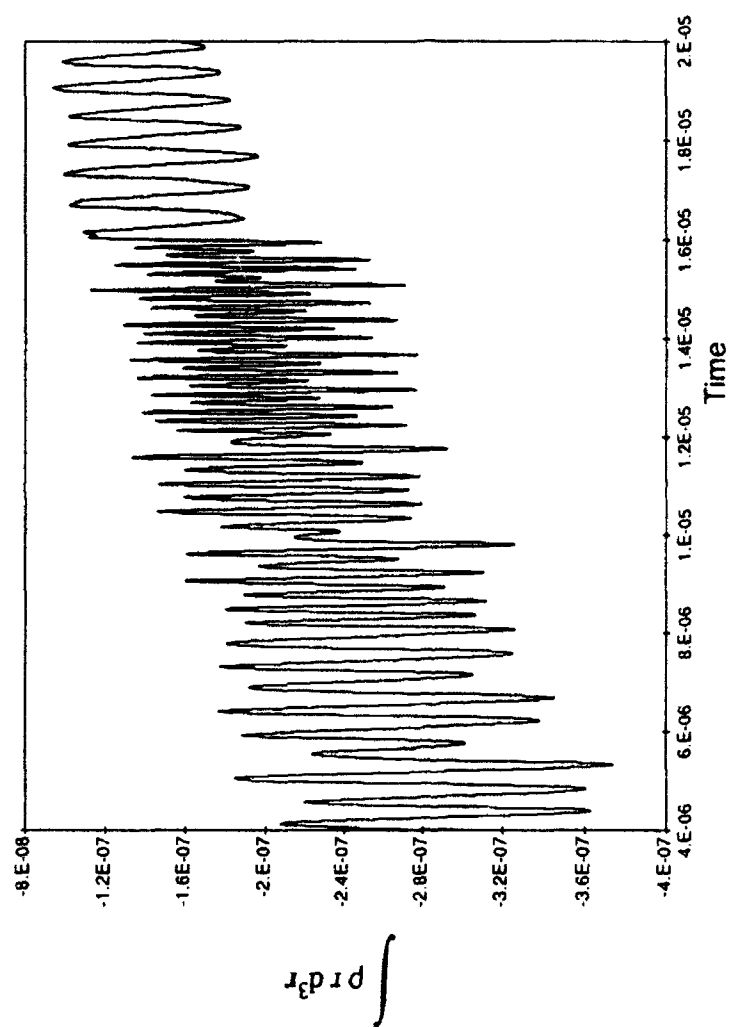
Centerline

Fig. 14. The quantity $\int \rho\, r\, d^3r$ for the beam electrons, showing the lack of dependence on strong current changes.
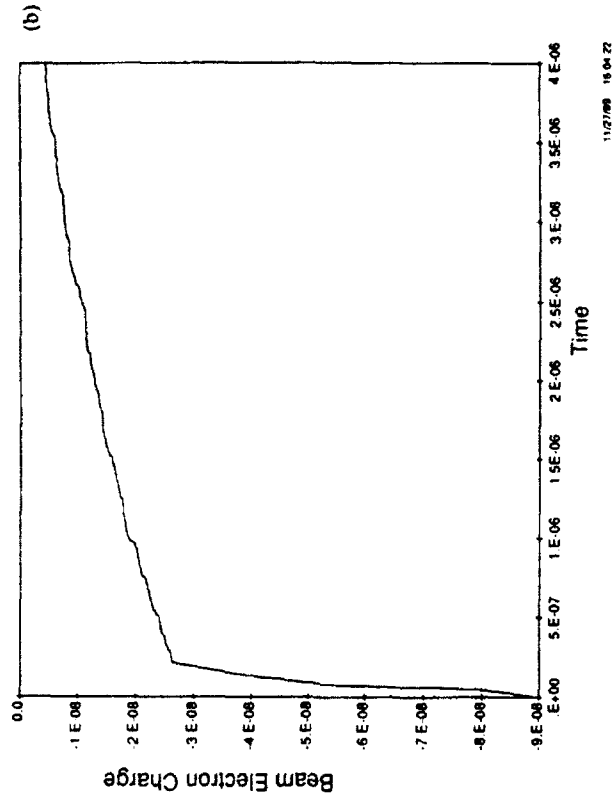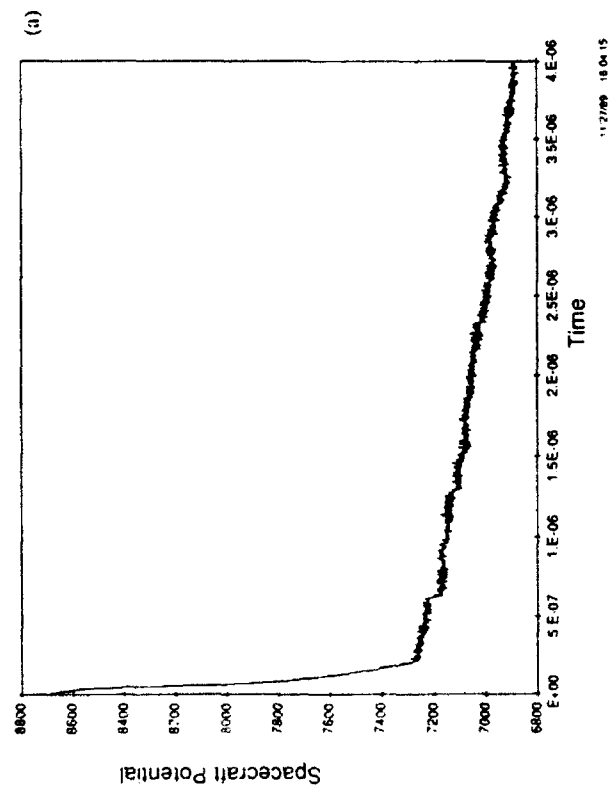
484

Fig. 15.   Behavior following beam turn-off: (a) spacecraft potential; (b) beam electron charge.

SPACECRAFT CHARGING DURING ELECTRON BEAM INJECTION AND TURN-OFF

R. M. Winglee

Department of Astrophysical, Planetary and Atmospheric Sciences

University of Colorado, Boulder, CO 80309-0391

Abstract. During electron beam injection, particularly at currents exceeding about 100 mA, the spacecraft can become positively charged with potentials as high as the beam energy being observed. After beam turnoff, the spacecraft can become negatively charged. Two-dimensional electromagnetic particle simulations are used to investigate the characteristics of the spacecraft charging, particle acceleration and wave emissions during beam injection and turnoff. It is shown that during beam injection, the beam current is neutralized by a spatially separate return-current region extending several tens of meters from the beam region, with the currents being closed across the field lines by the perpendicular acceleration of ambient plasma ions into the beam region. At beam turn-off, this current system reverses, leading to (i) extended electron collection by the spacecraft near the beam region, (ii) preferential ion collection by sections of the spacecraft magnetically connected to the initial return current regions and (iii) the creation of hot plasma extending well into the return current regions. Collisional effects are shown to reduced the magnitude of the potential swing, as well as the extent of the heating of the ambient plasma.

486

1. Introduction

During electron beam injection, the spacecraft can become charged up to about the beam energy, particularly for currents exceeding about 100 mA and low plasma densities. Examples of experiments where such strong charging is observed include the SEPAC experiment on the Spacelab 1 [*Obayashi et al.*, 1985; *Sasaki et al.*, 1986] and the recent sounding rocket experiments CHARGE 2 and ECHO 7 experiments [*Banks et al.*, 1988; *Winckler et al.*, 1989]. This spacecraft charging is important as it can modify the properties of the beam as it tries to propagate away from the spacecraft, thereby modifying the beam-plasma interaction. The level of spacecraft charging is also dependent on the presence of neutrals in the near vicinity of the spacecraft. Observations showing large reductions in spacecraft potential during neutral thruster firings have been reported by *Banks et al.* [1988], *Gurnett et al.* [1988], *Gilchrist et al.* [1989] and *Winckler et al.* [1989].

Several particle simulations have been performed in an effort to understand some of the above observations and the properties of the beam-plasma interaction [e.g., *Winglee and Pritchett*, 1987, 1988; *Pritchett and Winglee*, 1988]. These initial simulations were electrostatic and collisionless with emphasis on determining the conditions under which the beam can escape with minimum distortion and the properties of the return currents and electrostatic wave emissions. More recently, electromagnetic [*Winglee and Kellogg*, 1989] and collisional [*Winglee*, 1989; *Chin et al.*, 1989] effects have been included to allow more complete modelling of the induced wave emissions and the modelling of the injection of neutrals via thruster firings. These simulations were able to account for some of the observed properties of the beam and wave emissions during ECHO 7.

The above observations and simulations have concentrated primarily on beam injection. To date, processes induced as the beam is turned off have received little attention. Such processes are nevertheless important as they can modify the

spacecraft charging and the local plasma environment which can in turn affect the beam-plasma interaction and spacecraft charging during subsequent beam injections. Such effects are of particular importance during pulsed beam injection. The purpose of this paper is to investigate the properties of the beam and spacecraft charging during electron beam injection and turn-off in both collisionless and collisional plasmas, using two-dimensional (three velocity) electromagnetic particle simulations.

In section 2, the simulation model is described. In section 3, the particle dynamics for injection into an essentially collisionless plasma is discussed. Differences in the particle dynamics due to the presence high neutral densities are discussed in section 4. The spacecraft potential and induced wave fields for injection into collisionless and collisional plasmas are presented in section 5. A summary of results is given in section 6.

2. Simulation Model

In order to investigate the beam-plasma interaction and spacecraft charging during beam injection and turn-off, the Beams-In-Geospace including Electromagnetic Radiation code (BIGER) which is two-dimensional (three velocity) relativistic electromagnetic particle simulations with collisional processes included was utilized [cf., *Winglee*, 1989]. A schematic of the simulation model is shown in Figure 1. The spacecraft is indicated by the rectangle and immersed in a plasma of uniform density which is typically 10^4 – 10^5 cm^{-3} for most active beam experiments. The spacecraft size is taken to be $4\Delta \times 32\Delta$, with the system size being $512\Delta \times 128\Delta$, where Δ is two plasma Debye length (i.e., $2v_{Tc}/\omega_{pe}$). For the parameters considered here $\Delta \simeq 10$–20 cm. The beam is injected at 45 degrees to the ambient magnetic field (which is in the x direction) with a parallel velocity 10 times the ambient electron thermal velocity (i.e., $v_{xb} = 10v_{Tc} = 0.17c$) and a beam width of 2Δ. This beam
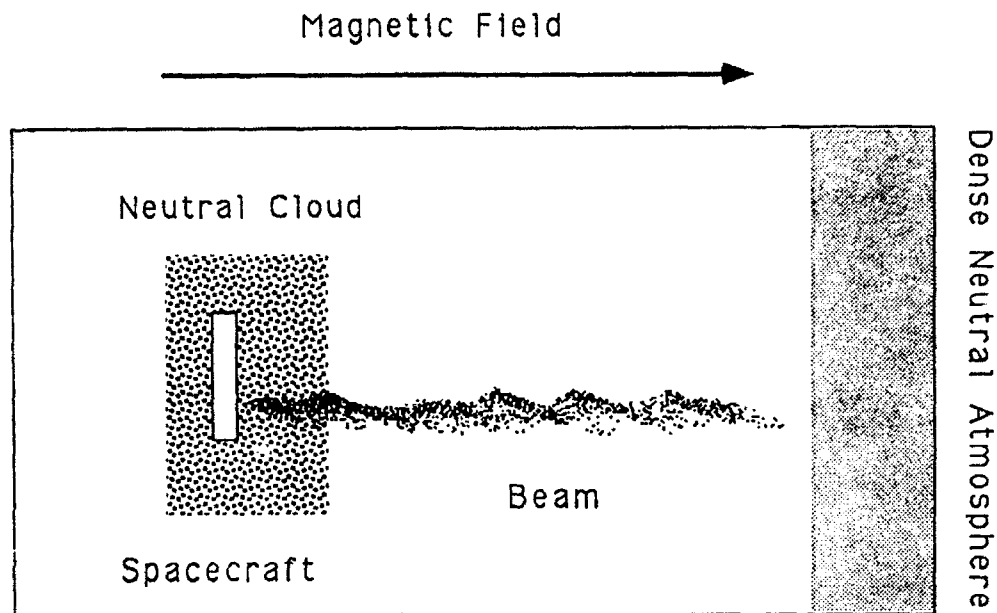
Figure 1. Schematic diagram of the simulation model.

width is the minimum beam width that can be easily simulated and represents some initial expansion of the beam within the first few tens of centimeters, due to the opening or cone angle of the gun and/or to beam-plasma interactions. As a result of the large beam width assumed in the simulations, the beam density relative to the ambient density assumed to be 4 with the total beam current being similar to the maximum beam current emitted during CHARGE 2, i.e. about 100 mA. The ratio of the electron cyclotron frequency Ω_e is assumed to be equal to ω_{pe}, similar to the plasma conditions during CHARGE 2. These parameters are also similar to those used in previous simulations by *Winglee and Pritchett* [1988] and *Winglee* [1989] except that the relative spacecraft size is twice as large, which reduces the amount of spacecraft charging and allows more of the beam to propagate outwards.

The effects of neutrals and their ionization are incorporated into the simulations as follows. A region of neutrals with a given density is specified on the simulation grid. These neutrals (assumed to be molecular nitrogen) can be placed

around the mother or daughter. A dense neutral region is also placed near the right hand boundary representing the lower ionosphere. The electrons and ions are subjected to elastic scattering collisions with cross-sections as given by *Strickland et al.* [1976]. In addition to these collisions, energetic electrons ($\gtrsim$ 100 eV) are subject to ionizing (inelastic) collisions. The ionization cross-section as given by *Banks and Kockarts* [1973] has the feature that it increases rapidly once the electron energy is above a few tens of eV, reaching a maximum at about 100 eV and then decreasing approximately inversely proportional to v. For numerical simplicity, the rise in ionization cross-section at low energies is approximated by a sharp cutoff at 100 eV (i.e., $v \simeq 3.3v_{T_e}$). This cutoff excludes ionization processes by nonaccelerated ambient plasma electrons which are assumed to be in equilibrium with the ambient neutrals. This cutoff has the effect of underestimating the number of low energy electrons produced by ionizing collisions. This approximation is not restrictive since *these low energy* electrons have a large scattering cross-section which reduces their mobility and hence their contributions to any return currents.

All electrons with higher energies above 100 eV are then binned in levels of speeds relative to $3.3v_{T_e}$, with the cross-section decreasing inversely with bin number. The required number of (primary) electrons determined from the collision cross-section is then chosen randomly from each bin. The velocity of the primary is reduced by about a third and a secondary electron and ion are added to the system with the secondary electron having a velocity one third of the initial velocity of the primary with a differential scattering cross-section as given by *Mott and Massey* [1965].

In the following there is always a neutral cloud placed around the spacecraft. In the first case, the collision period is long compared with the duration of the beam injection ($\nu = 1.25 \times 10^{-3}\omega_{pb}$ where ω_{pb} is the beam plasma frequency which corresponds to a neutral density $n_n \simeq 6 \times 10^{10}$ cm^{-3}) and is hereafter referred to as

490

"collisionless". In the second case, hereafter referred to as "collisional" the collision period is compared to the beam injection period, i.e $\nu = 2 \times 10^{-2} \omega_{pb}$, $n_n \simeq 1 \times 10^{12}$ cm^{-3}. In both cases, beam injection at constant current occurs during the period $0 \leq \omega_{pb} t \leq 12$J.

3. Particle Dynamics For Beam Injection into a Collisionless Plasma

Particle Dynamics : Beam Injection

.⟨≈⟩. Beam Electrons
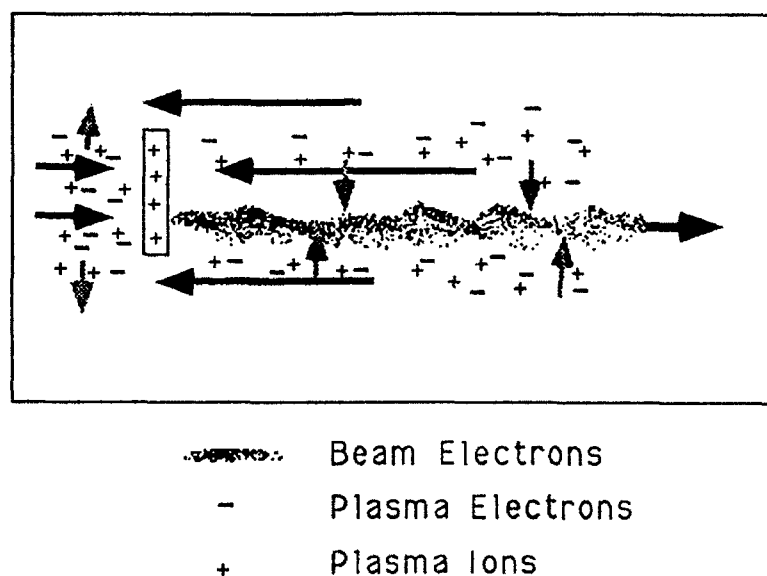−   Plasma Electrons
+   Plasma Ions

Figure 2. Schematic of the beam-plasma interaction during beam injection.

The dynamics of the beam-plasma interaction when the beam is on is shown schematically in Figure 2. The figure is derived from previous simulations results of *Pritchett and Winglee* [1987] and *Winglee and Pritchett* [1988]. During beam injection, the spacecraft becomes positively charged and return currents flow along the regions adjacent to the beam region, as well as from behind the spacecraft. Because the beam and return currents are spatially separate, plasma ions are accelerated across the field lines into the beam region to produce current closure. As shown in the following, after beam turn-off, the spacecraft can become negatively charged

due to an overshoot of return current into the spacecraft and the beam region can become positively charged due to the outflow of beam electrons. As a result, the electric fields and associated current system reverses, leading to strong deceleration of beam particles in the trailing edge of the pulse, and the formation of high energy tails in the ambient plasma in the return-current regions.

The evolution of the beam phase space is shown in Figure 3. At the earliest of times (Figure 3a), the ambient plasma is unable to respond to the beam injection and a virtual cathode or stagnation region develops, with many of the beam particles being reflected (i.e., attaining negative velocities) toward the spacecraft. At later times when the ambient plasma is able to respond to the injection and reduce the spacecraft charging (Figures 3b and c), a larger fraction of the beam is able to propagate outwards, although it is strongly distorted, as evidenced by large velocity spread at $x/\Delta \gtrsim 150$ and the vortex structure (or space-charge oscillation) at $x/\Delta \simeq 140$.

At beam turn-off, the outflowing beam electrons are no longer replaced by freshly injected electrons, so that a space-charge field is induced between these electrons and the ions left behind in the beam region. This space-charge field inhibits further outflow of beam electrons and in fact prevents some of the beam electrons emitted in the trailing half of the pulse from escaping from the near environment of the spacecraft (Figures 3d-f). Moreover, many of the beam electrons continue to overshoot into the spacecraft which causes, in part, the negative charging of the spacecraft.

At later times (Figures 3c and f), the energy of the inflowing beams electrons is seen to decrease. Note their maximum speed is rippled in space due to their interaction with induced wave turbulence and this rippling is convected back to the spacecraft. As a result, the energy of the electrons approaching the spacecraft varies in time, so that during periods where low energy electrons are arriving at

492
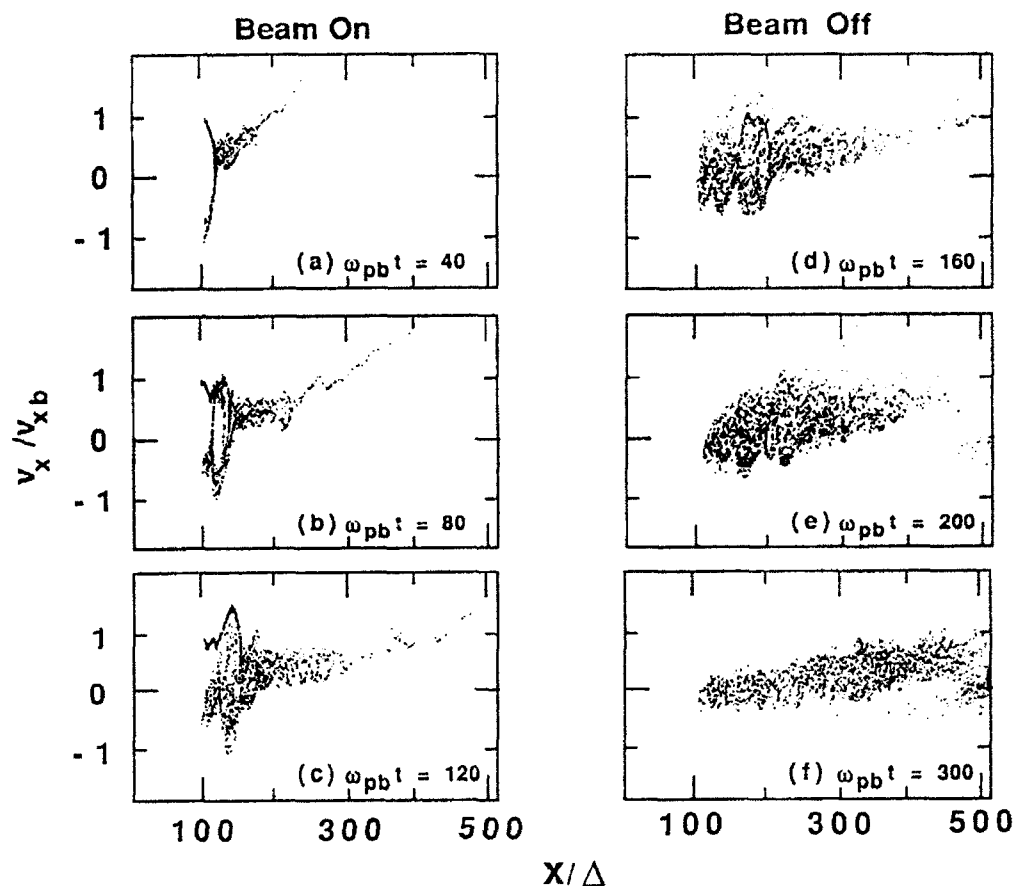
Figure 3. The $v_x - x$ phase space of the beam electrons

the spacecraft, its potential is able to reflect the electrons and slow its collection of negative charge. However, when the higher energy electrons arrive at the spacecraft tuat they are not reflected and the negative charge on the spacecraft charging can increase. Thus, the effect of the wave turbulence and its convection toward the spacecraft, causes the spacecraft potential to fluctuate and to remain at a net negative value over a much longer period than it would to a simple negative charged body to discharge (see section 5).

The properties of the plasma electrons, including the return-current electrons, is illustrated in Figure 4 which shows their field-aligned velocity v_x for a cut across the field lines between 60 and 180 Δ in front of the spacecraft. The
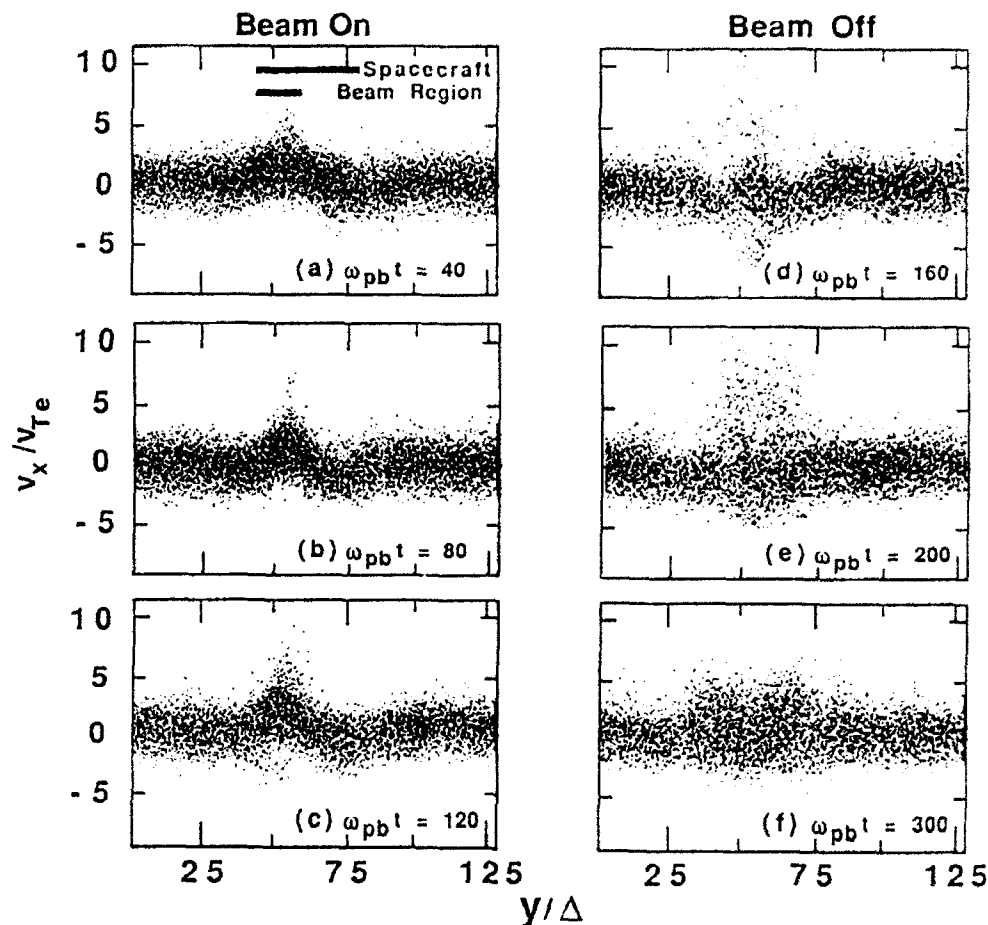
Figure 4. The $v_x - y$ phase space of the plasma electrons showing a cut across the field lines from 60 – 180 Δ in front of the spacecraft. Positive velocities indicate flow away from the spacecraft and negative velocities represent flows toward the spacecraft. The positions of the beam region and spacecraft are indicated in (a).

positions of the beam and spacecraft are indicated by the dotted and solid lines, respectively. During beam injection, electrons in the beam region are accelerated outwards reaching maximum velocities approximately equal to the beam parallel velocity. On adjacent field lines, electrons are accelerated toward the spacecraft (negative velocities), with those electrons magnetically connected to the spacecraft having the highest negative velocities of about -4 $v_{Te} = -0.4v_{xb}$ (Figure 4c).

At beam turnoff, these return current electrons continue to flow into the spacecraft (Figure 4d) until it is sufficiently negatively charged so that it reflects these electrons and eventually they attain positive velocities (Figures 4e and f). In addition, with the reversal of the current, those electrons in the return current regions with positive velocities at beam turn-off are seen to be accelerated to moderately high velocities ($v \gtrsim 5v_{Te}$), producing a hot electron region well outside the initial beam region.

Within the beam region, the velocity of many of the electrons is seen to reverse after beam turn-off, similar to the beam electrons. The speed of these electrons tends to be much greater than those of the return-current electrons, primarily due to (i) the large potential needed to stop the outflow of the beam electrons and (ii) the large amplitude turbulence excited by the beam electrons. Due to their relatively high velocity, there is a net flow into the spacecraft well, after the flow in the return-current regions have ceased (Figure 4f).

The ion motion across the field lines is illustrated in Figure 5 which shows the ion perpendicular velocity v_y for the same region as in Figure 4. The motion into the beam region during injection is seen as increase in v_y for ions below the beam region (i.e., small y) and negative increase for those ions above the beam region (i.e., large y; Figures 5a–c). The energy attained by these ions is comparable to the return-current electrons.

At beam turnoff, the beam region develops a positive charge excess due to the outflow of beam electrons, as discussed above. This change in sign causes the electric field driving the cross-field ion motion to reverse. As a consequence, the ions that were beginning to enter the beam region are reflected whereas, the ions which are near the beam center at turn-off are accelerated outwards (Figures 5e and f). This latter effect causes further acceleration of some of the ions up to energies comparable to the beam energy. These energetic ions continue outward
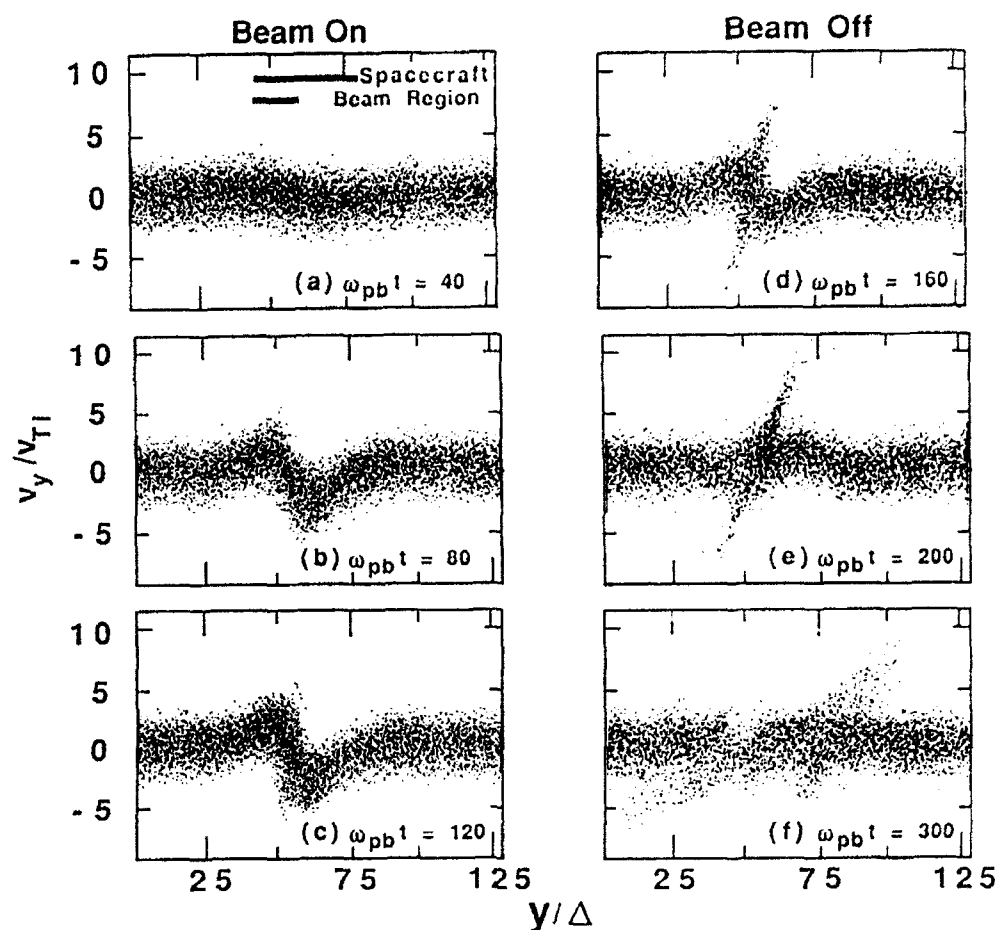
Figure 5. The $v_y - y$ phase space of the plasma ions for the same region as Figure 4.

into the return current regions, creating a hot population of ions well outside the beam region. The presence of such an extended region of hot plasma is consistent with observations from the Echo series [*Arnoldy et al.*, 1985; *Winckler et al.*, 1986, 1989].

The above properties of the induced plasma flows at beam turn-off are shown schematically in Figure 6. These flows are essentially a reversal of those during beam injection. However, as shown above, some plasma which is moving in the same

Particle Dynamics : Beam Turn-Off
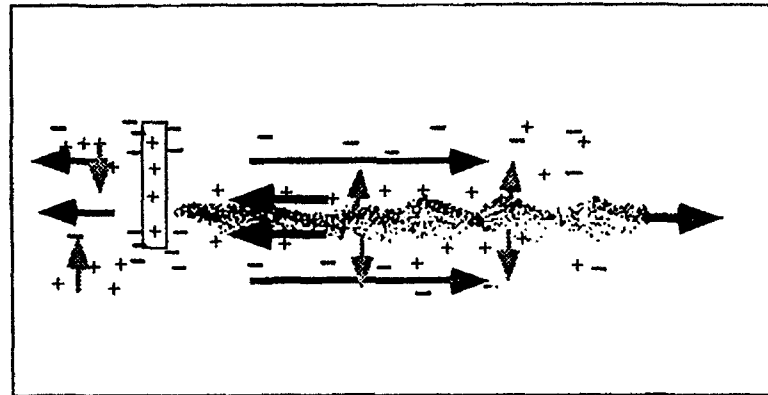
Figure 6. Schematic of the beam-plasma interaction during beam turn-off.

direction as the field reversal can attain high energies leading to the appearance of hot plasma regions well outside the beam region.

4. Collisional Effects

Figure 7 illustrates the change in the characteristics of the electron dynamics in the presence of high neutral densities which shows the beam and plasma electron phase spaces starting at the end of beam injection. Due to the choice of a relatively low charging-beam configuration and short period of beam injection, there is little difference in the phase spaces during injection (Figures 7a and d), except that there is enhanced electron densities in the beam region due to beam ionization of neutrals which results in (i) a reduction in the maximum energy attained by the plasma electrons, (ii) a return current which is more closely confined to the beam region and (iii) and an enhancement of short-scale turbulence in the beam region.

At beam turn-off, the development of high speed electrons in the beam and return current regions is suppressed. This is due to scattering collisions between the low energy particles and the neutrals. In the collisionless case, the unconstrained inflow of these particles causes the negative charging of the spacecraft. In the present

497
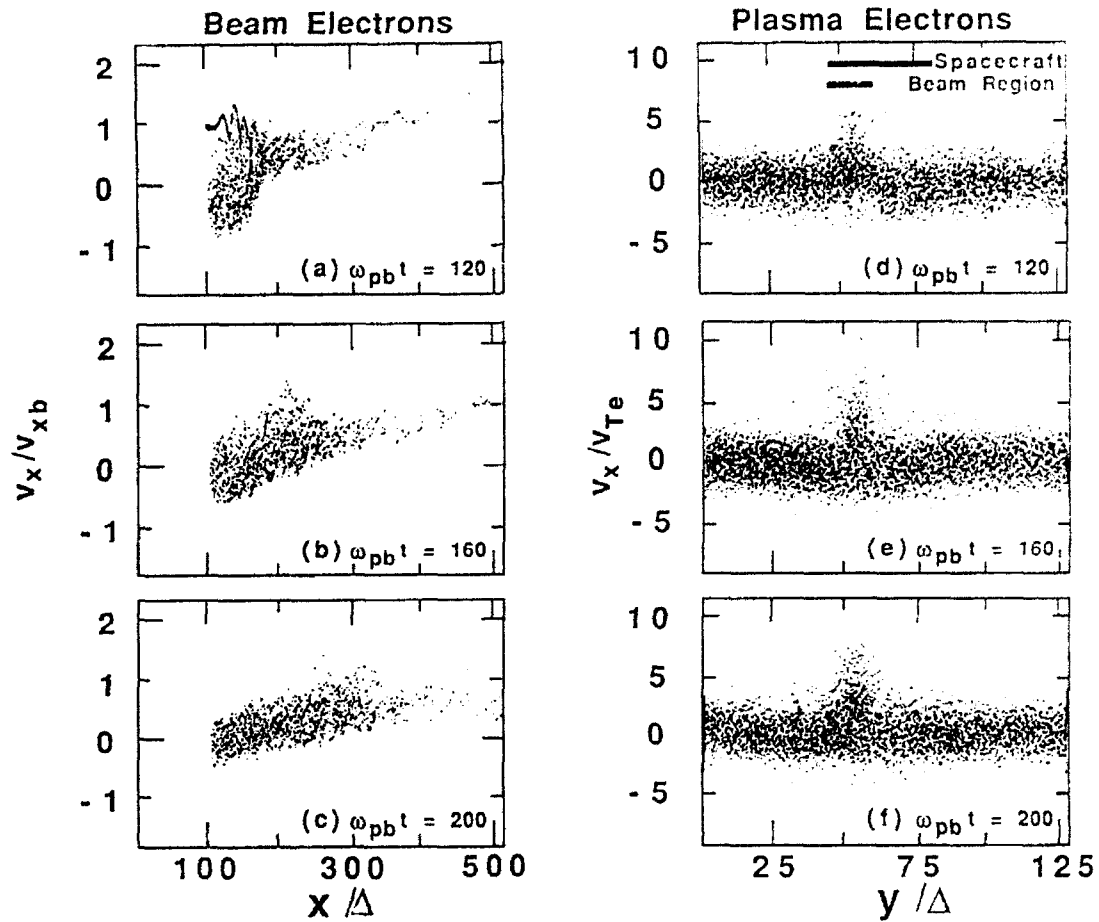
Figure 7. Electron phase spaces for the collisional case for the same regions as in Figures 3 and 4. At beam turnoff, the swing in electric field is reduced leading to a reduction in the heating of the plasma particle.

case, their flow is im· ˸ded by collisions and the large overshoot in current collection does not occur. As a result, the swing in electric field is not as large, thereby reducing the heating of the plasma at beam turn-off. This reduction in heating is seen in Figure 7e and f where the return current regions have a very much smaller temperature than in Figure 4. Note also that the region of hot ambient electrons
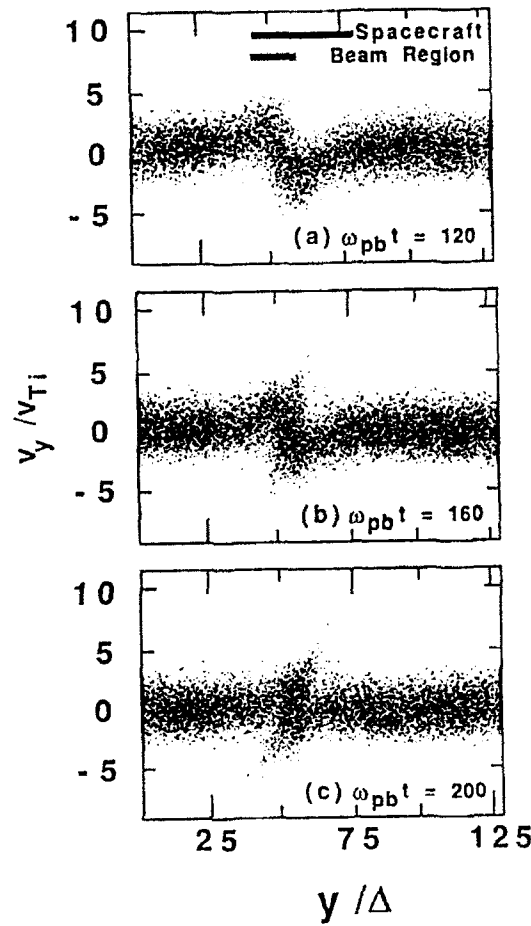
Figure 8. The ion $v_y - y$ phase space corresponding to the example in Figure 7.

is much more closely confined to the beam region compared with the collisionless case.

The reduction in the swing in the electric field at beam turn-off also suppress the acceleration of the ambient ions. This reduction is illustrated in Figure 8 which shows the ion $v_y - y$ phase space for the same times and region as in Figure 7. It is seen that the overall evolution is similar, with the ions moving into the beam region during injection and out of the region after turnoff. However, the maximum velocity attained by the ions is about half as small. With the reduction in the ion acceleration, the ions are unable to propagate as far across the field lines (which
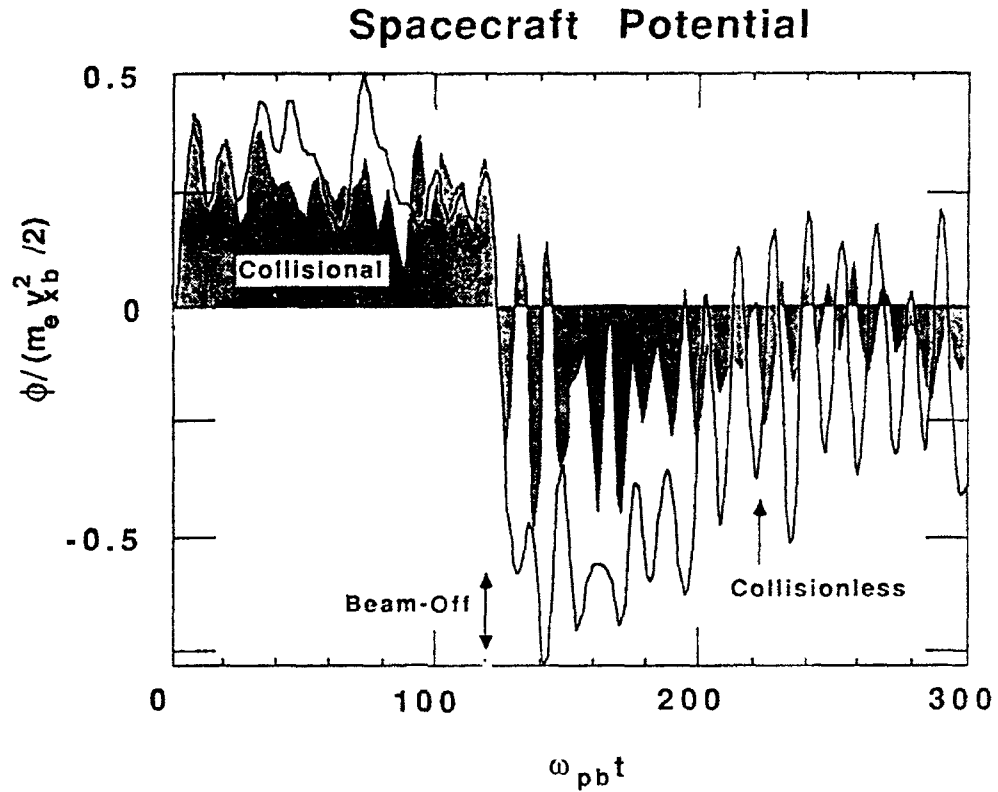
is proportional to their gyroradius and hence velocity) so that the heated region of plasma ions and electrons appears closer in to the beam region, as it is for the electrons.

5. Spacecraft Potential and Wave Emissions

Time histories of the spacecraft potential for the collisionless and collisional cases are shown in Figure 9. The potential shortly after beam injection starts ($\omega_{pb}t \lesssim 20$) is approximately the same for the two cases, since there is insufficient time for the ambient plasma to respond to the injection nor to produce substantial ionization of the neutrals. At later times ($20 \lesssim \omega_{pb}t \lesssim 120$), the potential in the collisionless case tends to increase on average, although it is modulated by large amplitude oscillations associated with the space-charge fields induced by the beam injection.

At beam turn-off, there is an overshoot of electrons into the spacecraft as discussed above. This overshoot dri.es the spacecraft potential negative reaching a peak amplitude of 75% of the parallel beam energy which is nearly twice the magnitude of the potential during beam injection. This high potential is due to the inflow of energetic beam electrons. The potential remains approximately constant until $\omega_{pb}t \simeq 200$. After this time, ion collection by the spacecraft is able to reduce the negative charging with the magnitude of the potential reaching a local minimum at $\omega_{pb}t \simeq 240$. However, with the reduction in potential, hot electrons are again able to flow into the spacecraft (section 3) so that there is an increase in the magnitude of potential at $\omega_{pb}t \gtrsim 250$ and the spacecraft is unable to reach zero potential by the end of the simulation.

In the collisional case, the potential is also modulated but to a lesser extent due to collisional damping via the neutrals. Moreover, during beam injection the overall potential is reduced. The magnitude of the reduction would be larger if the

500

Spacecraft Potential

$\phi/(m_e v_b^2/2)$

0.5

0

-0.5

Collisional

Beam-Off

Collisionless

0   100   200   300

$\omega_{pb} t$

Figure 9. Spacecraft potential for the collisionless and collisional cases. The potential in the collisionless case is modulated by large amplitude oscillation during and after beam injection. These oscillations are reduced in the collisional case and the average potential is about half as small after beam turn-off.

beam injection was longer [cf. *Winglee*, 1989]. Here the beam is turned off at the point were the instantaneous potential for the two cases are approximately equal. At beam turn-off, the spacecraft becomes negatively changed as in the collisionless case, but the average spacecraft potential is about half as small. The collisional case is also similar in that the magnitude of the potential reaches a local minimum at $\omega_{pb} t \simeq 240$, after which the spacecraft becomes negatively charged due to further electron collection.

The time histories of the current collected by the spacecraft for the collisionless and collisional cases is shown in Figure 10. The current collected is divided into two parts, that which strikes the spacecraft on the lower half of the spacecraft from which the beam is emitted and the upper half of the spacecraft which is passive. In both cases, the beam emitting portion of the spacecraft collects most of the current at early times ($\omega_{pb}t \lesssim 60$). At later times during beam injection in the collisionless case, the passive section starts to collect a higher fraction of the current since electrons in the beam region are either collected on the spacecraft at early times or are accelerated forward (section 3). For beam injections of longer duration than shown, this collection can cause depletion of the ambient plasma, leading to a decrease in return current and an increase in spacecraft charging [cf. *Winglee*, 1989]. In the collisional case, the active section of the spacecraft collects a much larger percentage of the current due to a continual creation of electrons via ionization.

At beam turnoff, both proportions of the spacecraft collect net electron charge until about $\omega_{pb}t \simeq 140$ at which time the lower beam-emitting region is able to collect some net ion charge. This initial localization of the ion current is primarily due to the fact that the bulk of the ambient ions have been drawn into the beam region by the time the beam has been turned off. The upper passive region is only able to collect net positive charge after about $\omega_{pb}t \simeq 200$, which corresponds to the outflow of ions from the beam region (Figure 5).

At about the same time as the upper section starts to collect net ion current, the lower section starts to collect net negative electron current. This reversal in charge collected is not just coincidental but a necessary feature for closing the current system. Specifically, the ions in the beam region flow outward across the field lines while the electrons in the return-current regions flow away from the spacecraft. This electron flow is in part matched by an electron flow in the beam region toward the spacecraft. These electrons which are preferentially collected by the lower
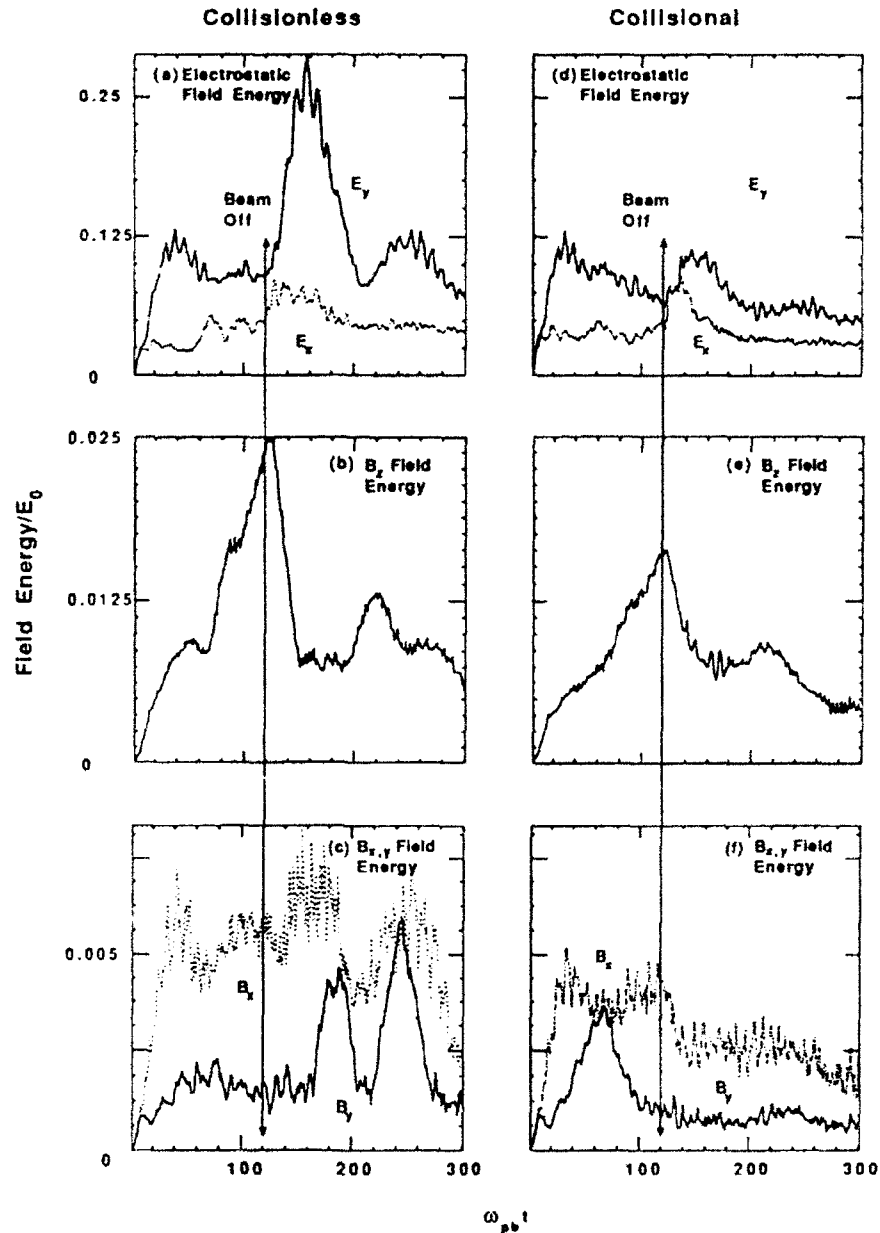
(a) Collisionless
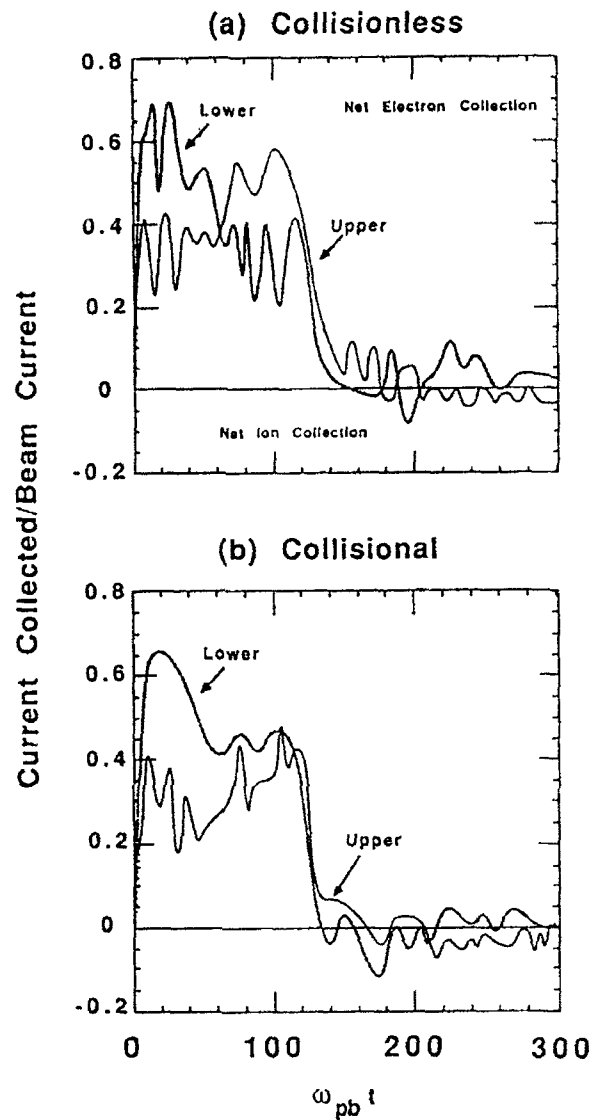
(b) Collisional

Figure 10. Time histories of the current collected by the spacecraft for the collisionless and collisional cases respectively. The dotted curves marked "lower" show the current collected by the beam-emitting lower portion of the spacecraft while the solid curve marked "upper" indicates that collected by the upper passive portion of the spacecraft where return current electrons most often strike the spacecraft.

section are then redistributed across the spacecraft (since it is an equipotential)

503

providing some cross-field current which partially offsets the plasma-ion current. In addition, ions must be collected by the spacecraft in order to reduce its charging. These ions must be collected by the passive section of the spacecraft with the skin of the spacecraft redistributing the charge to the lower active section in order to provide a balancing ion flow to match the plasma-ion current.

As indicated above, with beam turn-off there is a reversal of the fields and currents. This reversal is accompanied by a temporally increase in some of the electric field components in the system. This increase is illustrated in Figure 11 which shows the time histories of the dominant field components for the collisionless (left hand side) and collisional (right hand side) cases. The electrostatic fields are the most energetically important fields (Figures 11a and d). Shortly after beam turn-off, the energy in these fields in the collisionless case is seen to nearly double. This large increase is required in order to stop the outflow of beam particles. In the collisionless case, the parallel electrons field E_x increases by about the same amount but the increase in the perpendicular electric field E_y is substantially reduced. This reduction is due to the collisional damping of the overshoot in current collection by the spacecraft.

The magnetic field component B_z which is an indicator of the electromagnetic parallel currents in the system (middle panels) has a much slower rise time that the electrostatic fields. This slow rise time is in part due to the penetration of the current system into the plasma as well as due to the finite inductance of the plasma. At beam turn-off, the currents are reduced and the B_z fields decrease rapidly. The presence of collisions provide an extra mechanism for the dissipation of the electromagnetic currents so that the field energy in the collisional case in Figure 11e is smaller than that in Figure 11b. This is also true for the other electromagnetic field components (Figures 11c and f) which are driven by Hall currents (B_x) and by wave emissions, primarily whistlers.

Figure 11. Time histories of the field energies for the collisionless and collisional cases. The electrostatic fields are energetically the most important. The energy of these fields tend to increase temporarily after beam turn-off, although the increase in the perpendicular component is suppressed in the presence of high neutral densities.

As an example of the induced wave emissions across the system, Figure 12 shows the spectra of the perpendicular electric field taken 60Δ in front of the

505

spacecraft at points (a) centered in the beam region and (b) in the return current region 24Δ across the field lines from the beam region. Results for the collisionless case are shown on the left hand side and those for the collisional case on the right hand side. The spectra have been integrated over $200/\omega_{pb}$ on either side of beam turn-off.
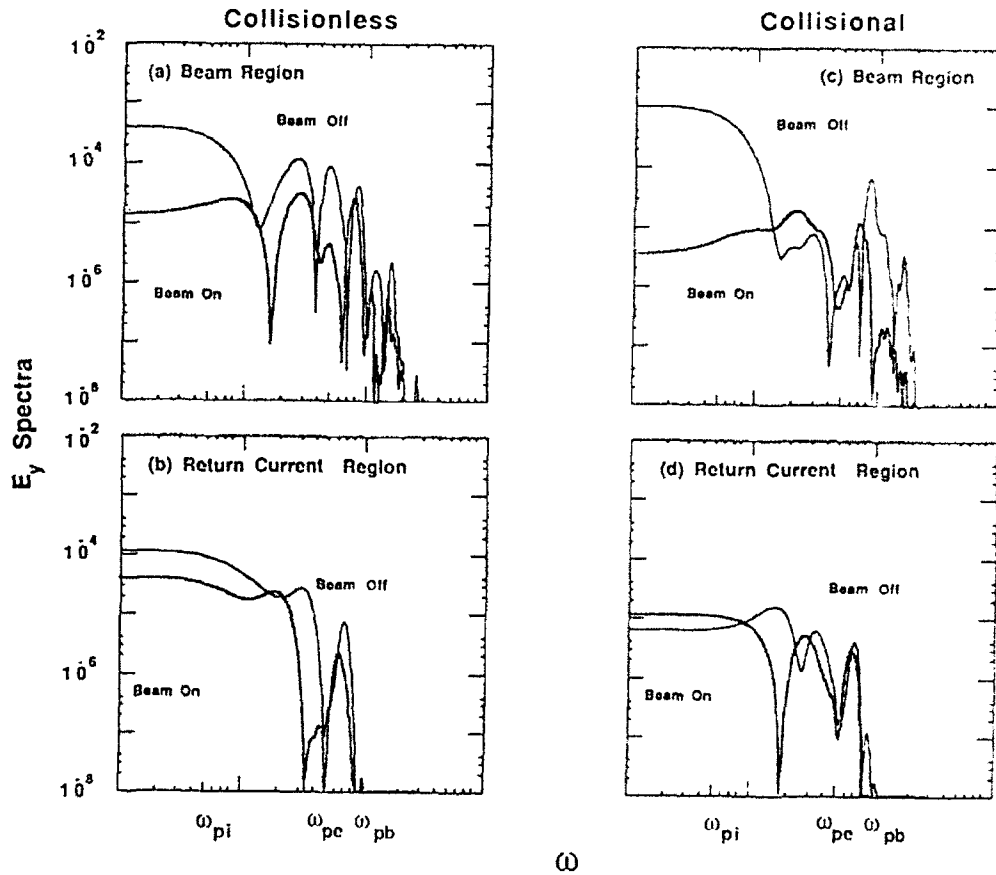
Figure 12. Wave spectra of the dominant field E_y in the beam and return-current regions during beam injection and turn-off. Results for the collisionless case are shown on the left hand side and those for the collisional case on the right hand side.

Broadband emissions are present in both the beam and return current regions, although the upper cutoff of the emissions is highest in the beam region and the waves are more intense. These waves include Lamguir, upper-hybrid and lower-hybrid waves. The spectra taken after beam turn-off for the collisionless case shows an increase over essentially the full range of frequencies in both the beam and return current regions. For the collisional case, there is primarily only an enhancement in the field strength in the beam region at the highest frequencies and in the quasi-static (low frequencies) fields, with little increase in the wave emissions in the return-current region. These differences are due to the collisional damping of the wave emissions and the closer confinement of the heated plasma to the beam region, as discussed above.

6. Summary

During electron beam injection, particularly at currents exceeding about 100 mA, the spacecraft can become positively charged with potentials as high as the beam energy being observed. After beam turnoff, the spacecraft can become negatively charged. Two-dimensional electromagnetic particle simulations are used to investigate the characteristics of the spacecraft charging, particle acceleration and wave emissions during beam injection and turnoff. It is shown that during beam injection, the beam current is neutralized by a spatially separate return current region extending several tens of meters from the beam region, with the currents being closed across the field lines by the perpendicular acceleration of ambient plasma ions in the beam region. Just after beam turnoff, the electrons in the return current regions continue to flow into the spacecraft due to their finite inertia causing the spacecraft to charge sufficiently negative to reflect these incoming electrons. Electrons in this region but travelling away from the spacecraft at beam turn-off are accelerated forward by the same electric field decelerating the incoming electrons

to energies of a few hundred eV, so that a hot plasma region appears well outside the beam region.

Within the beam region, a space-charge field develops between the outflowing beam electrons and the ions left behind. This electric field accelerates some of the ions drawn into the beam region outwards across the field lines to energies of the order of the beam energy. The same electric field causes many of the beam electrons injected near the end of the pulse to be decelerated and drawn into the spacecraft. These reflected beam electrons have sufficient energy to propagate through the spacecraft potential and reach the spacecraft so that there is negative-charge collection on the spacecraft near the beam region well after the beam is turned off. The negative charge of the spacecraft is eventually neutralized by ion flow into the spacecraft which preferentially occurs along the passive surfaces of the spacecraft magnetically connected to the original return current regions.

The presence of high neutral densities in the vicinity of the spacecraft can reduce the magnitude of the spacecraft charging during both beam injection and turn-off. This reduction is achieved by several interrelated processes. First, the ionization of the neutrals provides enhanced plasma densities for return currents into the spacecraft during beam injection and as a result the average energy of the return current electrons is reduced. Second, elastic scattering of the low-energy return-current electrons off the neutrals reduces the overshoot of electrons into the spacecraft at beam turn-off. Thirdly, there is suppression of quasi-static fields driving the currents as well as wave emissions, particularly outside the beam region. As a result of these processes, most of the heating of the ambient plasma is very much more closely confined to the beam region.

Acknowledgements.

References

Arnoldy, R. L., C. Pollock, and J. R. Winckler, The energization of electrons and ions by electron beams injected into the ionosphere, *J. Geophys. Res.*, *90*, 5197, 1985.

Banks, P. M., and G. Kockarts, *Aeronomy*, Academic Press, New York, Part A, 184, 1973

Banks, P. M., B. E. Gilchrist, T. Neubert, N. Myers, W. J. Raitt, P. R. Williamson, A. Fraser-Smith, and S. Sasaki, CHARGE-2 rocket observations of vehicle charging and charge neutralization, *Adv. Space Res.*, in press, 1989

Gilchrist, B. E., P. M. Banks, T. Neubert, P. R. Williamson, N. B. Myers, W. J. Raitt, and S. Sasaki, Observations of electron collection enhancement using neutral gas thruster jets on an isolated charged vehicle in the ionosphere, *Geophys. Res. Lett.*, in press, 1989.

Gurnett, D. A., W. S. Kurth, J. T. Steinberg, and S. D. Shawhan, Plasma wave turbulence around the shuttle: Results from the Spacelab-2 Flight, *Geophys. Res. Lett.*, *15*, 760, 1988.

Lin, C. S., J, Koga, and R. M. Winglee, Particle simulations of spacecraft charging by electron beam injection into a background of plasma and neutral gas, *Proc. Spacecraft Charging Technology Conference*, this volume, 1989.

Mott, N. F., and H. S. Massey, *The Theory of Atomic Collisions*, Oxford University Press, New York, 1965.

Obayashi, T., and 12 others, Initial results of SEPAC scientific achievement, *Earth Orient. Applic. Space Technol.*, *5*, 37, 1985.

Pritchett, P. L., and R. M. Winglee, The plasma environment during particle beam injection into space plasmas: 1. Electron beams, *J. Geophys. Res.*, *92*, 7673, 198.

Sasaki, S., N. Kawashima, K. Kuriki, M. Yanagisawa, and T. Obayashi, Vehicle charging observed in SEPAC Spacelab-1 experiment, *J. Spacecr. Rockets*, *23*, 129, 1986.

Strickland, D. J., D. L. Book, T. P. Coffey, and J. A. Fedder, Transport equation techniques for the deposition of auroral electrons, *J. Geophys. Res.*, *81*, 2755, 1976.

Winckler, J. R., Y. Abe, and K. N. Erickson, ELF waves and ion resonances produced by an electron beam emitting rocket in the ionosphere, in *Ion Acceleration in the Magnetosphere and Ionosphere*, Geophysical Monograph 38, AGU, 191, 1986.

Winckler, J. R., and 12 others, Echo 7: An electron beam experiment in the magnetosphere, *EOS, 70*, 657, 1989.

Winglee, R. M., and P. L. Pritchett, Space charge effects during the injection of dense electron beams into space plasmas, *J. Geophys. Res.*, *92*, 6114, 1987.

Winglee, R. M., and P. L. Pritchett, Comparative study of cross-field and field-aligned electron beams in active experiments, *J. Geophys. Res.*, *93*, 5823, 1988.

Winglee, R. M., and P. J. Kellogg, Electron beam injection during active experiments 1. Electromagnetic wave emissions, *J. Geophys. Res.*, in press, 1989.

Winglee, R. M., Electron beam injection during active experiments 2. Collisional Effects, *J. Geophys. Res.*, in press, 1989.

Three-Dimensional Computer Models of the Currents Collected by Active Spacecraft In Low Earth Orbit

I. Katz, M. J. Mandell, G. A. Jongeward, J. R. Lilley and V. A. Davis

S-CUBED Division of Maxwell Laboratories, Inc., La Jolla, CA

David L. Cooke

Geophysics Laboratory/PHK, Hanscom Air Force Base, MA

There has been much progress in determining the physical mechanisms that control the flow of charged particles from the ionosphere to spacecraft at potentials large compared with the ambient plasma temperature. At altitudes greater than a few hundred kilometers, space charge dominates ion collection, while both space charge and magnetic fields limit electron collection. At lower altitudes, ion collection remains space-charge limited, but electron collection is dramatically enhanced by ionization within the sheath. The NASCAP/LEO and POLAR codes solve Poisson's equation, in three dimensions, for the potential in the vicinity of arbitrary geometry spacecraft. The plasma currents collected by spacecraft are calculated by tracking representative particle orbits through the sheath. The validity of the code's underlying algorithms are discussed and comparisons with flight experiments are shown. A comparison of CHARGE-2 calculated and measured currents shows that both the 3-dimensional geometry and the self-consistent space charge are important to obtain agreement with the flight data. SPEAR I calculations show that the interaction between ion and electron collecting sheaths breaks the symmetry and permits more electrons to be collected than the spherical probe theory would suggest.

INTRODUCTION

During the past decade, there has been much discussion about how spacecraft collect current from the ionosphere (Winckler, 1980). Even though the basic equations describing the plasma surrounding a high-voltage spacecraft are well known, there has been debate on what set of algorithms is both sufficient to describe the plasma interactions, and yet practical enough to provide answers in a reasonable time on available computers (LaFramboise, 1982). Recently, the NASCAP/LEO (NASA Charging Analyzer Program for Low Earth Orbit) and POLAR (Potential Of Large spacecraft in the Auroral Region) codes have successfully been used to model the current collecting sheaths of the SPEAR I and CHARGE-2 sounding rockets. The algorithms employed by these two computer codes provide insight into the mechanisms that control current collection from the ionosphere. The upcoming electrodynamic Tethered Satellite System (TSS-1) will have sufficient instrumentation to further test the adequacy of the physics in these computer codes.

THEORY

The basic approach employed is to consider a spacecraft as a large, asymmetrical, high-voltage probe immersed in a magnetoplasma. There has been extensive research into the current characteristics of probes in plasmas (Langmuir and Blodgett, 1924; Mott-Smith and Langmuir, 1926; Beard and Johnson, 1961; Chen, 1965; Laframboise and Rubinstein, 1976; Rubinstein and Laframboise, 1978, 1982, 1983; Parker and Murphy, 1967). Most of the published work has been for symmetric probes. The emphasis in this discussion is on the extension of the basic theories into algorithms that account for asymmetries and the earth's magnetic fields. The approach used is to examine the conservation laws that limit current collection, and to identify the ones that most limit the current. The algorithms in the computer codes satisfy the most severely limiting conservation laws.

The ionosphere is a cool dense plasma. For the sounding rockets, typical ionospheric plasma parameters are

$$n_e = n_i = 10^{11} \ m^{-3}$$
$$\theta_e = \theta_i = 0.1 \ eV.$$
$$B = 0.4 \ Gauss \tag{1}$$

The time and distance scales associated with this plasma are

$$\omega_{pe} = 2 \times 10^7 \ sec^{-1}$$
$$\omega_{ce} = 7 \times 10^6 \ sec^{-1}$$
$$\lambda_D = 0.007 \ m$$
$$\lambda_{ce} = 0.02 \ m$$
$$\lambda_{ci} = 3 \ m. \tag{2}$$

Typical active spacecraft experiments have dimensions of meters, potentials of hundreds of volts or more, and durations as long as seconds. For such spacecraft, the disparity between the time and distance scales of the spacecraft and those of the plasma is so great that direct simulation is not practical. Direct simulation, such as the use of Particle In Cell (PIC) codes, is appropriate when all the dimensions are comparable. The wide range of time and distance scales in the problem considered here allows approximations to be made that make the problem easier to solve than if the range were smaller.

The equilibrium state of the plasma surrounding a spacecraft can be described by Poisson's equation and the collisionless Vlasov equation,

$$\nabla^2 \phi = - \frac{\rho}{\epsilon_0} \tag{3}$$

$$\rho(x) = e \left(\iiint f_i(x, v) \, dv - \iiint f_e(x, v) \, dv \right), \tag{4}$$

where ϕ is the potential and f_i, f_e are the ion and electron distribution functions, respectively. The potential is measured with respect to the unperturbed plasma at great distances. The discussion below first examines restrictions on the particles that can be

512

collected by the spacecraft neglecting the charge density in equation (3). Then, the additional restrictions on the current due to finite space charge are considered.

If the range of the potential were infinite, the maximum impact parameter of particles collected would be limited by angular momentum. For a sphere of radius a and potential ϕ, plasma electrons with velocity v_{th} could be collected if their impact parameter, b, was less than the limiting value.

$$b \le a \, (v_f/v_{th})$$
$$b \le a \, (1 + \phi/\theta_e)^{1/2} \tag{5}$$

The collected current, which depends on b^2, increases linearly with potential. This type of collection is seen in hot, dilute plasmas, such as the magnetosphere, but is rarely observed in the ionosphere.

For electrons in the ionosphere, even if the range of the potential were infinite, the magnetic field introduces a canonical angular momentum that severely restricts the range of impact parameters which can be collected (Parker and Murphy, 1967),

$$p_\theta = mr^2 \left(\frac{d\theta}{dt} + \frac{\omega_{ce}}{2} \right)$$

$$b \le a \sqrt{1 + \left(\frac{8e\phi}{m\omega_{ce}^2 a^2} \right)^{1/2}} \tag{6}$$

Conservation of canonical angular momentum is typically the most limiting condition in the collection of electrons from the ionosphere. Early electron beam experiments aboard rockets reported currents much larger than implied by the Parker-Murphy theory, and others speculated that plasma turbulence scattered electrons across magnetic field lines (Linson, 1969). However, recent data at altitudes above 250 km show clear evidence of magnetic limiting. These results imply that the earlier results were due to ionization of the background neutral gas.

The angular momentum limits described above are predicated on an infinite range of the attracting potential. This condition is clearly violated in the ionosphere for spacecraft at high potentials. A space charge sheath forms around a high potential spacecraft. This sheath shields the bulk of the plasma from the potential. Since electric fields are very small in the surrounding plasma, the sheath satisfies the condition that the sheath space charge balances the spacecraft surface charge,

$$\iiint_{sheath} \rho \, dx + \oint_{spacecraft} \sigma \, dS = 0. \tag{7}$$

The space charge of the attracted electrons or ions would shield a ± 8000 volt potential on a 1-meter sphere in 8 meters. For ions, this is a much shorter distance than either angular momentum limit. For electrons, the magnetic limit is a factor of two less than the space charge limit. Equation (7) provides insight into magnetically limited sheaths.

513

Although scattering can leave electrons trapped in the sheath, the number that are trapped cannot be substantial, unless they generate enough ions to balance their space charge. For large sheath dimensions, compared with the effective radius of the spacecraft, the surface charge depends only weakly on the sheath radius. Thus, while the magnetic field may modify particle trajectories and the sheath shape, the total number of electrons in the sheath is the same with or without the magnetic field.

Outside of the space charge sheath, the ionosphere is perturbed by weak electric fields that focus thermal current to the sheath edge and allow the plasma to satisfy the Bohm criterion at the sheath edge. How this is accomplished in a magnetoplasma is not known. For nonmagnetized plasmas, Parrot, *et al.* (1982) calculated self-consistent potentials and densities for the quasi-neutral presheath. Their analysis lead to a sheath edge potential of $0.7\theta_e$ and an incident current of $1.45 j_{th}$. These results, modified to account for spacecraft motion, are used in the computer calculations.

ALGORITHMS

The analysis above describes the plasma surrounding a high-voltage spacecraft in terms of a nonneutral space charge sheath, a quasi-neutral presheath, and the undisturbed plasma. The potential variation in the presheath is small, less than θ_e. For spacecraft potentials of a hundred volts or more, this is beyond the accuracy of the calc—¹ ons, and the potential variation in the presheath is ignored.

Throughout space, NASCAP/LEO and POLAR solve the variational form of Poisson's equation

$$\delta \iiint \left(\frac{\varepsilon_0}{2} |\nabla\phi|^2 + \rho\phi \right) dx = 0. \tag{8}$$

The variational form of Poisson's equation is used because it is easier to generalize to three dimensions and irregular zoning. A finite element approach is used to interpolate between nodal values of the potential. Equation (8) is solved using a scaled conjugate gradient algorithm.

The solution of Poisson's equation is straightforward; the complications stem from the determination of the space charge density. Outside of the sheath, the plasma is assumed to shield linearly,

$$\rho = -\frac{\varepsilon_0 \phi}{\lambda_D^2} \quad , \quad |\phi| \leq 0.7\theta_e . \tag{9}$$

This approximation is used in both the NASCAP/LEO and POLAR codes. The use of an analytic approximation for the presheath charge density is necessary to prevent outrageous computing requirements. For a problem space of 10m x 10m x 10m, on the order of 10^9 macro particles would be needed to keep numerical fluctuations below the thermal energy of the particles.

Inside the sheath, NASCAP/LEO and POLAR use different algorithms to obtain the charge density. In POLAR, macro particles are tracked in from the sheath edge and their contribution to the space charge is accumulated in each element. The equations of motion

514

of the macro particles include the Lorentz force, so the resultant charge density includes the effects of the earth's magnetic field. POLAR iterates calculations of space charge and potentials until convergence is obtained. This frequently requires days of computing on a desktop workstation. Some particles are neither collected by the object nor ejected from the sheath. These particles are followed for some number of bounces within the sheath. The number of bounces followed is the only free parameter in a POLAR calculation, and is usually chosen high enough (around 10) so that only a few percent of the particles are still bouncing at the end of the calculation.

NASCAP/LEO uses a simple, nonlinear analytical formula for the space charge. The function used is

$$\rho = -\frac{\varepsilon_0 \phi}{\lambda_D^2} \left(\frac{1 + \frac{\phi}{\theta} C(\phi, E)}{1 + \sqrt{4\pi \left|\frac{\phi}{\theta}\right|^3}} \right) \tag{10}$$

where the first factor represents the linear Debye screening from Equation (9), the numerator represents the density increase due to trajectory convergence, and the denominator reflects the density decrease due to particle acceleration in the sheath. Figure 1 shows equation 10 without the convergence factor. The convergence factor, $C(\phi, E)$, is a function of local field and potential.

$$C(\phi, E) = \left(\frac{\theta}{\phi}\right)\left(\frac{r_{sh}^2}{r^2} - 1\right) \tag{11}$$

where

$$\frac{r_{sh}^2}{r^2} = 2.29 \left(\frac{E\lambda_D}{\theta}\right)^{1.262} \left(\left|\frac{\theta}{\phi}\right|\right)^{.509}. \tag{12}$$

The quantities r_{sh} and r refer to radii of an effective spherical diode. The numerical values were obtained by a fit to Langmuir-Blodgett spherical sheath results. C is zero for planar sheaths. When convergence is negligible. Equation (10) reduces, in the limit of large potentials, to the charge density of the accelerated plasma thermal current,

$$\rho = -\frac{j_{th}}{v}, \quad \phi \to \infty. \tag{13}.$$

Poisson's eq·ation is solved iteratively with Equation (10) for the sheath potentials and fields. Equation (10) is not only used in NASCAP/LEO, but also in POLAR , where it is used to provide an initial potential estimate for the particle pushing iterations.

While the analytic charge density does not include magnetic field effects, it yields sheath potentials that lead to particle currents similar to particle currents computed from the self-consistent solutions. This occurs for two reasons. First, equation 7 says that the total charge in the sheath is the same whether there is a magnetic field or not. The formula in equation 10 distributes the charge incorrectly. but it gives the total charge correctly.

Second, the potential has about the right shape in the region from which particles are collected. Most of the particles collected are collected in less than a Larmor period, and thus their orbits are not perturbed that much by the magnetic field.

In both POLAR and NASCAP/LEO, macro particle trajectories are followed to determine how much current is collected by the spacecraft. The distribution of currents on the spacecraft is not particularly accurate because small perturbations near the sheath boundary lead to substantial errors at the end of the orbit. A new code with quadratic interpolants for the potentials, DynaPAC, is under development. DynaPAC will allow more accurate trajectory calculations.

COMPARISON WITH FLIGHT DATA

Calculations using both NASCAP/LEO and POLAR have recently been compared with flight data. The details are contained in three papers (Katz et al., 1989; Neubert et al., 1989; Mandell et al., 1989). Below the major conclusions are summarized; the discussion focuses on the comparisons with experiment and the agreement between calculations using particle-tracked and analytical charge densities.

Space Power Experiments Aboard Rockets I (SPEAR I) was a sounding rocket designed to measure electron collection from the ionosphere. Two 10-cm radius spheres were biased up to 46,000 volts with respect to the rocket body. The experiment measured the steady-state current to the spheres and the floating potential of the rocket body. The rocket body potential with respect to the ionospheric plasma adjusted to achieve a balance between the electron current collected by the spheres and the secondary electron enhanced ion current to the rocket body. Both NASCAP/LEO and POLAR calculations show that current balance was achieved when the ion collecting sheath encompassed much of the electron sheath, reducing the electron currents. The calculations also show that the asymmetry introduced by the floating rocket body permitted almost all the electrons entering the sheath to be collected by the spheres; magnetic limiting played no role in the measured currents. Figure 2 shows calculated results from NASCAP/LEO for SPEAR I with one sphere biased to 46 kV and the spacecraft ground at -6 kV. Figure 2a shows potential contours and figure 2b shows the path of an electron in the potentials. Figure 3 shows a comparison between the measured and calculated currents. For SPEAR I, NASCAP/LEO and POLAR give almost identical results. The NASCAP/LEO calculations, using Equation (10) for the charge density, took a few CPU hours each. POLAR, pushing particles to obtain a self-consistent charge density, took a week of computer time for a single calculation.

The CHARGE-2 rocket consisted of a main payload section, containing an electron gun, and a smaller "daughter" payload section connected to the mainsection by a conducting tether. The NASCAP/LEO calculated ion currents collected were in agreement with the observed currents. The agreement extends to the currents to four small probes designed to measure sheath potentials. Electron collection by the mother had been first reported to exceed the magnetic limits of Parker and Murphy (Myers et al., 1989). The Parker and Murphy limit was calculated using spherical probe whose surface area was equal to that of the rocket For data obtained above 250 km, NASCAP/LEO and POLAR calculations (Table 1), both agree with the measurements. The NASCAP/LEO and POLAR calculated currents are almost a factor of two greater than the spherical probe estimates. This

demonstrates the importance of using the correct, 3-dimensional geometry. The POLAR self-consistent current is about 50 percent greater than the non-self-consistent NASCAP/LEO result. The POLAR calculation shows that sheath contraction, due to the effect of the magnetic field on electron trajectories, enables a larger number of electrons entering the sheath to be collected by the rocket body. Figure 4 shows the sheath contraction in the direction perpendicular to the magnetic field. Below 250 km, the measured currents were higher than either code predicts. Presumably, the higher currents were due to ionization of background gases by the electron beam.

CONCLUSION

Algorithms have been developed that calculate the plasma currents collected by high-voltage spacecraft in the ionosphere. The algorithms assume the plasma shields very small potentials ($|\phi| < 0.7\theta_e$) linearly on the Debye length scale. For larger potentials, NASCAP/LEO uses an analytic formula based on current continuity for the charge density. POLAR iterates particle-tracked densities and potentials until a self-consistent solution is achieved. Both codes push particles in from the sheath edge to determine how much current is collected. In both codes the full Lorentz force is used to determine the force on the particles. Comparisons with flight data from SPEAR I and CHARGE-2 show that the 3-dimensional geometry plays a major role in the determination of collected currents. The CHARGE-2 calculations show that self-consistent space charge increases the magnetic-limited electron currents.

REFERENCES

Beard, D. B., and F. S. Johnson, Ionospheric limitations on attainable satellite potential, *J. Geophys. Res.*, *66*, 4113, 1961.

Chen, F. F., Electric probes, in *Plasma Diagnostic Techniques*, edited by R. H. Huddleston and S. L. Leonard, pp. 113-200, Academic, Orlando, Fla., 1965.

Katz, I., G. A. Jongeward, V. A. Davis, M. J. Mandell, R. A. Kuharski, J. R. Lilley, Jr., W. J. Raitt, D. L. Cooke, R. B. Torbert, G. Larson, and D. Rau, Structure of the bipolar plasma sheath generated by SPEAR I, *J. Geophys. Res.*, *94*, 1450, 1989.

Laframboise, J. G., and J. Rubinstein, Theory of a cylindrical probe in a collisionless plasma, *Phys. Fluids*, *19*, 1900, 1976.

Laframboise, J. G., and M. Kamitsuma, The threshold temperature effect in high-voltage spacecraft charging, Proceedings of the Air Force Geophysics Laboratory Workshop on Natural Charging of Large Space Structures in Near Earth Polar Orbit: 14-15 September, 1982, AFGL-TR-83-0046, pp. 293-308. **ADA134894**

Langmuir, I., and K. B. Blodgett, Currents limited by space charge between concentric spheres, *Phys. Rev.*, *24*, 49, 1924.

Linson, L. M., Current-voltage characteristics of an electron emitting satellite in the ionosphere, *J. Geophys. Res.*, *74*, 2368, 1969.

Mandell, M. J., J. R. Lilley, Jr., I. Katz, T. Neubert, and N. B. Myers, Computer modeling of current collection by the CHARGE-2 mother payload, Submitted to *J. Geophys. Res.*, 1989.

Mott-Smith, H. M., and I. Langmuir, The theory of collectors in gaseous discharges, *Phys. Rev.*, *28*, 727, 1926.

Myers, N. B., W. J. Raitt, B. E. Gilchrist, P. M. Banks, T. Neubert, P. R. Williamson, and S. Sasaki, A comparison of current-voltage relationships of collectors in the earth's ionosphere with and without electron beam emission, *Geophys. Res. Lett.*, *16*, 365, 1989.

Neubert, T., M. J. Mandell, S. Sasaki, B. E. Gilchrist, P. M. Banks, P. R. Williamson, W. J. Raitt, N. B. Myers, K. I. Oyama, and I. Katz, The sheath structure around a negatively charged rocket payload, To be published in *J. Geophys. Res.*, 1989.

Parker, L. W., and B. L. Murphy, Potential buildup on electron-emitting ionospheric satellites, *J. Geophys. Res.*, *72*, 1631, 1967.

Parrot, M. J. M., L. R. O. Storey, L. W. Parker, and J. G. Laframboise, Theory of cylindrical and spherical Langmuir probes in the limit of vanishing Debye number, *Phys. Fluids*, *25*, 2388, 1982.

Rubinstein, J., and J. G. Laframboise, Upper bound current to a cylindrical plasma probe in a collisionless magnetoplasma, *Phys. Fluids*, *21*, 1655, 1978.

Rubinstein, J., and J. G. Laframboise, Theory of a spherical probe in a collisionless magnetoplasma, *Phys. Fluids*, *25*, 1174, 1982.

Rubinstein, J., and J. G. Laframboise, Theory of axially symmetric probes in a collisionless magnetoplasma: Aligned spheroids, finite cylinders, and disks, *Phys. Fluids*, *26*, 3624, 1983.

Winckler, J. R., The application of artificial electron beams to magnetospheric research, *Rev. Geophys.*, *18*, 659, 1980.

Table 1. Calculated and measured collected current (mA)

Altitude [km]	Potential [volts]	Measured	Parker-Murphy[a]	NASCAP/LEO Collected Current	NASCAP/LEO Sheath Current	POLAR Self-consistent
165	390	35.8	0.4	0.6	8.3	-
168	150	6	0.3	0.5	3.5	-
232	475	20.4	5.5	7.9	42	-
251a	560	12.2	8.5	13.0	60	-
251b	440	14	8.1	12.9	52	-
256	440	15.6	8.6	13.5	54	-
260	440	18	8.9	14.1	55	22

[a]Calculated for sphere of radius 0.6 meters.
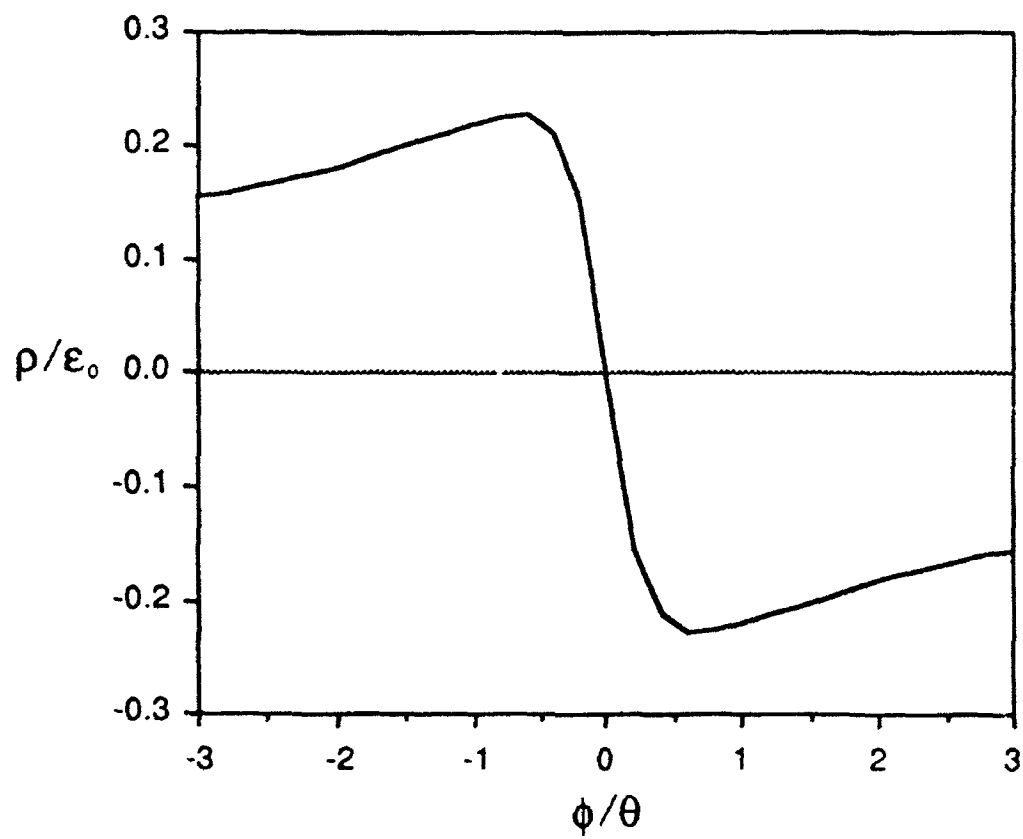
Fig. 1. Charge density as a function of potential from equation 10 for $\lambda_D = 1$ m.

(a)

Contour Levels
-1000
-100
-10
-1
1
10
100
1000
10000

(b)
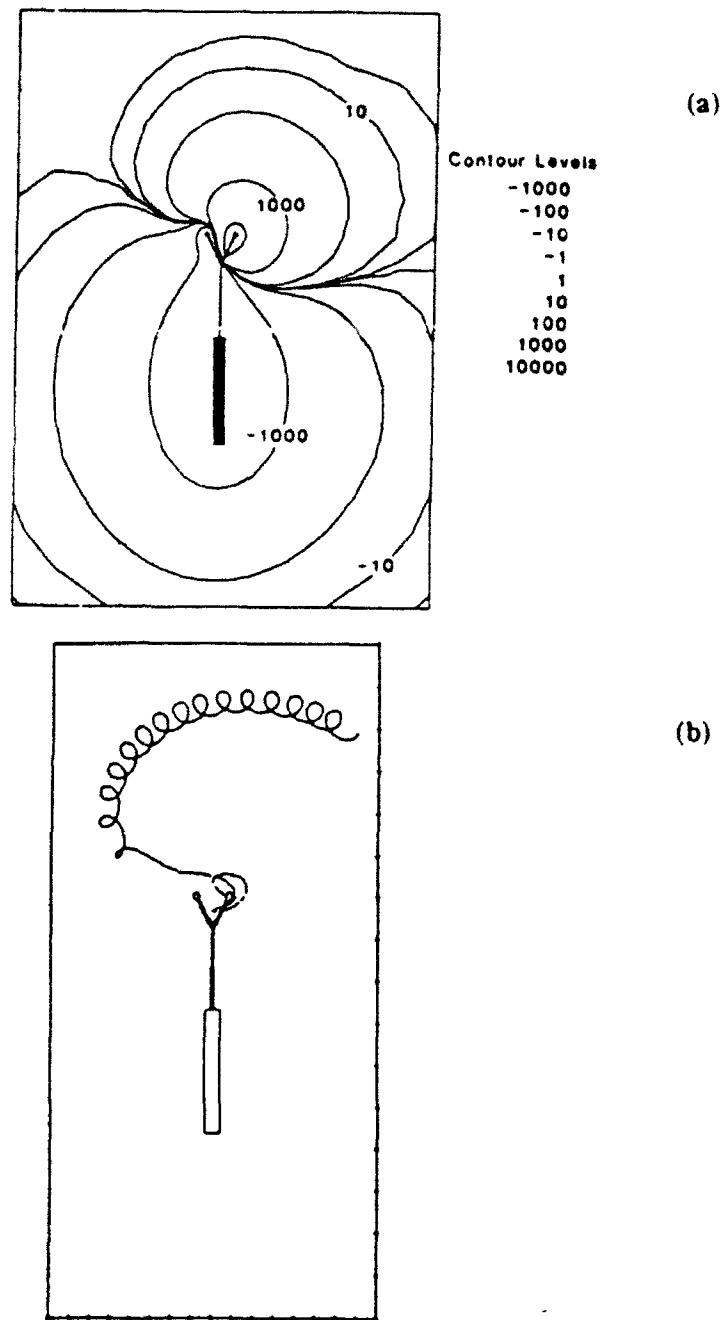
Fig. 2.   (a) Potential contours calculated by NASCAP/LEO for the case with one sphere biased to 46 kV and the spacecraft ground at -6kV and (b) path of an electron in the potentials shown in (a). Note that the path is dramatically influenced by the presence of the ion-collecting sheath.
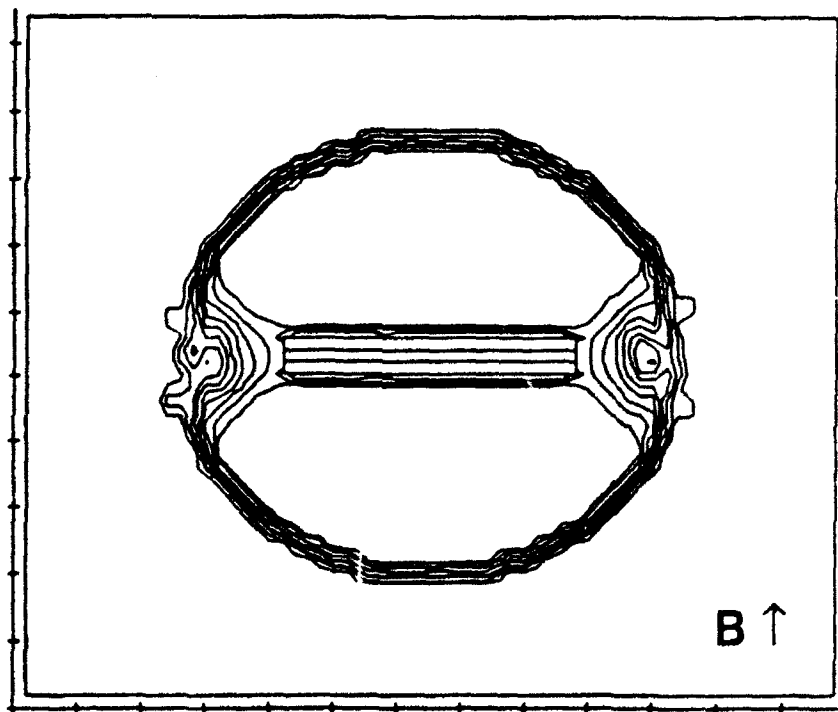
521
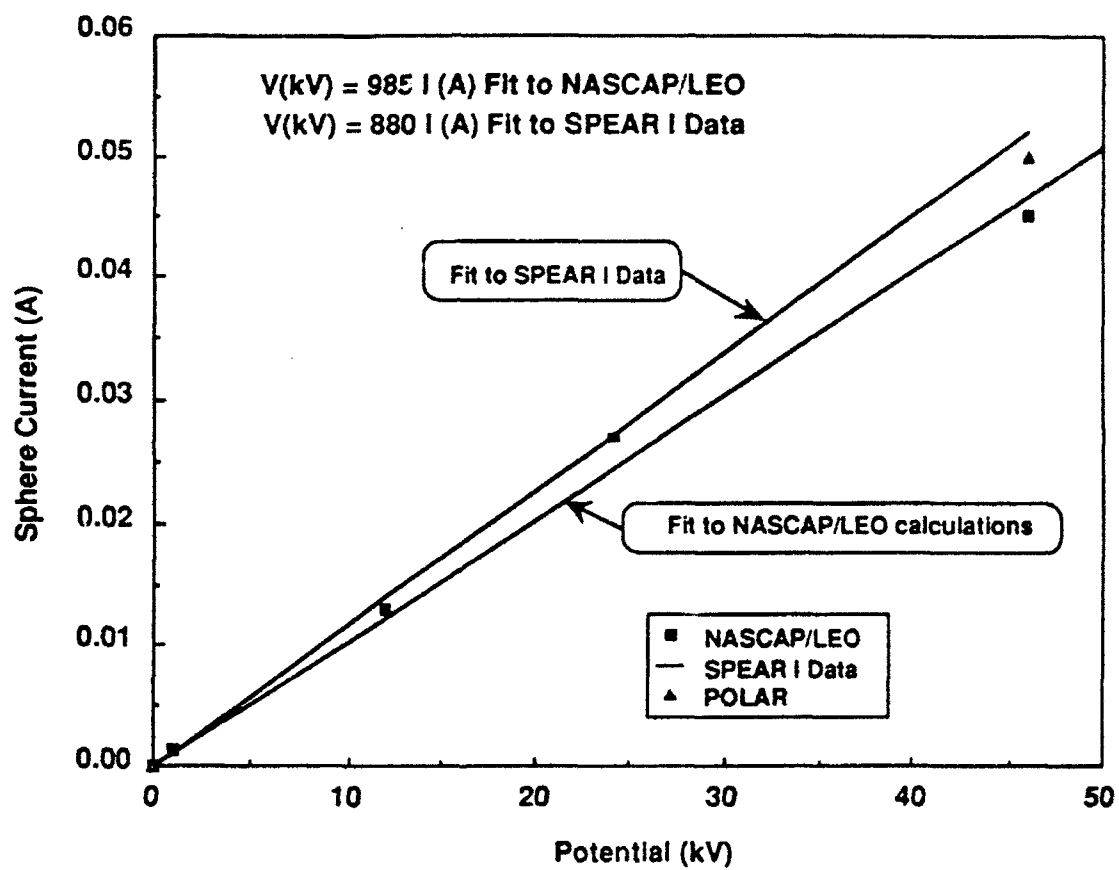
Fig. 3. Observed and calculated current collected by the 46 kV sphere as a function of applied potential.
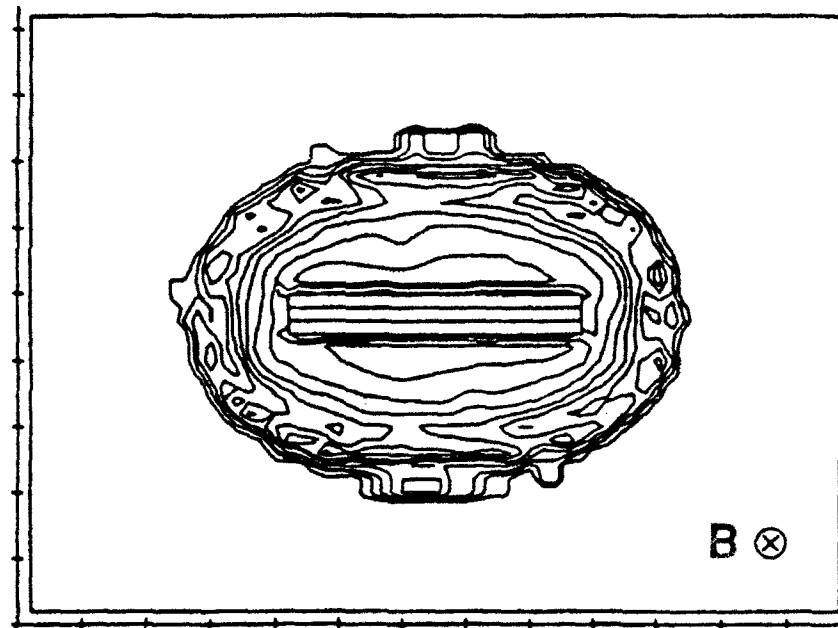
Fig. 4. POLAR calculations of the sheath about the CHARGE-2 rocket perpendicular to and in the plane of the earth's magnetic field. Note how the sheath extends much farther away from the rocket in the direction of the earth's magnetic field.

ENVIRONET: A SPACE ENVIRONMENT DATA RESOURCE

Michael Lauriente
NASA Goddard Space Flight Center, Greenbelt, MD 20771

Henry Berry Garrett
Jet Propulsion Laboratory, Pasadena, CA 91109

ABSTRACT

This paper reviews the EnviroNET space data resource. This computerized data base provides rapid access to the latest information on a variety of environments and interactions of importance to the space community. Although primarily intended as a source for Space Shuttle users, the EnviroNET has information on spacecraft charging and the near-Earth charging environment of potential value to the conference attendees. These products, particularly as they relate to spacecraft charging and environmental interactions, are presented and the means for accessing them addressed.

INTRODUCTION

EnviroNET is a NASA service facility that can provide the spacecraft interactions community with on-line, dial-up technical information concerning environmental conditions likely to be encountered on station in a variety of orbital regimes. This information is intended to help scientists and engineers design equipment that will operate successfully in the possibly hostile spacecraft charging environments. Figure 1 illustrates the advantages of this system for the potential user. In particular, the system incorporates a combination of expository text and numerical tables and programs that currently model several natural environments required for spacecraft charging studies. The text is under continuous review by technical subpanels (each corresponding to the subject areas of the database) of experts who correct and augment the database to keep it accurate and current. A partial list of the current topics contained in EnviroNET is shown in Figure 2. Following a brief description of the data base as a whole and as an illustration of its contents, two areas of direct importance to this conference will be discussed in more detail: the subpanel on Surface Interactions which contains information on charging-related interactions with spacecraft and the Natural Environments subpanel. The paper concludes with a call for the conference attendees to review EnviroNET and to recommend changes so that it can better support the spacecraft charging community.

BACKGROUND

Early in the development of the Space Shuttle, payload planners recognized the need for a detailed description of the environmental interactions with Shuttle and its payloads. The extreme complexity and size of the Shuttle made it very difficult to characterize these environments by direct computation. At the urging of the NASA payload community, the Shuttle Program agreed to fly instruments (in early Orbital Flight Tests) that would measure various elements of payload environment. In the fall of 1982, NASA conducted its first Shuttle Environment Workshop [*Systematics Corp., Contract NAS5-27326, February 1983*] to describe what had been learned from these measurements. This led to concerns voiced with regard to the need for up-to-date information, on a continuing basis, about these and new concerns. To address the issues, NASA's Office of Space Science and Applications (OSSA) requested that a focal point be established for this environmental information, and that the activity be coordinated with other NASA centers, government agencies, and the user community. In mid-1983, Shuttle Payload Engineering Division asked that Goddard Space Flight Center (GSFC) lead an Agency-wide effort to identify Shuttle environment data that could be used by Shuttle payload planners and developers. It also suggested that the data obtained from this activity be put into an electronic database which could be accessed by any interested user. It is from this base that the current EnviroNET user resource grew.

A multi-center Shuttle Environment Working Group was organized through the efforts of OSSA and GSFC, with a Working Group established to prepare the charter and framework within which this group would function, Figure 3. The Working Group began organizing in late 1983. Three major panels were established with the functions and duties as follows:

o The Natural and Induced Environments Panel, Figure 4, gathers and organizes data for input into the database

o The User Panel, Figure 5, provides for interaction between disciplines and users.

o The Information Management Panel, Figure 6, provides the database structure and manages the database.

The ultimate goal of the Working Group panels was to establish a comprehensive database of current information regarding the Shuttle Environment, readily accessible in a user-friendly format. Specific objectives for the Shuttle Environment Working Group (see

Figure 3), the working group relevant to this conference, included:

o Assessing the user requirements for environmental data at all
  stages of experiment definition and development.

o Obtaining and distilling the pertinent environmental
  data from available sources.

o Working with the sources to obtain a common database that
  will be reviewed by experts in the specific areas.

o Developing an information accessing system that is user-friendly.

o Providing a network accessible by a wide variety of existing
  computer terminals and peripherals.

o Coordinating these activities with other NASA centers, government
  agencies, and the user community.

Subpanels were created to address each of 10 environmental interactions identified as
critical to the Shuttle program, Figure 4. These interaction areas were subsequently filled
in at a series of workshops over the last 6 years (see later examples). Currently, more
specific tailoring of the data base is underway, with models under development to provide
tabular outputs to the screen or to files, and for plotting the resultant models. Orbit dosage
models designed to allow the user to predict the radiation dosage for a given orbit or to
predict densities and temperatures encountered along a given orbit are now available.
Computer models are being expanded beyond the current models (thermosphere,
ionosphere, energetic particles, magnetic field) to include gravity, radiation, meteoroids,
space debris, and spacecraft anomalies. A simple spacecraft charging code will hopefully
be available in the future for on-line use.

ENVIRONET AND SPACECRAFT CHARGING

The main EnviroNET topical areas of interest to spacecraft charging technology are
found in Sections 8.0 and 11.0, Figure 2, Natural Environment and Surface Interactions
respectively. A short summary and rationale for each of these chapters is presented in the
following. As these sections contain a tremendous amount of data on the particular topics,
it will only be possible to provide a brief overview of each (we urge the reader to actually
try EnviroNET, don't just read about it!).

526

Consider first the chapter on the Natural Environment. The purpose of this EnviroNET section is to describe the ambient natural environment that a vehicle will encounter while orbiting the earth. The natural environment includes neutral atmosphere, electromagnetic radiation (EMR), meteoroids, space debris, magnetic and gravitational fields, physical constants, and, of direct importance to spacecraft charging, plasma and charged particle radiation. Much of the content has been derived from JSC 30425, "Space Station Program Natural Environment Definition for Design." However, the material has been extensively edited and new material is continually being added to EnviroNET (it should always be kept in mind, however, that although EnviroNET is a NASA/AF product, it does not represent a contractually acceptable definition of the natural environment for payload design and development; it is provided only as a convenient information source to EnviroNET users).

The Natural Environment section (Figure 3) does not cover the induced environment or other effects resulting from the presence of the orbiting vehicle. Certain man-made factors were included, however, as part of the ambient natural environment (i.e., space debris and radio frequency (RF) noise generated on Earth), because they are not caused by the presence of the vehicle but form part of the ambient environment that it experiences. Each subsection contains an explanation and numerical description of the natural environment phenomena to which it is devoted. It was intended that these data would be sufficient for defining most preliminary hardware and experiment concepts. It is important to note that many of the natural environments discussed in EnviroNET are strong functions of time, varying with the solar cycle and the strength of the Earth's magnetic field, for example. Thus, for critical applications, it is important to use both an accurate model and the most up-to-date solar activity and field strength predictions. EnviroNET attempts to provide wherever possible specific instructions to the user on what is actually required and information on possible sources where day to day data are required.

As an example of the use of the Natural Environment section, consider Figure 7 and the path to it. This is part of the documentation material contained in EnviroNET on the MSIS model, a major code for predicting the neutral atmosphere. Figures 8 and 9 illustrate another part of the Natural Environment section--the modelling section. Figure 9 is an example of a user-friendly model for the 1986 Mass Spectrometer Incoherent Scatter Model (Hedin, 1987). The boundary conditions are shown above as input parameters. The output shown on the right is blank until the computer is asked to run the model (R) with keyed in values. A surface plot from the output of the model for atomic oxygen is shown in Figure 9. In this part of the data base, the user can thus obtain estimates of the atmospheric density and temperature from the MSIS model. Such information would be valuable for drag calculations or in estimating oxygen erosion. Note in particular this capability of the EnviroNET to provide graphical output in real time. For spacecraft charging studies, it is

planned to add models of the geosynchronous plasma and of the aurora that can be used to estimate the currents to the vehicle in these environments. Currently available is the IRI or International Reference Ionosphere model which is required for computing charging at low altitudes. As in the case of MSIS, help screens, a program description, and plotting capability are available.

The EnviroNET section on Surface Interactions contains the majority of the material of relevancy to this conference. As is well known to the attendees, the space environment at Shuttle altitudes can seriously affect spacecraft surfaces. Besides contamination and particle damage (covered by other sections), several such interactions with spacecraft surfaces have been observed in the last few years. The principle ones discussed in this section are:

1) spacecraft surface charging   2) V x B induced currents   3) High-voltage surface interactions   4) shuttle Ram/Wake plasma variations   5) shuttle surface glow   6) Atomic oxygen effects (spacecraft surface erosion)

Whereas at Shuttle altitudes, glow, surface erosion, and high-voltage surface interactions (resulting in power loss and increased surface arcing) are considered the most serious as they pose direct threats to operations, spacecraft charging is primarily a geosynchronous phenomenon--why then is it included in EnviroNET? The reasons for including spacecraft charging in EnviroNET should be obvious to the participants, however. Evidence from AF experiments on the Defense Meteorological Satellite Program (DMSP) have indicated that potentials as high as 1 kV may be observed in the auroral zone at low Earth orbit--hence, the justification for including spacecraft charging in the EnviroNET. Likewise, variations in the shuttle plasma sheath are tied to interactions with the shuttle surface potentials. These variations, and the regions of plasma enhancement and depletion and charging that they create, will greatly influence the environment around the Shuttle and therefore must also be included in a Shuttle data base and accurately characterized. V x B effects are probably the least serious of the "spacecraft charging" interactions included in EnviroNET. Even so, given the size of the Shuttle and some of the proposed shuttle-based systems such as the tether, the electric field induced by V x B may significantly affect operations. Thus, spacecraft charging and related phenomena are a critical component of the EnviroNET.

The data in the Surface Interaction section of EnviroNET are organized into the following subsections:

11.3 Spacecraft Charging (I. Katz and A. Rubin)

528

11.4 V x B (I. Katz and W. Raitt)
11.5 High Voltage (I. Katz)
11.6 Ram/Wake (A. Rubin, W. Denig, and W. Raitt)
11.7 Glow (H.B. Garrett, A. Chutjian, and S. Gabriel)
11.8 Atomic Oxygen Effects (L. Leger)

Each section is then broken down along the following lines:

1. Description
2. References
3. Key Players
4. Existing Data
5. Required Data
6. Possible Experiments
7. Mitigation

A sample screen from the "Description" part of the spacecraft charging subsection is presented in Figure 10. A list of "key players" from the data base is presented in Figure 11. Currently, the spacecraft charging section needs to be updated. The presentation of EnviroNET at this conference is intended to spur interest in this process and to allow us to provide you the user with the most up-to-date on this critical problem.

In addition to the obvious interest of the participants in this conference in sections on charging, V x B, Ram/Wake effects, and high voltage interactions, EnviroNET provides an additional service. Under the subsection on oxygen erosion, EnviroNET has stored up-to-date oxygen erosion rates for most common spacecraft surfaces. This information is critical in the selection of surface materials for charge control--materials subject to rapid oxygen erosion should not be used for conductive outer coatings (as an example, surfaces covered with ZOT paint for electrical and thermal control on Galileo were found to erode during a few days of exposure at Shuttle altitudes and loose their conductive properties). Although currently not available on EnviroNET, lists of secondary, photoelectron, and backscattering properties of common materials could be similarly provided if the attendees find this to be a useful addition.

UPDATING ENVIRONET

EnviroNET is a living document. Thus, workshops are conducted periodically for the panel leaders and subpanels. The results of these workshops are printed as informal documents for the purpose of feedback of information essential to the improvement of the services to users and to take advantage of the advancements in communications. These

documents are available upon request. As an example, at the mini-workshop held by the Natural Environment Panel, recommendations were made to add models that will generate energetic electron and proton environment values for a point in space, calculate orbital integrations of particle fluence, provide magnetic field traces and calculate ionospheric parameters. Besides now featuring interactive software, the system will eventually simplify space environment mission analysis. More recently, a mini-workshop was held on environmentally induced spacecraft anomalies [Belmont Conference, 1989]. The four main types of anomalies of concern are surface charging, bulk charging, single event upset, radiation dose. Plans are underway to develop a new chapter on this subject. A test bed is also planned for an expert system on spacecraft anomalies in cooperation with the Air Force.

CONCLUSION

EnviroNET is an operational system available to the scientists, engineers, satellite operators and users concerned with space environments who have access to a terminal or dial-up port. It is a tail node on SPAN accessible directly or through the national networks via NPSS. The EnviroNET staff welcomes comments and suggestions for how to improve this service. In particular, spacecraft charging is an area that would greatly benefit from the services that EnviroNET could provide--by serving as a source of computer models of the environment and charging, through lists of electrical properties of materials, and as a clearing house for the most recent papers and results. To summarize, the benefits to using EnviroNET include:

1) Validated NASA environmental information and interactive
   space models

2) Facilitating analysis of the natural space environment
   for missions

3) Easy access to expert assistance

Note: for EnviroNET to succeed, *user feed back is critical!*

APPENDIX: USING ENVIRONET

The following is intended as a very brief introduction to using EnviroNET and it structures (for details, the potential user is referred to the "EnviroNET User's Guide, 1989"). Specifically, the files, stored on a MicroVAX II computer at Goddard Space Flight Center (GSFC), can be accessed 24 hours a day by the user via modems or the NASA Space Physics Analysis Network (SPAN), (Green, 1988). SPAN is available via more than 1000 space science computer systems throughout the U.S. Canada and Europe. The database retrieval program features many user friendly options including transportability of data, software, and interactive computer modeling capability.

EnviroNET is accessed through the very well known SPAN system. SPAN uses Digital Equipment Corporation computers as network nodes (usually already paid for by NASA for a wide number of missions), and communicates over a combination of leased circuit switches and packet switching lines using the DECnet protocol. The SPAN topology, Figure 12, features four primary routing centers in the United States: Goddard Space Flight Center (GSFC), Johnson Space Flight Center (JSC), the Jet Propulsion Laboratory (JPL), and Marshall Space Flight Center, (MSFC), as well as one routing center at the European Space Operations Center (ESOC) in Darmstadt, Germany. There are approximately 1200 registered SPAN nodes. EnviroNET may be accessed via modem-equipped terminals, SPAN, or network servers at the routing centers.

The SPAN system allows the space scientific community to share information at speed of light. The network supports the transmission and reception of manuscripts. Data and Graphics files can be transferred between network nodes. The graphics bit map program written for EnviroNET has a transparent data compression program for speeding the transmission of the graph. SPAN now supports several types of network-to-network connections which provide access to SPAN.

Once the user reaches EnviroNET, he is presented with the "Main Menu". The Main Menu system (Environet User's Guide, 1989), Figure 13, which controls the EnviroNET activity on the MicroVAX II, is frequently updated in response to user suggestions and changing needs of the database activity. This menu allows one to run BROWSE, access the data files, download graphics and text, send mail to the system manager, read bulletin board notices, use the models or exit the system. The principal retrieval program, called BROWSE, is continually being updated in response to user and subpanel suggestions. With BROWSE, simple command choices allow one to page through the EnviroNET database sequentially, or jump to points of interest. To use BROWSE, one must have a VT100 compatible terminal or emulation. BROWSE has three menus: Main Topics, Data and Table of Contents/Index. One can move among the three menus to any part of the

531

database, or back to the EnviroNET main menu with a single keystroke. As you BROWSE about the database and change menus, the information on the terminal screen will change, but the basic layout of the screen will remain the same. Information is displayed in three windows: the page window at the top right, the data window at the center, and the option window at the bottom, Figure 14.

ACKNOWLEDGMENTS

REFERENCES

1. Green, James L. The Space Physics Analysis Network. Computer Physics Communication 49, pp. 205-213, North-Holland, Amsterdam, 1988.

2. Proceedings: The Shuttle Environment Workshop. Prepared for NASA by Systematics Corp., Contract NAS5-27326, Feb. 1983.

3. Wilkerson, Thomas D., Michael Lauriente,and Gerald W. Sharp. Space Shuttle Environment. Library of Congress Catalog No.: 85-81606, ISB No-939204-28-2

4. The EnviroNET User's Guide. Code 410.1, NASA/GSFC, Greenbelt, MD 20770.

5. Johnson, D .L. and R. E. Smith. The MSFC/J70 Orbital Atmosphere Model and the Data Bases for the MSFC Solar Activity Prediction Technique. NASA TM-86522, 1985.

6. Hedin, Alan E. The MSIS-86 Thermospheric Model, J. Geophys. Res., vol. 92, pp. 4648-4662, 1987.

7. Solar-Geophysical Data Part I (prompt reports), issued monthly by National Geophysical Data Center, NOAA/NESDIS, E/GC2, 325 Broadway, Boulder, CO 80303.

8. Journal of Geophysical Research (Space Physics), issued monthly by American Geophysical Union, 2000 Florida Ave, N.W.,Washington, D.C. 20009.

9. Accessing SPAN From Non-SPAN Nodes, National Space Science Center (NSSDC)/Work Data Center-A for Rockets and Satellites (WDC-A-R&S), NASA GSFC, Greenbelt, MD 20771.

FIGURES

ENVIRONET

- CENTRALIZED COMPUTER-BASED INFORMATION ON NATURAL AND INDUCED
  ENVIRONMENTS OF SHUTTLE AND SPACE STATION

- BASED ON MEASURED DATA (SHUTTLE) AND EMPIRICAL MODEL VALIDATED
  BY DISCIPLINE PANELS

- FOR SCIENTISTS AND ENGINEERS USE IN THE DESIGN AND DATA ANALYSIS
  OF FLIGHT HARDWARE

- MAINTAINED CURRENT BY NASA THROUGH COOPERATIVE EFFORTS
  OF INDUSTRY, OTHER GOVERNMENT AGENCIES, THE EUROPEAN SPACE
  AGENCY, ACADEMIA, AND THE NASA COMMUNITY

Figure 1: Advantages of EnviroNET

ENVIRONET MAIN TOPICS

Section	Chapter	Page
1.0	INTRODUCTION	1-1
2.0	THERMAL AND HUMIDITY	2-1
3.0	VIBRATION AND ACOUSTICS	3-1
4.0	ELECTROMAGNETIC INTERFERENCE	4-1
5.0	LOADS AND LOW FREQUENCY DYNAMICS	5-1
6.0	MICROBIAL AND TOXIC CONTAMINANTS	6-1
7.0	MOLECULAR CONTAMINATION	7-1
8.0	NATURAL ENVIRONMENT	8-1
9.0	ORBITER MOTION	9-1
10.0	PARTICULATE ENVIRONMENT	10-1
11.0	SURFACE INTERACTIONS	11-1
12.0	DEFINITIONS AND ACRONYMS	12-1

Figure 2: Current Topics
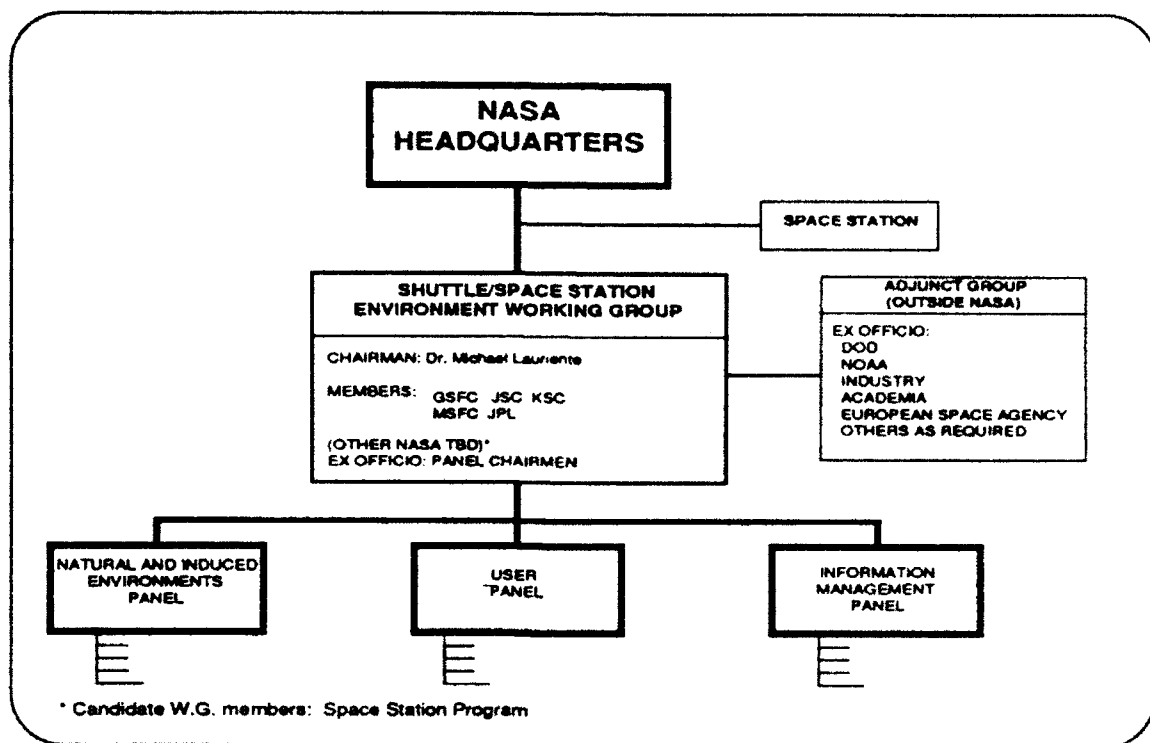
Figure 3
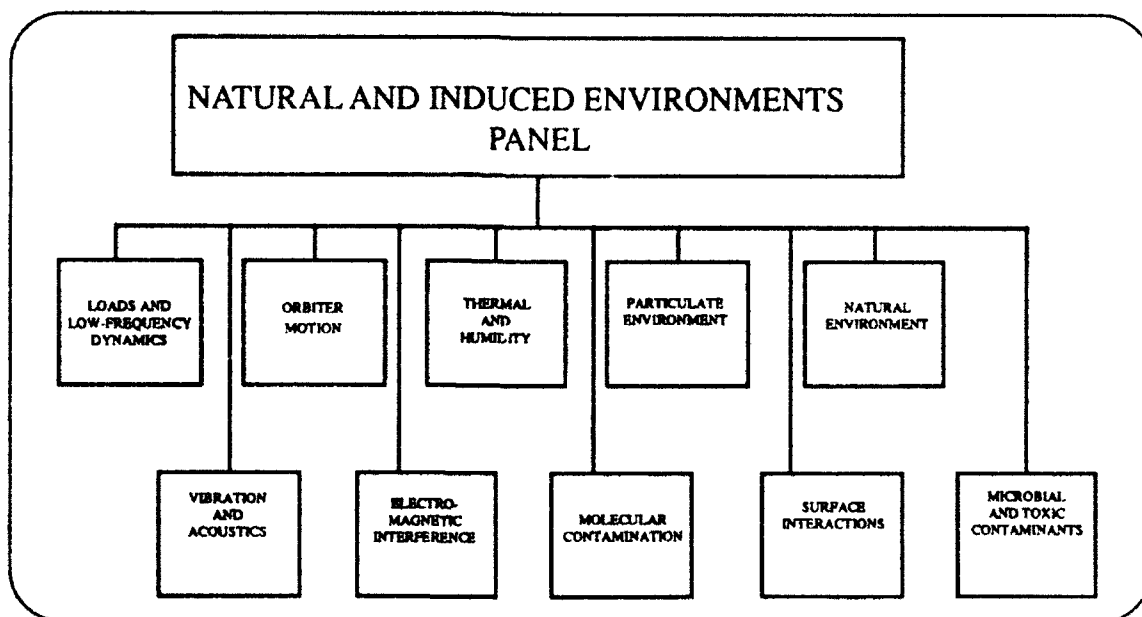
Figure 4
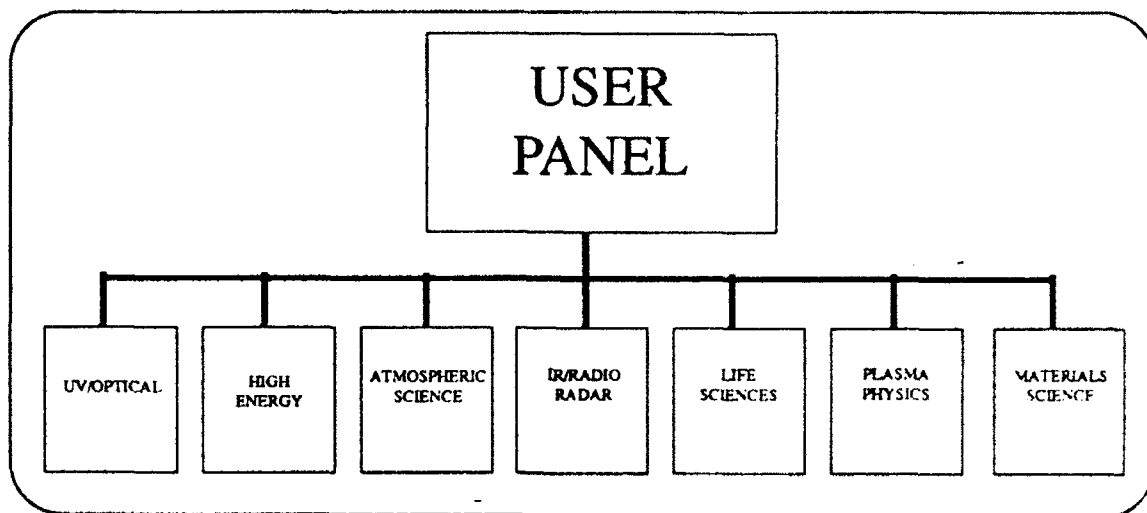
Figure 5
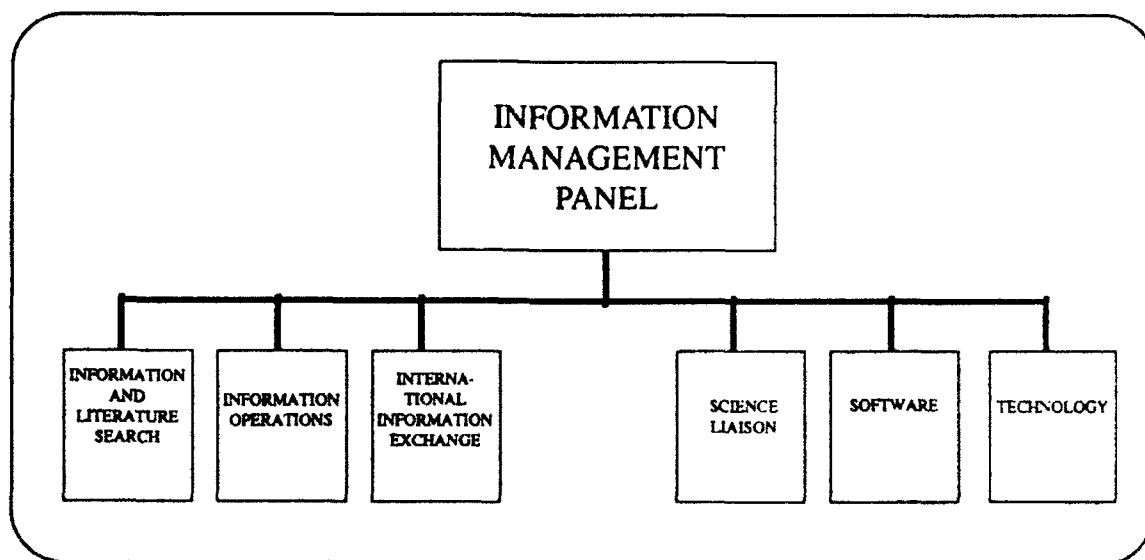
Figure 6

8.3.2.4 MSIS86 MODEL

The neutral model, MSIS-86 (The MSIS-86 Thermospheric Model by A.E.Hedin, J. Geophys. Res., Vol 92, pp. 4648-4662, 1987), which can now be accessed through the EnviroNET menu, was chosen for the 1986 COSPAR International Reference Atmosphere. This model is based primarily on in-situ (mass spectrometer) composition and temperature measurements and ground based radar measurements. MSIS provides densities of individual constituents and is based on data covering periods from low to high solar activity.

8.3.3 SOLAR ACTIVITY DATA

Table 3-1 lists the 13-month smoothed values of the 10.7 centimeter solar radio flux (F10.7) and the Ap throughout an eleven year solar cycle. The values in the table are based on a statistical analysis

Figure 7

```
                        MSIS MODEL

                          Input Ranges
Day number.................... 1 to 365  Local solar time (hrs)......... 0 to 24
Altitude (km)............... 85 to 1000  Average F10.7 flux........... 65 to 300
Geodetic latitude (deg)...... -90 to 90  Current F10.7 flux........... 65 to 300
Geodetic longtitude (deg).. -180 to 180  Magnetic index AP............. 0 to 400

        Input Parameters                          Output Values
1) Day of year............. 44            H   (Number/cm3)........ 1.41E+07
2) Altitude................ 100           N   (Number/cm3)........ 6.54E+05
3) Latitude................ 40            HE  (Number/cm3)........ 9.64E+07
4) Longtitude.............. -75           O   (Number/cm3)........ 4.03E+11
5) Local time.............. 12            N2  (Number/cm3)........ 7.85E+12
6) Average F10.7........... 100           O2  (Number/cm3)........ 2.02E+12
7) Current F10.7........... 200           AR  (Number/cm3)........ 1.19E+11
8) Magnetic index  AP...... 300           Total (gm/cm3).......... 4.91E-10
                                          TN(INF) (deg K).......... 1300.8
                                          TN (deg K)..............  194.0

 Do you want to (R)un the model with the current values, change some
 (1 through 8) or (A)ll the values, or (Q)uit?
```

Figure 8
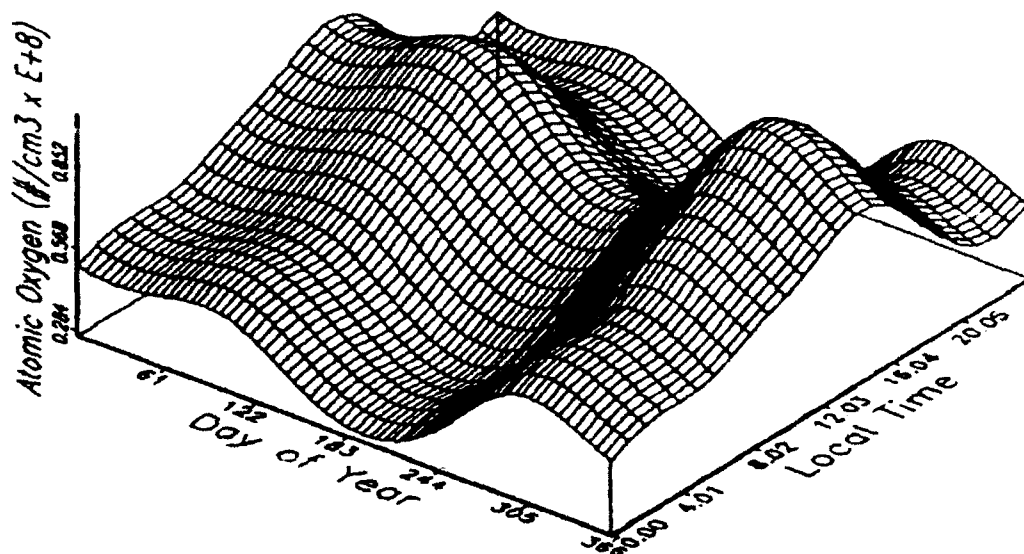
Figure 9: An example surface plot from the output of the MSIS-86 Model
F10.7 = 150; Ap = 200; Lat = Long = 0; Alt = 500

11.1 SPACECRAFT CHARGING
     (By I. Katz and A. Rubin)

11.1.1 DESCRIPTION

        Spacecraft charging occurs at geosynchronous orbit during
magnetic substorms, when dense clouds of kiloelectron volt plasma
envelop spacecraft. These kilovolt plasma clouds charge up the
spacecraft surfaces to potentials which range up to 19 kilovolts.
Surface potentials of many kilovolts lead to arc discharges, with
accompanying currents of up to 1000 amps, which radiate rf power into
the spacecraft electronics, and have led to false commands, upsets
and, in one case, complete loss of a spacecraft.

        At Shuttle Orbiter altitudes of 200 to 500 km, the ionospheric
plasma is cold and dense, a state which ordinarily would not support
charging. Special conditions must exist to permit spacecraft
charging, and these special conditions exist in polar orbit, when the

Figure 10

Figure 11

ACCESSING SPAN FROM NON-SPAN NODES

Figure 12

```
                    ENVIRONET MAIN MENU
                    ======================


     B  ->  BROWSE  -  Text Retrieval Subsystem (Requires VT100 emulation)

     U  ->  User Message Service  -  Leave messages for other users

     N  ->  Bulletin Board Notices  -  Changes to the database

     D  ->  Download Specific Chapter

     M  ->  Mail System  -  Mail us your comments about the system

     F  ->  Function Calculation System  -  Natural Environment Models

     G  ->  Graphics  -  Download high resolution graphs

     L  ->  Logoff  -  End ENVIRONET session

     Enter appropriate letter, followed by RETURN  :
```

Figure 13

```
                                                  Pg 9- 2
as a platform for microgravity experiments or for astronomical
observations which require fine pointing accuracy.  Ideally, one wishes
for these activities a platform in a perfect state of free fall.  In
practice, the orbiter is prevented from attaining any such state of
tranquility by several perturbing forces.  The forces may be classified
into three types:

9.2.1  TYPES OF DISTURBANCE FORCES

     1.  Steady or Slowly Time-Varying Forces
         Examples of this type are the gravity gradient over the length
         of the orbiter and the residual atmospheric drag on therbiter.
         These forces are characterized entirely by their magnitude
         and direction; information on frequency content or duration
         would be meaningless.

     2.  Periodic Forces

(A)head page    (T)OC      (P)age/section    (R)eturn    (H)elp

(B)ackpage      (I)ndex    (M)aintopics      (Y)memory (F)indword (E)xit
```

Page Window

Data Window

Option Window

Figure 14

Modification of Spacecraft Charging and the Near-Plasma Environment Caused by the Interaction of an Artificial Electron Beam With the Earth's Upper Atmosphere.

T. Neubert[1], P. M. Banks[1], B. E. Gilchrist[1], A. C. Fraser-Smith[1],
P. R. Williamson[1], W. J. Raitt[2], N. B. Myers[2], and S. Sasaki[3]

Abstract. The Beam-Atmosphere Interaction (BAI) involves the ionization created in the earth's upper atmosphere by electron beams emitted from a low altitude spacecraft. This process is described by two coupled non-linear differential electron transport equations for the up-going (along a magnetic field line) and down-going differential energy flux. The equations are solved numerically, using the MSIS atmospheric model and the IRI ionospheric model, yielding estimates of the differential electron energy flux density at the spacecraft location. At altitudes below 200-250 km and for beam energies around 1 keV, it is shown that secondary electrons supply a significant contribution to the return current to the spacecraft and thereby reduce the spacecraft potential. Our numerical results are in good agreement with observations from the CHARGE-2 sounding rocket experiment. A more detailed study of the BAI as it relates the CHARGE-2 observations are found in [*Neubert et al.*, 1990].

1. Introduction

The return current to an electron beam-emitting spacecraft will, in general, have two components arising from completely different processes. The first component is the "classic" current that flows from the ambient plasma to a charged conductor, which we will refer to as the passive current [*Langmuir and Blodgett*, 1924; *Beard and Johnson*, 1961; *Parker and Murphy*, 1967]. The second component, the active current, relies on the electron beam or the charged spacecraft as a generator of return current electrons. Experiments performed from the space shuttle [*Waterman et al.*, 1988] and rockets [*Winckler et al.*, 1975; *Myers et al.*, 1989] have pointed out the importance of this component. The active current my be generated by a Beam-Plasma Interaction (BPI), a Beam-Plasma Discharge (BPD), a Beam-Atmosphere Interaction (BAI), or a Penning type discharge (PD). For a review see *Linson* [1982].

The CHARGE-2 tethered rocket experiment has provided the first direct measurements allowing to differentiate between the active and passive components of the return current, at least for the altitude range from 160 - 260 km [*Myers et al.*, 1989; *Gilchrist et al.*, 1990]. The observations indicated to us that the BAI was a likely candidate for the generation mechanism of the active current. Furthermore, quantitative estimates of the electron fluxes and electron energy spectra generated as a result of this process are possible and has been done for the case of energetic auroral electrons precipitating in the earth's upper atmosphere [*Banks et al.*, 1974].

This paper presents a summary of the results presented at the conference on spacecraft charging held in Monterey in October, 1989. A more detailed presentation is given in *Neubert et al.* [1990]. The following section describes briefly the CHARGE-2 experiment and the observations of the return currents to the spacecraft during electron beam emissions. Then follows a description of the method developed to study electron fluxes generated by artificial electron beams. Finally, we

[1] STAR Laboratory, Department of Electrical Engineering Stanford University, Stanford, CA 94305-4055
[2] Center for Atmospheric and Space Sciences, Utah State University, Logan, UT 84322-4405
[3] Institute for Space and Astronautical Sciences, Tokyo 153, Japan

model the BAI return current for the CHARGE-2 experiment and find good agreement between observed and modeled currents.

2. THE CHARGE-2 EXPERIMENT

The CHARGE-2 payload consisted of two sections, a Mother and a Daughter section, which were electrically connected by an insulated tether. The experiment was designed to study phenomena related to electron beam emissions from spacecraft as well as the electrodynamic interaction of a tethered system with ambient ionospheric plasmas [Sasaki et al., 1988]. During the flight, the two sections drifted apart in a direction roughly perpendicular to the spacecraft velocity and to the earth's magnetic field. Apogee was at 261 km altitude and the maximum separation distance of the two payloads was 426 m, reached at the end of the flight.

A schematic drawing of the CHARGE-2 payload is shown in Figure 1. The Mother carried an electron beam accelerator emitting beams with electron energies of 1 keV and currents up to 48 mA. Return currents were collected by both the Mother (I_M) and the Daughter (I_D) during beam injections. The electron beam current (I_{beam}) was measured by a Rogowski coil and the tether current (I_{tether}) was measured by a tether current monitor. Assuming that the beam escaped the Mother payload, we have $I_D = I_{tether}$ and $I_M = I_{beam} - I_{tether}$

The tether impedance was relatively low (4 kΩ) in certain experimental sequences and the tether current was typically less than 6 mA. As a consequence, the potential difference between the two payloads was less than 24 V and small compared to the potentials of 200-600 V reached by the Mother payload. Thus the two payloads were at almost the same potential during these particular sequences. Since the Daughter was separated by up to several hundred meters from the Mother in the direction perpendicular to the earth's magnetic field and therefore was well outside of the disturbed region around the beam column, the Daughter return current represents a measurement of the passive return current. The return current to the Mother contains both a passive and an active component.

Figure 2 shows the fraction of the beam current collected by the Daughter as a function of altitude. The labels SQ2 through SQ6 mark the beam emission sequences performed during the flight numbered in time-sequential order. Also indicated is the ratio of the Daughter collecting area to the collecting area of both payloads, A_D/A_{total}. At high altitudes, around 250 km, the tether current approaches 0.3 times the beam current. This value is close to A_D/A_{total}, indicating that the two payloads collect return currents roughly in proportion to their areas, which is to be expected for passive current collection. Thus at high altitudes, where the ambient plasma density is large and the neutral density is low, the payloads mainly collect currents from the ambient plasma. The return currents and corresponding spacecraft potentials observed during the flight have been found in accordance with the model of Parker and Murphy [Myers et al., 1989; Mandell et al., 1990].

As the altitude decreases, the current collected by the Daughter decreases such that by an altitude of 180 km and below almost no current is collected by the Daughter. Assuming that the beam escapes the near environment of the Mother payload, we conclude that the active component of the return current, which flows directly to the Mother, increases with decreasing altitude. Since the ambient neutral atmospheric density also increases with decreasing altitude, such an altitude dependence is suggestive of a BAI process. In the following section we describe the method developed to quantify the fluxes generated by BAI.

3. THE BEAM-ATMOSPHERE INTERACTION MODEL

The code developed to study the interaction of an electron beam with the earth's upper atmosphere solves two coupled first order non-linear differential equations in the forward and the backward flux of electrons streaming in the direction of the ambient magnetic field. The equations coupling the forward differential energy flux, Φ^+, and the backward flux, Φ^-, are given by

$$\frac{d\Phi^+(z,E)}{dz} = -\sigma_2(z,E)\Phi^+(z,E) + \sigma_1(z,E)\Phi^-(z,E) + Q^+(z,E) - L(E)\Phi^+(z,E) \qquad (1)$$

$$\frac{d\Phi^-(z,E)}{dz} = \sigma_2(z,E)\Phi^-(z,E) - \sigma_1(z,E)\Phi^+(z,E) - Q^-(z,E) + L(E)\Phi^-(z,E) \qquad (2)$$

Here $\sigma_2(z,E)$ is the cross section describing the loss of flux in the energy range E to $E + dE$, $\sigma_1(z,E)$ is the cross section describing the elastic back-scattering of electrons, $Q(z,E)$ is the electron production rate in the range E to $E + dE$ due to ionization processes and cascading of electrons down in energy from higher energy bins, and $L(E)$ describes the losses due to a finite spacecraft velocity. The cross sections take into account ionization of the atmospheric neutral species, back-scatter of electrons by neutral and charged particles, elastic and inelastic collisions, cascading of electrons down in energy etc. The coordinate system is chosen such that the z-axis is along the magnetic field with Φ^+ streaming in the positive direction. To account for pitch angle effects, an average pitch angle of $54.76°$ was used. The equations in their detailed form, excluding the term describing losses due to finite spacecraft velocities, are discussed in detail in *Banks et al.* [1974].

The altitude domain is divided into two regions: one is between the lower altitude boundary (70 km) and the spacecraft altitude, and the other is between the spacecraft altitude and the upper altitude boundary (900 km). First, the differential electron flux of a beam emitted from the spacecraft is assumed at the spacecraft altitude. The beam may be emitted either up or down, but let us assume in the following that the beam is emitted down. The fluxes are then determined in the region between the lower boundary and the spacecraft altitude in the same way as was done for the case of auroral electron fluxes. Next, the upward return flux found at the spacecraft altitude is emitted upwards, and the flux equations are solved in the region from the spacecraft altitude and to the upper boundary. The downward flux generated at the spacecraft altitude is added to the beam flux and the procedure is repeated until satisfactory convergence is reached.

The effect of a finite spacecraft velocity has been approximated by the inclusion of the loss term $L(E)$ in equations (1) and (2). The loss term can be determined from the following considerations: The beam is assumed to fill a volume with the dimension dx perpendicular to the magnetic field. The spacecraft velocity component perpendicular to the magnetic field, $v_\perp$, gives rise to a perpendicular flux $\Phi_\perp$ through the area element $dxdz$ as seen in the spacecraft reference system. This flux is lost to the beam flux-tube and the loss term can be expressed as

$$L(E) = \frac{v_\perp}{v_\| dx} \qquad (3)$$

where $v_\|$ is the particle velocity along the field.

The electron beam flux is modelled by a Gaussian distribution in energy centered around 1 keV and with an energy width of 10%. The beam is assumed to fill a flux-tube with a dimension perpendicular to the magnetic field of 10 m, which corresponds to 4 beam electron gyro-radii (for $90°$ pitch angle). This choice of beam column width is in accordance with observations obtained in the Spacelab-2 experiment flown on the space shuttle [*Frank et al.*, 1989] and in the ECHO-7 sounding rocket experiment [*Winkler et al.*, 1989]. The beam is emitted downwards for the range of spacecraft altitudes and corresponding perpendicular velocities obtained in the CHARGE-2 experiment and it is assumed that the Mother collects only a small fraction of the return fluxes. The MSIS/86 model [*Hedin*, 1987] is used for the neutral atmosphere (N_2, O_2 and O) and the IRI model [*Bilitza*, 1986] is used for the ionosphere. The models are those corresponding to the local time, season, geographic location etc. of the launch. The IRI model of electron densities compares well with the electron densities observed during the flight [*Myers*, 1989].

543

4. Model Calculations

An example of the differential energy flux spectrum obtained at the location of the Mother platform when it is at an altitude of 260 km is shown in Figure 3. The two components of the fluxes shown are the flux streaming in the direction of the beam (down) and the flux streaming counter to the beam (up). The downward flux consists of two contributions. the primary electron beam which is seen with a peak at the beam energy. and the flux incident from above the spacecraft, seen at lower energies.

The fluxes as a function of altitude and for fixed energies are shown in Figure 4a for the 1-keV electron beam energy and in Figure 4b for 10-eV electrons. The spacecraft altitude is again 260 km as indicated on the figures and the beam is emitted downwards. The downward flux shown in Figure 4a is discontinuous at the spacecraft altitude. This fact simply reflects the location of the beam source at this altitude. If aimed downwards. a spectrometer mounted on the spacecraft will observe a value of the back-scattered flux corresponding to Φ_{up} at the spacecraft altitude. If the spectrometer is aimed upwards and in the opposite direction to the beam it will observe a flux corresponding to the value of the upper branch of Φ_{down} at the spacecraft altitude. The downward flux shown in Figure 4b is continuous because no beam electrons are emitted at 10 eV.

As can be seen from Figures 4a and 4b, energetic electron fluxes are generated along the magnetic field out to considerable distances from the spacecraft. At low altitudes the electron fluxes approach zero and become omni-directional because of scattering in the dense atmosphere. The upward flux decreases relatively slowly with altitude. This effect is caused by a decrease in the ambient neutral density or an increase in the mean free path which allow the electrons to escape almost freely. Similarly, the downward electron flux increases from essentially zero at high altitudes to large values at lower altitudes. The creation of electron fluxes extending along the direction of the magnetic field both above and below the payload to distances far beyond the payload potential sheath region is in qualitative agreement with optical observations made during the Excede 2 [O'Neil et al, 1978] and the Echo 7 [Winckler et al., 1989] sounding rocket experiments.

The current densities, $J^{BAI}(z_o)$, at the spacecraft location, z_o, can be found by integrating the return fluxes over energy. Since the fluxes and thereby the BAI return currents are proportional to the emitted beam current it is convenient to define the parameter Λ as the sum of the current densities from both directions normalized to the emitted beam current density.

$$\Lambda(z_o) = \frac{J_{down}^{BAI}(z_o) + J_{up}^{BAI}(z_o)}{J_{beam}} \tag{4}$$

As can be seen from (4), Λ represents a gain factor. In Figure 5 is shown the variation of Λ during the CHARGE-2 flight. The different values of Λ during the upleg and the downleg are caused by changes in $v_\perp$. During the upleg $v_\perp$ was larger than during the downleg.

The values shown in Figures 3-5 have been calculated assuming that only a small fraction of the flux is collected by the spacecraft. As shown in Neubert et al. [1990] the sheath area of the Mother, A, is about 12.8 m^2 when charged to 400 V. With the assumption that the flux-tube cross-sectional area is 100 m^2, the payload actually collects about 13% of the electrons in the flux-tube and thus the values shown in Figures 3-5 are slightly overestimated.

The return current to the Mother given by the NASCAP/LEO estimates (the passive current) is shown in Figure 6a as a function of the observed return current. For most of the values the model current is lower than the observed current. Extreme differences can be seen. especially for the data point marked with an asterisk. This observation was performed at a low altitude during the downleg. Here the model current is less than 1 mA while the observed return current was 36 mA.

Figure 6b shows an estimate of the return current when the BAI current is added to the passive current. The BAI current has been found from the relation

$$I_{BAI} = I_{beam} \cdot \Lambda \cdot \frac{A}{dx^2} \tag{5}$$

As can be seen from Figure 6b, the agreement between this new model estimate of the return current and the observed return current is much better. The data point marked with an asterisk is now lifted to a value slightly larger than the observed value.

5. SUMMARY

Under the simple assumption that the beam flux-tube has a cross-sectional area of 100 m^2, the total return current to the Mother payload is found to be in reasonable agreement with the observed return current. We also find that the predictions from the model of electron fluxes extending to large distances in the direction of the emitted beam as well as in the opposite direction is in qualitative agreement with optical observations performed in past experiments [*O'Neil et al,* 1978; *Winckler et al.,* 1989]. Similarly, the prediction of electron fluxes incident on the spacecraft from both hemispheres is in qualitative agreement with observations [*Winckler et al.,* 1975]. A quantitative investigation of the BAI currents generated during electron beam emissions in experiments other than the CHARGE-2 experiment will be reported in a separate publication.

One of the main shortcomings of the model is the uncertainty of the cross-sectional area of the beam flux-tube and the variation of the electron fluxes across this area. A more rigorous treatment of the problem would involve Monte Carlo techniques to determine the dimension and the distribution of electrons across the flux-tube.

We have shown that a hot electron distribution will be generated by the BAI. The observations of a hot component is then not an immediate evidence for BPI. In fact, the hot component generated through BAI may dominate the cold ambient plasma component and therefore be important for a realistic model of BPI. To illustrate this, we show in Figure 7 the beam current, I_{limit}, defined as the beam current for which $I_{BAI} = I_{thermal}$, as a function of altitude. The arrows indicate the upleg and downleg portions of the curve. In the region of high beam current, to the right of the curve, the BAI current is larger than the thermal current. This implies that in this region the plasma in the flux-tube around the beam and the payload is dominated by a hot component. This will be the case in particular for the forth-coming Charge-2B rocket experiment scheduled for 1991. Here, it will be attempted to emit beams with energies of 3 keV and currents of 3 A, with neutral gas releases and thruster emissions as means of enhancing the return current collection to the spacecraft.

ACKNOWLEDGEMENTS

REFERENCES

Banks, P. M., C. R. Chappell, and A. F. Nagy, A new model for the interaction of auroral electron beams with the atmosphere: spectral degradation, backscatter, optical emission, and ionization, *J. Geophys. Res.*, *79*, 1459, 1974.

Beard, D. B., and F. S. Johnson, Ionospheric limitations on attainable satellite potential, *J. Geophys. Res.*, *66*, 4113, 1961.

Bilitza, D., International reference ionosphere: Recent developments, *Radio Sci.*, *21*, 343, 1986.

Frank, L. A., W. R. Paterson, M. Ashour-Abdalla, D. Schreiver, W. S. Kurth, D. A. Gurnett, N. Omidi, P. M. Banks, R. I. Bush, and W. J. Raitt, Electron velocity distributions and plasma waves associated with the injection of an electron beam into the ionosphere, *J. Geophys. Res.*, *94*, 6995, 1989.

Gilchrist, B. E., P. M. Banks, T. Neubert, P. R. Williamson, N. B. Myers, W. J. Raitt, and S. Sasaki, Electron collection enhancement arising from neutral gas jets on a charged vehicle in the ionosphere, *J. Geophys. Res.*, *95*, 2469, 1990.

Hedin, A. E., MSIS-86 thermospheric model, *J. Geophys. Res.*, *92*, 4649, 1987.

Langmuir, I., and K. B. Blodgett, Current limited by space charge flow between concentric spheres, *Phys. Rev.*, *24*, 49-59, 1924.

Linson, L. M., Charge neutralization as studied experimentally and theoretically, in *Artificial Particle Beams in Space Plasma Studies*, edited by B. Grandal, p. 573, Plenum Press, New York, 1982.

Mandell, M. J., J. R. Lilley, Jr., I. Katz, T. Neubert, and N. B. Myers, Computer modelling of current collection by the CHARGE-2 mother payload, *Geophys. Res. Lett.*, *17*, 135, 1990.

Myers, N. B., W. J. Raitt, B. E. Gilchrist, P. M. Banks, T. Neubert, P. R. Williamson, and S. Sasaki, A comparison of current - voltage relationships of collectors in the ionosphere with and without electron beam emission, *Geophys. Res. Lett.*, *16*, 365-368, 1989.

Myers, N. B., Studies of the system-environment interaction by electron beam emission from a sounding rocket payload in the ionosphere, *Ph.D. Dissertation*, Utah State University, Center for Atmospheric and Space Sciences, Logan, Utah, 1989.

Neubert, T., P. M. Banks, B. E. Gilchrist, A. C. Fraser-Smith, P. R. Williamson, W. J. Raitt, N. B. Myers, and S. Sasaki, The interaction of an artificial electron beam with the earth's upper atmosphere: Effects on spacecraft charging and the near-plasma environment, *J. Geophys. Res.*, in press, 1990.

O'Neil, R.R., O. Shepherd, W. P. Reidy, J. W. Carpenter, T. N. Davis, D. Newell, J. C. Ulwick, and A. T. Stair, Jr., Excede 2 test, an artificial auroral experiment: Ground-based optical measurements, *J. Geophys. Res.*, *83*, 3281, 1978.

Parker, L. W., and B. L. Murphy, Potential buildup on an electron-emitting satellite in the ionosphere, *J. Geophys. Res.*, *74*, 1631-1636, 1967.

Sasaki, S., K. I. Oyama, N. Kawashima, T. Obayashi, K. Hirao, W. J. Raitt, N. B. Myers, P. R. Williamson, P. M. Banks, and W. F. Sharp, Tethered rocket experiment (Charge 2): Initial results on electrodynamics, *Radio Sci.*, *23*, 975-988, 1988.

Waterman, J., K. Wilhelm, K. M. Torkar, and W. Riedler, Space shuttle charging or beam-plasma discharge: what can electron spectrometer observations contribute to solving the question ?, *J. Geophys. Res.*, *93*,

4134, 1988.

Winckler, J. R., R. L. Arnoldy, and R. A. Hendrickson, Echo 2: A study of electron beams injected into the high-latitude ionosphere from a large sounding rocket, *J. Geophys. Res.*, *80*, 2083, 1975.

Winckler, J. R., P. R. Malcolm, R. L. Arnoldy, W. J. Burke, K. N. Erickson, J. Ernstmeyer, R. C. Franz, T. J. Hallinan, P. J. Kellogg, S. J. Monson, K. A. Lynch, G. Murphy, and R. J. Nemzek, ECHO 7 An electron beam experiment in the Magnetosphere, *EOS*, *70*, 657, 1989.

FIGURE CAPTIONS

Figure 1. Configuration of the CHARGE-2 payload and the electron current system around the payload during electron beam emissions. I_{beam} is the emitted beam electron current, I_{tether} is the electron current in the tether, I_M is the return current to the Mother, and I_D is the return current to the Daughter.

Figure 2. Tether to beam current ratio, I_{tether}/I_{beam}, as a function of altitude. SQ2 through SQ6 marks in time-sequential order the experimental sequences performed during the flight. Also indicated is the ratio of the Daughter collecting area to the total collecting area of Mother and Daughter, A_D/A_{total}.

Figure 3. The upward and the downward differential electron flux as a function of energy at the spacecraft altitude (260 km). The beam is emitted downward with an energy of 1 keV and a current of 100 mA (the fluxes scale linearly with the beam current). The primary beam is seen as the peak at 1 keV in the downward flux.

Figure 4. The differential electron fluxes as function of altitude for the same parameters used in Figure 3. (a) 1-keV electrons and (b) 10-eV electrons.

Figure 5. Λ as a function of altitude.

Figure 6. Model estimates of the return current to the Mother vs. observed return current. a) The model assumes passive current collection only (NASCAP/LEO estimates). b) The model includes passive and BAI return currents.

Figure 7. The beam current for which the thermal current to the Mother equals the BAI current as a function of altitude. The arrows indicate the upleg and downleg portions of the flight.

CHARGE - 2

Figure 1

Figure 2

Charge 2: Altitude = 260.0 km

Φ_{up}

Φ_{down}

Figure 3

a) Charge 2: E = 1.0 keV

b) Charge 2: E = 10.0 eV

Figure 4

CHARGE - 2
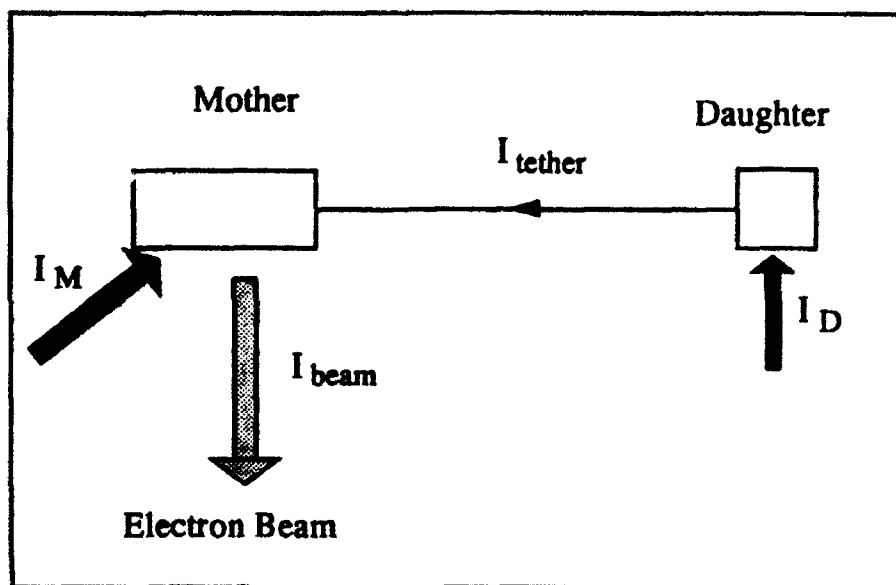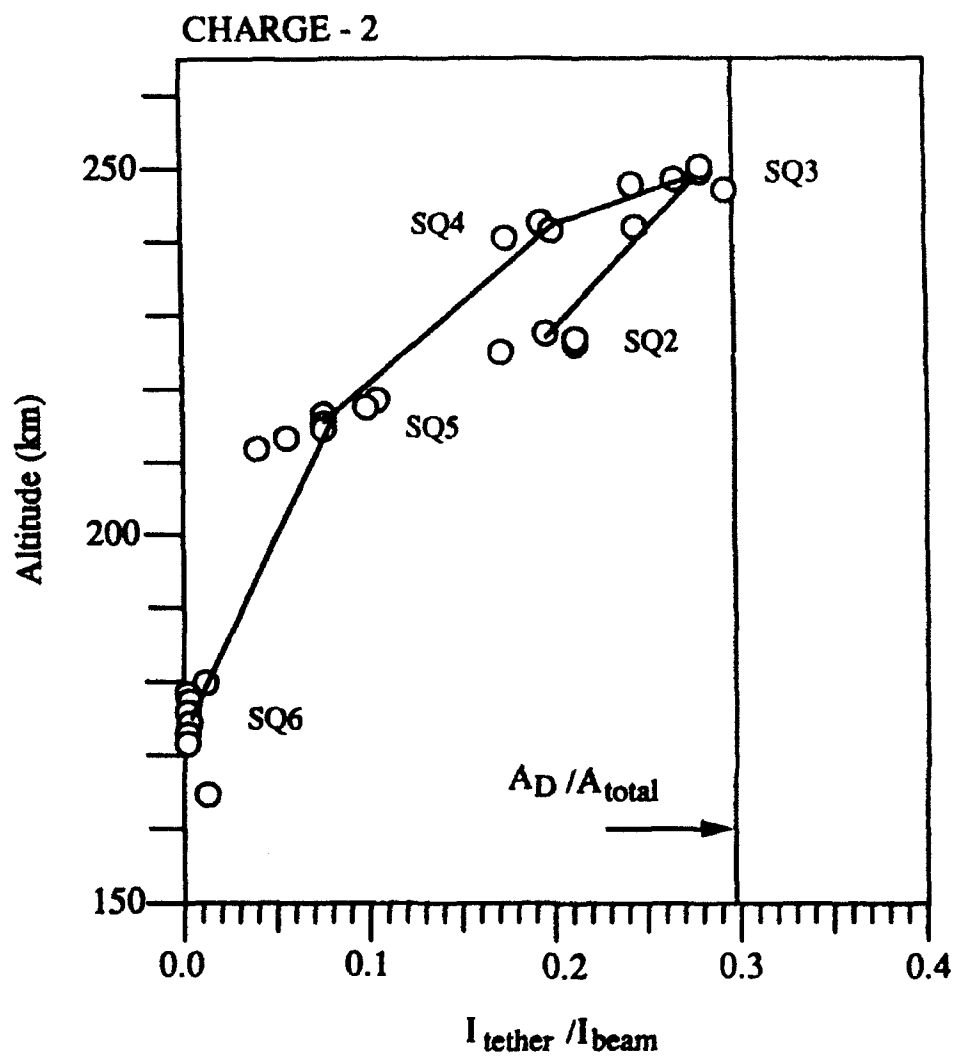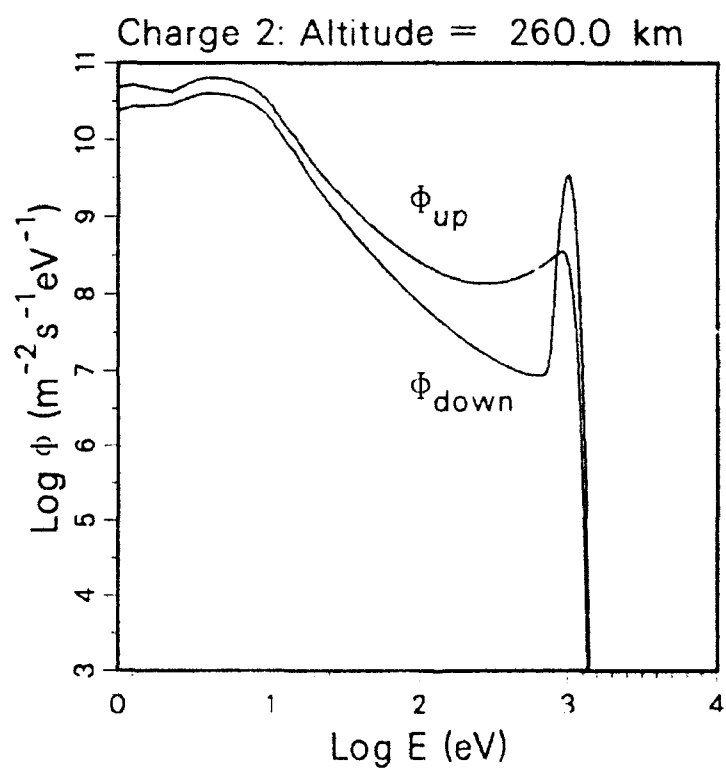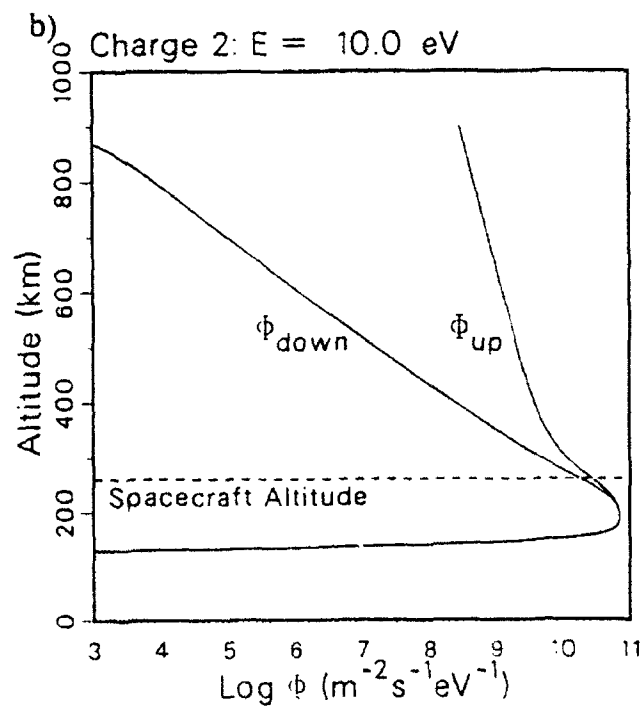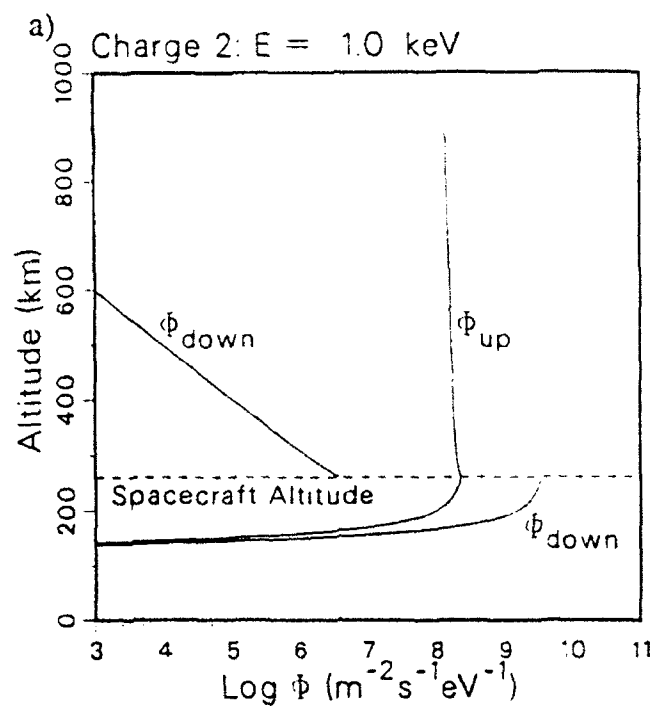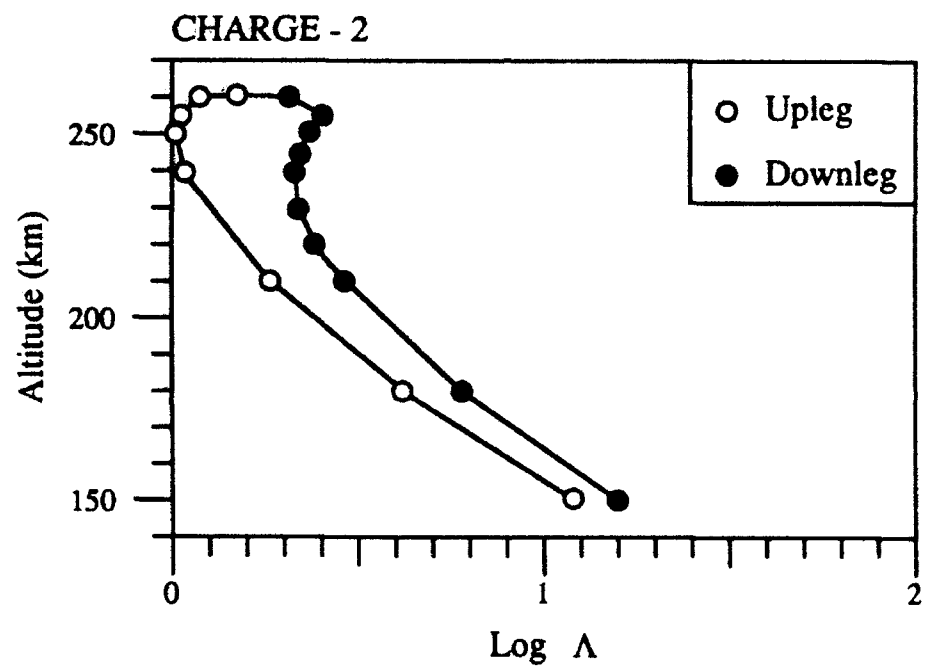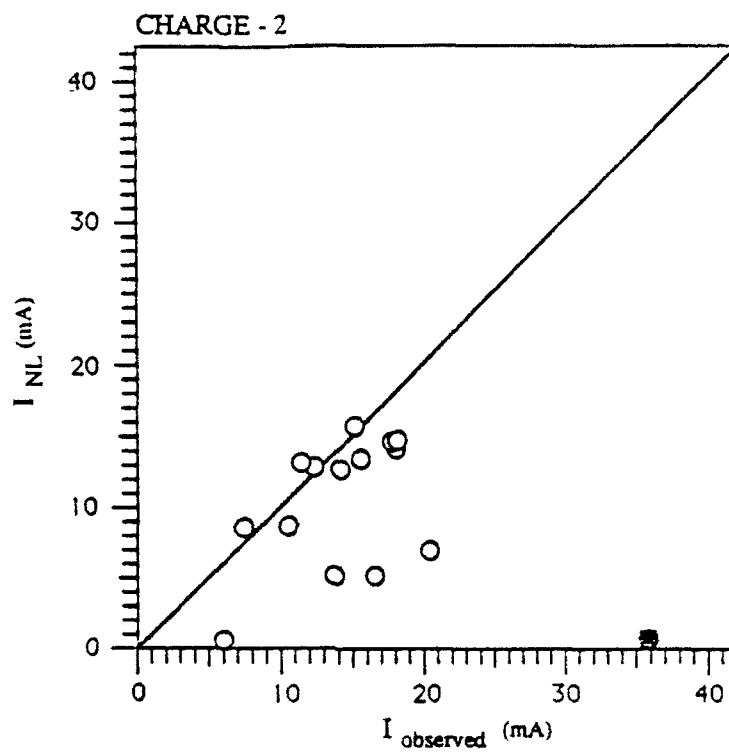
Figure 5

Figure 6a

Figure 6b
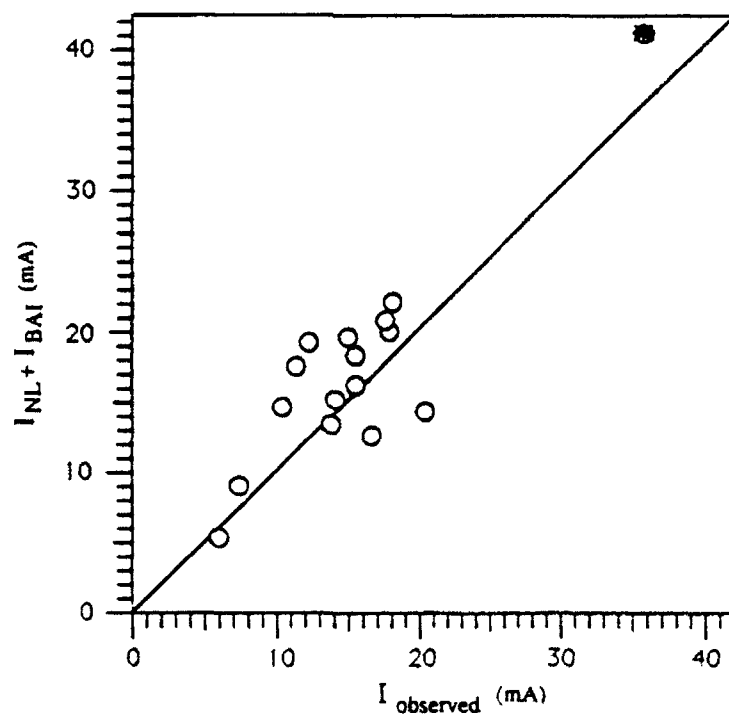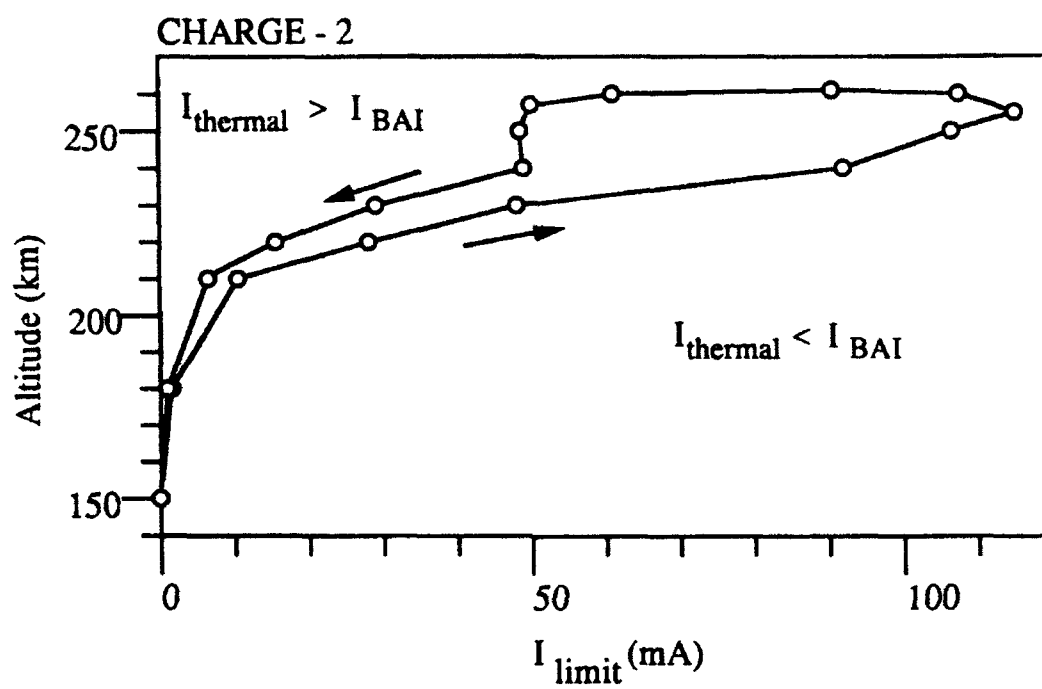
Figure 7

NEUTRAL ENVIRONMENT WITH PLASMA INTERACTIONS MONITORING
SYSTEM ON SPACE STATION (NEWPIMS)

Elden C. Whipple
Center for Astrophysics and Space Science
University of California at San Diego
La Jolla, CA 92093

and

Joseph N. Barfield
Southwest Research Institute
San Antonio, TX 78284

ABSTRACT

The U. S. Space Station Freedom will be the first large-scale, permanent, manned space operation. The size of the Station, variety of materials and resources, and the many different vehicles and payloads in its vicinity will present significant perturbations to the ambient environment. In addition, Station operations will be affected in yet undefined ways by the environment.

A system to provide comprehensive environmental and interaction measurements on Space Station is planned. This system, called the Neutral Environment With Plasma Interactions Monitoring System, or

"NEWPIMS"

will monitor the impact of the Station on the environment and vice versa. NEWPIMS will supply a long-term database and interaction models to the Space Station community that can be employed to analyze Station/environment interactions and to unfold natural from induced changes in the Station environment. The system will include neutral environment instruments, electric and magnetic field sensors, charged particle detectors, and remote sensing of radiation and particulates. Sets of instruments will be provided by the international community and permanently deployed at strategic locations on the Station.

I. THE SPACE STATION

The Space Station will present unprecedented challenges in U. S. space activities. It will be the first large-scale, permanent space operation. The Space Station will provide structural support, electrical energy, data processing, communication and life-support resources. It will serve as a vehicle fueling and repair facility. Proximate traffic will include the Space Shuttle, the Orbital Maneuvering Vehicle, and other as-yet undeveloped space vehicles. Thus, the Space Station will be a large, complex, busy structure in space. The size of the Space Station, the variety of materials and resources, and the many different vehicles and payloads in its vicinity will present significant perturbations to the ambient environment. Additionally, the operations on the Space Station will be affected in yet undefined ways by the environment.

Operationally, the large scale of the Space Station, the inclusion of many high-current electrical paths, and the large number of simultaneous communications links will produce many environmental perturbations, the nature and magnitude of which are quite uncertain. As a result, the environment of the Space Station will need to be verified as the Station is constructed, and as operations commence and continue. A comprehensive set of measurements of the resulting environment of the Space Station will be needed for the life of the Station, to aid in compensating for perturbations experienced and for design guidance in Station growth.

Users of the Space Station will have a critical need for knowledge of the actual environment within which measurements will be made. For instance, electrical noise levels may exceed the sensitivity of many instruments at various locations on the Station structure. Telemetry and sensor signals may be masked by the noise, leading to false conclusions due to defective data. Thus, a continuous ongoing data base that characterizes the environmental parameters of and around the Space Station as functions of time and location is critically needed.

In addition to the above needs, there also is a strong need for the monitoring of the Space Station "weather". That is, the operators and users will require an ongoing characterization of the environmental conditions within which events occur and are measured. Such a characterization will be required to separate the natural episodic changes at the Station from induced changes.

II.   ENVIRONMENT/SPACE-STATION INTERACTIONS

1. Release of gases

The Space Station will release gases by outgassing from materials, by venting, by leakage from pressurized volumes, by the operation of engines and thrusters, by extra-vehicular activity (EVA) and the use of airlocks. Additional gases will be released during shuttle and orbiting maneuverable vehicle (OMV) rendezvous. As a result there will be a more-or-less continual gas cloud around the Space Station which will have a much higher concentration than the natural environment at the Space Station altitude. The gas cloud will also have a composition different from the natural environment.

This cloud of gas will scatter and absorb light. It will also emit radiation by spontaneous and induced emission processes. The gas can be ionized by sunlight and by energetic particles to produce ions and electrons. The constituents in the gas will react with each other, with the surface of the Space Station, and with the constituents in the natural environment.

2. Release of particulate matter

In addition to releasing gases, the Space Station will also release copious amounts of particulate matter in the form of dust swept along with the venting gases. Released water vapor can condense and freeze into ice grains. These particles will also absorb, scatter, and emit light. They can become electrically charged and then re-attracted to the Space Station where they can impact, react with, and adhere to surfaces and change the surface properties.

3. Impact of environmental matter

Environmental particulate matter including orbital debris as well as micrometeors will impact the space station, causing erosion, sputtering, and deposition. Again, the surface properties of the

Space Station can be modified by these impacts. The impact of environmental atoms, especially atomic oxygen, can produce surface reactions, cause surface erosion, and induce emissions such as the "ram surface glow". Environmental ions, electrons, and neutral atoms can also react chemically with the outgassing material in various ways such as by charge exchange, attachment, disassociation, ionization, etc. Energetic ions and electrons from the environment can penetrate the surface, erode materials, and be deposited in sub-surface layers.

4. Electrical interactions

The Space Station itself will charge electrically because of the impact of ions and electrons from the natural and induced environment, and because of photoemission from its surfaces. There will be a plasma sheath around the Space Station and a plasma wake behind it caused by its orbital motion through the plasma environment. Surfaces such as the solar arrays which may be charged to large electrical potentials will interact strongly with the local plasma. There will be leakage currents across insulating surfaces and possibly arcing and multipacting.

The motion of the Space Station through the earth's magnetic field will induce an electric field of approximately 0.25 volts/meter in its vicinity which will distort the plasma sheath and wake. This electric field will accelerate local charged particles to energies comparable to the potential drop across the Station, i.e. to energies on the order of tens of electron-volts for singly charged particles, and to higher energies for particles with multiple charges.

5. Electrical noise

The Space Station will be a source of electrical noise from the power, communications, and other electrical activity on board. As a result there will be a large electromgnetic noise field in its vicinity which will interact with the local plasma, possibly interfering with experiments, causing plasma waves, and accelerating charged particles.

6. Long-term changes

The presence of the Space Station for many years in orbit could possibly induce long-term secular changes in the environment. The release of gases over many years could represent a significant source of new material for the earth's ionosphere. The release of particulate matter could contribute significantly to the accumulation of orbital debris at spacecraft altitudes.

III. THE PIMS STUDY

1. Initial study phase

The "Plasma Interaction Monitoring System" (PIMS) study was originally formed in February, 1988, under the auspices of the Space Station Plasma Interactions and Effects (SSPIE) Working Group chaired by Dr. Carolyn Purvis of the NASA Lewis Research Center. The PIMS study team interacted closely with that working group and derived the basic PIMS charter with inputs from SSPIE.

They were charged with five tasks:
  (1) To define the objectives of environmental monitoring at SSF;
  (2) To identify environmental measurements required to monitor the plasma
      environments at SSF;
  (3) To recommend instrumentation necessary for SSF environment monitoring;
  (4) To identify possible system mechanical configuration, module placement,
      and deployment sequence;
  (5) To initiate and coordinate the international "NEWPIMS" program.

2. The PIMS Study Team

The PIMS study team members were selected to provide guidance to the study from many perspectives. The team has collective in-depth experience in measurements of space plasmas and fields, neutral gases, and particulates; design and development of space flight instrumentation; and modelling of the space environment. Team members were also selected who have extensive backgrounds in simulation of space environment interactions and laboratory experimentation with basic plasma physics processes.

Table 1 shows the PIMS team members and the additions to the team for Phase 2 when the study was renamed "NEWPIMS".

3. Evolution of the PIMS/NEWPIMS Study

June 87   Space Station Plasma Interactions and Effects Working Group was Established

October 87   Space Station external contamination study was started focussing on neutral gases
             and particulates, and visible and infrared emissions.

February 88 Original PIMS study focussed on charged particles and fields.

July 88   PIMS team and External Contamination Study team agreed that the PIMS system
             should include measurements of neutral environment interactions.

February 89 PIMS Phase 2 study was initiated. Study team expanded to include selected External
             Contamination Study members and international representatives.

August 89   PIMS name changed to NEWPIMS

October 89   First international NEWPIMS workshop in Tokyo, Japan.

4. Present NEWPIMS Objectives

(1) Space Station:
    -Verify Space Station environment specifications;
    -Satisfy requirements for external environment monitors for individual work packages;
    -Develop a long-term environment data base.

(2) Experiment Support:
    -Monitor environment perturbations created by active experiments;
    -Monitor environment in support of experiments;
    -Monitor environment for unacceptable contamination levels.

(3) Experiment Operations:
    -Monitor experiment problems;
    -Provide real-time information on contamination levels.

(4) Space Station/Environment Interactions:
    -Study electrical charging of large space structures;
    -Study wake and sheath;
    -Study electromagnetic field interactions.

(5) Historical Analyses:
    -Study environmental variability;
    -Assess environmental change;
    -Analyze environmental response.

(6) Problem Detection and Location:
    -Detect and locate leaks in coolant loops;
    -Detect and locate seal failures in modules and nodes;
    -Detect and locate power system arcing and corona;
    -Detect and locate material degradation.

(7) Instrument Design:
    -Improve instruments for environment extremes;
    -Improve instruments based on perturbation levels;
    -Design instruments for baseline background;
    -Design to identify and locate contamination sources;

(8) Space Station Growth Development:
    -Provide information on material/system deterioration;
    -Provide perturbation variability;
    -Provide models of environment and interactions.

IV. THE PROPOSED NEWPIMS SYSTEM

The NEWPIMS system consists of sets of instrument packages; their deployment and operation on Space Station; acquisition of data and its distribution and archiving; and modelling of the Space Station environment and of the environment/Space Station interactions.

Table 2 shows the set of instruments which have been identified for NEWPIMS instrument packages and the allocation of instruments for the first three instrument packages.

Figure 1 shows the first three NEWPIMS units and Figure 2 shows the proposed placement of the first three units and the possible locations for two later units on Space Station. Five NEWPIMS units are now envisioned for Space Station Freedom. The placement of the units will be in two phases, three units in the initial phase, and possibly two additional units in a growth phase. The placement is such that instruments may be directed toward both solar arrays, laboratory and habitat modules, into and orthogonal to the velocity ram and velocity wake, and may scan through payload attach points. Additionally, a NEWPIMS unit is proposed for the Japanese Experiment Module Exposed Facility and will obtain environmental information from this location. It is highly desirable to include a sixth NEWPIMS as a mobile system (which may be maneuvered by the Mobile Service Center) that can be moved along the truss structure and deployed some distance away from the truss itself.

The NEWPIMS concept will impose minimum requirments on the Space Station and its systems. Each unit has a mass of about 100 kg and will require about 100 watts of power and 100 kilobits per second for data. Thermal control will be handled by the NEWPIMS units themselves. A preliminary assessment has shown that the units may be attached at the truss nodes using a simple screw adapter and plate. Periodic command rates of 1 kilobit per second or less will be required to rotate the units and to change instrument settings. Special autonomous, low-data-rate configurations are being studied for possible deployment in the early launch phase of Space Station when no power or data resources will be available.

Figure 3 illustrates the NEWPIMS system consisting of the instrument packages on the Space Station, the data base, the environment and interaction models, and the various users. The data base must have sufficient flexibility to provide environmental data despite changing Space Station configurations and payload manifests, operational perturbations, and natural events. The data base must also provide for the long term archiving of data so that environmental trend analyses may be performed. It is therefore important that this system be addressed and a first order definition established early.

V. NEWPIMS STATUS

Discussions are being carried out with possible international partners.

Costing studies are in process.

OSSA and OSS are discussing possible NEWPIMS implementation.

STUDY TEAM

NAME	AFFILIATION	PRIMARY INTEREST
* JOE BARFIELD	SOUTHWEST RESEARCH INSTITUTE	MAGNETIC VARIATIONS
* JIM BURCH	SOUTHWEST RESEARCH INSTITUTE	SPACE PLASMAS
* GEORGE CARIGNAN	UNIVERSITY OF MICHIGAN	NEUTRAL SPECTROMETRY
* NICK EAKER	SOUTHWEST RESEARCH INSTITUTE	SYSTEM ENGINEERING
* IRA KATZ	S-CUBED	ENVIRONMENT MODELING
*** DAVE KENDALL	CANADA	ATMOSPHERIC CHEMISTRY & EMISSIONS
** BILL KURTH	UNIVERSITY OF IOWA	SPACE PLASMAS
*** BERNT MAEHLUM	ESA (EUROPE)	SPACE PLASMAS
* GERALD MURPHY	JET PROPULSION LABORATORY	ELECTROMAGNETIC WAVES
* RAY RANTANEN	SCIENCE AND ENGINEERING ASSOC	ENVIRONMENT MODELING
*** SUSUMU SASAKI	ISAS (JAPAN)	SPACE PLASMAS
** JIM SPANN	MARSHALL SPACE FLIGHT CENTER	NEUTRAL COMPOSITION & DYNAMICS
* JIM SULLIVAN	MIT	DATA MANAGEMENT
* BILL TAYLOR	TRW	ELECTRIC & MAGNETIC FIELDS
** MARSHA TORR	MARSHALL SPACE FLIGHT CENTER	NEUTRAL COMPOSITION & DYNAMICS
* HUNTER WAITE	SOUTHWEST RESEARCH INSTITUTE	SPACE PLASMAS
* ELDEN WHIPPLE	UCSD	THEORETICAL STUDIES
* DAVE YOUNG	SOUTHWEST RESEARCH INSTITUTE	ION SPECTROMETRY

* Original PIMS Team
** U.S. Representative added for Phase 2
***International Representative added for Phase 2

TABLE 1

562

NEUTRAL ENVIRONMENT WITH PLASMA INTERACTION SYSTEM (NEMPIMS)
INSTRUMENT DEPLOYMENT SCHEDULE

INSTRUMENTS	UNIT 1	UNIT 2	UNIT 3
LANGMUIR PROBE (electron density and temp)	▲	▲	▲
PRESSURE GAUGE (total pressure)	▲	▲	▲
QCM (6/UNIT) (deposition rates)	▲	▲	▲
NEUTRAL MASS SPECTROMETER (neutral gas)		▲	
ELECTRON SPECTROMETER (energetic electrons)		▲ (LOW E)	▲ (HIGH E)
THERMAL ION MASS SPECTROMETER (ions)		▲	▲
MEDIUM ION MASS SPECTROMETER (ions)		▲	▲
MAGNETOMETER (magnetic field)	▲	▲	
ELECTRIC FIELD MONITOR (electric field)	▲	▲	
ION/NEUTRAL MASS SPECTROMETER (ion/neutral)	▲	▲	
ENERGETIC PARTICLE DETECTOR (radiation)	▲		
NUV/VUV SPECTROMETER (ultraviolet)	▲		
VISIBLE SPECTROMETER (visible)	▲		
NEAR IR SPECTROMETER (infrared)		▲	▲
LASER RADAR (particulates)		▲	

TABLE 2

563

NEWPIMS UNITS

NEWPIMS Unit 1

THERMAL CONTROL COVER NOT SHOWN
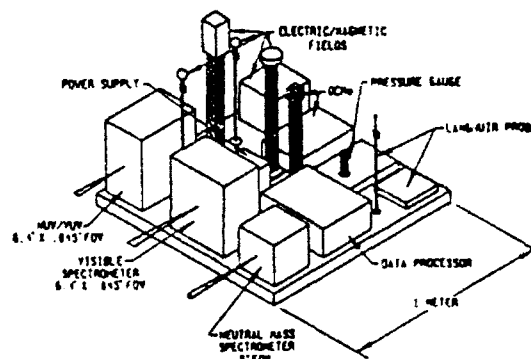
NEWPIMS Unit 2

THERMAL CONTROL COVER REMOVED
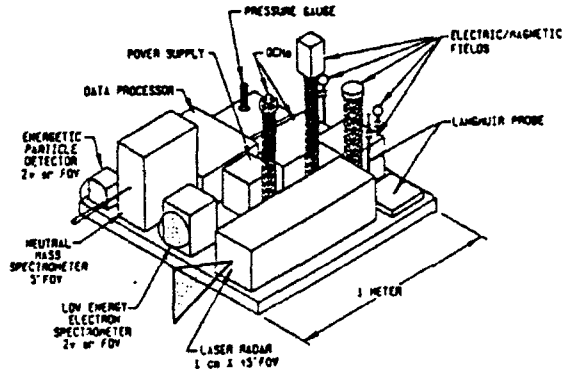
NEWPIMS Unit 3

THERMAL CONTROL COVER REMOVED
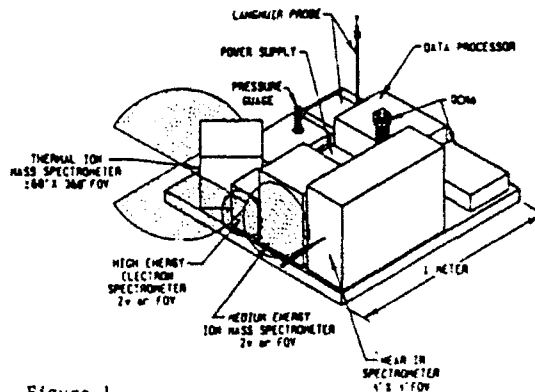
Figure 1
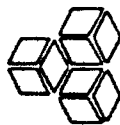
newPIMS With 3 Units
Provides Adequate Measurements Of The Space Station Environment

☒ MAXWELL

Objective : Determine minimum units necessary to monitor the SpaceStation environment.

Solution : 3 initial units with fields of view covering

    left, middle, & right

    top & bottom

    solar arrays & habitats

  2 units later on to measure

    JEM

    habitat wake region

Rational : Multiple units required because

- station so large (100+ meters) that single location would give misleading results.

- multiple units necessary to correlate with global models of station environment

- 2 axis platforms reduce numbers of units by increasing fields of view
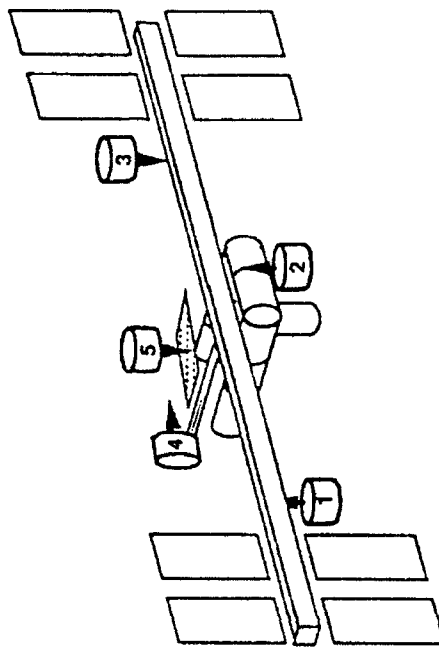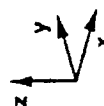
newPIMS will combine neutral and plasma monitors on pointable platforms to monitor both contaminant levels and locate their sources

PIMS 8-89

Figure 2

565

NEWPIMS DATABASE AND MODELLING SYSTEM
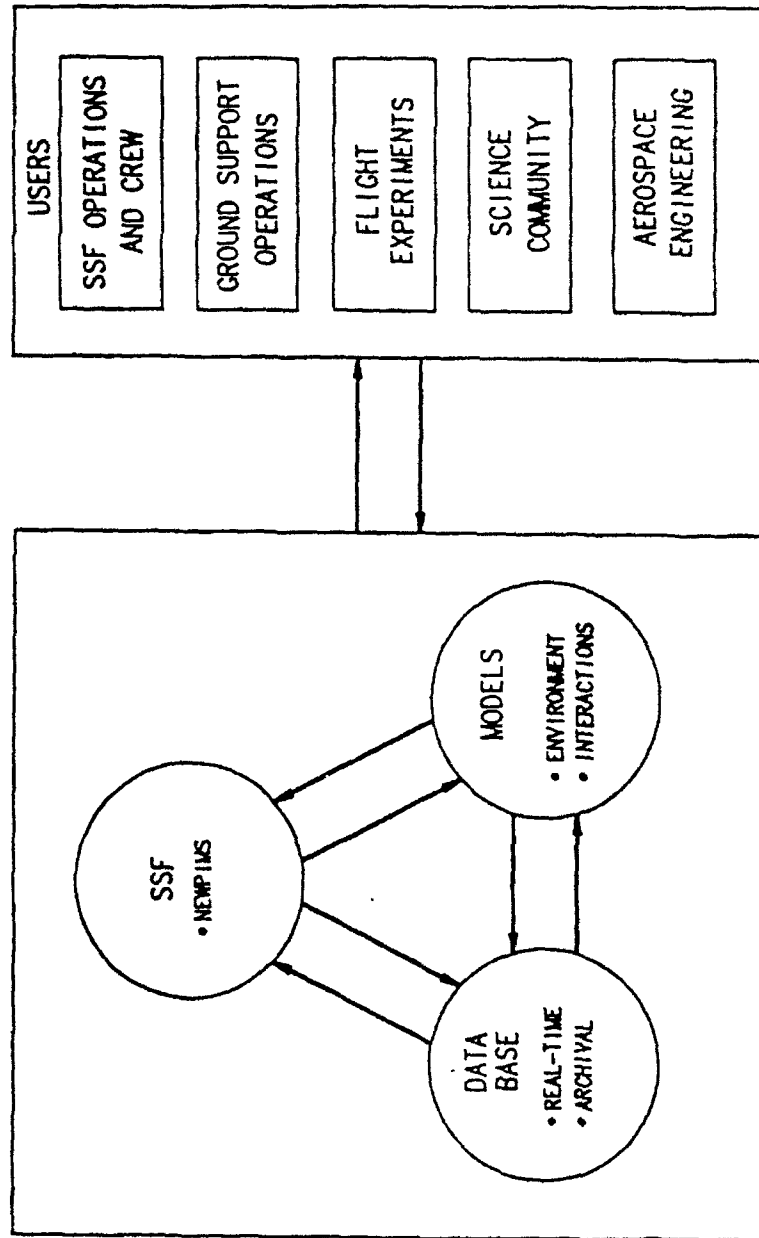
Figure 3

BEAR Electrostatic Analyzer: Description and Laboratory Results

Douglas W. Potter, Hugh R. Anderson, Joseph R. Olson

Science Applications International Corporation
13400B Northup Way, Suite 36, Bellevue, Washington   98005

3 January 1990

The Electrostatic Analyzer (ESA) measured the intensity of charged particles returning to the BEAR payload during flight on 13 July 1989. These particles form part or all of the current that returns to the payload to neutralize the charge ejected with the beam. By measuring the return flux with high time resolution, we can study the physics of charging processes. However, the need for high time resolution and sufficient statistics to make a good measurement make design of an appropriate instrument difficult. We solved the major problems and built an instrument with one microsecond time resolution and adequate energy resolution and response.

To support flight measurements, we made a series of measurements in a large plasma chamber at the University of Maryland. The measurements indicate that under most conditions, the level of charging can be determined quite accurately by the Electrostatic Analyzer.

INTRODUCTION

The *geometric factor* of a particle spectrometer is the ratio of the counting rate of the detecting device to the incoming particle intensity in physical units, typically particles/sec-cm^2-ster-eV. The rate must be large enough to pass sufficient particles within the appropriate counting interval to be statistically significant yet low enough to not saturate the detector at its maximum counting rate, typically on the order of 10 MHz. Above the maximum counting rate, the detector typically produces the maximum rate; then, as the input increases still higher, the output drops to zero.

For BEAR, we wanted to get high time resolution to allow examination of the rapid charging process. With the charging process expected to occur on a time scale the order of microseconds or shorter and with a beam pulse only 50 microseconds long, we wanted the time resolution to be one microsecond. With the considerations above, this gives a very small window for accurate measurements. A counting rate of 1 MHz is one count in a microsecond, not really enough to be statistically significant. At ten times that, the detector saturates.

Unfortunately, no theory is available to accurately predict the extremes of intensity. In fact, small changes in assumptions about the nature of the expected environment make changes in the expected intensity of several orders of magnitude. It did appear however, that with most estimates, it would require a very large detector to get a significant number of counts in a microsecond. Since physical space was limited, we elected to make the geometric factors as large as possible within the physical constraints. We reasoned that even if the estimates of high intensity were accurate, it is better to saturate the detector and know that a signal is there than get no signal at all. With limited telemetry (and limited processing capability), we developed a time sampling scheme that called for *one microsecond samples* during and shortly after the pulse, then longer samples to cover most of the interpulse period of 200 milliseconds.

567

The *energy range* should cover the maximum expected charging potential and overlap the Langmuir probe instrument at the low end. The trade off on energy resolution is that the wider the range, the higher the geometric factor and the lower the number of channels needed to cover a given energy range. A narrower range gives more information on the actual energy. We selected an *energy resolution of 23%*. To avoid convolving time and energy dependence it is absolutely necessary to hold the *selected energy constant* during a given beam pulse cycle. This also helps if there are not enough counts to be statistically significant in one microsecond; we can add together samples until we do get enough counts. Ideally we would use many spectrometers, each of fixed energy, to cover the energy range of interest. Unfortunately limited resources precluded this, so the energy selected by each of the five spectrometers steps after sampling before each new beam pulse. Two detectors cover each of the two species, positive ions and electrons. One of the two covers the range 20-300 eV, the other 200-3000 eV. The fifth spectrometer is a retarding potential analyzer that measures the integral flux above the selected energy.

INSTRUMENTATION

The instrument envelope is a rectangular case 11" x 7" x 10" plus a small top section. Particles are admitted through apertures in the front face. A lining of conetic alloy reduces the magnetic field inside to <10% of the external value.
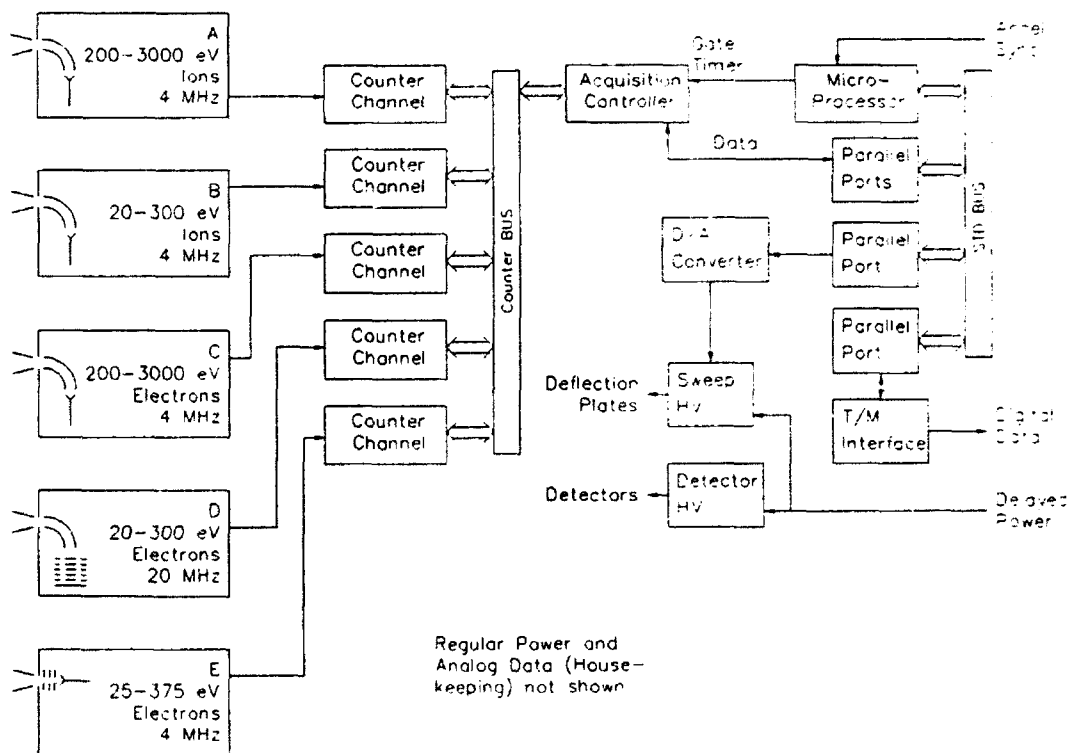
Figure 1. ESA Block Diagram.

Figure 1 is a functional block diagram. There are four curved plate analyzers, two each for electrons and ions. One of each species covers 20-300 eV, the other covers 200-3000 eV. The plates are sections of spheres using 90 degree deflection angle. By focussing a long entrance slit onto the short exit slit, this geometry allows a large geometric factor. The fifth channel is a retarding potential analyzer (RPA) that covers the range 25-375 eV. The geometric factor of the deflection analyzers is about $0.01E$ [cm²-ster] with E the center energy of the passband, and the factor of the RPA is 0.01 [cm²-ster] with all energies above the selected threshold accepted. Using the RPA partially overcomes the problem of not looking at all energies on each beam pulse.

All but the low energy electron channel D use a conventional channel electron multiplier (Galileo channeltron) and a 4 MHz Amptek preamplifier/discriminator. The low energy electron analyzer uses a focussed mesh electron multiplier made by Johnston Labs and a 50 MHz preamplifier/discriminator made by Modern Instrumentation Technology. All multipliers run in the pulse counting mode.

The accelerator sync pulse (prefire pulse), which comes 448 microseconds before the beam-on (rf) pulse, triggers data collection. The microprocessor initializes each of the counter channels and arranges for them to collect data. As Figure 2 shows, two microseconds before the rf pulse, the ESA starts collecting data. First it collects counts in 150 one microsecond long sample gates, then in a variety of longer gates up to one millisecond. The 60 microsecond wide rf pulse represents the time when the rf acceleration is on in the accelerator. Under ideal conditions, the actual pulse comes up to full output 10 microseconds after the rf pulse starts, then ends at the end of the rf pulse.
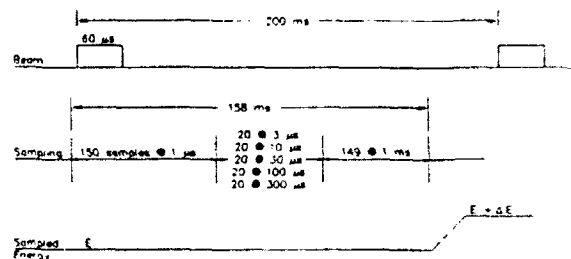
Figure 2. ESA Data Sampling Scheme.

The energy that the analyzers sample is constant for each beam cycle, then steps to the next higher energy for the next beam pulse. In flight, the steps are logarithmically spaced 23% apart - it takes 14 steps to cover the energy range. For most of the laboratory data, we used a mode with 10% spaced steps - which takes 29 steps to cover the energy range.

The Ground Support Equipment (GSE) operates the ESA separate from the BEAR payload by simulating the power and telemetry interface to the instrument and providing the sync signals in lieu of the accelerator. A fiber optic link and isolation power transformer connect elements of the GSE so that the ESA can operate at a potential elevated from laboratory ground.

The GSE uses a PC-AT as a controller and to display and record data from the ESA. This PC generates spectral figures, displays numerical data, and records data on hard disk and tape cassette for later analysis. Figure 3 is a schematic of both the data collection cycle and our typical data display. Note that energy increases towards the front of the plot.

The GSE could also accept data from the telemetry system and display it in real time using the same software as during standalone operation. This allowed us to monitor the behavior of the flight instrument during integrated tests with the entire payload, and to study data promptly after the flight and during laboratory tests.

TEST AND CALIBRATION

Most of the spectrometer calibration was done with spectrometer units outside the ESA. The fast time sampling is not needed for these measurements, and the separate spectrometers can be mounted and rotated in the electron and ion beams of the SAIC calibration system. The experimental results agree well with the calculated response. The calculated response [Morse, 1989] is an expansion of Gosling *et al.* [1984].
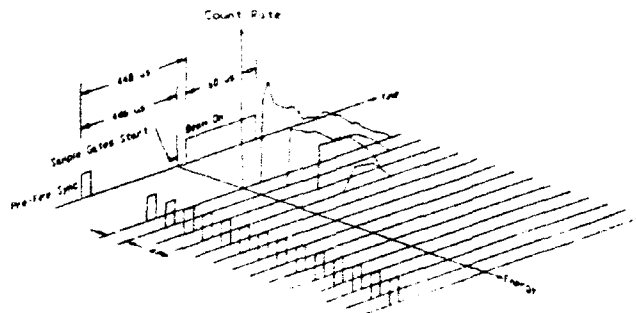
Figure 3. Schematic of GSE Data Display.

OBSERVATIONS

To help characterize the instrument's response to various charging levels, we performed experiments in a large (2m D x 4m) plasma chamber at the University of Maryland (Figure 4). A plasma source in a smaller chamber at one end used 50 eV electrons from a hot filament to ionize nitrogen gas. This filled the main chamber with plasma of density 10^3 to 3×10^5 cm^{-3}. A langmuir probe furnished with the chamber measured the density. External field coils nulled the geomagnetic field (within 10%) while a second set of coils applied an axial field up to 30 gauss. Most of our measurements were with the geomagnetic field nulled and an axial field of 0.5 gauss.
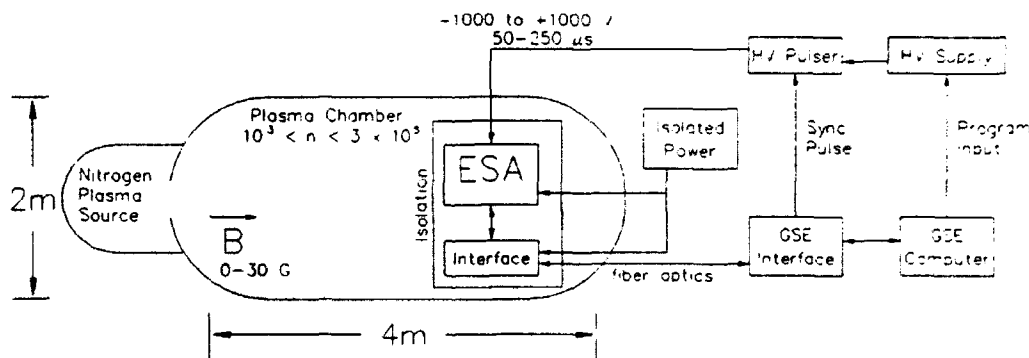
Figure 4. Experimental Setup at the University of Maryland. The ESA can be rotated so that the magnetic field is parallel or perpendicular to the apertures.

We suspended the ESA on the axis of the chamber about 1 meter from the end opposite the plasma source. Signal connections through optical fiber and a power transformer kept the instrument isolated from the chamber walls (laboratory ground). For most measurements the ESA either faced away from the source so that detected particles moved parallel to the magnetic field or faced the chamber side wall so that detected particles moved perpendicular to the field.

Through a triggered switch we applied voltage pulses of various magnitudes up to 1000 volts of both polarities to the instrument while varying the plasma density. The switch either clamped the ESA at ground potential or at the power supply potential with rise and fall times < 100 nanoseconds. The pulse length was either 50 or 250 microseconds.

We emphasize that this particular setup does not accurately mimic the situation in space with an ejected beam because the pulse amplitude is a controlled potential, not a current. Thus these laboratory experiments investigate how the ESA senses a known potential under various conditions, not what that potential is as a function of current to the ESA. Of course the presence of chamber walls does not mimic space either. The dimensions of the chamber were large compared with debye length and electron gyro radius, but small compared with ion gyro radius. The range of plasma densities did cover that expected during the BEAR flight. As a matter of fact the ionospheric density during flight ranged from 1 to 3 x 10^3 /cm^3, the low end of the laboratory range.
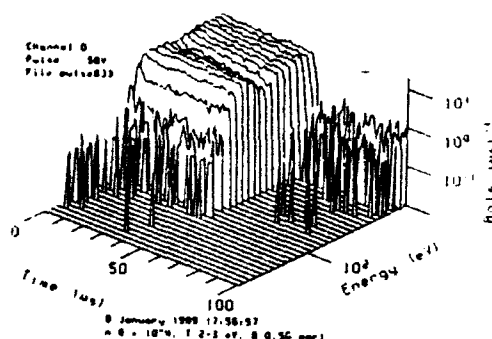
Figure 5. Electron spectrum during a positive pulse of 50 V, parallel orientation.
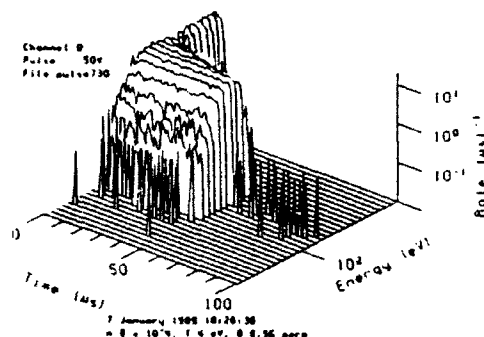
Figure 6. Electron spectra from applied potential of 50V, perpendicular orientation.
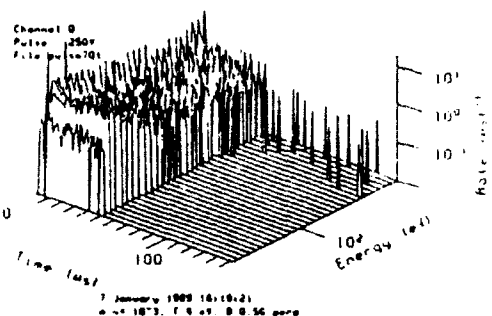
Figure 7. 20-300 eV spectrum from an applied pulse of 250V.
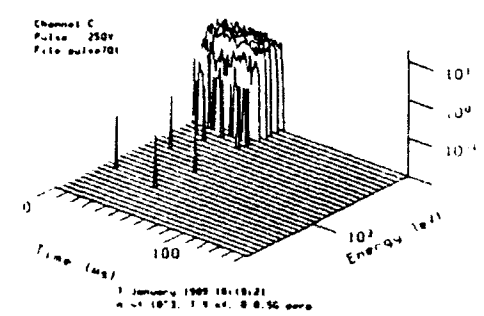
Figure 8. 200-3000 eV Spectrum from a 250 V pulse at plasma density < 10^3.

Figure 5 shows a 20-300 eV electron spectrum for orientation parallel to the field and potential pulse amplitude 50 V. Note the fairly square response to the pulse in the lower energy channels, while at the higher energies, there is relatively little response. The square response may be somewhat misleading as the maximum count rate of 17 MHz is the apparent maximum for this channel (D). The trace on the leading edge of the peak corresponds to 78 eV. The trace immediately behind it is 70 eV.

Figure 6 shows the same situation except that the orientation of the ESA is perpendicular to the field instead of parallel. The response is similar to the parallel case except that there is a notch behind the energy that corresponds to the applied potential of 50 V. This is a typical distinction between parallel and perpendicular geometry. The traces at the top of the front of the peak are the 78 and 70 eV channels as in Figure 5.

Figure 7 shows the response to a pulse of higher potential but with lower background plasma density. Because the count rate is lower, the detector is in no danger of saturating. The spectrum drops off sharply at the energy that corresponds to the pulse potential of 250 V. The trace at the top energy corresponds to 300 eV, the next lower trace corresponds to 272 eV.

Figure 8 is the same conditions as Figure 7 except that the spectrum is of the 200-3000 eV channel instead of the 20-300 eV channel. The trace across the front face of the pulse is 294 eV.
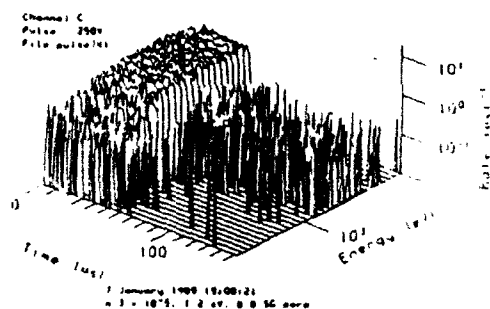
Figure 9. 200-3000 eV electron spectrum for plasma density $3x10^5$, pulse potential 250 V.
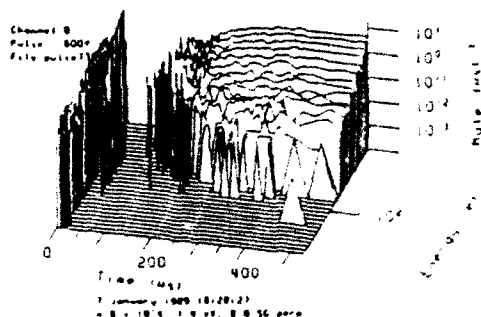
Figure 10. Electron spectrum from a 600 V pulse, plasma density $8x10^4$. Data are from Channel D.
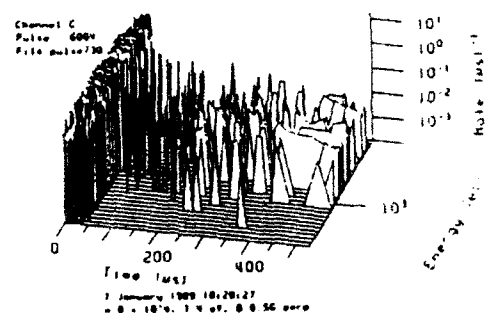
Figure 11. Same as Figure 10 except Channel C (200-3000 eV electrons).
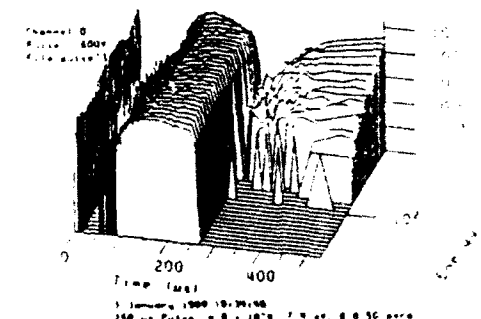
Figure 12. Electron Spectrum from a 250 microsecond long pulse.

Figure 9 is the same conditions as Figure 8 except that the plasma density is much higher at $3x10^5$. The high energy tail of electrons above the energy corresponding to the applied potential makes determination of the charging level difficult.

Figure 10 and Figure 11 show the response to a 600V pulse, plasma density $8x10^4$; the two figures show channels D and C, high and low energy electrons. As Figure 10 is the 20-300 eV spectrum and the orientation is perpendicular, it shows the notch behind the energy corresponding to the pulse potential. Note that the time axis extends for 500 microseconds instead of the 100 microseconds in the previous figures.

Figure 12 is exactly the same conditions except that the pulse is 250 instead of 50 microseconds long. The 50 microsecond long pulse was not long enough to reveal the rather noticeable notch in the response at about 30-70 microseconds. At least in the lab, the spectral response is dynamic for longer than 50 microseconds.
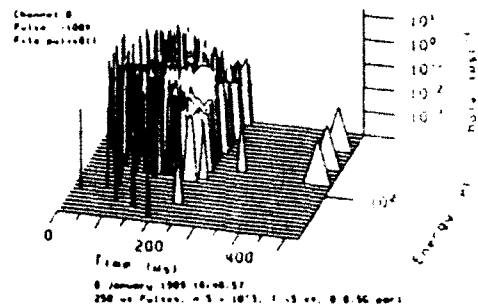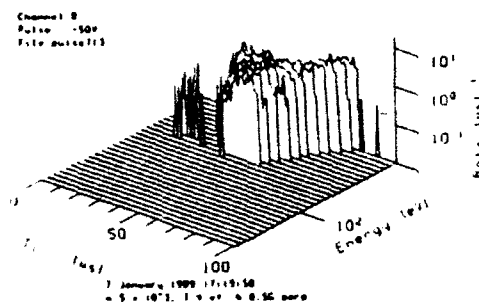
Figure 13. 20-300 eV ion spectrum from applied pulse of -50 V.   Figure 14. Ion spectrum from a -100 V 250 microsecond pulse.

Figure 13 is the *ion* response to an applied pulse of -50 V. The trace on the front of the pulse corresponds to 53 eV. The response takes much (relatively speaking) longer than the corresponding electron response. Still the edge of the spectrum corresponds to the charging potential. Figure 14 is the ion spectrum from a 100 V pulse of length 250 microseconds. Because of the parallel geometry, the spectral edge only gets to its expected value after the first 50 microseconds.

Figure 15 shows that the edge of the electron spectrum follows the applied potential extremely well over a wide range of conditions. Figure 16 shows that the ion response is similar except that at parallel geometries and low potentials, the ions do not respond in sufficient time to reach the energy that corresponds to the pulse amplitude.

CONCLUSIONS

The ESA responded satisfactorily over the entire range of plasma densities and applied voltages. Although the electron multipliers ran at their maximum rate with the higher densities, this did not obscure the correspondence between spectra and voltage pulse amplitude.

The spectra of collected particles extend from the lowest energy channel to the value corresponding to the amplitude of applied voltage. Above this energy the spectra dropped sharply. An exception was that at the highest plasma densities a tail of high energy electrons appeared in Channel C, making the spectral edge less sharp. In the case of perpendicular motion the spectra are continuous during the first several microseconds to the energy corresponding to the pulse, just as in the case of parallel motion. Thereafter a notch appears in the spectra at energies a little below the edge.

573

The electron spectra developed rapidly after the (positive) voltage pulse was applied. Ion spectra, on the other hand, required some tens of microseconds to develop after a (negative) pulse was applied. In some cases the ion spectra did not fully develop during 50 microseconds. The longer 250 microsecond pulses revealed fuller development.

These ion observations were similar for both parallel and perpendicular motion with respect to the magnetic field B. However, the delay in ion development was more pronounced for parallel motion.

Figure 15 and Figure 16 show that we can infer the voltage applied to the ESA from the spectra it observes.

Figure 15. Spectral edge vs. applied pulse potential for electron response to positive charging.

REFERENCES

Gosling, J. T., M. F. Thomsen, and R. C. Anderson. A cookbook for determining the essential transmission characteristics of spherical section electrostatic analyzers. LANL Report LA-10147-M. 1984.

Morse, D. L. Bear ESA instrument spectrometer response, calibration, and modelling. SAIC Report SAIC/NW-89-DLM-996-50. 1989.
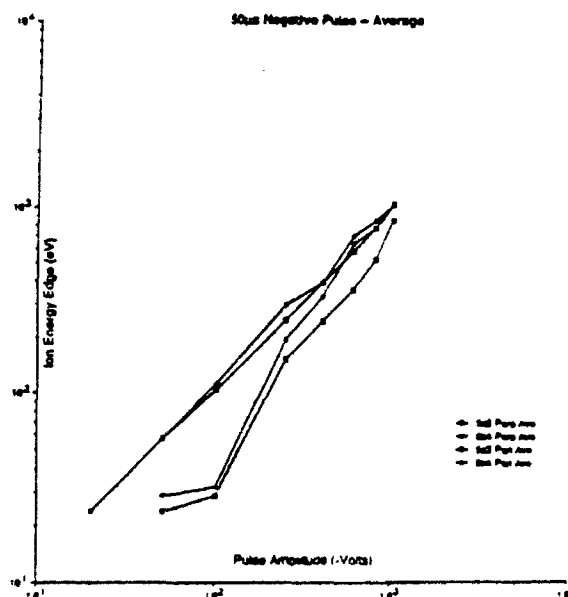
Figure 16. Ion response to negative charging.

BEAR Electrostatic Analyzer: Flight Results

HUGH R. ANDERSON, DOUGLAS W. POTTER,
DAVID L. MORSE, JOSEPH R. OLSON, J. LORRAINE JOHNSON

Science Applications International Corporation
13400B Northup Way, Suite 36, Bellevue, Washington 98005

MORRIS PONGRATZ

BEAR Project Office, Los Alamos National Laboratory, Los Alamos, New Mexico

3 January 1990

The Electrostatic Analyzer (ESA) measured the intensity of charged particles returning to the BEAR payload during flight on 13 July 1989. These particles form part or all of the current that returns to the payload to neutralize the charge ejected with the beam. By measuring the return flux with high time resolution, we can study the physics of charging processes.

When the neutralizer was off, the payload emitted 10 mA negative and charged to several hundred volts with a maximum of ~800V. With the neutralizer on (normal configuration) the payload emitted ~ 1mA negative and received electrons with energies up to a few hundred volts in some attitudes. This suggests charging to a few hundred volts. The charging rate of the payload is consistent with the rocket body capacitance with respect to a vacuum.

INTRODUCTION

The Electrostatic Analyzer's (ESA) function on BEAR is to measure the energy spectrum of particles carrying current that returns to the payload to neutralize charge removed with the beam pulses. From these data it is possible, with some assumptions, to deduce the voltage to which the payload charges. The data directly show what particles are bombarding the surface of the payload.

The accompanying paper [Potter *et al.*, 1990] describes the ESA instrument in detail as well as its calibration and testing. In short, the ESA measures the energy spectra of electrons and ions from 20 eV to 3000 eV with 23% energy resolution and temporal resolution of 1 microsecond. The accelerator on BEAR produces 5 beam pulses per second, each 50 microseconds long. Operation of the gas neutralizer determined the composition of the emitted beam. A magnet captures stripped electrons, so only ions and neutrals escape. The ESA obtained data during and after each beam pulse; it steps through its energy range every fourteen pulses. The ESA mounts in the Physics/Telemetry Section of the BEAR payload looking radially outward perpendicular to the spin axis and at the 90 degree azimuth location.

We have obtained data from two sets of measurements: a series of experiments conducted in a space simulator prior to flight, and the flight of the BEAR rocket. Potter *et al.* describe the simulator data. From these data we conclude that we can infer the voltage applied to the ESA from the spectra it observes.

FLIGHT DATA

Charging data could be obtained under three major conditions during flight. During most of the flight the accelerator produced 10 mA of 1 MeV negative hydrogen ions at the output of the HEBT, and the neutralizer operated *normally* to produce a net beam current of about 1 mA negative. During two intervals the neutralizer was turned off so that the full negative ion output of the HEBT (10 mA when working correctly) left the payload. Finally, just before reentry the beam was *over-neutralized* so that about 1 mA positive was emitted. In addition the accelerator did not always produce any beam at the programmed times although its controller generated synch pulses regularly. That is, the output of the HEBT was zero although the synch pulse from the accelerator triggered ESA data collection.

The payload was initially aligned parallel to the geomagnetic field **B** so that beam injection was parallel to the field. In this orientation the ESA, because of its mounting, accepts only particles moving normal to **B**. The payload was then turned so that its axis and the beam injection were nearly perpendicular to **B**. In this condition the ESA scans all incoming pitch angles as the payload rolls. Neutralizer off and over-neutralize data were obtained only in this attitude, but the NORMAL neutralizer operation occurred in both attitudes.

INSTRUMENT PERFORMANCE

The ESA functioned correctly throughout the flight until increasing atmospheric density at about 95 km on the downleg caused the high voltage to arc over, as would be expected. Low voltage power was on before and during launch so that all housekeeping and digital functions were observed. High voltage turned on at the programmed time with no difficulties. There were virtually no extraneous counts in any channel from electronic pickup internal to the payload. The ESA was as quiet or quieter than it had been during systems tests.

Two secondary results are immediately evident in the data.

1.   When the accelerator skips sending out beam, the ESA shows zero counts. This is particularly evident during the neutralizer off period, when there is a large response if beam is emitted.

2.   During the period of over-neutralization the ESA did not see collection of ions. We believe that this is because the payload was so low, with consequent high neutral density, that little charging occurred and the ESA may have been operating with decreased efficiency.

During the other operating conditions the ESA measured return current as detailed below.

NEUTRALIZER OFF

During the first off period there were 16 pulses of 8 - 10 mA emission, and one with about 5 mA where the HEBT output was low. In the second off period there were two pulses with output above zero, and both of these had low HEBT current. The first neutralizer off lasted 9 seconds so that 45 beam pulses were possible. Figure 1 shows Channel D data for the neutralizer off period; missing pulses are evident. Figure 2 shows similar Channel C data. From these data one readily sees that electrons appear up to several hundreds of eV energy, and that the time history of the response depends upon energy. The next steps of analysis examine the temporal history of the pulses, and the energy spectrum of the returning particles.
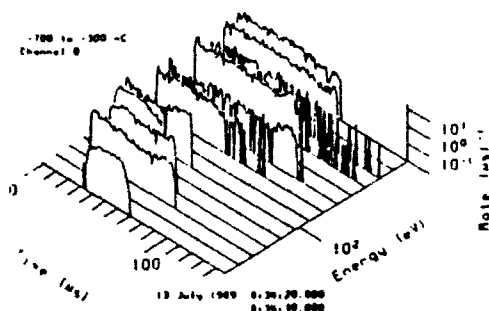
Figure 1. Channel D (20-300 eV electron) data with neutralizer off; emitted charge about 500 nC.
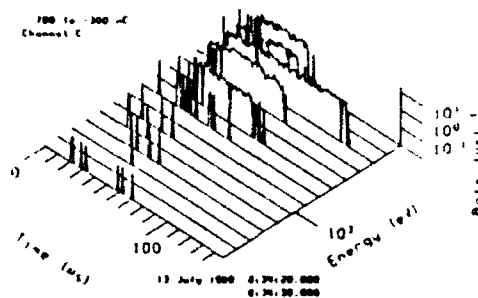
Figure 2. Same as Figure 1 for Channel C (200-3000 eV electrons).

To examine these data more carefully we plot the counting rates from the channels and the output of the beam current monitor *vs.* time. Figure 3 shows such data during and after one beam pulse. Figure 4 shows the temporal extent of all the data when the neutralizer was off. It is evident that the returning particles appear only *after* the beam starts coming out, and that more energetic particles appear after a longer delay. There is some tendency for more energetic particles to disappear more quickly, but the trailing edge is ragged. If the appearance of particles with increasing energy is interpreted as evidence of charging, then the observed response is consistent with vacuum charging of about 200 pf capacitance by the beam current. This is a reasonable capacitance value for the actual BEAR payload.

Figure 5 shows the average counting rates during the interval 20-80 microseconds after start of data collection, converted to a spectrum of intensity versus energy. The offset between channels C and D comes from our estimation that C has 85% efficiency, and D 30%. Using the same efficiency would make the two channels match in the 200-300 eV range, just as normalizing the flight data would. Note, however, that the two channels do not cover this range on the same accelerator pulses since when Channel D measures 300 eV, Channel C measures 3000, and so on. We hope to improve this normalization by further study of the space simulator results.

Figure 3. ESA response (counts/microsecond) and beam current (measured by BCM) vs. time with neutralizer off. Channels C and D are electrons; A and B are ions; and E is the RPA electrons.

Careful examination of the response to individual beam pulses shows that the spectra of returning particles are different for different pulses.

577

Thus Figure 5 represents an envelope of sorts. The maximum returning energy varies from 100 to near 800 eV.

Theory is not yet available to explain the details of time and energy dependence. It is likely that the continuum below the spectral edge is secondaries knocked off the skin of the payload. Based on the space simulator results, where the spectral edge corresponds to the voltage applied to the instrument, we interpret the spectra as showing that BEAR charged to +100-800 volts when emitting 10 mA negative beam pulses. The level is different with different pulses for reasons not currently known.

Figure 4. Duration of response at different energies for neutralizer off.

NEUTRALIZER ON

When the neutralizer was on, the accelerator produced about 265 pulses with net current negative 1 mA, the remainder being zero. The ESA measured some returning particles (2 or more counts) from about one-fifth of these; the others produced no response. At this writing we have not identified what conditions cause or prevent the response, although we are pursuing evidence that it may relate to thruster firings and associated depression in plasma density. We are able to sort the response by received pitch angle.

Figure 6 and Figure 7 show Channels D and C during the period when the payload was aligned with B (Pitch angle of injected beam is 0°). At this time the ESA received particles moving perpendicular to B. Figure 8 and Figure 9 show the same after the payload pitched over so that injection was near 90° pitch angle. In the latter data set the pitch angle of received particles varies from 0° to 180° as the payload rolls.

With this in mind we sort the data into three groups:

Figure 5. Envelope of intensity of return vs. energy with neutralizer off.

578

a) Injection near 0°;

b) Injection near 90° with receiving angle near 90°;

c) Injection near 90° with receiving angle away from 90°.

As with the neutralizer off data, we examine the duration of returning bursts and their energy spectra.
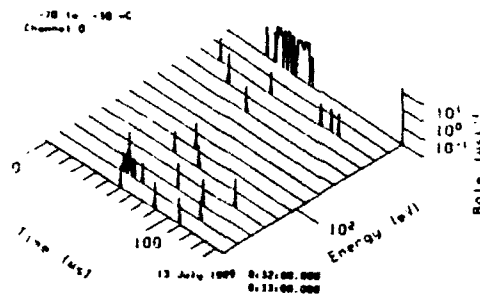
Figure 6. Channel D (20-300 eV electrons) data with neutralizer on (about 50 nC emitted). Payload is field aligned.
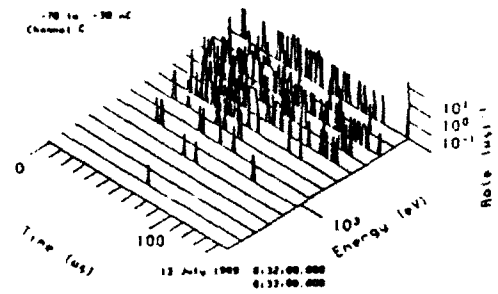
Figure 7. Same as Figure 6 for Channel C (200-3000 eV electrons).
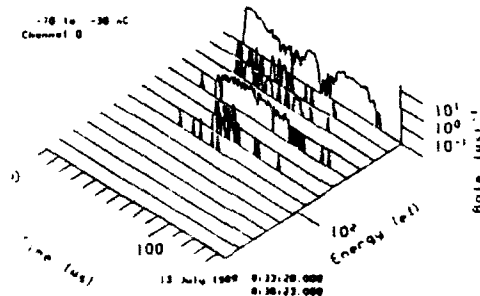
Figure 8. Same as Figure 6 except payload is aligned normal to B.
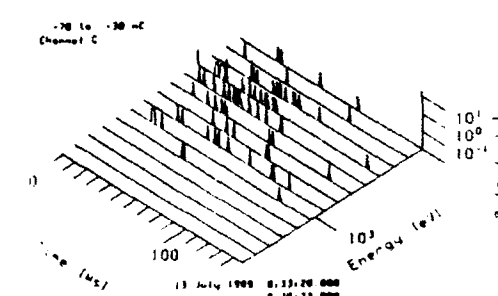
Figure 9. Same as Figure 6 for Channel C.

Figure 10 shows the spectrum for condition a). Note that almost entirely energetic electrons appear, but that both Channels C and D responded. Figure 11 shows conditions b) and c) together, while Figure 12 and Figure 13 show them separately. Note the similarity of conditions b) and a) and the difference of c). Clearly the receiving angle being near or far from 90° is significant; injection pitch angle (or equivalently payload attitude) are not. We expect that the charging might depend upon vehicle attitude, but not upon roll azimuth. The latter simply allows the ESA to sample different portions of the returning velocity distribution function. Charging would also depend upon ambient plasma density as perhaps modified in the vicinity of the vehicle by thruster firings.
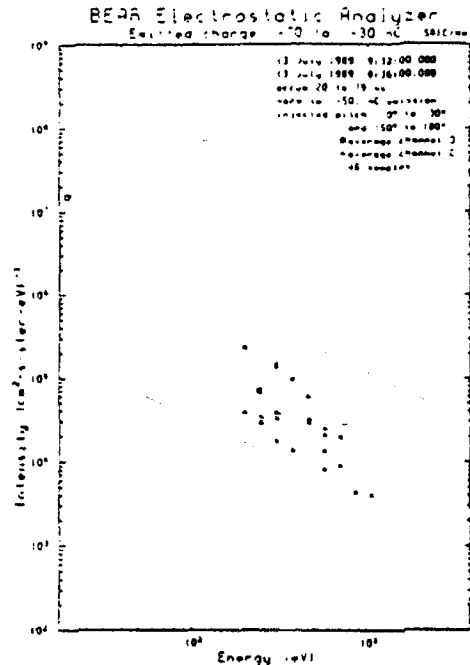
Figure 10. Intensity of returning electrons with neutralizer on. Payload is field-aligned with injection and receive pitch angles near 0° and 90°. The straight lines correspond to 1, 10, and 100 counts in 100 microseconds.
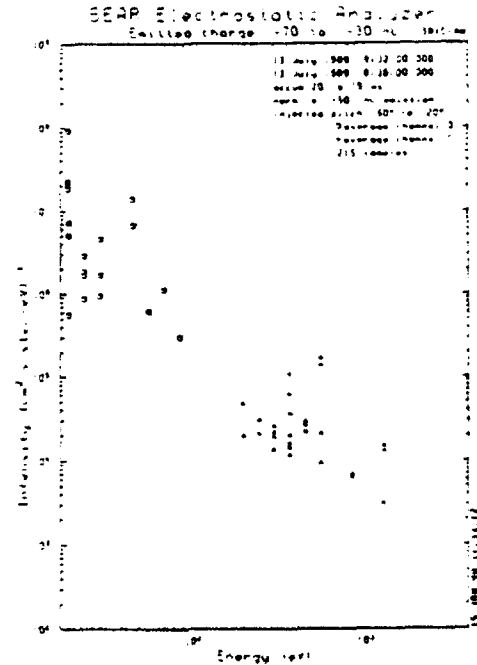
Figure 11. Intensity of returning electrons for payload perpendicular to B (90° injection angle) and all received pitch angles.

Figure 14 shows time durations under conditions b and c together. Note the contrast with Figure 4.

It is clear that some 1 mA beam pulses produced returning electrons of several hundred eV energy both before and after pitch over. The energetic electrons seem to move preferentially perpendicular to the local B field. It may be that every beam pulse produced such electrons, but that the ESA was not always positioned or set to detect them. These data demonstrate clearly that a more complete instrument would measure many energies and angles simultaneously with the high time resolution of the BEAR ESA. As is discussed in the accompanying paper, we recognized this during the design phase, but various constraints prevented our making a more elaborate instrument.

In the absence of current understanding of what controls the appearance of energetic returning particles it is difficult to make a detailed statement about charging. However it does appear that under some circumstances charging to several hundred volts resulted from emission of negative 1 mA. It is certain that electrons of such energy bombard the payload during emission of this and larger currents.

580

BEAR ESA Flight Results
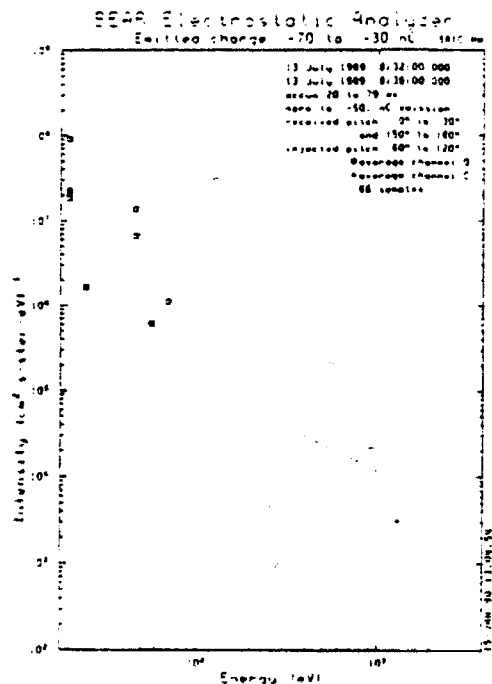
Figure 12. Same as Figure 11 but only received pitch angles *not* near 90°.
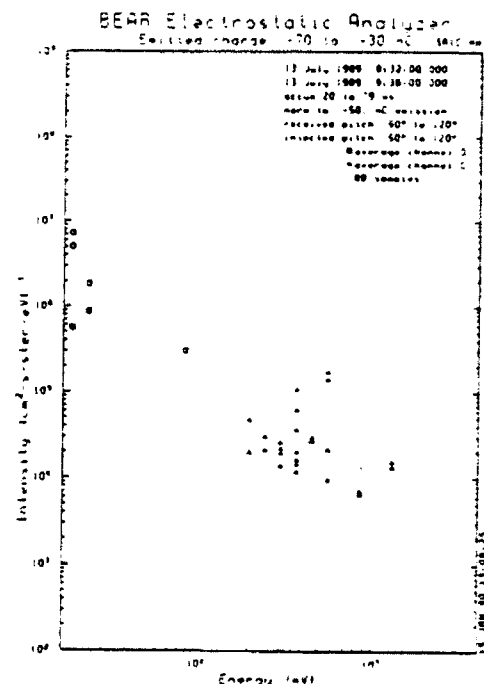
Figure 13. Same as Figure 11 but only received pitch angle near 90°

REFERENCES

Potter, Douglas W., Hugh R. Anderson, and Joseph. R. Olson. BEAR Electrostatic Analyzer: Description and Laboratory Results. *These Proceedings.* 1990.
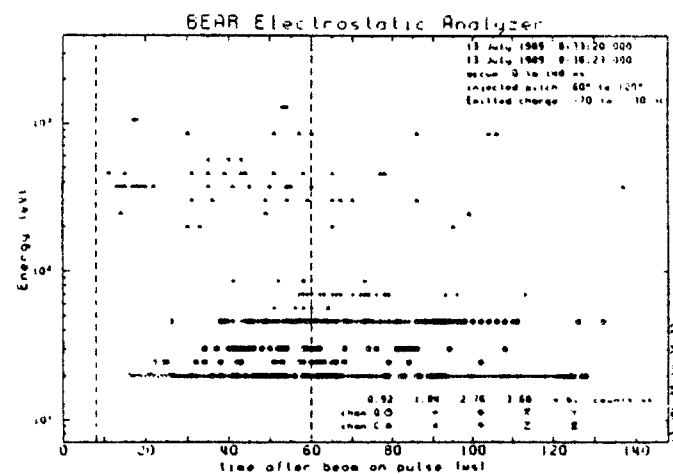
Figure 14. Duration of response for various energies with neutralizer on and injected pitch angle near 90°

SHEATH WAVES ON CONDUCTORS IN PLASMA
AND THEIR IMPLICATIONS FOR LOW-EARTH-ORBIT SYSTEMS

K.G. Balmain and C.C. Bantin, University of Toronto, T   onto
H.G. James, Communications Research Centre, Ottawa
G. Morin, Department of National Defence, Ottawa
A.G. McNamara, National Research Council of Canada, Ottawa

Abstract

The ion sheath, a region of low electron density that exists adjacent to any material surface immersed in a plasma, provides a channel for wave propagation when the surface is a conductor. For a sheath represented as a vacuum gap next to homogeneous, isotropic, cold plasma, sheath waves can propagate from zero frequency up to $1/\sqrt{2}$ times the plasma frequency. In anisotropic, cold plasmas with a magnetic field parallel to the surface, it is known that sheath waves can propagate in the direction of the magnetic field from zero frequency up to $1/\sqrt{2}$ times the upper-hybrid frequency. The theoretical basis for these properties and the supporting laboratory evidence is reviewed in this paper, with emphasis on computed and measured dispersion curves.

The first results of the relevant parts of the OEDIPUS rocket-borne tether experiment of January 1989 are presented. Early in the flight, the rocket separated at its mid-point into two halves connected by a thin wire referred to as the "tether" which was unreeled to a maximum length of almost one kilometre. In the experiment, the tether was maintained in a direction nearly parallel to the ambient magnetic field, and the rocket was launched into a region of auroral activity so that other researchers could use the tethered system to measure magnetic-field-aligned auroral electric fields. The experiment of primary interest in this paper was the transmission of a swept-frequency HF signal along the tether, and the main result is clear evidence of a sheath-wave passband from zero frequency to approximately $1/\sqrt{2}$ times the upper hybrid frequency. Within the passband, resonances at tether lengths that are multiples of a half-wavelength give the phase velocity of sheath waves along the tether. Other pass and stop bands appear to be associated with electron cyclotron harmonic frequencies. It is concluded that sheath waves will have to be taken into account when estimating the coupling of electromagnetic interference between any two points on any large space structure in low orbit.

Introduction

When a plasma is in contact with a metallic surface (or almost any other material surface), it is well known that there exists near the surface a region known as the sheath in which the electron density is much lower than in the surrounding plasma. Ions predominate in the sheath but, because they are so much more massive than the electrons, their inertia makes them nearly immobile at the frequencies to be considered here. If one views the sheath region adjacent to a good conductor as a vacuum gap, and if one views the plasma rather loosly as a poor conductor at low frequencies, the existence of electromagnetic waves in the sheath region between these two conductors seems entirely plausible. Indeed, sheath waves do exist and their properties have been studied for over twenty-five years.

Sheath waves can be understood by considering first a planar interface between a vacuum and a homogeneous, isotropic, cold plasma. It is straightforward to show that electromagnetic surface waves can exist, decaying exponentially to either side of the interface, and propagating at a velocity slower than that of a uniform plane wave in a vacuum. As the frequency is raised, the decay rates increase and the wave becomes more tightly bound to the interface, until cutoff is reached at $1/\sqrt{2}$ times the plasma frequency. Now, if a perfectly conducting surface is introduced in the vacuum region such that a vacuum gap separates the perfect conductor from the plasma, it is also straightforward to show that waves can propagate from zero frequency up to the same cutoff frequency just mentioned. At low frequencies, the fields are concentrated in the vacuum gap region, and the wave propagation is almost dispersionless, exhibiting a phase velocity lower than that of light in a vacuum. As the frequency is raised, the phase velocity decreases, and the fields become more tightly bound to the vacuum-plasma interface, resembling more and more the fields that exist in the absence of the perfect conductor, until the cutoff frequency is reached. The tight binding of the fields to the planar vacuum-plasma interface at frequencies somewhat below cutoff suggests that a model with a more realistic, gradual transition from sheath to plasma could have a strong effect on predictions of wave propagation near cutoff and on the predicted cutoff frequency itself.

Some historical background is in order. *Seshadri* [1965] calculated the dispersion of sheath waves on a cylindrical conductor, using a vacuum-gap sheath and warm plasma theory. *Miller* [1968] did a similar study for an infinite dipole antenna, including a steady magnetic field. Experimental studies were included in the papers by *Ishizone et al.* [1969, 1970a, 1970b], *Lassudrie-Duchesne et al.* [1973], *Meyer et al.* [1974], *Marec* [1970, 1974] and *Marec and Mourier* [1970, 1972]. *Mushiake* [1964] derived the dispersion relation for surface waves along a thin, unsheathed wire parallel to a steady magnetic field, and *Adachi* [1977] proposed a transmission-line theoretical model to calculate the impedance of a sheathless dipole antenna with an arbitrary orientation relative to the magnetic field. *Laurin* [1986] and *Laurin et al.* [1989] deduced sheath-wave dispersion relations from measured antenna input impedance for the case of a cylindrical monopole antenna parallel to the magnetic field, and made a qualitative comparison with calculations for a planar geometry involving a vacuum-gap sheath and a cold magnetoplasma.

Isotropic Plasma

A few key results from the work of *Morin* [1987] will be summarized here, on the propagation of sheath waves along a cylinder in a warm, inhomogeneous, isotropic plasma. Figure 1 shows the cylinder together with qualitative graphs of electron density profiles. The continuous density profile closely represents physical reality and ranges from N_s at the probe surface to the ambient electron density N_0 at a great distance. In a computational model, the continuous profile could be approximated by a sequence of closely spaced steps, with the validity condition that the computed results would smoothly approach the results for the continuous profile as the number of density steps was increased. The minimal stepwise approximation is the single-step case shown in Figure 1, in which the sheath-region density is N_s, and in which the sheath radius r_1 has to be established by some means such as comparing a single-step calculation with a calculation using the continuous density profile (this usually fixes r_1 at or very close to the point where the sheath electron density is half the ambient density). In many situations, especially when the cylinder has a moderate to high negative voltage bias with respect to a different electrode elsewhere in the plasma, the sheath density is low enough to be approximated as zero, giving the "vacuum-gap" sheath representation.

A typical continuous sheath profile (for high negative bias) taken from *Laframboise* [1966] is shown in Figure 2 along with a multi-step approximation to it. Morin's calculations of the sheath-wave complex wavenumber are shown in Figure 3 for a single-step approximation to the continuous density profile, and in Figure 4 for the multi-step approximation. The real parts in the two figures are nearly identical at frequencies ranging from zero up to about 1/3 of the plasma frequency, indicating nearly dispersionless propagation at about 0.3 times the velocity of light. The cutoff frequency can be associated with the peak in the attenuation curve, so the cutoff frequency is about 0.83 ω_p in the single-step case and 0.55 ω_p in the multi-step case. These two values derived from warm-plasma theory straddle the expected cutoff frequency of 0.71 ω_p deduced from the elementary cold-plasma, vacuum-gap theory described earlier, and the low-frequency phase velocities are essentially the same as the elementary cold-plasma vacuum-gap values.

An experimental program was carried out by Morin using the arrangement shown in Figure 5. The DC bias circuit puts a small positive bias on the outer conductor of the coaxial cable, relative to the discharge-tube anode. This collapses the sheath around the cable outer conductor, thereby attenuating sheath waves along it and preventing coupling into the laboratory environment. The complex wavenumber was measured by using multiple lengths of the extended inner conductor of the coaxial cable as a monopole antenna, achieved without affecting the plasma, by pulling the inner conductor out and cutting off the excess wire before re-attaching an RF connector, for each monopole length. The experimental results are shown in Figure 6, having been corrected for unwanted system reflections. The experimental conditions were: wire length = 20.05 to 7.85 cm; wire radius = 0.45 mm; cable outer diameter = 3.6 mm; cable bias = 4.0 V; helium gas at a pressure of 80 m Torr; electron temperature = 0.19 eV; plasma frequency = 1030 MHz; wire bias = -2.0 V = floating potential. The corresponding theoretical calculations were done using the multi-step warm-plasma profile of Figure 7, producing the computed results of Figure 8 which are very close to the experimental results of Figure 6.

It will be noted in the profile of Figure 7 that there is a large density jump to the ambient density, a jump that does not approximate the quite gradual continuous density profile. It was established that this density jump does not affect the wavenumber calculations at low frequencies (although it would have a large effect at frequencies approaching cutoff). The reason for this is the concentration of low-frequency wave fields in the region between the metallic surface and the point in the sheath where the electron density is half the ambient density, which makes exact modelling of the outer region of the sheath less important. Therefore it is concluded that the warm-plasma multi-step density profile model is valid at low frequencies for isotropic plasmas.

Anisotropic Plasma

The propagation of sheath waves in a direction parallel to the magnetic field has been investigated by *Laurin et al.* [1989]. Typical cold-plasma theoretical results for a planar geometry and a vacuum-gap sheath are shown in Figure 9. The main result is that, relative to the isotropic case, the cutoff frequency has risen to $\omega_{uh} / \sqrt{2}$ where ω_{uh} is the upper-hybrid frequency. The low-frequency sheath waves are nearly dispersionless as before, with a phase velocity about 1/4 the velocity of light in a vacuum. Experiments were done on a wire monopole antenna in a magnetized laboratory plasma, and qualitative agreement with the planar theory was established. As one might expect, the phase velocities for the wire monopole were higher than for the planar geometry, the wire sheath-wave velocities being of the order of 1/2 the velocity of light in vacuum. An interesting observation was made in both theory and experiment, that the wavenumber tended to be independent of the ambient density at frequencies in the vicinity of the cyclotron frequency.

The "OEDIPUS A" Rocket Experiment

The OEDIPUS experiment's primary mission was to measure magnetic-field-aligned electric fields in the ionosphere under auroral conditions. The procedure was to create a double probe by having the rocket separate into two parts connected by a thin, insulated wire (or "tether"), and to let the wire unreel to a maximum length of about one km, all the while keeping the wire nearly parallel to the earth's magnetic field.

This configuration was ideal for a study of sheath waves propagating parallel to the magnetic field, so a stepped-frequency pulsed transmitter and a synchronized receiver were added to the nose and tail sections of the rocket, as shown in Figure 10. The transmitter output was fixed at 50 volts rms. Between the transmitter and the spool, a 2000 ohm resistor was inserted to reduce tether input current variations with frequency. The receiver input impedance was 100 ohms. The receiver samples the intermediate-frequency signal, and post-flight processing of the sampled data involves squaring and averaging over a time window around the received pulse. The tether/spool subsystem specifications are given in Table 1.

The OEDIPUS A rocket was launched from Andoya, Norway on January 30, 1989. The tether unreeled as planned, reaching a maximum length of just under 1 km about half-way through the flight, as indicated in Figure 11 which also shows a maximum altitude of just over 500 km, so that for most of the flight the rocket was above the F-region maximum in electron density.

The main result of the flight, from preliminary processing of the data, is the gray-scale plot of Figure 12 in which there are 8 gray levels in equal increments on a log scale. The darker the gray shading, the higher the signal level at the receiver in the tail section. The lines superposed on the figure are the cyclotron frequency f_c with its 2nd, 3rd and 4th harmonics, as well as the plasma frequency f_p deduced from Langmuir probe measurements, the upper hybrid frequency f_u deduced from f_p and f_c, and the estimated sheath cutoff frequency $f_s = f_u / \sqrt{2}$. The strongest passband extends from zero frequency up to about f_s as expected for sheath wave propagation. Other passbands and stopbands appear to be bordered by the cyclotron harmonic frequencies, reminiscent of cyclotron-harmonic waves (Bernstein waves) that propagate at right angles to the magnetic field.

Within the lower passband, interference fringes are visible and are shown in Figure 13 after enhancement by gray-scale adjustment. It was speculated that these might be sheath-wave resonances, so lines are shown on Figure 13 for the conditions that the tether length is an integral multiple of a half-wavelength, assuming a phase velocity 2/3 the velocity of light in a vacuum (i.e. the sheath-wave refractive index is 1.5). The excellent fit suggests strongly that the sheath-wave resonance postulate is correct. Moreover, the easy visibility of these resonances indicates that the sheath waves are not greatly attenuated.

Figure 14 shows frequency sweeps at four times during the flight. The passbands, stopbands and resonances are clearly visible, with the resonance nulls being deeper at the shorter tether lengths. The first stopband is remarkably deep, in most cases over 60 dB below the lowest-frequency passband.

Moment-Method Calculations

A thin-wire method-of-moments computer program written by *Richmond* [1974] and improved by *Tilston* [1989] is applicable to wires in isotropic cold plasma with a thin vacuum-gap sheath around the wire. A number of multi-frequency calculations of the input impedance of dipoles in plasma served to identify resonances and deduce phase velocities, using the actual tether wire size and a 2.5 cm estimate of the actual sheath thickness. The purpose was to get an estimate of the phase velocity of sheath waves for realistic parameters but ignoring the plasma anisotropy. Figure 15 shows two curves, one obtained by equating the plasma frequency in the moment-method calculation with the ionospheric plasma frequency, and the other obtained by equating the plasma frequency in the moment-method calculation with the ionospheric upper-hybrid frequency. The sheath-wave wavenumbers deduced from the various resonances in Figure 13 are also shown, and the fit is especially good when the upper-hybrid frequency is employed in the moment-method calculation. The values of the wavenumber (refractive index) are

clustered around the 1.5 value used in Figure 13 for the resonance lines. Besides lending some credibility to the sheath-wave interpretation of the data, this moment-method analysis also suggests that isotropic-plasma calculations may have a certain degree of utility in estimating sheath-wave behaviour, in the absence of a rigorous anisotropic-plasma theory.

Relevance to EMI Coupling

On large structures in the ionosphere (such as the Space Station) the possibility exists that electromagnetic interference emitted at one location will be coupled to other locations via sheath waves. The evidence already presented indicates a broad sheath-wave passband up to 1.5 to 2.0 MHz in which electromagnetic waves can propagate with little dispersion and little attenuation, so it is clear that transient signals could propagate easily as sheath waves provided that their spectra are concentrated below 2 MHz.

Estimates of electromagnetic coupling and electromagnetic compatibility standards are generally based on the assumption of a vacuum (air) environment. A comparison between vacuum and plasma media can be made using the moment-method program already referred to. The configuration representing the tether is shown in Figure 16 along with the computed results for vacuum and plasma, and for two different tether lengths. The plasma frequencies selected correspond to the two tether lengths. The same 2.5 cm sheath thickness was assumed. The crucial result is that, at frequencies below [1] MHz, coupling in the plasma medium is 20 dB to 60 dB greater than it is when the surrounding medium is a vacuum. This suggests that estimates of EMI coupling between points on large space structures could be too low by a large margin if they do not take into account the plasma environment and the existence of an ion sheath. Moreover, sheath-wave resonances could increase coupling if the structure is long enough.

Conclusions

Reported in this paper is what is believed to be the first measurement of sheath-wave propagation along a wire in the ionosphere. The low-frequency passband and the first stopband are in the frequency range predicted theoretically, and the phase velocity deduced from resonance frequencies has a value essentially as expected from various theoretical considerations. The existence of readily identifiable resonances indicates that sheath waves propagate with little attenuation. The strength of all the phenomena measured suggests that sheath waves are easy to excite. Moreover, sheath-wave phenomena are more complex than expected, as evidenced by the observation of passbands and stopbands bordered by the electron cyclotron harmonic frequencies.

It is clear that sheath waves must be taken into account when predicting or interpreting the properties of antennas in the ionospheric plasma, certainly at all frequencies below 5 or 6 MHz. In anisotropic plasma, sheath-wave propagation has been identified even in frequency ranges where the medium can propagate uniform plane waves, which

is in contrast to the isotropic plasma case where sheath waves can propagate only at frequencies appreciably below the electron plasma frequency.

The properties of sheath waves are such that they could readily carry electromagnetic interference between any two sites on a large structure in the ionosphere, and the coupled power level could be orders of magnitude higher than in free space. This means that estimates of electromagnetic interference levels could be grossly incorrect if they do not take the plasma medium into account. Therefore EMI/EMC standards need to be reviewed to see if they are applicable to large structures in the ionosphere. Useful estimates of sheath wave interference effects can be deduced from moment-method computational techniques valid for a cold, isotropic plasma.

EMI/EMC standards for space systems relate not only to theoretical estimates of interference levels in space, but also to ground-based compliance testing. The analogy between sheath-wave propagation and coaxial cable propagation suggests a configuration for ground-based testing. It would involve wrapping space devices with an appropriately modified wire mesh spaced a distance of one sheath width (a few cm) from the device using some material such as polystyrene foam for support. There remains the necessity to establish the details of the wire mesh modification required to ensure the validity of this procedure, that is, there remains the necessity to establish an equivalence between the wire-mesh sheath edge and the physical sheath-plasma transition region.

Acknowledgment

References

Adachi, S., T. Ishizone, and Y. Mushiake, Transmission line theory of antenna impedance in a magnetoplasma, *Radio Sci.*, *12*(1), 23-31, 1977.

Ishizone, T., S. Adachi, K. Taira, Y. Mushiake, and K. Miyazaki, Measurement of antenna current distribution in an anisotropic plasma, *IEEE Trans. Antennas Propag.*, *AP-17*(5), 678-679, 1969.

Ishizone, T., S. Adachi, and Y. Mushiake, Electromagnetic wave propagation along a conducting wire in a general magnetoplasma, *Proc. IEEE*, *58*(11), 1843-1844, 1970a.

Ishizone, T., S. Adachi, and Y. Mushiake, Measurement of the phase constant along a conducting wire in a magnetoplasma, *Proc. IEEE*, *58*(11), 1852-1854, 1970b.

Laframboise, J.G., Theory of spherical and cylindrical Langmuir probes in a collisionless Maxwellian plasma at rest, University of Toronto Ph.D. Thesis and UTIAS Report no.100, 1966.

Lassudrie-Duchesne, P., G. Dubost, et C. Terret, Mesure de la distribution de courant à la surface d'un doublet immergé dans un plasma chaud isotrope, *C.R. Acad. Sc. Paris*, t. 276, série B, 207-210, 1973.

Laurin, J.-J., Study of sheath wave propagation in a magnetoplasma, M.A.Sc. thesis, 155 pp., Univ. of Toronto, Toronto, Ont., Sept. 1986.

Laurin, J.-J., G.A. Morin, and K.G. Balmain, Sheath wave propagation in a magneto-plasma, *Radio Sci.*, 24(3), 289-300, May-June, 1989.

Marec, J.L.E., Propagation d'ondes électrostatiques dans les gaines au voisinage d'un conducteur, thèse de doctorat 3rd cycle, 99 pp., Fac. des Sci. de Paris, Paris, Nov. 1970.

Marec, J.L.E., Ondes de gaine, amortissements non collisionnels, Thèse de doctorat ès-sciences, Univ. de Paris, 1974.

Marec, J., and G. Mourier, Sur la propagation des ondes de surface et la nature des résonances électrostatiques de gaine, *C.R. Acad. Sc. Paris*, Série B, t. 271, 367-370, 1970.

Marec, J., and G. Mourier, Sur l'admittance d'entrée d'une antenne plane immergée dans un plasma, *C.R. Acad. Sc. Paris*, Série B, t. 274, 471-474, 1972.

Meyer, P., N. Vernet, and P. Lassudrie-Duchesne, Theoretical and experimental study of the effect of the sheath on an antenna immersed in a warm isotropic plasma, *J. Appl. Phys.*, 45(2), 700-706, 1974.

Miller, E.K., Characteristic waves on an infinite cylindrical antenna in a plasma medium, *Radio Sci.*, 3(12), 1175-1178, 1968.

Morin, G.A., Radio-frequency fields around conductors in plasma, University of Toronto Ph.D. Thesis, 1987.

Mushiake, Y., Electromagnetic waves along an infinitely long and thin conducting wire in a magneto-ionic medium, *J. Res. NBS, Sect. D*, 69(4), 503-510, 1964.

Richmond, J.H., Radiation and scattering by thin-wire structures in the complex frequency domain, NASA Contractor Report CR-2396, May 1974.

Seshadri, S.R., Propagation coefficient for the current distribution along a cylindrical antenna immersed in a warm plasma, *Proc. IEE*, 112(5), 877-882, 1965.

Tilston, M.A., Thin-wire reciprocal multiradius implementation of the electromagnetic moment method, University of Toronto Ph.D. Thesis, 1989.
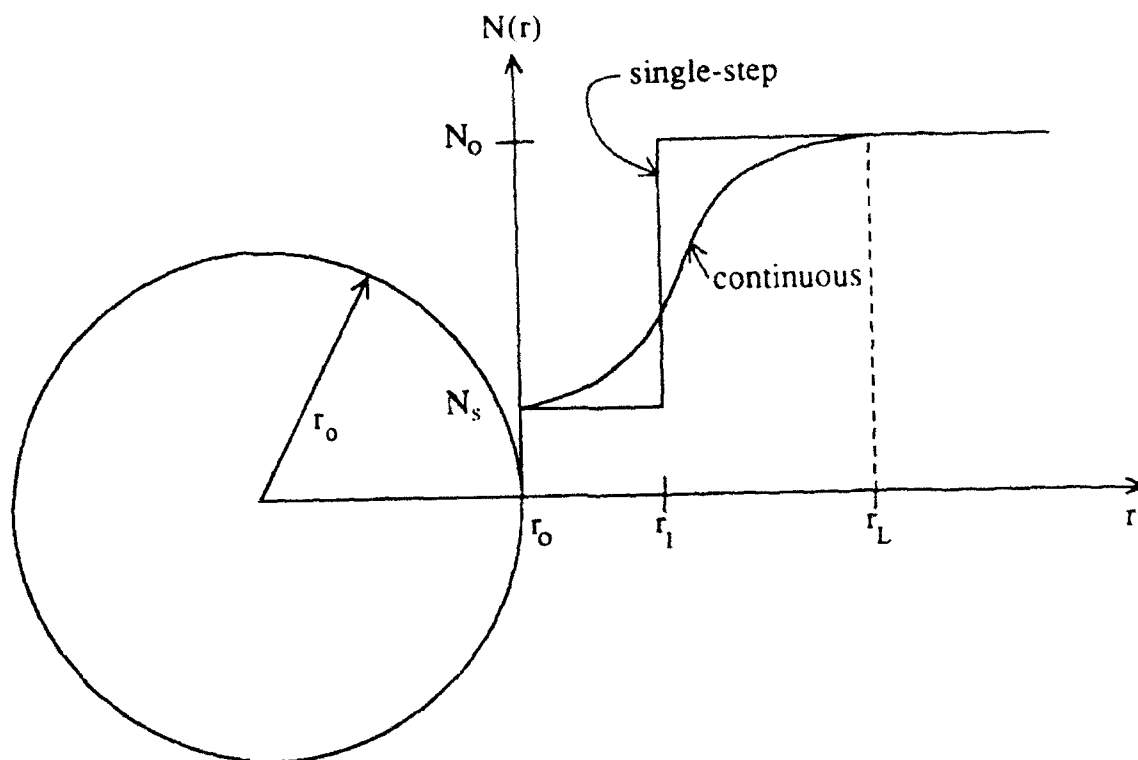
Figure 1. Cross-section of cylindrical conductor in plasma with sheath profiles of electron density.
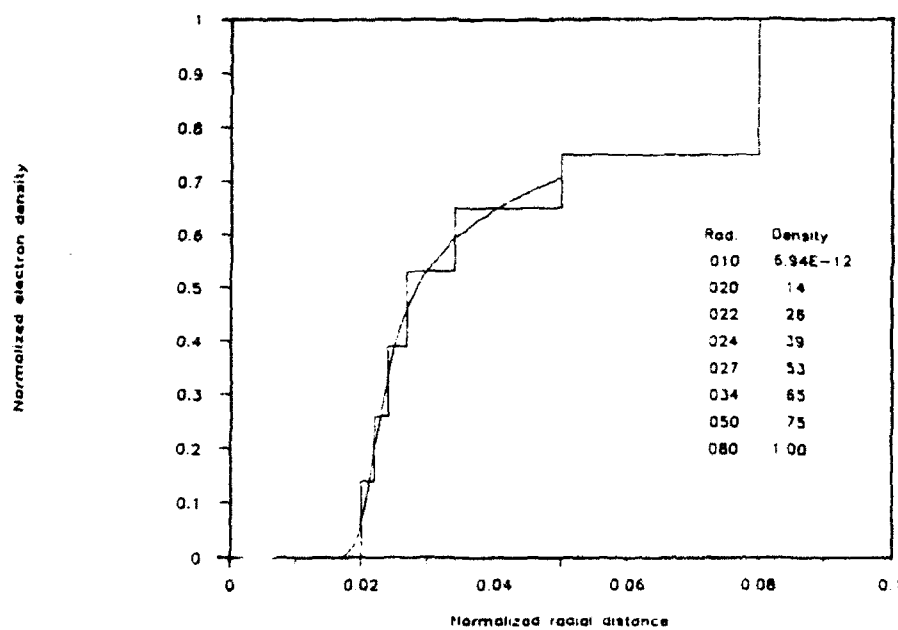
Figure 2. Electron density profile for -25V bias as calculated by *Laframboise* [1966].

Log (Real & -Imag. (Complex Wavenumber))
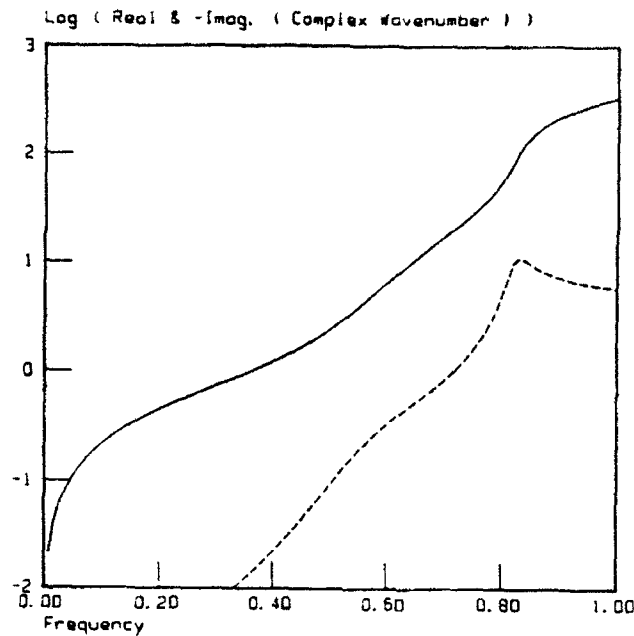
Figure 3.   Complex wavenumber for -25V bias (solid line is real part, dashed line is imaginary part representing attenuation) for single-step density profile. Norm. collision freq. = .01 = v / ω_p, norm. thermal vel. = .001 = V_{th} / c, norm. probe radius = .01 = $r_o \, \omega_p / c$, norm. sheath radius = .028 = $r_1 \, \omega_p / c$, sheath electron density = 6.94×10^{-12} cm^{-3}.

Log (Real & -Imag. (Complex Wavenumber))
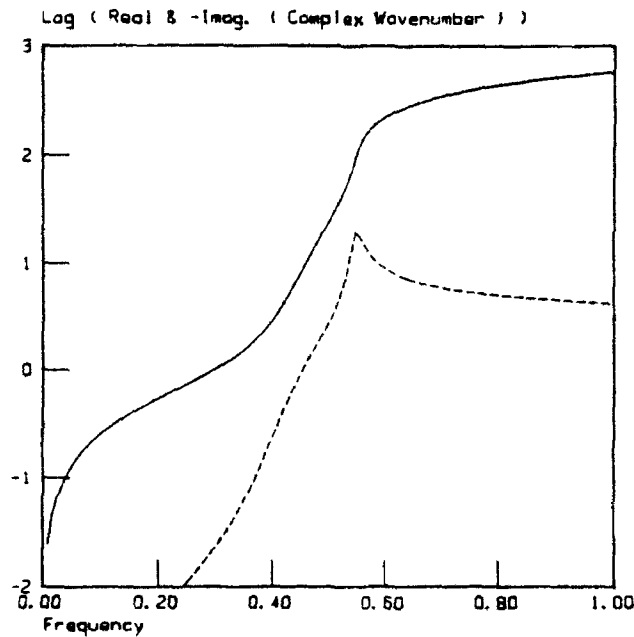
Figure 4.   Complex wavenumber for -25V bias for multi-step density profile as in Figure 2. Parameters same as in Figure 3.

591
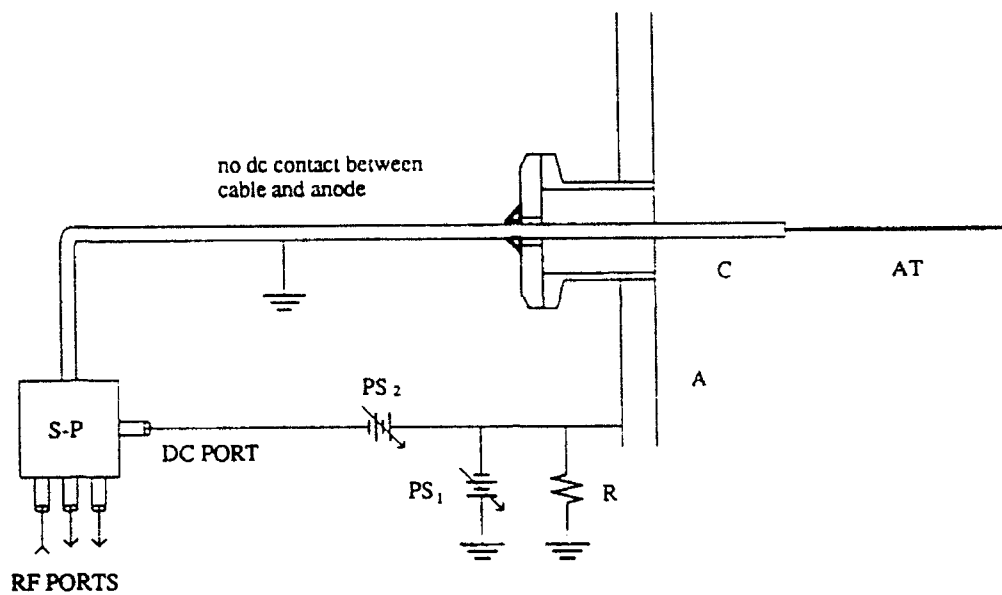
Figure 5.   Antenna in laboratory plasma, showing cable biasing circuit. A denotes
             anode, AT antenna, C cable, R = 1500 Ω, PS_1 cable bias, PS_2 antenna bias,
             S-P is S-parameter test set.
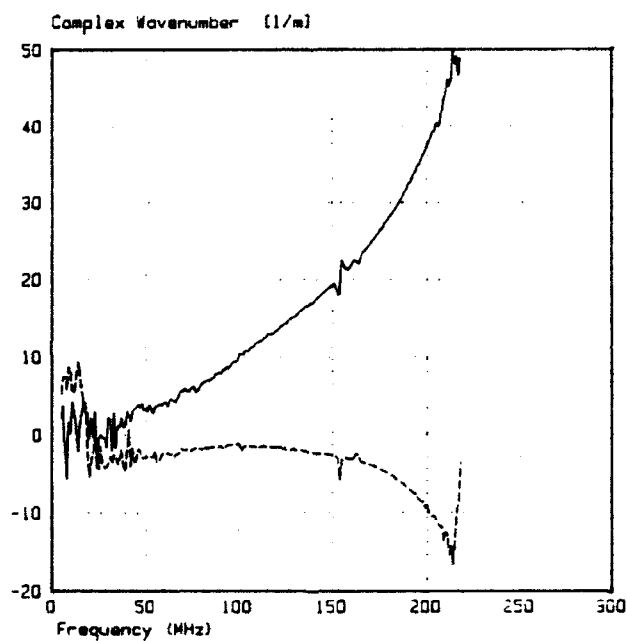
Figure 6.   Experimental complex wavenumber as corrected for stray reflections
             (crosses show uncorrected real part obtained from specific resonances).
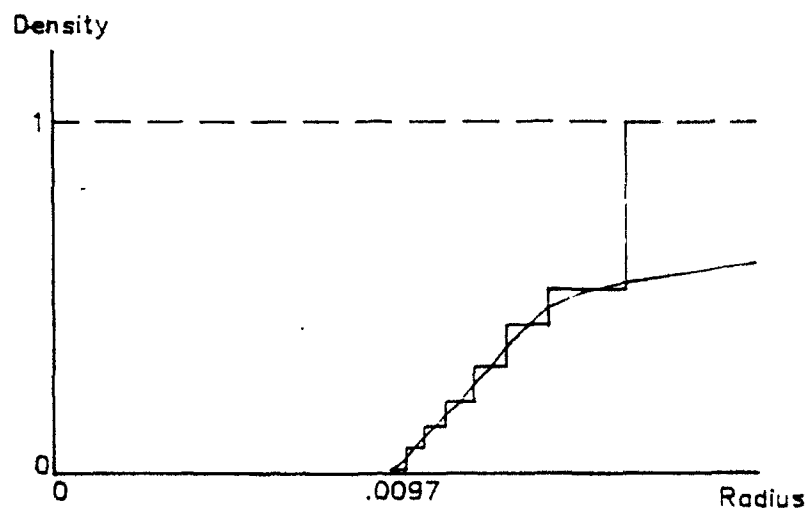
Figure 7.   Theoretical electron density profile used to represent laboratory experimental conditions.
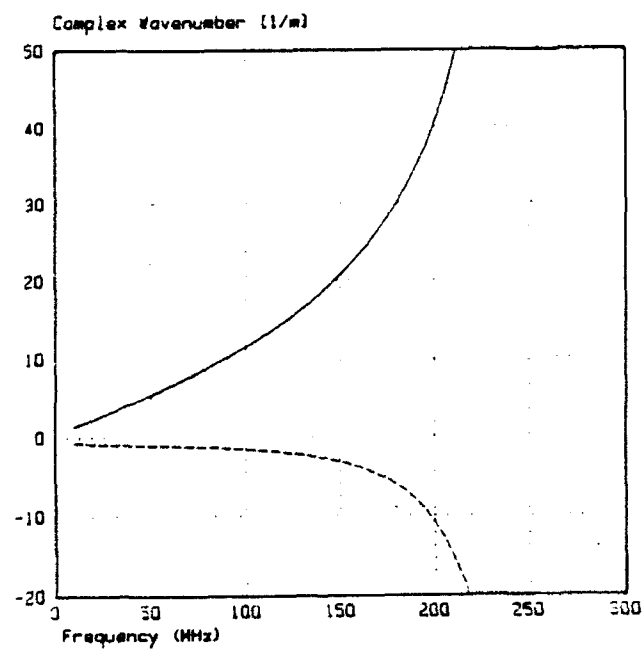
Figure 8.   Calculated waenumber for profile of Figure 7.
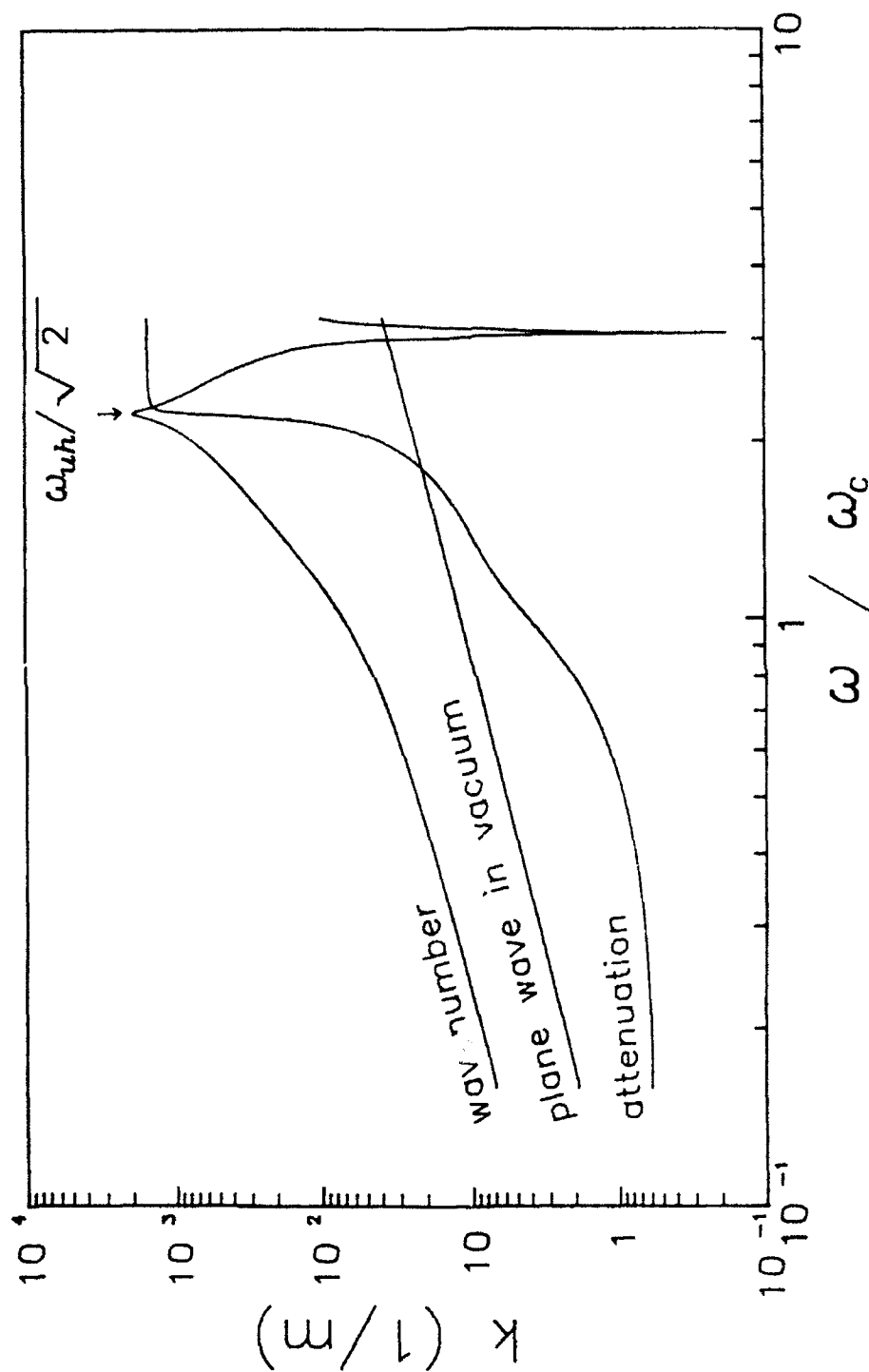
Figure 9.   Typical theoretical sheath-wave dispersion curves for planar geometry and magnetic field in direction of propagation. $\omega_c = 3.52 \times 10^9$ rad/s, $\omega_p = 3\omega_c$, $\nu = \omega_c/28$, sheath thickness $= 0.1$ cm.
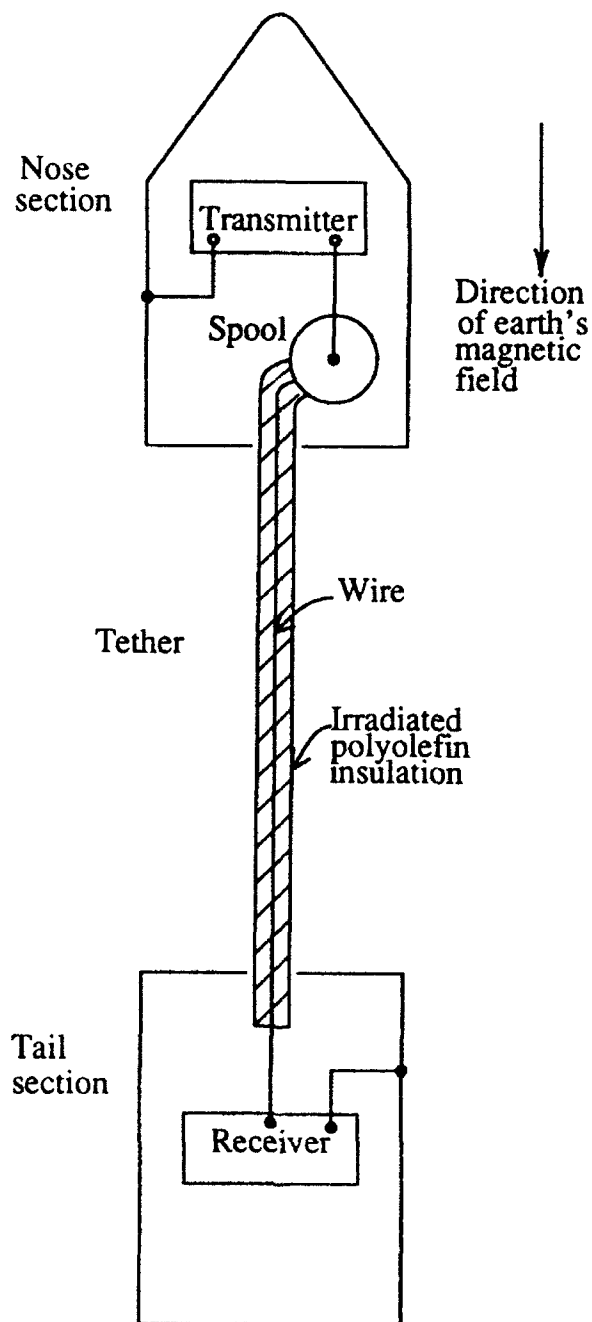
Figure 10. Diagram of the OEDIPUS A rocket experiment configuration used for the study of sheath waves.

Table 1. Tether Spool Subsystem

Tether wire length : 1300 meters

Tether wire : No. 24 AWG , 19 strands of

No. 36 copper , diameter 0.020"

Tether wire coating : irradiated polyolefin ,

diameter 0.057" , $\varepsilon_r = 2.32$

Wire resistance : < 100 ohms over 1300 meters

Spool - to - chassis resistance : $> 3 \times 10^{14}$ ohms

Contact : slip ring

Braking : constant - torque of 6.5 oz - in
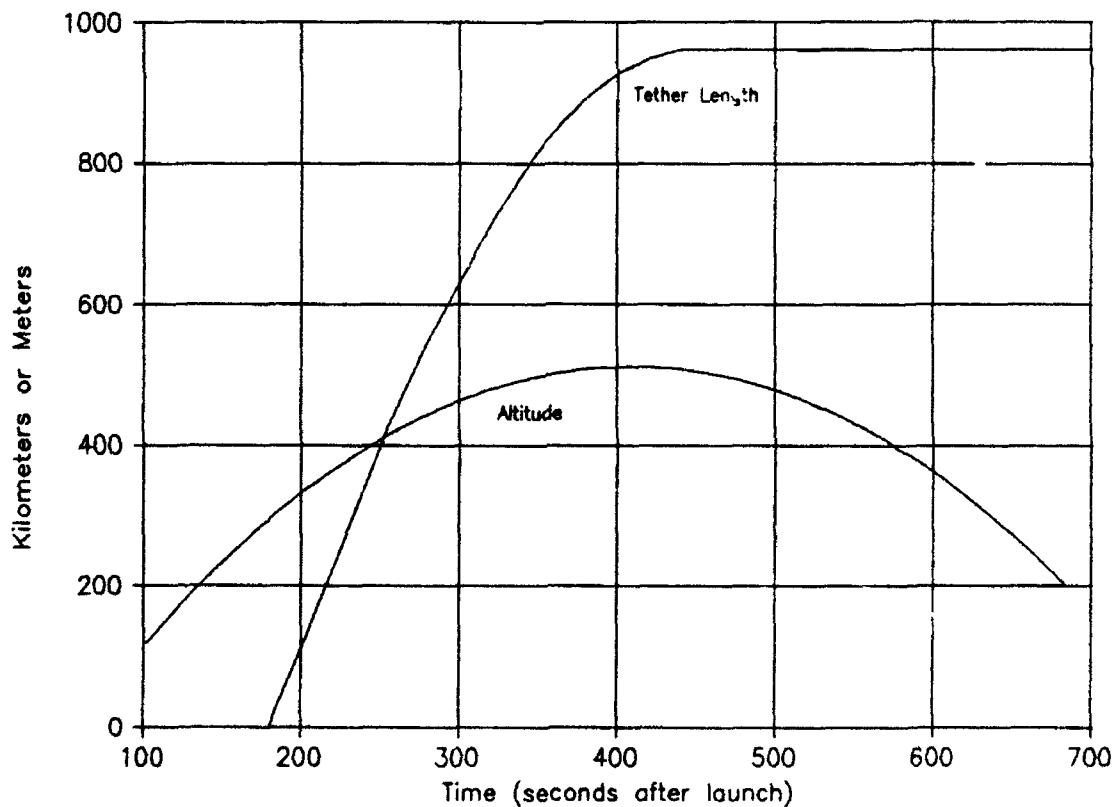
Figure 11.   Tether length and altitude as functions of elapsed time.

596
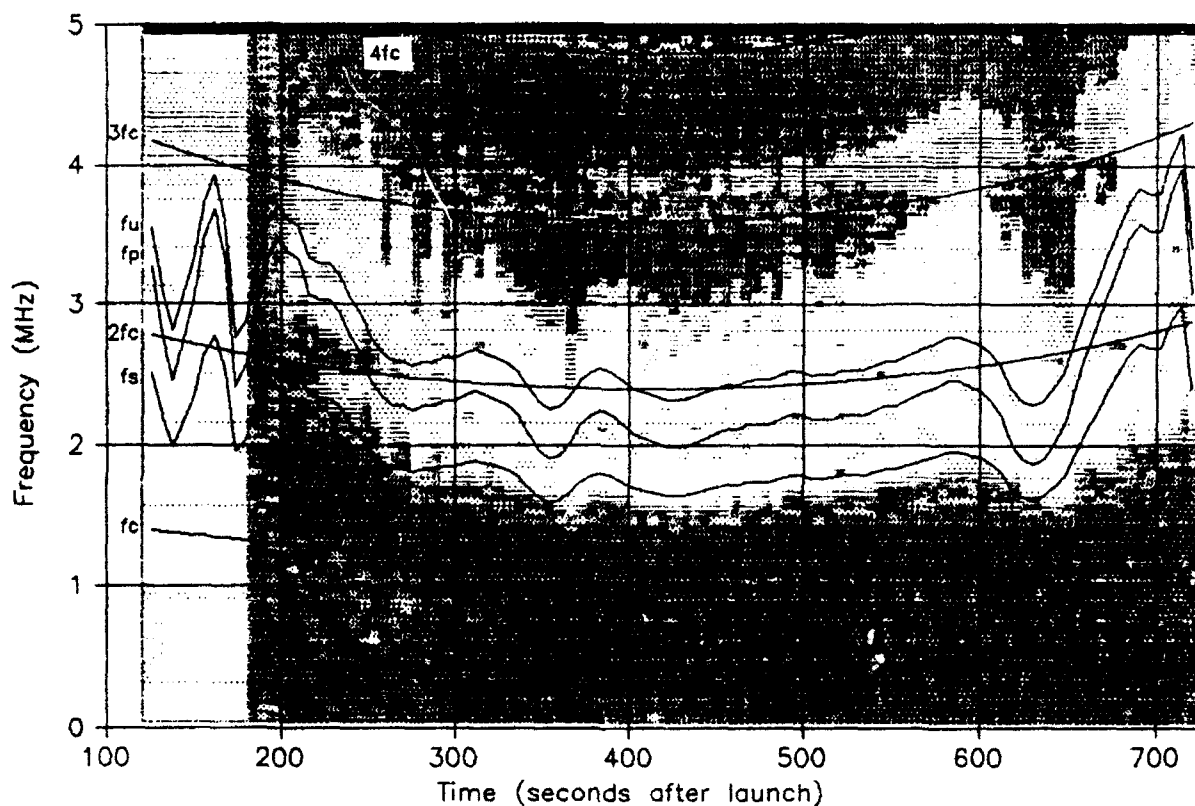
Figure 12. Received signal strength (darker gray scale means higher signal level) showing the cyclotron frequency f_c and its harmonics, the plasma frquency f_p, the upper-hybrid frequency f_u, and the nominal sheath-wave cutoff frequency $f_s = f_u / \sqrt{2}$.
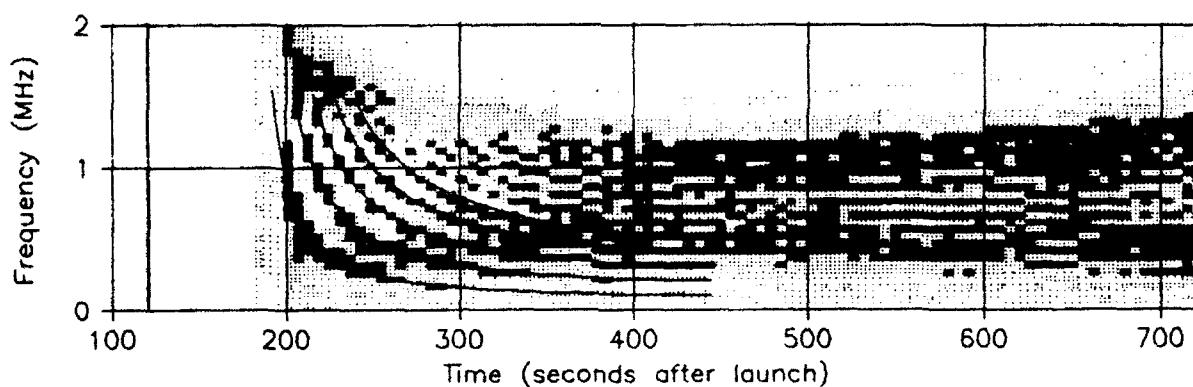
Figure 13. Received signal strength with gray-scale adjusted to show tether-length resonances. Lines show where tether is a multiple of a half wavelength long, assuming a wavenumber of 1.5.

Figure 14.   Frequency sweeps of received signal level at elapsed times 234 sec., 270
sec., 318 sec., and 384 sec.
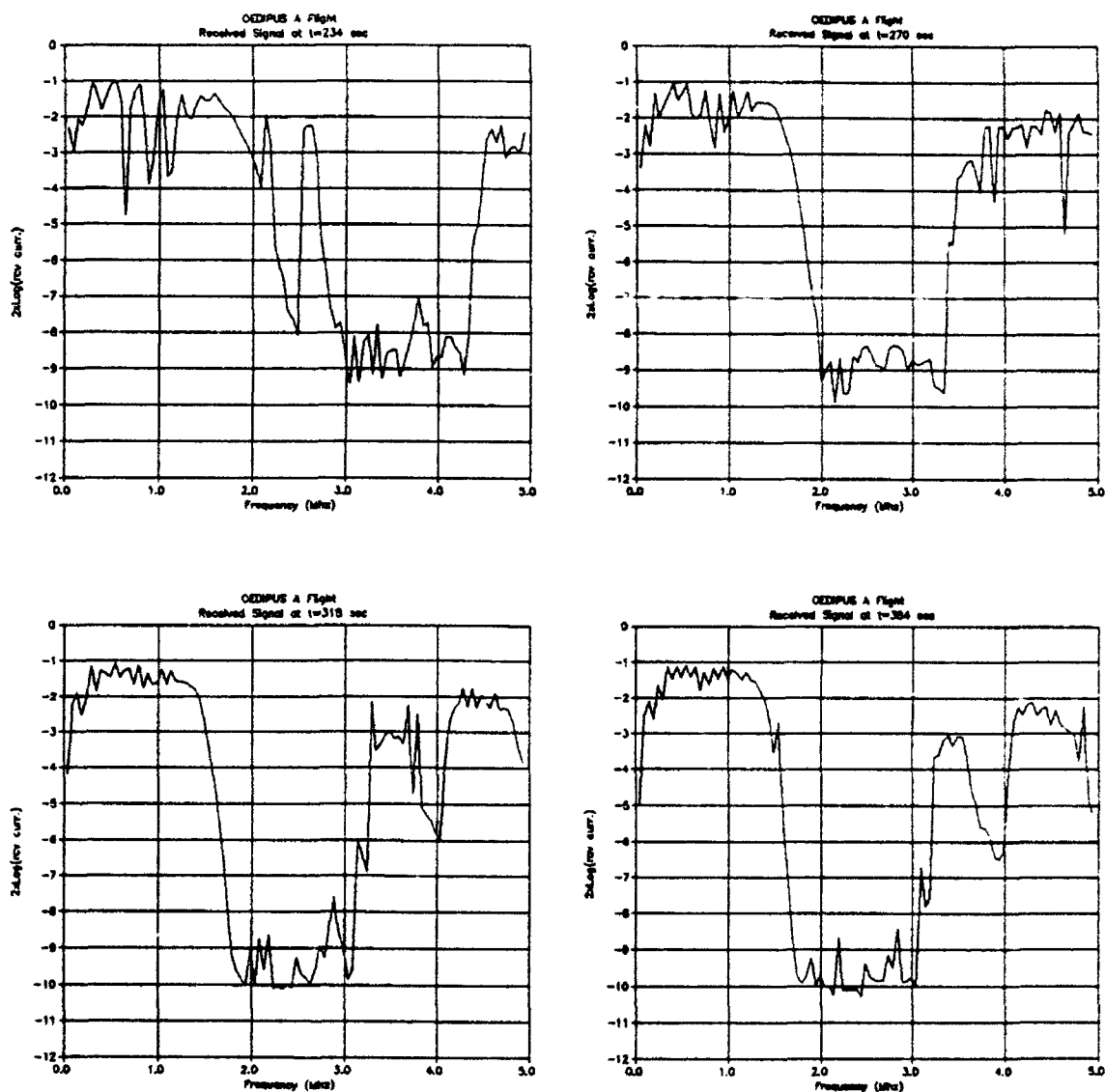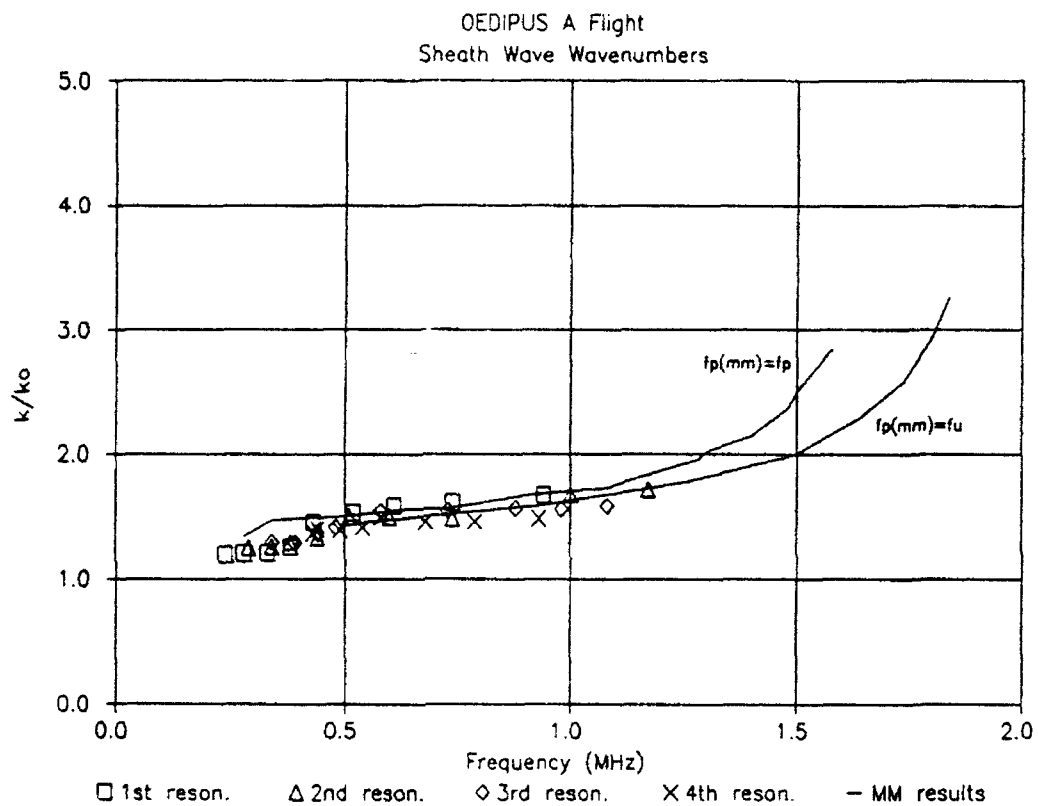
Figure 15. Wavenumbers derived from various resonances, together with moment-method calculations of wavenumbers using two different ways to specify the ambient plasma frequency.

Figure 16. Moment-method calculation of coupling from one end of the tether to the other, for both free space and plasma environments and for two different tether lengths. The plasma densities correspond to the tether lengths chosen.

OEDIPUS A Flight Simulation
Moment Method End-Plate Model
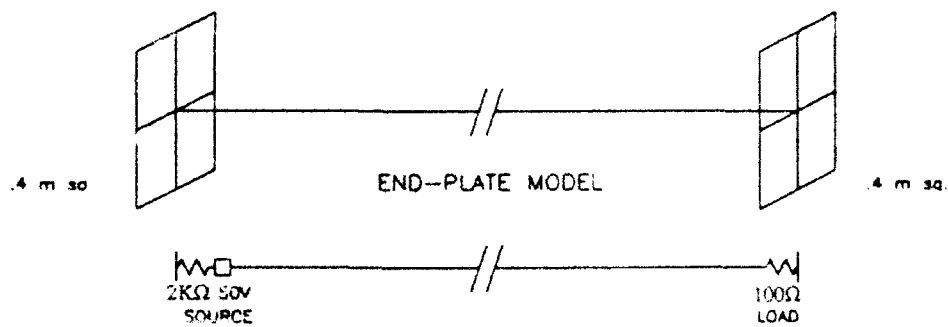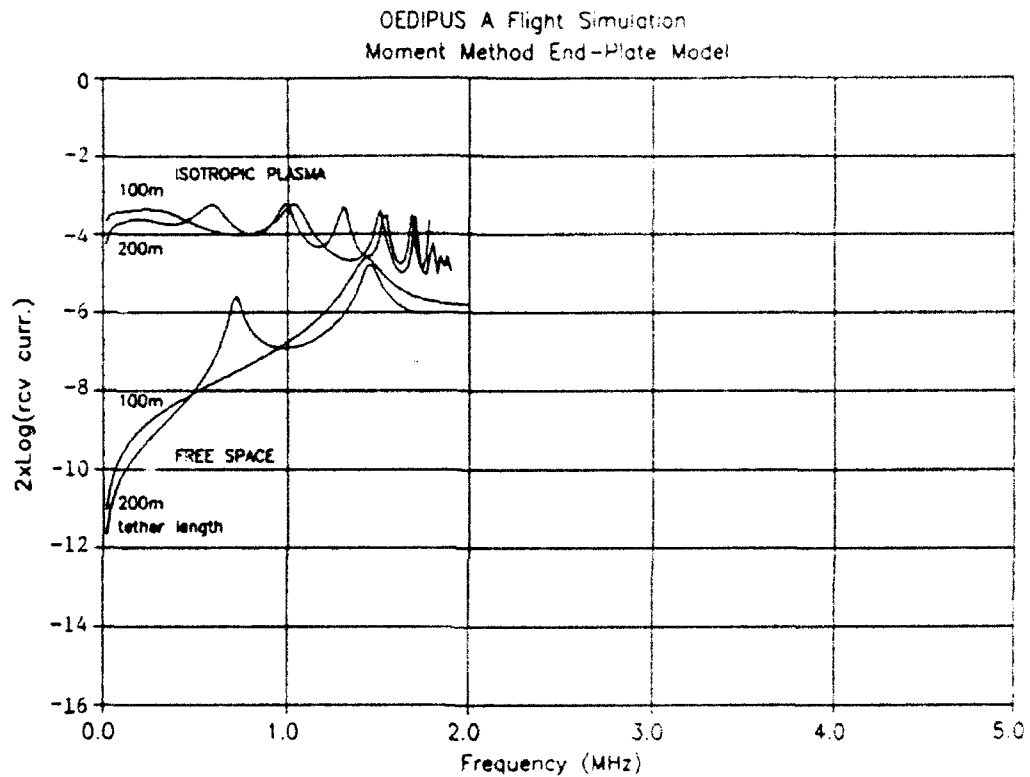
Current Collection in a Spacecraft Wake; Laboratory and Computer Simulations

Chung Chan, Jim Browning, Steve Meassick
Department of Electrical and Computer Engineering
and Center for Electromagnetics Research
Northeastern University, Boston, MA 02115

M.A. Morgan
AMPTEK Inc.
6 DeAngelo Drive, Bedford, MA 01890

David L. Cooke, C. L. Enloe
Air Force Geophysical Laboratory
Hanscom AFB, MA 01731

Maurice F. Tautz
Radex Incorporated
3 Preston Ct., Bedford, MA 01730

I. Introduction

The current-voltage (IV) characteristic of a charged object in the wake of another, larger body in Low Earth Orbit (LEO) is an issue that is relevant to spacecraft design and operation. Deep in the wake of a platform that is possibly thousands of Debye lengths across, the plasma density and currents will be reduced to a fraction of their values in the ambient stream creating conditions where high voltage power equipment could be hidden from the plasma or an astronaut on EVA in polar orbit might become charged by auroral electrons. The wake charging problem, as it is called, is difficult to analyze because plasma currents will remain small until the object potential is sufficient to pull charged particles from the dense plasma stream across an ion void and, in the case of ion collection, overcome a significant angular momentum barrier. The wake charging problem has received some attention to date, (Jongeward, 1986) but the use of the theoretical tools used in that study was somewhat idealized, and no in-situ measurements were available to validate the predictions.

We have begun a series of laboratory experiments to study the wake charging of a very negatively biased body. In the present experiment, an ion thruster is used to produce a flowing plasma in a large vacuum chamber. A 10 cm diameter aluminum disk is inserted into this plasma to produce a wake. A smaller spherical probe is mounted on an XY table and inserted into the disk's wake where its (ion) IV characteristic can be measured as a function of location and potential. This "small beam in a large chamber" approach is adopted to minimize the effects of charge exchange ions and the chamber walls.

A common and reasonable goal of a laboratory plasma simulation is to provide scientific and engineering data that can be *scaled to space*. That sort of approach is limited in this problem because of the size of the parameter space that determines the current, I. The minimum set of dimensionless parameters are expressed,

$$I = I(\Phi_p, \Phi_d, R_p, R_d, M, D_{pd})$$

where $\Phi = eV/kT$, e is the electron charge, k is Boltzman's constant, T is the plasma temperature, V is the potential on both the disk V_d and the probe V_p, and $M = Velocity / \sqrt{2kT/m}$ is the ion Mach speed of the flow. The R's are radii of the disk and probe normalized by the Debye length, $\lambda_D = e\sqrt{N/kT\epsilon_0}$ and $D_{pd}=d/\lambda_D$ is the normalized separation distance. Certainly, if this list is complete, and each of the parameters are identical between two configurations, the currents should scale as well. Less trivial is the sort of scaling where one asks "how does *this* scale with *that*?", which is equivalent to knowing the physical law relating *this* and *that*, but with a minimum of 6 parameters, such laws are actually large families of relations that would be difficult to use even if known. One way to enhance the scalability of the laboratory results is to develop and/or apply a suitable computer model that can reproduce the laboratory results, and provide predictions for problems that are not parametrically identical to what was studied in the lab.

The Air Force Geophysics Laboratory has a 3D computer code, POLAR (*P*otential of *L*arge *O*bjects in the *A*uroral *R*egion; Cooke, 1985) to address this and other LEO spacecraft-plasma interactions. POLAR is a Poisson-Vlasov code that was written to model the interactions of large spacecraft with the LEO plasma and is somewhat specific to the space environment. POLAR can accept chamber plasma parameters, but cannot account for many other differences between chamber and space conditions, such as ion beam anisotropy and divergence, and thermo-electric (wall) effects.

A second computer code, MACH, has also been useful in this investigation. MACH (*M*esothermal *A*uroral *CH*arging; Tautz, 1987) is a [2D-3V] axisymmetric program that can perform both chamber and space simulations with an approach that differs significantly from POLAR.

In this paper, we describe the laboratory experiment and compare our results with both the MACH and the POLAR codes. We have found reasonable agreement in the results of the experimental and two numerical simulations. MACH produced a close match on structure of both 'ambient' and the high potential region close to the probe. POLAR's predicted current-voltage curve for the probe reproduces many of the curve characteristics. There does, however, appear to be secondary current effects that neither code predicted.

II. Laboratory Experiment

Our experiments were performed in a large cylindrical vacuum chamber with a diameter of 1.7m and a length of 1.7m. An ion gun (a three-grid Kaufman thruster) produces a flowing Argon plasma into which an aluminum disk of radius $b = 10 cm$ is inserted. A stainless steel spherical probe with radius $a = 0.5 cm$ is placed behind the disk along the axis of the disk and the ion gun. The separation between the ion gun and the disk is approximately 35 to 40 cm while the separation between the disk and the spherical probe can be varied from 1 to 15 cm. The configuration of the chamber simulation viewed from the top and the side, is depicted in Fig. 1.
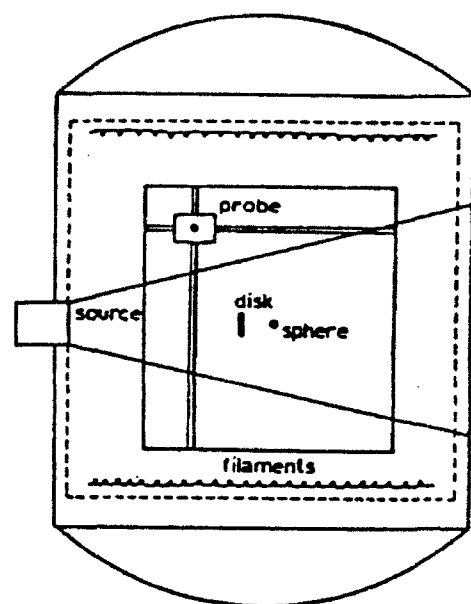
top view
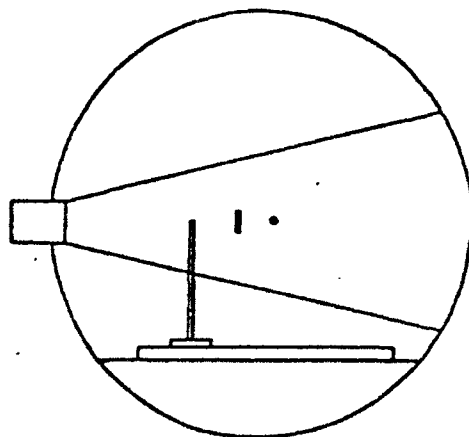
side view

Figure 1. Configuration of the Chamber simulation

Various Langmuir probes, emissive probes and retarding potential analyzers (RPA's) can be mounted on a XYZ table to perform three dimensional mapping of electron and ion current densities, temperatures, and plasma potential. For the ion current collection experiment, singly charged ions are accelerated across a 100V net potential drop to produce the flowing stream, then neutralized by electrons from a hot filament located near the last ion electrode. At a typical ion current of $I_b = 32\,mA$ and a neutralizing electron current of $I_n = 35\,mA$, the beam energy is measured by the RPA to be $90\,eV$ with a thermal energy width parallel to the beam of $T_{//} = 10\,eV$. The beam width (FWHM) is $40\,cm$ at the location of the disk and the corresponding plasma density is $N_p = 10^8\,cm^{-3}$. Using this density and the $T_{//} = 10\,eV$ produces a Debye length, $\lambda_D = 0.2\,cm$, making the disk about 42 λ_D across. The background pressure of the chamber is normally in the $10^{-7}\,Torr$ range and increases to 1 to $2x\,10^{-6}\,Torr$ when the ion gun is operated. Less than one percent of the ion species are found to be charge exchange cold ions with temperature less than $1\,eV$. The electron temperature is in the range of $5 - 8\,eV$, and the ion Mach number, $M \geq 3$. Near the beam center, the average plasma potential is 2 to 4 volts above ground which is in agreement with the plasma potential distributions calculated by the MACH code (see section VI).

In the present experiment, the sphere is biased from $V_p = 0$ to $-10kV$ and the collected ion current is measured with the circuit shown in Fig. 2. A current limiting resistor $R = 1MW$ is employed in the circuit to prevent current run away at high negative voltage with unexpected pressure rise due to arcing. The value of the current limiting resistor is chosen so that the I-V curve will

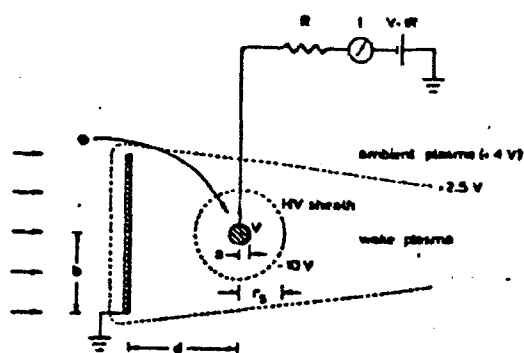not be distorted at its high-current end.

Figure 2. Schematic for Current Collection in the Wake

An emissive probe is used to measure the plasma potential around the charged sphere and in the wake of the disk. A small tungsten filament (1 *mil* in diameter) is heated to emission with a current of approximately 3 *mA*. A sweep generator is then used to vary the filament bias over a range from −30 to 30V. When the probe is biased more negatively than the plasma potential, the prob : will emit. This emission can be detected by measuring the voltage across a resistor to ground. As the bias voltage is swept from negative to positive, the emission will approach zero at the plasma potential. Using this technique, the potential around the charged sphere is measured with an error of ±0.2 V. The probe has a spatial resolution of 0.5 cm.

III. Observations

In Fig. 3, we show the ion current collected by the sphere as a function of the sphere bias voltage when the sphere is at a distance of 2, 4 and 10 cm behind the disk which is at ground potential. The current saturation at high bias voltages is a real

phenomenon and not an artifact due to the limiting resistor. The ion current increases almost vertically at −2.5kV when the operating neutral pressure is increased to $2 \times 10^{-5} torr$. At such high pressure, the high voltage can produce significant ionization which leads to current run away.

Upon careful examination of data such as Fig. 3, the following phenomena were observed: (1) There is a threshold voltage, V_{tr}, at which a rapid increase of ion current to the sphere is observed; (2) V_{tr} increases as the separation, d, between the disk and the sphere decreases (e.g. $V_{tr} = -2.2 kV$ at $d = 2 cm$ and $V_{tr} = -1.6 kV$ at $d = 10 cm$); and (3) The magnitude of collected ion current increases as d increases.
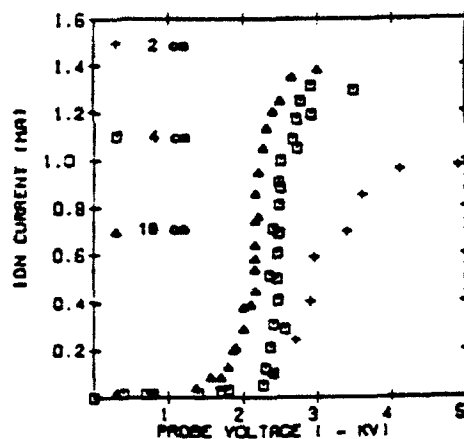

Figure 3. Measured Current collection versus Separation

Another observation, not obvious from Fig. 3, is an ion current relaxation at successive sphere voltage steps, the relaxation time t_o being typically a few minutes. The data presented in Fig. 3 is obtained by waiting 10 minutes between each voltage step. Data obtained in this fashion was reproducible from day to day and with only minor variations up to a few months during the course of this experiment.

However, swept I-V curves with each voltage step taken less than a few minutes apart (as in the case of a space experiment) may be problematic in the high voltage regime. The current fluctuations may be a result of reaching equilibrium between various processes (e.g. secondary electron emission, sputtering and of outgassing from the surface of the sphere) as the voltage increases by 20 to 50 V (a typical voltage step in our experiment). It may also be affected by the high voltage sheath capacitance in series with the current collecting circuit and the limiting resistor, R.

The collection of ions in the wake of a small object, as shown in Fig. 3, can be understood by studying the high voltage sheath in the wake of the disk. In Fig. 4, we show the three-dimensional plasma potential contours in the wake when $d = 5cm$ and the bias voltage on the sphere is $-5kV$. Because of the strong potential gradient near the sphere, the approximately 250 data points were taken with as fine a spatial resolution as possible (~ 0.5 cm). As the data was taken and the potential variation was observed, the mesh was varied accordingly. Therefore, must of the data points were taken near the sphere and the disk where the strongest gradients occurred. However, when the plasma potential was less than $-10V$, the emission of the probe was so small that accurate estimates of the potential were difficult. In addition, heating the probe to higher emission greatly reduced the probe's lifetime. Hence, the minimum potential measured was $-10V$ as indicated by the inner contour. To insure consistent measurements, the filament current was held constant through the entire data set.

The high voltage sheath is approximately spherical and bounded by the wake of the disk. If we assume that the $-10V$ equipotential contour represents the sheath edge,

the sheath thickness (radius) d_s increases from 2 to $4cm$ when the bias voltage V_p varies from $-1kV$ to $-5kV$.
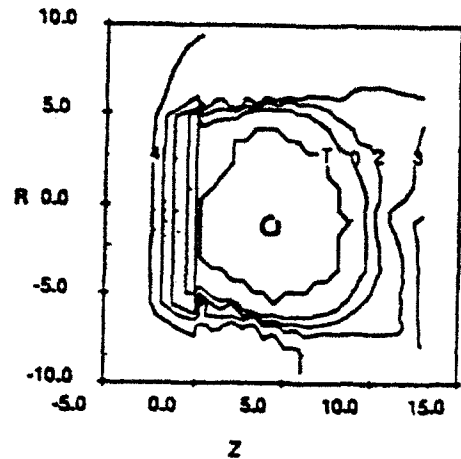

Figure 4. Measured Potential Contours for -5 KV probe Bias and separation $d = 5$ cm. Voltage Contour levels are:
$-10.0 = T$, $0.0 = 0$,
$2.0 = 2$, $3.0 = 3$,
$4.0 = 4$

The most obvious and significant results of the chamber tests is the observation of a sudden onset of ion current collection once a threshold voltage is attained. The magnitude of this threshold voltage is seen to vary with the separation between disk and sphere.

IV. Analysis

Our objective in this experiment, is to understand the magnitude and the morphology of the observed I-V curve, and to validate the computer models. Our analysis is based on the presumed interplay between three effects: sheath formation in the wake, conservation of angular momentum within the sheath, and the effect of weak non-radial fields outside of the sheath.

The electric fields reach saturated strength when the the space charge sheath

that the probe would attain outside of the wake begins to exceed the dimension of the wake. We claim that a sheath extending beyond the disk is a necessary but not sufficient condition for the current collection voltage threshold. Using the Langmuir-Blodgett (Langmuir, 1924) spherical sheath model, the sheath thickness can be expressed as (Parker, 1980):

$$d_s = a\left\{\frac{1}{2} + \left[\frac{1}{4} + \frac{d_{cl}}{a}\right]^{1/2} + 0.052\frac{d_{cl}}{a}\right\} \quad (1)$$

where $a = 0.5$ cm is the radius of the sphere and

$$d_{cl} = 1.26\lambda_D\left[\frac{eV_p}{kT}\right]^{3/4} \quad (2)$$

where d_{cl} is the thickness of the planar Child-Langmuir sheath and λ_D is the Debye length. For our experiment, using $\lambda_D = 0.23$ cm and $T = T_{//} = 10\,eV$ gives $d_s = 3.8$ cm at $V_p = -2kV$, which is a bit less than the disk radius $b = 5$ cm. $T = T_{//} = 10\,eV$ is, however, an overestimate of the appropriate temperature, since at $V_p < V_{tr}$, it is $T_\perp$ that specifies the flux into the wake, and for an idealized beam, $T_\perp$ can be undefined. The temperature that produces $d_s = b$ is $T = 5.5\,eV$, which might be reasonable. The value of this portion of our analysis is to identify the interaction of sheath and wake, and what is required of numerical tools to properly account for actual configurations.

The symmetry of the chamber experiment suggests that conservation of angular momentum will be another constraint on current collection. Letting the radius of the disk define a minimum impact parameter necessary for collection of the streaming ions by the sphere, the angular momentum, L_i, of ions relative to the sphere is initially,

$$L_i = b\left[2\frac{E_b}{m_i}\right]^{1/2} \quad (6)$$

and at the surface, biased to V_{tr}

$$L_f = a\left[2\frac{(E_b + eV_{tr})}{m_i}\right]^{1/2} \quad (7)$$

Setting these equal, conservation requires that:

$$V_{tr} = \frac{E_b(b^2 - a^2)}{e\,a^2} = 8.9\,kV \quad (8)$$

using $E_b = 90\,eV$, $b = 5\,cm$, and $a = 0.5\,cm$. This voltage threshold is significantly higher than what is measured. Furthermore, the angular momentum argument predicts no dependence on the separation between the disk and the sphere. This arises from the implicit assumption that the forces acting on the ion are spherically radial. While this is true in and near the sheath (that is, for most of the time the ion is accelerated), it is untrue near the edge of the disk where the electric field is more cylindrically radial as can be seen in Fig. 4, and 9. The electric field structure is such that an ion passing near the edge of the disk will be subjected to an impulse directed cylindrically radially inward. Suppose that an ion is turned though an angle θ at the edge. As Fig. 5 illustrates, it now approaches the sphere with an effective impact parameter b' that is less than b. This effective impact parameter may be shown to be:

$$b' = b\cos\theta - d\sin\theta \quad (9)$$

Substituting b' for b in Eq. 8 and solving for V as a function of d gives the results shown in Fig. 6, for $a = 0.5\,cm$ and $b = 5\,cm$. Qualitatively, the experiment results are predicted; as the separation d increases, the threshold voltage decreases.
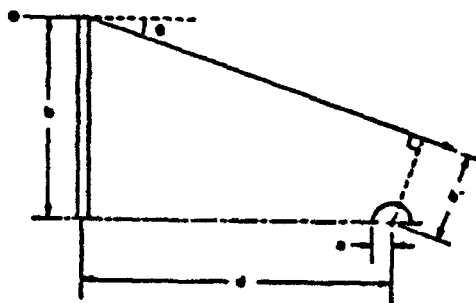
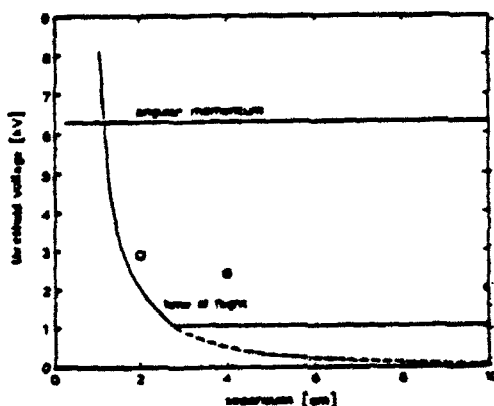*Figure S. Angular Momentum for Ions in the Wake*

Figure 6. Calculated Theshold Voltage Versus Probe Separation

The measured threshold voltages are also indicated on the figure. The measurements indicate that if the modified angular momentum criterion is correct, the deflection of the ions at the edge must be between approximately 10 and 25 degrees. We check this by making the assumption that the electric field near the edge of the disk is on the order of $kT_\perp / e \, \lambda_D$. Applying a time of flight analysis, where the length of the

interaction region is L, the angular deflection is given by

$$\theta = \tan^{-1}\left[\frac{V_\perp}{V_{//}}\right] = \tan^{-1}\left[\frac{LkT}{\lambda_D \, 2 E_b}\right] \quad (10)$$

Using $\lambda_D = 0.23 \, cm$, $kT_\perp/e = 4 V$, $E_b = 90 \, eV$ and $L \approx 4 \, cm$, Eq. 10 predicts $\theta = 20°$.

The angular momentum criterion provides another necessary but not sufficient bound on the threshold voltage required to attract ions to a small body in the wake of a larger body. The current collection is however, quite sensitive to the details of the field structure, especially near the edge of the shadowing body.

V. Enhanced Secondary Emission

The magnitude of the ion current collected by the sphere would also depend on several atomic processes occurring on the surface of the sphere. The first process is the sputtering of the surface by the energetic ions. Since the the sphere is biased at very negative potential, sputtered ions or back scattered ions off the sphere would be repelled back to the sphere by the ion sheath. The second process is emission of secondary electrons and negative ions which enhance the current to the sphere.

Enhanced secondary emission has been observed from a strongly negatively biased sphere inserted in an ion beam. Preliminary results indicate that this emission may increase the apparent ion current collected by the sphere by a factor of 2 - 3.

The enhanced secondary current was observed by placing in a beam plasma the same stainless steel sphere (0.5 cm radius) as was used in wake experiment just described. For this measurement, the sphere was

surrounded with a grounded spherical wire mesh, having a radius of 4.0 cm. The wire mesh ensured that the ion flux being accelerated into the negatively biased sphere was constant and independent of the bias voltage. In this configuration, the sphere was biased over the same range of negative potential as before, and current recorded. This current is the sum of the beam ion current and any secondary currents being emitted by the sphere or mesh. Fig 7. shows the amount of current collected by the sphere as a function of the bias voltage. It can be seen that the current rapidly rises for low bias voltages, rises more slowly just past -500 V, but rises more rapidly again at bias voltage greater than -2000 V. This current profile is consistent with the picture of beam ion current saturating near -500 V, and a secondary process providing current enhancement for more negative voltage. For bias potentials above -2000 V the rapid increase in the current collection would seem anomalous since all ions are already being collected by the biased sphere and the grounded spherical wire mesh prevents the expansion of the ion collection sheath.
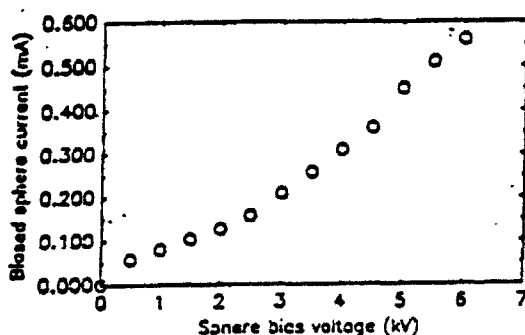

Figure 7. Measured Sphere Current Versus Bias Voltage

In order to ascertain that this increase in current is due to the emission of secondary particles, a gridded particle energy analyzer was placed at a radius of 5.4 cm from the biased sphere and looking radially inward. The energy analyzer was biased to reject all ions and electrons with an energy of less than 70 eV, which is higher than the beam energy of 20 eV, but less than the energy of a negative particle originating from the biased sphere surface. It was noted that the amount of current collected by the energy analyzer is small until the sphere is biased to approximately -1500, after which it increases rapidly. This is the same voltage at which the current to the sphere starts to increase again.

By moving the energy analyzer azimuthally around the biased sphere in the plane of the beam the total amount of secondary current can be calculated. This amounts to approximately 50% of the total current collected by the biased sphere when the bias is set at -4000 V. This compares favorably with the amount of current expected if one extrapolates the saturation current of the biased sphere to -4000 V. Both of these measurements indicate that the secondary current is comparable to the primary ion current and even exceeds it for sphere bias voltages more negative than -4000 V.

The energy distribution of the secondary particles was also measured. Fig. 8 shows the amount of current collected by the energy analyzer as a function of the repeller voltage. The sphere bias was set to -4000 V. The sharp cutoff of the analyzer current above 4000 V indicates that all of the particles coming from the biased sphere have an energy of 4000 eV. If the electrons (or ions) were born anywhere but on the sphere, as in the ionization of neutral gas in the gap between the sphere and mesh, a broader particle energy distribution would result.
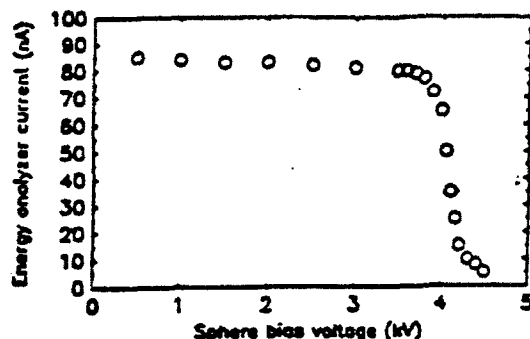
Figure 8. Measured Energy Analyser Current Versus Bias Voltage

The anticipated secondary electron yield for ion bombardment of stainless (composition uncertain) is about 10 to 20% over most of our energy range. The sputtering yield, however, of the constituent stainless metals under Argon bombardment rises to values greater than 1 or 2. This points to sputtering as a possible contributor to our high secondary current observations. Whether ions or electrons actually carry the secondary current remains to be determined.

VI. The MACH Code

The MACH (Tautz, 1987) code, derived from the earlier program TDWAKE (Parker, 1976), solves the Poisson-Vlasov equations self-consistently on a discrete cylindrical (R,Z) mesh. MACH solves the Poisson equation by simple first order differencing and point successive over relaxation with a space charge iteration similar to that of POLAR. A reversed trajectory "inside-out" method is used to calculate densities and currents by employing the result of Liouville's Theorem, "The distribution function, $f = f(v,r)$, is constant along a particle trajectory". Thus we build up and

integrate f to obtain densities and higher moments at each node in the grid, by tracing reverse trajectories to where f is known. This makes the specification of charged particle boundary conditions quite straght forward. This method of obtaining densities has a fundamental appeal, since there are no approximations beyond collisionless-ness. There is a presumption of trajectory accuracy, and that f can be sampled with sufficient resolution. We have been able to improve the resolution and efficiency of the method by employing a velocity space topology search, VSTS. At each node, trajectories are "launched" initially at coarse intervals. Intervals are repeatedly halved on subsequent passes, if inspection of f on the previous interval indicates that a region needs greater resolution. VSTS has significantly extended the high voltage capability of the inside-out method, however velocity space resolution still sets the high voltage limits of the method.

The wall boundary conditions for the chamber simulations are zero potential and no emission. The ion gun is represented as a zero potential boundary emitting a a drifting Maxwellian ion distribution. Electrons from the neutralizing filement are represented by an isotropic Maxwellian source. All particles incident on the probe, the disk or the walls are assumed to be absorbed.

Possibly the most fundamental difference between chamber and space plasma is the electron population and in particular how trapped electrons are modeled. In space, a collisionless (Vlasov) plasma has $n(e) \approx n(i)$, and $j(e) \gg j(i)$ whereas our plasma source produces $j(e) \approx j(i)$ and $n(e) \ll n(i)$. Modeling the plasma with only Vlasov electrons results in violently unphysical space charge instability. MACH has a trapped electron model in which the ion space charge creates a potential well for

electrons, of depth Φ. The code assumes that electrons scatter into this well and establish an isotropic equilibrium, with a temperature equal to the Vlasov electrons.

For comparison with this experiment MACH simulations were done with the front disk at zero potential and the sphere biased to $-1, -3$ and $-5KV$. The separation distance between the disk and the probe was taken to be $d= 5$ cm. The potential contours for the $-5KV$ case are shown in Figure 9. It can be seen that the MACH solutions and the measurements both consist of an approximatley spherical region of high negative potential centered on the probe which decreases through zero into regions of positive potential where trapped electrons balance the source ions.
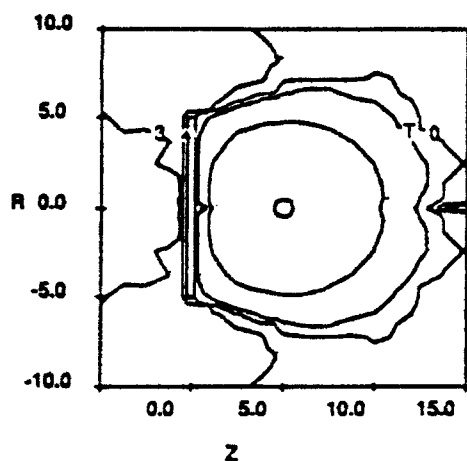
Figure 9. MACH Code Simulation of Potentials for -5 KV probe Bias and separation of d = 5 cm
Voltage Contour levels are:
-10.0 = T   ,0.0 = 0,
2.0 = 2   ,3.0 = 3,
4.0 = 4

We have performed experiments and Mach simulations of the ion gun plasma without the disk or the spherical probe. For our beam, both experiment and simulation show a maximum positive space potential of about 4 Volts with good agreement on the distribution of potential throughout the beam region. This can also be observed on the edges of Figures 4 and 9, although with the disk and biased probe, the agreement near the probe is not as good as without.

The probe currents predicted by MACH are shown in Fig. 12. That these are less than the experimental or POLAR currents is expected. In the case of the experiment the as yet unquantified secondary emission effects can lead to a large increases in current and secondary emission is not modeled in MACH.

VII. The POLAR Code

POLAR is a self-consistent three dimensional Poisson-Vlasov code, that provides steady state solutions by iterating between potential (Poisson) and density (Vlasov) solutions on a cubical mesh. A versatile set of building elements can be combined to form complex objects with a variety of surface materials and electrical connections. A surface charging module can be added to the iteration to provide the spacecraft charging response to both natural and induced charge drivers. The Poisson solver uses a finite element conjugate gradient method, with a unique technique of filtering charge densities to suppress grid noise, and produce stable solutions. POLAR calculates particle densities by a method that divides space into (one or more) sheath and non-sheath regions separated by a sheath edge(s). External to sheath regions, densities are determined by geometric ray tracing with first order electric field corrections. This approach has been shown to correctly predict wake formation about the Space Shuttle Orbiter (Murphy et.al., 1987). Internal to the

sheath, POLAR tracks ions and/or electrons to obtain densities. The POLAR method of particle tracking begins at a sheath edge, located as an equi-potential, near kT. External to this surface the plasma distribution is presumed to be Maxwellian with possible flow. Assuming a spherical r^{-2} potential variation outside of the sheath allows one to use the usual constants of motion and determine the flux and entry velocity of ions which are assigned to a super-particle and tracked. Densities are determined from the time spent in each volume element, and surface currents from their final deposition. When particles are repelled, their density is assumed to be Boltzmann.

POLAR was used to simulate the chamber experiment, using an octagonal disk, 9 grid units across, and a single unit cube for the probe. This is the minimum resolution that could be used, but higher resolution models indicated that it was adequate. Since POLAR does not trace trajectories outside of the sheath, the finite particle beam and walls could not be modeled. The Argon plasma input parameters were $N_e = 10^8 cc^{-1}$, $kT = 10 eV$ and the ion Mach number $M = 3$, The mesh spacing was $1.1 cm$. corresponding to a Debye length of $\lambda_D = 0.23 cm$, so that the disk was $42 \lambda_D$ across. The front disk was held at a bias of $V_d = -1.0 Volt$, and the probe voltage was swept from $V_p = -0.5$ to $-5.5 kV$ in a series of runs.

A two dimensional cut through the $-5 kV$ simulation is shown in Fig. 1., illustrating disk, probe, sheath and additional equipotential contours. We note that there are no positive potential contours which is reasonable since POLAR does not model the trapped electron population. Also shown in the plot are three out of the approximately 2000 trajectories traced by POLAR. Two of

these enter the sheath very near the disk and have sufficiently little angular momentum to be collected. One trajectory missed the probe and has begun to orbit. It has been truncated for the figure only. These psuedo-trapped particles pose great difficulty for any steady state calculation, since they continue to contribute space charge as they orbit indefinitally. In the next Poisson solution, enough of this charge will cause the sheath to contract and exclude many of the psuedo-trapped orbits in the next current cycle. This may be controlled numericaly, and in POLAR, the orbit count is reduced untill the cycle to cycle current fluctuations are reasonable. Although this phenomenon is numerical, it does however point to the possibility of oscillations on the ion time scale.
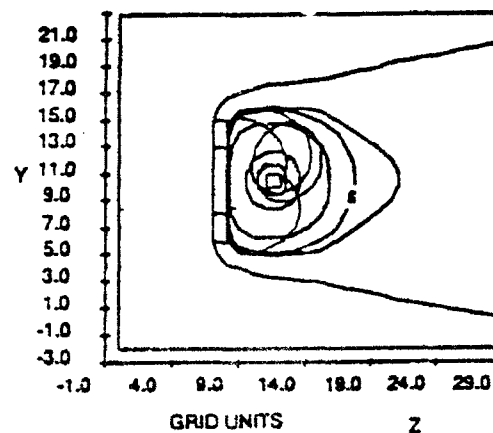

Figure 10. POLAR Code Potentials and Trajectories for -5 KV Probe Bias
Voltage Contour levels are:
-3000.0 , -1000.0
-100.0 , -20.0 = S
-10.0 , -1.0

The results of the complete suite of POLAR chamber runs are summarized in Fig. 11, where in addition to the voltage sweep, the separation distance between probe

and disk was varied through values of $d = 2.7, 3.8$ and $4.9\ cm$. The multiple points represent the degree of trapped orbit fluctuation.
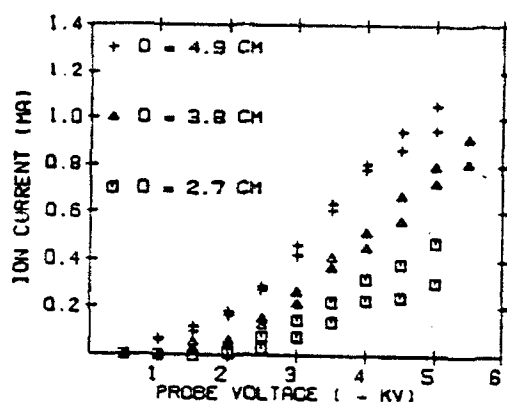

Figure 11. *POLAR Code Simulation of Ion Current*

The comparison between these results and the chamber measurements are better than expected considering the lack of finite beam and wall effects. In particular, there is close agreement between the measurements and POLAR's predicted onset for current collection and the variation with separation distance. At voltages above onset, POLAR, as MACH, underestimates the current. Some underestimate is to be expected since secondary emission is turned off in both codes. This was done to show just the ion current since the measurements seem to indicate an "xotic secondary emission mechanism.

VIII. *Comparisons and Discussion*

Our goals in this study were to learn something about the collection of current in the wake of and orbiting body, and to evaluate the effectiveness of our computational tools for this type of problem.

There are points of both agreement and disagreement between the simulations.

All three simulations were in close agreement on the voltage threshold for current collection. This implies that for at least the present set of parameters, our tools can model the combined contraints of angular momentum and spacecharge, or at least the more restrictive of the two. There is rough agreement on the magnitude of the current collection, but it could be better. The currents from the experiment and numerical simulations are shown together in Fig 12.
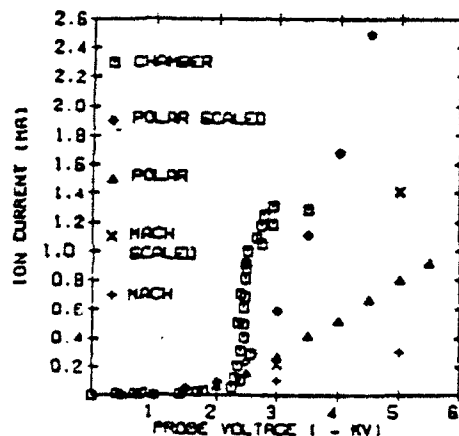

Figure 12. *Simulation Currents Versus Experimental Currents*

Some of the the dissagreement is certainly related to the unexpectedly high levels secondary emission discovered by the experiment. Secondary enhancement factors have been taken from the experiment, and applied to the the POLAR and MACH currents, and are displayed also in figure 12. In this case, the MACH predictions are now closer to the experiment and POLAR is too high. This is what was expected at the onset since POLAR includes a contribution from plasma beyond the extent of the experimental ion beam.

The agreement is worst on the overall morphology of the I-V curves. Although the experiment and numerical simulations agree on the turn-on inflection, the subsequent current rise is missed by both codes. Also missed was the second inflection at higher voltage where the experimental currents saturate, and the codes do not. This remains unexplained, but we can speculate on the cause of this effect. If the secondary current is carried by charged sputtered metalic ions, there would be a significant modification to the sheath spacecharge. At levels of secondary emission near the primary current, the effect would be to cancel some of the shielding Argon spacecharge and to enhance the current presuming that it was at least somewhat spacecharge limited. However, at the higher observed levels the surface charge of the probe would seem to 'come off' causing the primary ions to still enter the sheath but not find the probe. A similar effect has been noted in the operation of Hollow Cathodes in 'ignited' mode where the bulk of ionization begins to occur outside of the device in the nearby space (Wilber,1985; Cooke,1988)

Another parameter that has not been studied, but has been implicated as significant is the disk potential. The effect of this has been looked at by Katz et.al. (Katz, 1987) and found to indeed be significant.

Finally, we have used POLAR to take this issue to space. Scaling the chamber simulations Low Earth Orbit conditions while keeping the dimensionless variables described in section I constant, produced as anticipated, exactly scaled currents. This is of limited utility since an object only 40 Debye lengths ($\approx 40\,cm$) across is quite small, the scaled voltage threshold was only about 20 *Volts*, and the velocity was sub-orbital. A realistic suite of LEO condition runs has not yet been completed, but the POLAR runs so far indicate that for a Shuttle sized object (and 1/10 sized probe), the voltage threshold should be about a few hundred *Volts*.

II. References

Cooke, D.L., and I. Katz, "Ionization-Induced Instability in an Electron-Collecting Sheath", Journal of Spacecraft and Rockets Vol 25, #2, pp. 132-138, March 1988.

Katz, I., M.J.Mandell, D.E.Parks, K.Wright, N.H.Stone, and U.Samir, "The effect of Object Potentials on the Wake of a flowing Plasma" J. Appl. Phys. 62(7), Oct 1987, AFGL-TR-87-0023, 1986. ADA184038

Langmuir,I. and Blodgett,K. B.; "Currents Limited by Space Charge Between Concentric Spheres," Physical Review, 24, July, 1924.

Lilley J.R.Jr., D.L. Cooke, G.A. Jongward, I. Katz, "POLAR Users Manual", AFGL-TR-85-0246, 1985. ADA173758

Murphy, G., and I. Katz, "The POLAR Code Wake Model: Comparison with in Situ Observations", J.Geophys.Res., V94, pp. 1,450, 1989.

Parker, L.W. ; "Plasmasheath-Photosheath Theory for Large Space Structures", in Space Systems and Their Interactions with the Earth's Space Environment, Prog. in Ast. and Aero. Vol.71, ed. by H.B. Garret, and C.P. Pike, 1980.

Parker, L.W., "Computation of Collisionless Steady-State Flow Past a Charged Disk", NASA CR-144159, 1976.

Tautz, M.F., D.L. Cooke, A.G. Rubin, G.K.

Yates, "Preliminary Documentation of the MACH Code", AFGL-TR-88-0035, 1987, ADA198956

Wei, R., and P.J. Wilbur, "Space-Charge-Limited Current Flow in a Spherical Double Sheath", Jounrnal of Applied Physics, Vol 60, pp. 2280-2284, Oct. 1986

A Preliminary Spacecraft Charging Map for the Near Earth Environment

Robin Evans, Henry Garrett, Stephen Gabriel and Al Whittlesey

Jet Propulsion Laboratory

ABSTRACT

Spacecraft in the vicinity of the Earth can encounter many different spacecraft charging regions. Although in general each spacecraft along with its particular orbit should be evaluated for charging possibilities a generalized charging map of the magnetosphere can be useful for early evaluation of spacecraft charging. Here, a preliminary worst case charging map for the Earth's magnetosphere is presented for the purpose of providing quick estimates of possible problems. As would be anticipated, high level charging is generally confined to the magnetic field lines that map to the auroral oval and the plasmasheet, and moderate level charging (~100 V) occurs in the Magnetosheath. For the simple charging model considered, charging below 200 km in an auroral arc is in the -10's of Volts range Between 200 km and 2000 km, the charging rises to over -650 Volts. Above 2000 km the charging rises to -1000 Volts at 15000 km. In the plasmasheet (including GEO orbits), charging can be as much as -28,000 Volts.

INTRODUCTION

A generalized map of the near-Earth charging environment, with an estimate of "worst case" charging potentials is produced here for use in early mission development. The map is not to be used for analysis of specific spacecraft charging problems since the environment is much too variable, but as a quick visual aid for estimating whether charging will be of concern for a particular mission. It should also be of general value for discussing spacecraft charging problems with those not familiar with spacecraft charging, because it shows the regions of concern for the Earth environment.

The original impetus for this study resulted from a requirement for order of magnitude estimates of the possibility of ESD problems on some JPL missions. They were high inclination orbit missions which pass through the auroral zones. The time spent on the estimate was limited by the necessity of a rapid response for the projects. The locations of the serious charging levels is believed to be properly presented here (for $K_p = 5$, and local time = midnight) but the actual charging levels may change. Also since these environments are extremely variable, the locations and levels of charging will vary or disappear with different K_p and local times.

CHARGING MODELS

A simple charging model using current balance is used here. Incoming electrons and ions are balanced against backscattering and secondary emission. Photo-emission electrons are included in the model but are set to zero here (midnight - or shadow) to yield worst-case charging estimates. The program interates the potential until, at a particular voltage, these currents are balanced according to

$$I_e = I_I + I_{se} + I_{sI} + I_{BSe} + I_{ph} \tag{1}$$

where,

I_e = Incident electron current,

I_I = Incident ion current,

I_{se} = secondary emitted electron current due to I_e,

I_{sI} = secondary emitted electron current due to I_I,

I_{BSe} = Back scattered electron current due to I_e,

I_{ph} = photoelectron current.

For this particular study the electron and ion currents are taken from double Maxwellian distributions for the electrons and ions. Assuming that the secondary and backscatter terms can be parameterized, for an ambient Maxwellian plasma.

$$\sum_{i=1}^{2}(A_{ei} J_{ei}[1 - Se_i(V,T_{ei},n_{ei}) - BSe_i(V,T_{ei},n_{ei})] e^{(qV/kT_{ei})} - \sum_{k=1}^{2}(A_{Ik}J_{Ik} [1 + SI_k(V,T_{Ik},n_{Ik})] [1 - (qV/kT_{Ik})])$$
$$- A_{ph} J_{ph} f(X_m) = I_T = 0 \qquad \text{for } V < 0 \qquad (2)$$

where

J_{ei} = ambient electron current density,

J_{Ik} = ambient ion current density,

A_{ei} = electron collection area ($4 \pi r_s^2$ for a sphere)

A_{Ik} = ion collection area,($4 \pi r_s^2$ for a sphere),

A_{ph} = photoelectron emission area, (πr_s^2 for a sphere),

SE_i, SI_k, BSE_i = parameterized functions for secondary emission due to electrons and ions and backscatter electrons,

J_{ph} = saturation photoelectron flux,

$f(X_m)$ = percent of attenuated solar flux as a function of altitude X_m of center of sun above the surface of the Earth as seen by the satellite and the summation subscripts i and k are for the two Maxwellian populations assumed for the electron and ions respectively.

Equation (2) is appropriate for a small ($\approx$ 1 to 5 meter diameter), uniformly conducting satellite at geosynchronous orbit in the absence of magnetic field effects.

The charging model is further described in Garrett [1978 a and b], Garrett [1979], Garrett, et al. [1979] and Tsipouras et al. [1975]. It assumes a 1 to 5 meter aluminum sphere but has been validated by comparison to flight data. In general, but not included here, charging levels will also depend on surface electrical properties such as the exact value of the secondary electron emission coefficient, the directionality of the electron or ion fluxes, and the suppression of secondaries by magnetic mirroring.

ENVIRONMENTAL MODELS

Gussenhoven et al. [1985] and Deutsch [1981] are used to define worse case environments in two locations. Gussenhoven et al. [1985] found the highest charging in the aurora to be -679 Volts at 840 km altitude (measurement) and Deutsch [1981] found the highest charging at geosynchronous orbit could be

-28000 Volts in eclipse (calculated from a measured spectrum which charged ATS-6 to 2200 V while it was in sunlight). There is a discontinuity in the model between the plasma sheet and the inner magnetosphere produced by the termination of the low temperature plasma model used for background in the lower magnetosphere.

The auroral zone characteristics are difficult to accurately define. Several approximations were therefore necessary. The diffuse auroral zone is used to define the footprints of the magnetic field lines that carry the auroral electrons that will produce charging. The discrete aurora will produce the charging. A definition of the equatorward boundary of the discrete aurora was not available for this study. The poleward boundary seems not well defined during severe magnetic storms. Below 2000 km, the International Reference Ionosphere (IRI) model is used as a background plasma environment. Grebowosky et al. [1983] finds that there is a general weakening of the ionospheric densities near the poleward boundary of the auroral oval (drop of 1/5 above 1000 km) and Gussenhoven et al. [1985] finds sharper drops near regions of intense KeV electron precipitation (drop of 1/200 above 840 km). To reproduce the charging of Gussenhoven et al. [1985], the IRI densities need to be suppressed by a factor of 500. In general any charging level can be attained by suppressing the ionosphere by an arbitrary amount but the above suppression does not produces densities lower than those recorded in Gussenhoven et al. [1985]. Densities below 400 km are not suppressed because it is not known by measurements that this is the fact although swelling of the neutral atmosphere during storm conditions may accomplish this.

The auroral charging is estimated with a specific electron spectrum from the ATS-6 satellite. Gussenhoven et al. [1985]. In the aurora, the ionosphere which is used as a background (discharging) spectrum is suppressed to match the charging level found in Gussenhoven et al. [1985]. Above 800 km, the ionized hydrogen begins to dominate over ionized atomic oxygen and the charging level is reduced. As the IRI model only goes to 2000 km the plasmasphere model of Chiu et al. [1979] was used for background at higher altitudes (greater than 2000 km). Reiff et al. [1988] concludes that half of the acceleration of the discreet auroral electrons is above 2000 km altitude and Moser et al. [1980] concludes that the bulk of the acceleration is above 4000 km altitude. Here 2000 to 14000 km is used as the acceleration region.

In order to estimate the effect of a parallel electric field, no mirroring is assumed for the auroral electrons. It can be shown that mirroring is suppressed if a sufficiently large parallel electric field exist in the region. Simply, following Chen [1985], the force on a electron in a curved magnetic field with an electric field parallel to the magnetic field is given by

$$F_{\parallel} = -\mu \frac{\partial B}{\partial s} + qE,$$ (3)

where,

μ = the magnetic moment and

s = the pathlength along the field line.

The first term is the magnetic mirroring and the second is the electric field. For no mirroring this quantity should remain negative or zero. For this model the acceleration is assumed to be from a simple linear electric field.

The worst case auroral environment is assumed any time a spacecraft is inside the diffuse auroral oval defined by Whalen et al. [1985], where the equatorial boundary in geomagnetic latitude, GMB, is given by,

$$GMB \ (degrees) = 72 - 0.9Q - (5.1) \cos((360°/24)(t-12°) + \alpha K_p,$$ (4)

617

where,

Q = a magnetic index that is generally unknown other than by solving
      (range 1 to 8)
for it using this equation.'''

lt = local time of the spacecraft

α = a local time dependent parameter (Whalen et al. [1985]) and

K_p = the magnetic storm index.

The parameters Q and K_p are assumed to be 5 and 6 respectively in this study. The charging environment so defined roughly corresponds to a "worst-case" environment enveloping 95% of the charging events. The poleward boundary is found by measuring the thickness of the auroral oval for the proper local times off Figure 12-7 of Whalen et al. [1985].

Outside the ionosphere, diffuse aurora zone, acceleration region, and the plasmasphere are the plasmapause, the outer magnetosphere and the magnetosheath. The plasmapause is ignored in this study because, at night, it is a thin region without well defined boundaries. It has been modeled for use in a daytime estimate at a later date. The outer magnetosphere is modeled generically (one density/temperature fits all). This model produces no charging. The magnetosheath is the Garrett and Deforest [1979] equatorial model that has been made into a 3-D model by rotating it about the sun-earth axis.

No attempt has been made to account for time variations caused by the orientation of the Earth's magnetic polar axis. The model that produced the map does take these variations into account but to reproduce them in the map would make it too complex and therefore less useful for the stated purpose. The polar cusp is also ignored.

RESULTS

In general, charging is serious only along field lines that map to the auroral zone or inside that zone. This includes the plasmasheet and the magnetosheath regions, any location on a field line that maps down to the auroral zone, and any location past the magnetopause.

The models are constructed so as to reproduce worst case charging for the various regions and not to predict higher levels than has been reported (i.e., since the ionosphere's behavior under these circumstances is not well known, the 600 Volt level for DMSP is fitted and no attempt is made to find a spectrum that will exceed the 600 Volts). This assumption has the result of predicting what level of charging would be experienced at different altitudes for that same spectrum.

The locations for the charging are found for the conditions $Q=5$ (Q is the magnetic index that defines the auroral oval equatorial boundary) and $K_p=5$ (K_p is the magnetic storm index). A series of cases have been run at midnight for all latitudes at 281 degrees east longitude (this includes the north magnetic pole) for altitudes up to 100,000 km. The effect of varying the longitude, K_p or local time would be to shift the charging region to follow the footprints of the auroral oval. For sunlight, the map would only be good for parts of the spacecraft that are isolated electrically from the rest of the spacecraft and in shadow.

Charging levels are presented in the contour map accompanying this paper. Two regions are needed to produce the charging levels in the auroral/acceleration zone and the outer plasma sheet. Matching these two models together has not been accomplished yet so there is a region between the models where the charging levels are discontinuous as stated above. This will probably be eliminated in a later version of

the model.

USAGE

The original usage intended for this contour map was to advise managers of Earth orbiting satellites whether they should worry at all about spacecraft charging effects, given the proposed altitude and inclination. For that purpose, the contour map has met its goal.

For more specific questions involving specific satellite geometry and materials, charging magnitude, higher intensity storms, probability vs longitude or local time, etc., the manager should request and get a detailed calculation for that case.

It can be seen that many assumptions were necessary to provide the continuity in space from one regime to another, and to make the analytic models match the observed data. These difficulties are presented as a question to our colleagues to expand our knowledge of spacecraft charging environments so we can include them in our model.

Acknowledgements

REFERENCES:

Chen, F., "Plasma Physics and Controlled Fusion", Second Edition, Plenum Press, 1985, section 2.3.3

Chiu, Y., Luhmann, J. G., Ching, B. K., and Boucher, D. J. Jr., " An Equilibrium Model of Plasmaspheric Composition and Density", JGR, 84, A3, 909, 1979

Deutsch, M-J.C., "Worst case Earth Charging Environment", JSR, 19, 5, 473, 1981

Garrett, H.B., "Spacecraft Potential Calculations - A Model", AFGL-TR-78-0116, 1978, ADA060151

Garrett, H.B., "Modeling of the Geosynchronous Orbit Plasma Environment - Part I", AFGL-TR-77-0288, 1978, ADA053164

Garrett, H. B., "Quantitative Models of 0-100 KeV Mid-Magnetospheric Plasma Environment", in "Quantitative Modeling of the Magnetospheric Processes", Geophys. Monogr. Ser., 21, ed W. Olson, AGU 1979

Garrett, H.B., DeForest, S.E., " nalytical Simulation of the Geosynchronous Plasma Environment", Plan. Space Sci., 27, 1101, 1979

Grebowosky, J. and Talor, H., "Location and Source of Ionospheric High Latitude Troughs", Plan. Space Sci. 31, 1, 99, 1983

Gussenhoven, M. S., Hardy, D., Rich, F., and Burk, W. J., "High-Level Spacecraft Charging in the Low-Altitude Polar Auroral Environment", JGR, 90, A11, 11009, 1985

Moser, F., et al., "Satellite Measurements and Theories of Low Altitude Particle Acceleration", Space Sci. Rev., 27, 155, 1980

Reiff, P., Collin, H. L., Craven, J. D., Burch, J. L., Winningham, J. D., Shelley, E. G., Frank, L. A., and Frieman, M., "A Determination of Auroral Electrostatic Potentials Using High- and Low-Altitude Particle Distributions", JGR, 93, A7, 7441, 1988

Tsipouras, P. and Garrett, H.B., "Spacecraft Charging Model - Two Maxwellian Approximation", AFGL-TR-79-0153, 1979, **ADA077907**

Whalen, J. A., O'Neil, R., and Picard, R. H., "The Aurora, Chapter 12, Handbook of Geophysics and Space Environment", AFGL, ed. A. S. Jursa, 1985, **ADA167000**

CHARGING POTENTIAL (VOLTS)

Index of Authors